



**National Library
of Canada**

Canadian Theses Service

Ottawa, Canada
K1A 0N4

**Bibliothèque nationale
du Canada**

Service des thèses canadiennes

NOTICE

The quality of this microform is heavily dependent upon the quality of the original thesis submitted for microfilming. Every effort has been made to ensure the highest quality of reproduction possible.

If pages are missing, contact the university which granted the degree.

Some pages may have indistinct print especially if the original pages were typed with a poor typewriter ribbon or if the university sent us an inferior photocopy.

Reproduction in full or in part of this microform is governed by the Canadian Copyright Act, R.S.C. 1970, c. C-30, and subsequent amendments.

AVIS

La qualité de cette microforme dépend grandement de la qualité de la thèse soumise au microfilmage. Nous avons tout fait pour assurer une qualité supérieure de reproduction.

S'il manque des pages, veuillez communiquer avec l'université qui a conféré le grade.

La qualité d'impression de certaines pages peut laisser à désirer, surtout si les pages originales ont été dactylographiées à l'aide d'un ruban usé ou si l'université nous a fait parvenir une photocopie de qualité inférieure.

La reproduction, même partielle, de cette microforme est soumise à la Loi canadienne sur le droit d'auteur, SRC 1970, c. C-30, et ses amendements subséquents.



**National Library
of Canada**

**Bibliothèque nationale
du Canada**

Canadian Theses Service

Service des thèses canadiennes

Ottawa, Canada
K1A 0N4

The author has granted an irrevocable non-exclusive licence allowing the National Library of Canada to reproduce, loan, distribute or sell copies of his/her thesis by any means and in any form or format, making this thesis available to interested persons.

The author retains ownership of the copyright in his/her thesis. Neither the thesis nor substantial extracts from it may be printed or otherwise reproduced without his/her permission.

L'auteur a accordé une licence irrévocable et non exclusive permettant à la Bibliothèque nationale du Canada de reproduire, prêter, distribuer ou vendre des copies de sa thèse de quelque manière et sous quelque forme que ce soit pour mettre des exemplaires de cette thèse à la disposition des personnes intéressées.

L'auteur conserve la propriété du droit d'auteur qui protège sa thèse. Ni la thèse ni des extraits substantiels de celle-ci ne doivent être imprimés ou autrement reproduits sans son autorisation.

ISBN 0-315-55578-5

Canada

THE UNIVERSITY OF ALBERTA

A RELATIVISTIC TREATMENT OF PHOTONUCLEON KNOCKOUT REACTIONS

BY

GERHARD MARTIN LOTZ



A THESIS

SUBMITTED TO THE FACULTY OF GRADUATE STUDIES AND RESEARCH

IN PARTIAL FULFILMENT OF THE REQUIREMENTS FOR THE DEGREE

OF DOCTOR OF PHILOSOPHY

IN

NUCLEAR PHYSICS

DEPARTMENT OF PHYSICS

EDMONTON, ALBERTA

FALL 1989

THE UNIVERSITY OF ALBERTA

RELEASE FORM

NAME OF AUTHOR: GERHARD MARTIN LOTZ
TITLE OF THESIS: A RELATIVISTIC TREATMENT OF
PHOTONUCLEON KNOCKOUT REACTIONS
DEGREE: DOCTOR OF PHILOSOPHY
YEAR THIS DEGREE GRANTED: 1989

Permission is hereby granted to THE UNIVERSITY OF ALBERTA LIBRARY to reproduce single copies of this thesis and to lend or sell such copies for private, scholarly or scientific research purposes only.

The author reserves other publication rights, and neither the thesis nor extensive abstracts from it may be printed or otherwise reproduced without the author's written permission.



Permanent address:
9031-56 Street,
Edmonton, Alberta,
Canada, T6B 1J1.

Date: July 10, 1989

THE UNIVERSITY OF ALBERTA
FACULTY OF GRADUATE STUDIES AND RESEARCH

The undersigned certify that they have read, and recommend to the Faculty of Graduate Studies and Research for acceptance, a thesis entitled *A Relativistic Treatment of Photonucleon Knockout Reactions* submitted by Gerhard Martin Lotz in partial fulfilment of the requirements for the degree of Doctor of Philosophy in Nuclear Physics.

Henry S. Siff
Supervisor

John ...

Nathan Robinson

Arthur ...

J.P. Kingle

Geoff A. Miller
External Examiner

Date: June 6, 1989

ABSTRACT

Reactions in which an intermediate energy photon is absorbed by a nuclear target resulting in the emission of single proton or neutron with the residual nucleus being left in a definite state are investigated in a relativistic framework. The reaction mechanism that is studied in detail is the direct interaction of the photon with a single nucleon in the nucleus. In the model proposed the bound and continuum nucleon wave functions are solutions of Dirac equations that contain appropriate relativistic potentials. The binding potential is determined from relativistic Hartree calculations or is parameterized to have a geometry that follows the nuclear density. The continuum nucleon is modelled to interact with the nucleus through an optical potential that is determined from microscopic calculations or from a phenomenological analysis of the elastic scattering data.

The results of the direct mechanism calculation are compared with data for the $^{16}\text{O}(\gamma,p)^{15}\text{N}$, $^{40}\text{Ca}(\gamma,p)^{39}\text{K}$, $^{11}\text{B}(\vec{p},\gamma)^{12}\text{C}$ and $^3\text{H}(\vec{p},\gamma)^4\text{He}$ reactions. The calculations exhibit reasonable agreement with the available data at lower momentum transfers and there is an indication that other reaction mechanisms become important at higher momentum transfers. For photoneutron knockout reactions on the other hand the direct mechanism calculations significantly underestimate the available data. The sensitivity of the calculations to the particular potentials used is studied in detail.

The possibility of the photoemitted nucleon charge exchanging as it leaves the nucleus is also investigated. The charge exchange is mediated by a relativistic isovector optical potential that is determined from microscopic calculations. The results of this calculation for the $^{16}\text{O}(\gamma,n)^{15}\text{O}$ and $^{12}\text{C}(\gamma,n)^{11}\text{C}$ reactions show that the final state charge exchange amplitude is comparable with the direct amplitude. The data is not reproduced, however, which indicates that other reaction mechanisms are important for (γ,n) reactions.

ACKNOWLEDGEMENTS

I am grateful to my supervisor, Dr. Helmy Sherif, for his guidance, physical insight, patience and kindness in the course of this research. Helmy allowed me a great deal of independence in this learning experience which was combined with always valuable discussions that kept me more-or-less on track.

Dr. Tim Cooper was always ready to help with problems and offer new insights. His kindness is much appreciated. Discussions with Dr. Javed Iqbal, Dr. F.C. Khanna and Dr. A.N. Kamal also were very helpful in understanding aspects of the research. I thank all of you for your graciousness.

Thank you to my fellow students Geoff Edwards, Richard Tkachuk, Ron Mitchell, Ken Starko, Reyad Sawafta, Jon Johansson, Phil Langil and Evan Hackett for sharing your knowledge and friendship.

Finally, I acknowledge the financial support of the Natural Sciences and Engineering Council, the Government of Alberta and the Physics Department during my time as a graduate student.

Table of Contents

A Relativistic Treatment of Photonucleon Knockout Reactions

1. Introduction	1
2. A Review of Calculations for Photonucleon Knockout Reactions	6
2.1 The Quasideuteron Model	6
2.2 The Direct Mechanism	7
2.3 The $\Delta(1232)$ Isobar	10
2.4 Meson Exchange Currents	12
2.5 RPA Calculations	16
2.6 Discussion	17
3. Relativistic Nucleon Dynamics	20
3.1 Relativistic Hartree Description of Nuclei	20
3.2 Nucleon-Nucleus Scattering	23
3.2.1 Relativistic Hartree Description of Nucleon-Nucleus Scattering	23
3.2.2 Phenomenological Dirac Optical Potentials	24
3.2.3 The Relativistic Impulse Approximation	25
3.2.4 Microscopic Relativistic Nucleon-Nucleus Scattering	27
3.3 The Relativistic Nucleon Wave Functions	29
3.3.1 The Continuum Nucleon Wave Function	29
3.3.2 The Bound Nucleon Wave Function	34
4. The One Nucleon Model	39
4.1 The Lagrangian Formalism for the One Nucleon Model	39
4.2 The Scattering Matrix	42
4.3 The Plane Wave Born Approximation	45
4.4 The S -Matrix in the Distorted Wave Born Approximation	47
4.5 Observables for (γN) Reactions	51
5. Results of the One Nucleon Model for (γp) and (p, γ) Reactions	54
5.1 The $^{16}\text{O}(\gamma p)^{15}\text{N}$ Reaction	54
5.1.1 The $E_\gamma = 196$ MeV Differential Cross Section	54

5.1.2	Other Results	68
5.2	The $^{40}\text{Ca}(\gamma p)^{39}\text{K}$ Reaction	75
5.3	The $^{11}\text{B}(\vec{p}, \gamma)^{12}\text{C}$ Reaction	87
5.4	The $^3\text{H}(\vec{p}, \gamma)^4\text{He}$ Reaction	92
5.5	Discussion	97
5.5.1	Sensitivity of ONM Results to Wave Functions	97
5.5.2	Nuclear Recoil Corrections	99
6.	Final State Charge Exchange	102
6.1	The Charge Exchange Mechanism	102
6.2	The Isovector Optical Potential	105
6.3	The Relativistic Lane Equations and the Transition Matrix for a (γ, n) Reaction with Final State Charge Exchange	106
6.4	The Propagator Approach to (γ, n) Reactions with Final State Charge Exchange	109
6.5	Results of Final State Charge Exchange Calculations	116
6.6	Discussion	122
7.	Discussion and Conclusions	125
	<i>References</i>	132
	<i>Appendix A: Kinematics for Photonucleon Knockout Reactions</i>	139
	<i>Appendix B: Numerov Integration of Second-Order Differential Equations</i>	142
B.1	Homogeneous Equations	142
B.2	Inhomogeneous Equations	143
	<i>Appendix C: Numerics and the Calculation of Phase Shifts for the Nucleon Distorted Wave Function</i>	145
C.1	The Continuum Nucleon Distorted Wave Function	145
C.2	The Propagating Proton Wave Function	149
	<i>Appendix D: The Dirac Coulomb Wave Functions</i>	151
D.1	The Analytic Form of the Dirac Coulomb Wave Functions	151
D.2	Numerical Evaluation of the Dirac Coulomb Wave Functions	155
	<i>Appendix E: Numerics for the Bound Nucleon Wave Function</i>	158
	<i>Appendix F: Calculation of Observables for Photonucleon Knockout Reactions</i>	161
F.1	Cross Section	161
F.2	Polarization and Analyzing Power	164

List of Tables

Table	Description	Page
1.	Fields in the QHD-II Model of Serot and Walecka.	20
2.	Parabolic symmetric Woods-Saxon optical potential parameters determined for 200 MeV $\vec{p} + {}^{16}\text{O}$ elastic scattering.	62
3.	Woods-Saxon binding potential parameters for ${}^{16}\text{O}$	64
4.	Woods-Saxon optical potential parameters determined for 49.5 MeV $p + {}^{16}\text{O}$ elastic scattering.	74
5.	Woods-Saxon optical potential parameters determined for 100 MeV $p + {}^{16}\text{O}$ elastic scattering.	74
6.	Woods-Saxon binding potential parameters for ${}^{48}\text{Ca}$	84
7.	Woods-Saxon optical potential parameters used in the ONM calculations for the ${}^{11}\text{B}(\vec{p}, \gamma){}^{12}\text{C}$ reaction at $E_p = 50$ MeV.	92
8.	Woods-Saxon binding potential parameters for ${}^{12}\text{C}$	92
9.	Woods-Saxon optical potential parameters used in the ONM calculations for the ${}^3\text{H}(\vec{p}, \gamma){}^4\text{He}$ reaction at $E_p = 300$ MeV.	93
10.	Woods-Saxon binding potential parameters for ${}^4\text{He}$	94

List of Figures

Figure	Description	Page
1.	The Δ isobar contributions to nucleon photoemission.	10
2.	Photon interactions with the meson-baryon system.	12
3.	The contributions to the transition matrix of Eq. (2.13).	14
4.	Nonrelativistic calculations for the differential cross section of the 196 MeV $^{16}\text{O}(\gamma p)^{15}\text{N}$ reaction.	19
5.	Meson exchange diagrams for the NN amplitude in the first Born approximation.	27
6.	The upper and lower component momentum-space wave functions of the $1d_{3/2}$ proton of ^{40}Ca	38
7.	The Feynman diagram for a (γN) reaction in the One Nucleon Model.	39
8.	The coordinate frame in which the S -matrix is evaluated.	49
9.	Relativistic optical model calculation for observables of 200 MeV $\vec{p} + ^{16}\text{O}$ elastic scattering using the parabolic symmetric Woods-Saxon potential characterized by the parameters listed in Table 2.	56
10.	Phenomenological parabolic symmetric Woods-Saxon optical potential for 200 MeV $\vec{p} + ^{16}\text{O}$ elastic scattering characterized by the parameters listed in Table 2.	57
11.	Relativistic optical model calculation for observables of 200 MeV $\vec{p} + ^{16}\text{O}$ elastic scattering using the Fourier-Bessel parameterization for the potential shown in Fig. 12.	58

12.	Fourier-Bessel parameterized optical potential for 200 MeV $\vec{p} + {}^{16}\text{O}$ elastic scattering.	59
13.	Relativistic optical model calculation for observables of 200 MeV $\vec{p} + {}^{16}\text{O}$ elastic scattering using the microscopic potential shown in Fig. 14.	60
14.	Microscopic Dirac optical potential for 200 MeV $\vec{p} + {}^{16}\text{O}$ elastic scattering.	61
15.	ONM calculation for the differential cross section of the 196 MeV ${}^{16}\text{O}(\gamma p){}^{15}\text{N}$ reaction in which the Woods-Saxon binding potential of Table 3 and the parabolic symmetric Woods-Saxon optical potential of Table 2 are used.	65
16.	ONM calculations for the differential cross section of the 196 MeV ${}^{16}\text{O}(\gamma p){}^{15}\text{N}$ reaction in which a Hartree binding potential and various distorting potentials (solid: parabolic symmetric Woods-Saxon; dashed: Fourier-Bessel; dotted: microscopic) are used.	67
17.	ONM calculations for the differential cross section of the 257 MeV ${}^{16}\text{O}(\gamma p){}^{15}\text{N}$ reaction in which a Hartree binding potential and various distorting potentials (solid: parabolic symmetric Woods-Saxon; dashed: Fourier-Bessel; dotted: microscopic using 200 MeV NN t -matrices; dot-dashed: microscopic using 300 MeV NN t -matrices) are used.	69
18.	ONM calculations for the differential cross section of the 312 MeV ${}^{16}\text{O}(\gamma p){}^{15}\text{N}$ reaction in which a Hartree binding potential and a microscopic distorting potential are used.	70
19.	ONM calculations for the differential cross section of the 361 MeV ${}^{16}\text{O}(\gamma p){}^{15}\text{N}$ reaction in which a Hartree binding potential and two microscopic distorting potentials (solid: using 300 MeV NN t -matrices; dashed: using 400 MeV NN t -matrices) are used.	71

20.	ONM calculation for the differential cross section of the 60 MeV $^{16}\text{O}(\gamma p)^{15}\text{N}$ reaction in which a Hartree binding potential and a Woods-Saxon distorting potential are used.	72
21.	ONM calculations for the differential cross section of the 100 MeV $^{16}\text{O}(\gamma p)^{15}\text{N}$ reaction in which a Hartree binding potential and two distorting potentials (solid: Woods-Saxon; dashed: microscopic using 135 MeV NN t -matrices) are used.	73
22.	ONM calculations for the energy dependence of the differential cross section of the $^{16}\text{O}(\gamma p)^{15}\text{N}$ reaction at $\theta_p = 45^\circ, 90^\circ$ and 135° in which a Hartree binding potential and microscopic distorting potentials are used.	76
23.	ONM calculations for the differential cross section of the 151.3 MeV $^{40}\text{Ca}(\gamma p)^{39}\text{K}$ reaction in which a Hartree binding potential and various distorting potentials (solid: microscopic; dashed; case 1 global potential from Ref. 81; dotted: case 2 global potential from Ref. 81; dot-dashed: Woods-Saxon) are used.	78
24.	ONM calculations for the differential cross section of the 176.2 MeV $^{40}\text{Ca}(\gamma p)^{39}\text{K}$ reaction in which a Hartree binding potential and various distorting potentials (solid: microscopic; dashed; case 1 global potential from Ref. 81; dotted: case 2 global potential from Ref. 81; dot-dashed: Woods-Saxon) are used.	79
25.	ONM calculations for the differential cross section of the 201.2 MeV $^{40}\text{Ca}(\gamma p)^{39}\text{K}$ reaction in which a Hartree binding potential and various distorting potentials (solid: microscopic; dashed; case 1 global potential from Ref. 81; dotted: case 2 global potential from Ref. 81; dot-dashed: Woods-Saxon) are used.	80

26.	ONM calculations for the energy dependence of the differential cross section of the $^{16}\text{O}(\gamma p)^{15}\text{N}$ reaction at $\theta_p = 45^\circ, 90^\circ$ and 135° in which a Hartree binding potential and microscopic distorting potentials are used.	81
27.	ONM calculations for the energy dependence of the differential cross section of the $^{16}\text{O}(\gamma p)^{15}\text{N}$ reaction at $\theta_p = 45^\circ, 90^\circ$ and 135° in which a Hartree binding potential and phenomenological distorting potentials (solid curve: case 1 potentials of Refs. 81 and 82; dashed curve: case 2 potentials of Refs. 81 and 82; squares: Woods-Saxon optical potentials of Ref. 42) are used.	82
28.	ONM calculations for the energy dependence of the differential cross section of the $^{16}\text{O}(\gamma p)^{15}\text{N}$ reaction at $\theta_p = 45^\circ, 90^\circ$ and 135° in which the Woods-Saxon binding potential characterized by the parameters of Table 6 and phenomenological distorting potentials (solid curve: case 1 potentials of Refs. 81 and 82; dashed curve: case 2 potentials of Refs. 81 and 82; squares: Woods-Saxon optical potentials of Ref. 42) are used.	83
29.	ONM calculations for the energy dependence of the differential cross section of the $^{16}\text{O}(\gamma p)^{15}\text{N}$ reaction at $\theta_p = 45^\circ, 90^\circ$ and 135° in which bound nucleon wave functions that incorporate modifications to the Hartree approximation (solid: baryon vacuum fluctuations included in the Hartree calculation; dashed: Hartree-Fock bound nucleon wave function) and the case 2 global optical potentials of Refs. 81 and 82 are used.	85
30.	The meson exchange contributions to the Hartree-Fock potential.	86

31. ONM calculations for the differential cross section of the 50 MeV $^{11}\text{B}(\vec{p},\gamma)^{12}\text{C}$ reaction in which a Woods-Saxon distorting potential determined for 50 MeV $\vec{p} + ^9\text{Be}$ elastic scattering and either a Woods-Saxon binding potential (solid curve) or a Hartree binding potential (dashed curve) are used. 88
32. ONM calculations for the analyzing power of the 50 MeV $^{11}\text{B}(\vec{p},\gamma)^{12}\text{C}$ reaction in which a Woods-Saxon distorting potential determined for 50 MeV $\vec{p} + ^9\text{Be}$ elastic scattering and either a Woods-Saxon binding potential (solid curve) or a Hartree binding potential (dashed curve) are used. 89
33. ONM calculations for the differential cross section of the 50 MeV $^{11}\text{B}(\vec{p},\gamma)^{12}\text{C}$ reaction in which a Woods-Saxon distorting potential determined for 50 MeV $\vec{p} + ^{12}\text{C}$ elastic scattering and either a Woods-Saxon binding potential (solid curve) or a Hartree binding potential (dashed curve) are used. 90
34. ONM calculations for the analyzing power of the 50 MeV $^{11}\text{B}(\vec{p},\gamma)^{12}\text{C}$ reaction in which a Woods-Saxon distorting potential determined for 50 MeV $\vec{p} + ^{12}\text{C}$ elastic scattering and either a Woods-Saxon binding potential (solid curve) or a Hartree binding potential (dashed curve) are used. 91
35. ONM calculations for the differential cross section of the 300 MeV $^3\text{H}(\vec{p},\gamma)^4\text{He}$ reaction in which a Woods-Saxon binding potential and Woods-Saxon distorting potentials (solid: ^3He optical potential; dashed: ^4He optical potential) are used. 95
36. ONM calculations for the analyzing power of the 300 MeV $^3\text{H}(\vec{p},\gamma)^4\text{He}$ reaction in which a Woods-Saxon binding potential and Woods-Saxon distorting potentials (solid: ^3He optical potential; dashed: ^4He optical potential) are used. 96

37.	ONM calculation for the differential cross section of the 196 MeV $^{16}\text{O}(\gamma,p)^{15}\text{N}$ reaction in which a Hartree bound proton wave function and a plane wave continuum proton wave function are used.	98
38.	ONM calculations including recoil corrections (dashed curve: recoil corrections of Ref. 101; dot-dashed curve: recoil corrections of Ref. 102) for the differential cross section of the 196 MeV $^{16}\text{O}(\gamma,p)^{15}\text{N}$ reaction in which a Hartree binding potential and a microscopic distorting potentials are used.	101
39.	ONM calculation for the differential cross section of the 60 MeV $^{16}\text{O}(\gamma,n)^{15}\text{O}$ reaction in which a Hartree binding potential and the Woods-Saxon distorting potential characterized by the parameters of Table 4 are used.	103
40.	Feynman diagram for a (γp) reaction followed by a (p,n) reaction mediated by charged pion exchange.	104
41.	Diagrammatic representation of a (γ,n) reaction that proceeds through the photoemission of a proton followed by a single charge exchange that is mediated by the isovector optical potential.	105
42.	Final state charge exchange calculations for the differential cross section of the 60 MeV $^{16}\text{O}(\gamma,n)^{15}\text{O}$ reaction in which a Hartree binding potential, phenomenological isoscalar optical potential and microscopic isovector optical potential are used.	117
43.	Final state charge exchange calculations for the differential cross section of the 150 MeV $^{16}\text{O}(\gamma,n)^{15}\text{O}$ reaction in which a Hartree binding potential and microscopic isoscalar and isovector optical potentials are used.	119

44.	Final state charge exchange calculations for the differential cross section of the 200 MeV $^{16}\text{O}(\gamma,n)^{15}\text{O}$ reaction in which a Hartree binding potential, phenomenological isoscalar optical potential and microscopic isovector optical potential are used.	120
45.	Final state charge exchange calculations for the differential cross section of the 63 MeV $^{12}\text{C}(\gamma,n)^{11}\text{C}$ reaction in which a Hartree binding potential, phenomenological diagonal optical potential and microscopic isovector optical potential are used.	121
46.	Final state charge exchange calculations for the differential cross section of the 60 MeV $^{16}\text{O}(\gamma,p)^{15}\text{N}$ reaction in which a Hartree binding potential, phenomenological isoscalar optical potential and microscopic isovector optical potential are used.	123
47.	The radial function $y(r)$ for the $1d_{3/2}$ proton of ^{40}Ca	159

1. Introduction

Electromagnetic interactions with nuclei are a particularly valuable means of investigating the nature of the atomic nucleus. The interaction of a photon with the individual constituents of the nucleus is well-understood, and so investigating its interaction with these constituents while they are interacting among themselves can lead to very clean information about the dynamics of the nucleus. Furthermore, the small coupling constant characteristic of the electromagnetic interaction facilitates calculations in that first order perturbation theory is often sufficient. The distribution of charge in a nucleus determined from electron scattering and the energy levels of nuclei determined from low energy photon absorption are just two of a multitude of empirical results for electromagnetic reactions that enhance and test our understanding of the nucleus.

The specific photonuclear reaction that is investigated here is one in which a photon (γ) is absorbed by a nucleus, resulting in the emission of a single nucleon (N). The energy of the photon is in the range $50 \text{ MeV} \leq E_\gamma \leq 400 \text{ MeV}$. The wave number of such a photon corresponds to the size of a nucleon and so it is reasonable that the photon "sees" individual nucleons in the nucleus; the incident energy is high enough so that nuclear collective many-body effects will not be important. It is notable that the photon can interact with the uncharged neutrons, as well as the protons, through the interaction of the magnetic field associated with the photon and the magnetic moment of the neutron. For medium or heavy nuclei the emitted nucleon gains most of the absorbed photon energy. However, since the nucleon is massive, its momentum will be much greater than that of the photon.

The high momentum transfer involved in a photonucleon knockout, or (γN) , reaction makes it unique and interesting to study. The momentum transfer is typically from 2 fm^{-1} to 4 fm^{-1} . In the simplest picture, the photon interacts directly with a target nucleon, knocking it out of the nucleus. The bound nucleon that the photon interacts with must therefore have a very large momentum to account for the momentum mismatch between the photon and emitted nucleon. Thus, information about the high momentum components of a nuclear bound state wave function can potentially be obtained from a study of these reactions. Such spectroscopic information complements that obtained from $(p,2p)$ and $(e,e'p)$ reactions. Similar hopes for obtaining spectroscopic information

from the high momentum transfer (p,π) reaction are not forthcoming largely due to the uncertainty in the description of the interaction of the emitted pion with the residual nucleus⁽¹⁻³⁾. One of the welcome features of a (γ,N) reaction is that this type of obstacle does not exist for the photon probe which does not interact strongly with the nucleus.

The probability of a bound nucleon having a momentum much greater than the Fermi momentum is expected to be quite low. This suggests the possibility that the photon interacting with only one nucleon is not the predominant mechanism through which the reaction proceeds. Reaction mechanisms that involve two or more nucleons in conserving momentum could be important. For example, the photon could interact with a meson that is being exchanged between two nucleons, or it could excite a delta isobar that must decay by interacting with a nucleon through pion exchange. Hence the very interesting potential of seeing the mesons that are the intermediaries of the nuclear force and exotic baryons in the nucleus exists for (γ,N) reactions.

Although the desirability of photonucleon knockout reaction experiments is clear, the difficulty of such experiments has limited the number that have been done. Typically, the cross sections for single nucleon emission are of the order of microbarns for lower photon energies and nanobarns for higher photon energies and therefore the photon beam must be reasonably intense to produce a significant number of events. Generating such a monochromatic photon beam is not easy. Most experiments use the high energy tail of a beam of bremsstrahlung photons created by electrons striking a suitable radiator^(4,5). Alternatively, the photon energy could be "tagged" by detecting such a scattered electron^(6,7), or high energy photons could be created by electron-positron annihilation⁽⁸⁾. Although the background may be large, the detection of a photoemitted proton is straightforward, using a magnetic spectrometer for example^(4,5). This is not the case for the uncharged neutron and hence much fewer photoneutron knockout experiments have been performed. The neutron may be detected indirectly using a recoil proton spectrometer in which protons produced from $p(n,p)n$ forward scattering are signatures for the photoemitted neutron⁽⁹⁾.

Recent advances in experimental technology have resulted in high quality measurements of observables for (γ,N) reactions that have renewed interest in this field. Most of the experiments are done for the target nuclei ^4He , ^{12}C , ^{16}O and ^{40}Ca . The differential cross sections have predominantly been measured for the reaction going to the

ground state of the residual nucleus, although some data are available for the final nucleus being in a particular excited state. The data are more complete in the lower energy range with relatively few experiments having been done at higher energies. Cross sections and some analyzing powers have also been measured for the inverse (\vec{p}, γ) reaction. The main difficulties in doing these experiments are detecting the photons and extracting the photon events from the huge background of other possible reaction channels.

The theoretical description of the (γ, N) and (N, γ) data is unsatisfactory. Various authors disagree significantly on the relative importance of the direct reaction mechanism and the resonant (*i.e.*, including the delta isobar) and nonresonant meson exchange mechanisms. The calculations have been done in a nonrelativistic framework using the Schrödinger equation and by-and-large have preceded many of the recent experiments. Some of the recent data are in disagreement with all of the nonrelativistic calculations. These observations suggest that the theory for these photonuclear reactions should be reexamined.

The philosophy adopted here is that the direct reaction mechanism should be understood very well before looking at the contribution from other reaction mechanisms. Only with a good grasp of the contribution of this mechanism can the meson exchange mechanisms be investigated with certainty. The departure taken from the previous approaches is that the calculation for the direct mechanism is done in a relativistic framework; the Dirac equation is used to describe the dynamics of the nucleons and the interaction is described by a fully relativistic interaction Hamiltonian. The hope is that the additional physics incorporated in such a relativistic description will be important in explaining the empirical results.

There are a number of motivations for doing relativistic calculations for photonucleon knockout reactions. Perhaps a sufficient reason is that the energy involved in the reaction is a significant fraction of the nucleon rest mass energy. Relativistic kinematics are automatically incorporated and the interaction Hamiltonian is fully covariant, unlike the nonrelativistic one which neglects terms of higher order in the reciprocal nucleon mass. The latter point might be even more important for reaction mechanisms that include pion-nucleon interactions because an ambiguity emerges in the nonrelativistic reduction of the corresponding covariant Hamiltonian^(1,2). Furthermore, the relativistic nucleon wave functions are four-component spinors whose lower two components are naively thought

to be the relativistic part. At the momentum transfers involved in (γ, N) reactions the lower two components are not insignificant compared with the upper two components⁽¹⁰⁾, and thus the relativistic calculation might have fundamental differences from its nonrelativistic counterpart.

A relativistic calculation for a reaction is a logical extension of the growing "industry" of relativistic calculations in nuclear physics. The success of these calculations is very impressive for proton elastic and inelastic scattering and nuclear structure. In this sense this (γ, N) calculation is a new testing ground for the relativistic continuum nucleon wave functions that are determined from elastic scattering and for the relativistic bound nucleon wave functions that are determined from some many-body model. The bound nucleon wave function may intrinsically be better described in a relativistic theory. Although the binding energy of a nucleon in a nucleus is low, this is a consequence of the cancellation of very large "relativistic" potentials. These potentials are of the order of half the nucleon rest mass and hence the nucleon effective mass is significantly altered in the nucleus⁽¹¹⁾.

The outline of this investigation of relativistic calculations for photonucleon knockout reactions is as follows: In Chapter 2, representative nonrelativistic calculations for (γ, N) reactions are reviewed. The assumptions and approximations involved in these models are described and the associated problems are delineated. This is done in part to give guidance for the relativistic calculations. The models used and procedure for determining the relativistic nucleon wave functions is the subject of Chapter 3. The additional physics that is inherent in these wave functions beyond a nonrelativistic treatment is pointed out. Having determined the relevant wave functions, the amplitude for the direct reaction mechanism is formulated in Chapter 4. The rather formal derivation of the amplitude is accomplished using a field theoretic method that is particularly suited to relativistic nuclear physics. The unique features of the relativistic amplitude are stressed. In Chapter 5 the results of the relativistic calculations for the direct reaction mechanism are presented for a representative set of the experiments that have been done. The sensitivity of the results to the model used are explored in depth. Finally, in Chapter 6, an additional channel through which a (γ, N) reaction could proceed is explored. The two-step mechanism in which the directly emitted nucleon subsequently undergoes a charge exchange reaction is investigated especially for (γ, n) reactions. Details of the calculations are given in the appendices.

The notation and conventions used in this thesis are primarily the same as in Bjorken and Drell⁽¹²⁾. Physical units, in which $\hbar = c = 1$, are used consistently, except where specified. The factors of \hbar and c can be recovered in any equation by dimensional analysis.

2. A Review of Calculations for Photonucleon Knockout Reactions

The potential for learning unique information about the nucleus from photon induced single nucleon emission reactions has led to numerous theoretical investigations in this area. Recent advances in measuring observables for (γ,p) and (γ,n) reactions have spurred efforts to explain the experimental results. A selected sample of calculations for these photonuclear reactions, that are distinguished by the proposed reaction mechanism, are reviewed in this chapter. Other reviews in the literature^(13,14) may be referred to for supplementary information on theoretical investigations of photonuclear reactions. The theoretical approaches outlined below are nonrelativistic calculations that are limited to the intermediate photon energy range between about 50 MeV and 400 MeV. The lower energy limit is above the giant resonance region in which nuclear collective effects will be important. Furthermore, the target nuclei considered are many-body systems ($A \geq 4$); the related topic of the photodisintegration of the deuteron will not be addressed.

2.1 The Quasideuteron Model

One model for (γ,N) reactions that does not explicitly start with a proposal for a reaction mechanism is the quasideuteron calculation of Schoch⁽¹⁵⁾. The photon is assumed to be absorbed by a correlated np pair that is approximated by a deuteron wave function. The differential cross section for the reaction will then be the product of the differential cross section for the photodisintegration of the deuteron, some phase space factors, and the square of the overlap integral of the initial and final nuclear states. The latter factor represents the ability of the nucleon of the quasideuteron that remains in the nucleus to absorb the required momentum and also contains information about the number of np (quasideuteron) pairs in the target nucleus. The nucleus is described by a single-particle product wave function and the outgoing nucleon is taken to be a plane wave. The deuteron photodisintegration cross sections are taken from the theoretical calculations of Partovi⁽¹⁶⁾ for photon energies below 100 MeV and from the experimental data of Kose *et al.*⁽¹⁷⁾ for photon energies above 100 MeV. The results of Schoch's calculation produce qualitative agreement with the measured energy dependence of the differential cross section of the reactions $^{16}\text{O}(\gamma,p)^{15}\text{N}$ in the energy range

$E_\gamma = 60 - 300$ MeV and $^{16}\text{O}(\gamma, n)^{15}\text{O}$ in the energy range $E_\gamma = 60 - 80$ MeV for the nucleon scattering angles 45° , 90° and 135° . The slope of the low energy data is reproduced as well as the change in the slope of the (γp) data as the energy increases. There are deep minima in the theoretical results in the energy region $E_\gamma = 100 - 200$ MeV which are not present in the (γp) data. These are attributed to the use of plane waves for the continuum nucleon wave function.

Despite the restricted success of the quasideuteron model, the conclusions that can be drawn are very limited. Schoch claims that the success of the description might preclude the validity of a single-particle absorption mechanism or a contribution from the $\Delta(1232)$ isobar. There is no justification for this claim, however. The possible reaction mechanisms are concealed within the deuteron photodisintegration cross sections and hence the quasideuteron description does not specifically put forward any reaction mechanism. Therefore it is not clear how the results can rule out any reaction mechanism. Moreover, the unphysical view of a nucleus being composed of deuteron-like pairs and the amount of phenomenological input and *ad hoc* factors in the calculation casts doubt on any conclusions that are drawn from the results of the model.

2.2 The Direct Mechanism

The simplest mechanism by which a (γN) reaction can take place is one in which the photon interacts with a single target nucleon. The residual nucleus is effectively a spectator in this model. This so-called direct reaction mechanism is also referred to in the literature as the One Nucleon Model or the quasifree knockout (QFK) model. A number of authors have investigated this mechanism in a nonrelativistic framework⁽¹⁸⁻²⁰⁾. The following exposition follows the calculation by Londergan and Nixon⁽²¹⁾.

The nonrelativistic scattering amplitude for a (γN) reaction is the matrix element of the electromagnetic interaction Hamiltonian

$$H_{em} = -\int d^3x \mathbf{J}(\mathbf{x}) \cdot \mathbf{A}_\lambda(\mathbf{x}) \quad (2.1)$$

between initial and final nuclear states. In the direct reaction model the current is the one-body nuclear electromagnetic current

$$\mathbf{J}(\mathbf{x}) = e \sum_{j=1}^A \left\{ \frac{e_j}{2im} [\delta^3(\mathbf{r}_j - \mathbf{x}) \vec{\nabla}_j - \overleftarrow{\nabla}_j \delta^3(\mathbf{r}_j - \mathbf{x})] + \delta^3(\mathbf{r}_j - \mathbf{x}) \frac{\mu_j}{2m} \sigma_j \times \vec{\nabla} \right\} \quad (2.2)$$

consisting of convection and spin magnetic currents. The electromagnetic potential of a photon with polarization λ is

$$\mathbf{A}_\lambda(\mathbf{x}) = \frac{1}{(2\omega_\gamma)^{1/2}} e^{i\mathbf{k}_\gamma \cdot \mathbf{x}} \boldsymbol{\varepsilon}_\lambda . \quad (2.3)$$

In Eq. (2.2) m is the nucleon mass, e_j is the charge of the j th nucleon and μ_j is the magnetic moment in nuclear magnetons. The arrows over the gradient operators indicate the direction in which the gradient acts. In Eq. (2.3) ω_γ is the energy of the photon, \mathbf{k}_γ is the photon momentum and $\boldsymbol{\varepsilon}_\lambda$ is a unit polarization vector. In the spirit of the independent particle model of the nucleus, it is assumed that the final nuclear state is simply a one-hole state with respect to the initial nuclear state. If the final nucleus is in its ground state, the hole is the absence of a valence nucleon in the target nucleus. With these assumptions the reaction amplitude becomes proportional to the matrix element of the electromagnetic interaction Hamiltonian between a single-particle bound wave function and a nucleon continuum wave function

$$M_{fi}^\lambda \propto -\langle \chi_{\text{continuum}}(\mathbf{x}) | \mathbf{j}(\mathbf{x}) \cdot \mathbf{A}_\lambda(\mathbf{x}) | \phi_{\text{bound}}(\mathbf{x}) \rangle \quad (2.4a)$$

where the current is written as

$$\mathbf{j}(\mathbf{x}) = e_N \frac{\mathbf{p}_N}{m} + \frac{ie}{2m} \mu_N \boldsymbol{\sigma} \times \mathbf{k}_\gamma . \quad (2.4b)$$

The subscript N denotes quantities that are characteristic of the continuum nucleon.

The bound state wave function is either determined by solving a Schrödinger equation with Woods-Saxon binding potentials or is taken from Hartree-Fock calculations. The continuum wave function can be taken in the first Born Approximation to be a plane wave, in which case the differential cross section is proportional to the square of the single-particle momentum density. In order to include final state interactions, the continuum wave function can be approximated by a distorted wave that is determined from a Schrödinger equation with optical potentials that give a good account of the relevant proton-nucleus elastic scattering data.

It has been shown that the direct reaction model can reproduce (γp) cross sections for ^{12}C and ^{16}O target nuclei at incident photon energies of 60, 80 and 100 MeV⁽¹⁹⁾. The calculations are shown to be very sensitive to the bound and continuum wave functions used. The energy dependence of $^{16}\text{O}(\gamma p)^{15}\text{N}$ and $^{40}\text{Ca}(\gamma p)^{39}\text{K}$ reactions at proton scattering angles of 45° , 90° and 135° has also been investigated up to 200 MeV incident photon energy⁽¹⁹⁾. For the ^{16}O target the calculated differential cross sections fall increasingly below the 90° and 135° data for energies above 100 MeV. For the ^{40}Ca target, on the other hand, the agreement with the data is quite good for all the data up to 200 MeV.

One of the main criticisms of the direct mechanism for photonuclear reactions is that it cannot explain the experimental data for (γn) reactions. At energies below 100 MeV, it is found that the angular distribution for these reactions is comparable in both magnitude and shape to the (γp) results. The direct reaction model considerably underestimates the (γn) cross section because the convection current contribution vanishes for this case. It has been suggested that a (p, n) charge exchange subsequent to a (γp) reaction might account for the "missing strength" in the theoretical (γn) cross sections. Boffi *et al.*⁽²²⁾ have done calculations for such a charge exchange mechanism and have found that although the charge exchange contribution is large relative to the direct mechanism, it is still insufficient to explain the experimental results.

The failure of the direct reaction model for (γn) reactions suggests that other processes are important for this reaction. This does not, however, necessarily imply that the direct reaction calculations for (γp) reactions are invalid, or that it is a coincidence that the calculations give good results because of a fortuitous destructive interference of amplitudes from other processes. It is possible that other mechanisms give a greater contribution to the (γn) amplitudes than the corresponding mechanisms for the (γp) amplitudes⁽²³⁾.

One serious shortcoming of the direct mechanism is that the high momentum components of the bound state wave functions used in the calculation are uncertain. The bound state wave functions are determined from criteria that involve lower momentum transfers than are involved in (γN) reactions. In this sense, the (γN) reaction might provide spectroscopic information about the target nucleus. However, due to the uncertainty in the relative importance of various reaction mechanisms, good spectroscopic

information is yet to be realized.

2.3 The $\Delta(1232)$ Isobar

In addition to the direct photoejection mechanism, isobars may contribute to (γN) processes as illustrated in Fig. 1. The $\Delta(1232)$ isobar, which has spin and isospin $3/2$, may be created by the photoexcitation of a nucleon, resulting in an intermediate state which contains the propagating Δ and a one-hole state of the target nucleus. The isobar then decays into an unbound nucleon and a pion which is absorbed by the residual nucleus to produce the final nuclear state. The photon may also be absorbed by the isobar subsequent to its formation, resulting in the decay of the Δ into the unbound nucleon.

A nonrelativistic calculation for the two diagrams in Fig. 1 has been done by Londergan and Nixon⁽²⁰⁾. The amplitude for the diagrams with the Δ is

$$M_{fi} = \sum_{\text{intermediate states}} \langle \chi_N^{(-)} \psi_f^{A-1} | H_{\text{decay}} | \psi_{\Delta} \psi_{\text{int}}^{A-1} \rangle \frac{1}{E - (p_{\Delta}^2/2M_{\Delta} + M_{\Delta} - i\Gamma/2) - E_{\text{int}}} \langle \psi_{\Delta} \psi_{\text{int}}^{A-1} | H_{\text{prod}} | \psi_i^A \rangle$$

$$+ \langle \chi_N^{(-)} \psi_f^{A-1} | H_{\text{prod}}^{\dagger} | \psi_{\Delta} \psi_{\text{int}}^{A-1} \rangle \frac{1}{E - E_{\gamma} - (p_{\Delta}^2/2M_{\Delta} + M_{\Delta} - i\Gamma/2) - E_{\text{int}}} \langle \psi_{\Delta} \psi_{\text{int}}^{A-1} | H_{\text{decay}}^{\dagger} | \psi_i^A \rangle \quad (2.5)$$

where E is the total laboratory energy (photon energy E_{γ} plus target rest mass), E_{int} is the total energy (kinetic plus rest mass) of the intermediate state of the residual nucleus, M_{Δ} is the isobar rest mass (1232 MeV), and Γ is the isobar width in the nuclear

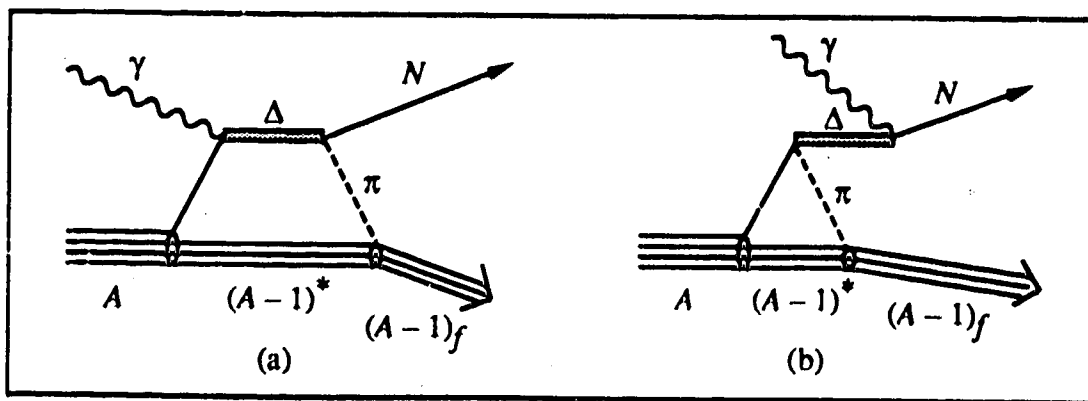


Fig. 1: The Δ isobar contributions to nucleon photoemission. (a) The Δ is created by the photoexcitation of a nucleon, propagates, and then decays to a nucleon which is emitted into the continuum and a pion which is reabsorbed by the nucleus. (b) The delta is created in the nucleus and then decays to the emitted nucleon by absorbing the incident photon.

medium (the width reflects the tendency of the Δ to decay). The sum over the intermediate states includes a sum over all quantum numbers of the intermediate nucleus as well as over all spin and isospin states of the isobar, and an integration over the isobar momentum p_Δ . The denotation of the wave functions is apparent.

The isobar production and decay matrix elements H are written in terms of the $\gamma + N \rightarrow \Delta$ production vertex and the $\Delta \rightarrow N + \pi$ decay amplitude, respectively. The form of the isobar production vertex is derived using a quark model for the baryons and the parameters involved are determined from isobar electroproduction cross sections. The coupling constants for the isobar decay amplitude are determined from independent experiments and the associated form factors are arrived at from neutrino reactions.

To evaluate Eq. (2.5), the final nuclear state and all intermediate states are taken to be one-hole states with respect to the target nucleus. Other approximations in the calculation are that the isobar-nucleus interaction is neglected (Γ is the free Δ width) and, in the spirit of the WKB approximation, the continuum nucleon wave function is taken to be a "modified plane wave"

$$\chi_p^{(+)}(\mathbf{r}) = \sqrt{\zeta} e^{i\mathbf{p}'\cdot\mathbf{r}}. \quad (2.6)$$

The modified momentum \mathbf{p}' is complex; the real part represents a shift in the asymptotic momentum due to the real part of the nuclear potential and the imaginary part takes into account the possibility of losing flux into other channels. The reduction factor $\zeta^{1/2}$ also accounts for a flux loss. This approximate form for the distorted wave simplifies the computations considerably.

Londergan and Nixon compare their calculations with the energy dependence of the differential cross section for the reaction $^{16}\text{O}(\gamma p)^{15}\text{N}$ at 45° , 90° and 135° scattering angles. They conclude that the delta isobar contributions to this reaction become important at photon energies above 100 MeV. As the photon energy approaches the Δ production threshold, the calculations indicate that the processes involving the Δ isobar are dominant in determining the cross section.

A similar investigation of the role of the Δ in the (γp) reaction by Cheung and Keister⁽²⁴⁾ disagrees with the aforementioned results. They find that although the Δ current is important, it does not dominate the reaction cross section. The main difference

between this calculation and Londergan and Nixon's is that Cheung and Keister neglect the Δ nonlocality; the Δ energy is fixed at a value determined by external kinematics. The authors claim that the quantitative implications of this approximation may not be large. The proton distortions are included more completely by Cheung and Keister by evaluating the proton wave function with an appropriate optical potential. This added feature of the calculation is not expected to significantly alter the results at higher energies from the case when the modified plane wave of Eq. (2.6) is used.

The reasons for the different results obtained in the two described calculations are not clear. The approximations that are made to facilitate the calculations are different in the two cases, but their validity seems to be justified. The discrepancies point to the precarious nature of doing calculations involving the Δ isobar. A great deal of care must be taken to treat the resonance properly, and the precise way of doing this is not well established.

2.4 Meson Exchange Currents

An extensive investigation into photonuclear reactions by Gari and Hebach⁽²⁵⁾ starts with the premise that the nucleus is a complex system of baryons and mesons. These authors argue that the mesonic degrees of freedom must be taken into account to obtain an accurate description of photonuclear reactions. The (γ, N) transition amplitude is written as the matrix element of the electromagnetic interaction Hamiltonian between the initial and final "total nuclear states" that include mesonic and resonance degrees of freedom. In effect, this means that the photon can interact with the various components of the meson-baryon system as shown in Fig. 2.

The total wave function of the nuclear system is very complicated, and so the full

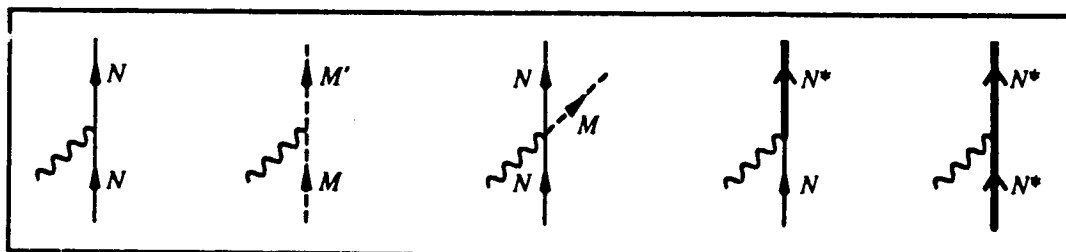


Fig. 2: Photon interactions with the meson-baryon system. Nucleons are denoted by N , mesons by M and M' and resonances by N^* .

space is truncated to get an amplitude that contains pure nucleonic states only. The transition matrix becomes

$$M_{fi} = \langle \chi_f | H_{em}^{eff} | \chi_i \rangle \quad (2.7)$$

where χ_f and χ_i are the usual nucleonic states (no mesons). The effective electromagnetic interaction in the subspace of nucleons is given by

$$H_{em}^{eff} \equiv \Omega = - \int \mathbf{A}(\mathbf{x}) \cdot [\mathbf{J}_{one-body}^{NN}(\mathbf{x}) + \mathbf{J}_{EXC}^{NN}(\mathbf{x})] d^3x = \Omega_{one-body} + \Omega_{EXC} . \quad (2.8)$$

The one-body current is given by Eq. (2.2) and gives rise to the direct mechanism described in Sec. 2.2. The form of the exchange current is

$$\mathbf{J}_{EXC}^{NN}(\mathbf{x}) = i [V_{eff}^{NN}, \mathbf{D}(\mathbf{x})] \quad (2.9a)$$

$$\mathbf{D}(\mathbf{x}) = \sum_{\alpha=1}^A e_{\alpha} \mathbf{x}_{\alpha} \delta^3(\mathbf{x} - \mathbf{x}_{\alpha}) \quad (2.9b)$$

where e_{α} is the charge of the α th nucleon and V_{eff}^{NN} is the effective nucleon-nucleon interaction, which may be taken as a theoretical one boson exchange potential or as a phenomenological potential. The form of the exchange current is derived in the low energy limit. It is a result of current conservation requirements and takes into account only two-body terms.

The nuclear states are calculated using a shell model expansion. The nuclear Hamiltonian is written as a sum of a shell model Hamiltonian and a residual interaction

$$H_N = T_N + V_{eff}^{NN} = (T_N + U) + (V_{eff}^{NN} - U) = H_o^{sm} + R . \quad (2.10)$$

The shell model Hamiltonian is a sum of the kinetic energy operator T_N for the nucleons and the single-particle potential U , and has eigenstates that satisfy

$$H_o^{sm} | \phi \rangle = E_o | \phi \rangle . \quad (2.11)$$

By retaining the residual interaction R , nucleon-nucleon correlations are included in the calculation. The full eigenstates of H_N are written in a perturbation expansion as

$$| \chi_f^{(\pm)} \rangle = | \phi_f^{(\pm)} \rangle + \frac{1}{E_f - H_N \pm i\epsilon} R | \phi_f^{(\pm)} \rangle \quad (2.12a)$$

$$|\chi_i\rangle = |\phi_i\rangle + \frac{1}{E_i - H_0^{sm}} PR |\chi_i\rangle \quad (2.12b)$$

where P is the projection operator

$$P = 1 - |\phi_i\rangle\langle\phi_i| \quad (2.12c)$$

and E_f and E_i are the energy eigenvalues associated with the final and initial states. The transition matrix with these states becomes

$$M_{fi} = \langle\phi_f^{(-)}| \Omega |\phi_i\rangle + \langle\phi_f^{(-)}| R \frac{1}{E_f - H_N + i\epsilon} \Omega |\phi_i\rangle \\ + \langle\phi_f^{(-)}| \Omega \frac{1}{E_i - H_0^{sm}} PR |\chi_i\rangle + \langle\phi_f^{(-)}| R \frac{1}{E_f - H_N + i\epsilon} \Omega \frac{1}{E_i - H_0^{sm}} PR |\phi_i\rangle. \quad (2.13)$$

Schematically, the contributions to the transition matrix are shown in Fig. 3.

The approximations that are made in evaluating Eq. (2.13) are: (1) V_{eff}^{NN} is taken to be a central potential of the Yukawa type containing an exchange mixture, (2) the nuclear correlations are calculated to first order only, and (3) intermediate states of the correlation terms are dominated by giant resonances of different multipolarities. The latter

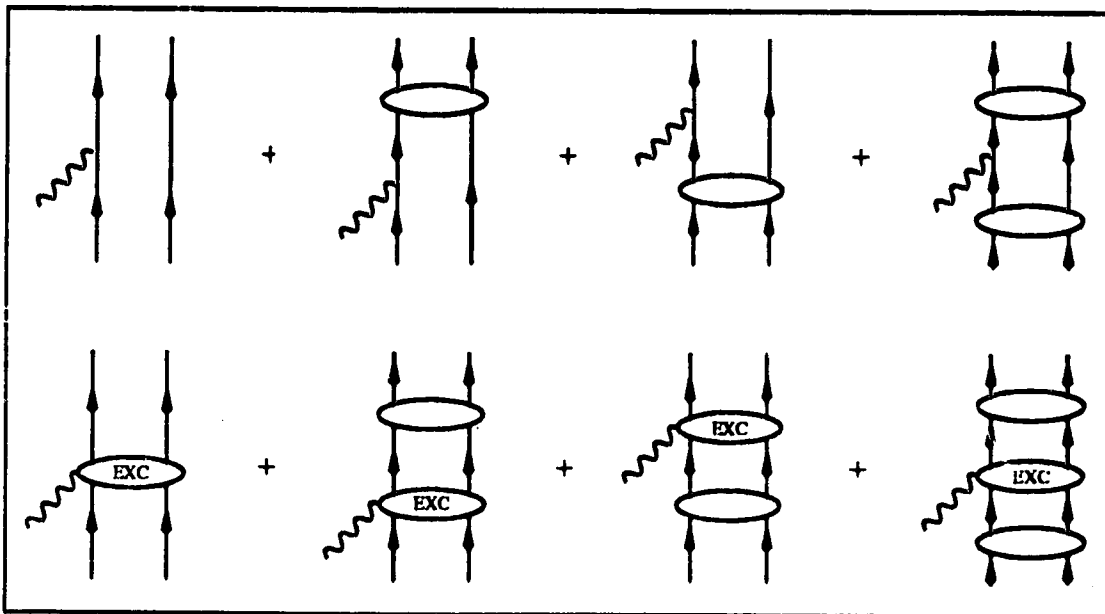


Fig. 3: The contributions to the transition matrix of Eq. (2.13). The empty ovals signify nucleon-nucleon correlations. The top four diagrams represent the interactions of the photon with the one-body nuclear current and the bottom four diagrams represent the exchange current contributions.

assumption allows the replacement of the Hamiltonian operators in Eq. (2.13) with their corresponding energy eigenvalues. Further features of the model are that a phenomenological effective current $J_{\text{EXC}}^{N\Delta}(\mathbf{x})$ is put into the calculation to account for the Δ isobar and the optical potential for the emitted nucleon is the same as the binding potential for the bound nucleon. The latter attribute preserves the orthogonality between the initial and final states.

The results of this meson exchange current calculation are compared with experimental data for (γ, p) and (γ, n) reactions on ^{16}O and ^4He over a fairly wide energy range. A detailed investigation of the relative importance of the various reaction mechanisms at different energies is carried out by the authors. The conclusion drawn by Gari and Hebach is that in general the exchange current contributions that do not include the Δ current are necessary to describe the data; the Δ resonance contribution is small. The direct reaction mechanism is found to be very inadequate by itself, in that it consistently underpredicts the measured cross sections. Nucleon-nucleon correlations are not very important except at the low photon energies that are of the same order as the excitation energies of the giant resonances.

One of the major shortcomings of this calculation is that the insistence on maintaining the orthogonality between initial and final states results in an unrealistic continuum nucleon wave function. The continuum wave function does not even remotely describe the elastic scattering data of the nucleon with the residual nucleus. Nonorthogonality is a result of restricting the possible reaction channels to a single channel. It is unrealistic to restrict the reaction channels and then to artificially impose wave function orthogonality as Gari and Hebach have done at the expense of the continuum nucleon wave function, especially when it has been shown (*cf.* Sec. 2.2) that the (γ, N) calculations are very sensitive to this wave function. Boffi *et al.*⁽²⁶⁾ have investigated the problem of the orthogonality defect for electromagnetic knockout reactions. They evaluate the difference between the cross sections calculated with wave functions orthogonalized by the Gram-Schmidt procedure and with the usual optical potential wave function. It is found that there is no effect for (γ, p) reactions if the nuclear structure information and the electromagnetic interaction are not factorized in the cross section. Therefore it seems that it is much more preferable to use a realistic continuum wave function that incorporates the effects of other reaction channels in an approximate manner through a complex optical

potential at the expense of wave function orthogonality.

Another criticism of the Gari and Hebach calculation is the form of the exchange current, Eq. (2.9). In the context of a different model (*cf.* Sec. 2.5), Ryckebusch *et al.*⁽²⁷⁾ show that the long wavelength approximation in which Eq. (2.9) is evaluated is inappropriate for photon energies above about 80 MeV. The problem of not knowing the precise form of the nuclear current is an outstanding problem for photonuclear reactions as well as for all of nuclear physics.

2.5 RPA Calculations

Ryckebusch *et al.*^(23,27) calculate cross sections for (γ, N) reactions using wave functions for the initial and final states that are evaluated in the Random Phase Approximation (RPA). RPA wave functions are calculated by diagonalizing the Hamiltonian which consists of matrix elements of a Skyrme residual interaction between particle-hole states. The particle-hole states are generated from Hartree-Fock calculations in which the same Skyrme interaction is used. The final state wave function that has a part containing an outgoing nucleon with definite momentum and spin projection, and a residual $(A - 1)$ nucleon system that is a pure hole state, is constructed from a linear combination of the RPA continuum wave functions.

In their initial paper⁽²³⁾, the authors use the one-body current of Eq. (2.2) in the electromagnetic interaction Hamiltonian and thus do calculations for the direct mechanism. However, since the wave functions are calculated from the RPA formalism, nucleon-nucleon correlations are also taken into account. The energy dependence of the cross sections for $^{16}\text{O}(\gamma, p)$ and $^{40}\text{Ca}(\gamma, p)$ reactions at 45° , 90° and 135° proton angles are reproduced reasonably well in the photon energy range between 50 and 300 MeV (for the ^{16}O target, the calculations are compared with data for the case in which the residual ^{15}N nucleus is left in the excited $(3/2^-, 6324 \text{ keV})$ state as well as in the ground state). The observed similar shape and magnitude of (γ, p) and (γ, n) reactions is investigated by doing calculations for the cross sections of $^{16}\text{O}(\gamma, p)^{15}\text{N}$ and $^{16}\text{O}(\gamma, n)^{15}\text{O}^*(3/2^-)$ reactions at $E_\gamma = 60 \text{ MeV}$. Both angular distributions are reproduced very well by the calculation, but it is shown that whereas the proton emission process is almost determined by the direct Hartree-Fock contribution (*i.e.*, the calculation is done using the Hartree-Fock wave functions rather than the RPA wave

functions), the neutron emission process is dominated by the RPA correlations. For the $^{16}\text{O}(\gamma p)^{15}\text{N}$ reaction at $E_\gamma = 196$ MeV, the RPA calculations overestimate the cross section by almost an order of magnitude at the forward scattering angles; better agreement is obtained for angles above 50° .

Ryckebusch *et al.* further investigate including an exchange current contribution in their calculations⁽²⁷⁾. The form of the exchange current is determined from current conservation requirements to be related to the commutator of the effective nucleon-nucleon interaction \hat{V} and the nuclear density $\rho(\mathbf{r})$ by

$$\nabla \cdot \mathbf{J}_{\text{exc}}(\mathbf{r}) = \frac{1}{i} [\hat{V}, \rho(\mathbf{r})] . \quad (2.14)$$

This is similar to the method used by Gari and Hebach described in Sec. 2.4, except that the exchange current is not evaluated in the low energy limit exclusively. The conclusions drawn for the $^{16}\text{O}(\gamma p)^{15}\text{N}$ reaction at $E_\gamma = 80$ MeV are similar to those of Gari and Hebach, except that correlation terms are found to be more important in this case. The cross sections are systematically overestimated when the exchange current is included in addition to the RPA one-body contribution.

The most serious problem with the RPA model is the result for the $^{16}\text{O}(\gamma p)^{15}\text{N}$ differential cross section at $E_\gamma = 196$ MeV. It would seem that the direct RPA calculation should give better results at lower momentum transfers and fall below the data as the momentum transfer increases. The inclusion of meson exchange currents would likely make the situation even worse. It is possible that the continuum RPA wave function is responsible for the discrepancy between the theory and experiment. Since the initial and final wave functions are constructed from the same Hamiltonian, orthogonality is preserved. Although this model for the wave functions is more convincing than the prescription described in Sec. 2.4, the continuum nucleon wave function still does not describe the related elastic scattering data.

2.6 Discussion

The theoretical models discussed above are in disagreement in the sense that each attributes its success in describing experimental data to different processes. Furthermore, most of these calculations were compared with the limited data available at the time they were put forward. A more comprehensive set of photonuclear data has become available

recently which has the potential of putting more severe constraints on the theory. It is instructive to examine various theoretical predictions for the same recent experiment. A number of theoretical predictions for the $^{16}\text{O}(\gamma,p)^{15}\text{N}$ differential cross section at $E_\gamma = 196$ MeV are shown in Fig. 4. It can be seen that none of the calculations adequately describes the data. It appears that some of the assumptions and approximations made in the calculations are not valid or at least not general to all kinematic conditions.

The outstanding problem of the 196 MeV $^{16}\text{O}(\gamma,p)^{15}\text{N}$ data highlights the desirability of a more refined treatment for (γN) reactions. The models which involve two nucleon mechanisms can be improved by making less simplifying assumptions. This would involve more lengthy calculations. Indeed, nucleon photoemission reactions are a good testing ground for meson exchange current calculations. As well, it certainly becomes possible that relativistic effects will become important as higher incident energies and momentum transfers are achieved.

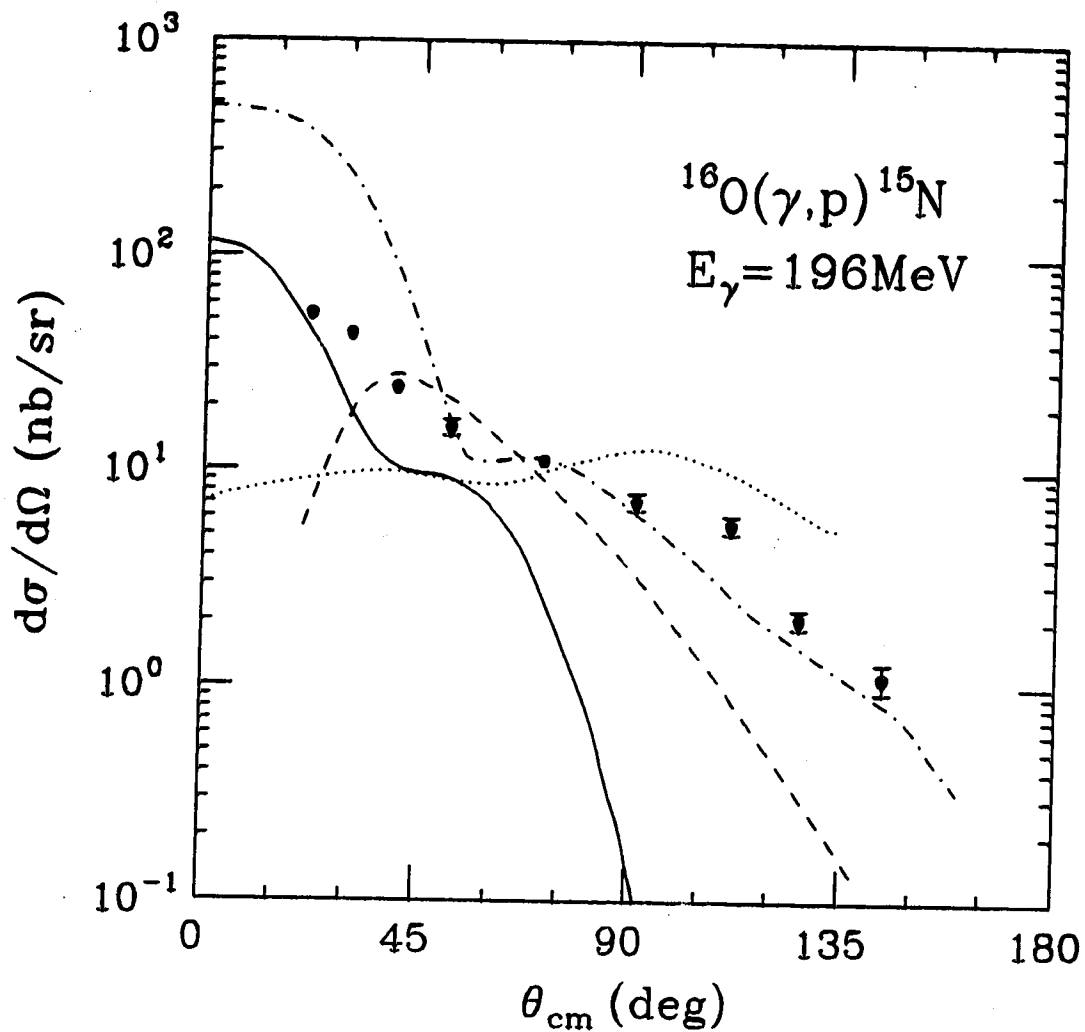


Fig. 4: Nonrelativistic calculations for the differential cross section of the 196 MeV $^{16}\text{O}(\gamma, p)^{15}\text{N}$ reaction. The experimental points are from Turley *et al.*⁽²⁸⁾. The solid curve is a result of the direct mechanism calculation of Turley⁽²⁹⁾, the dashed curve is the Londergan and Nixon calculation which includes the Δ isobar⁽²⁰⁾, the dotted curve represents Gari and Hebach's prediction with meson exchange current contributions⁽²⁵⁾ and the dash-dotted curve is the direct RPA result of Ryckebusch *et al.*⁽²³⁾.

3. Relativistic Nucleon Dynamics

One of the essential ingredients in doing relativistic calculations for photonuclear reactions is the description of the dynamics of the nucleons involved. The interaction between the photoejected nucleon (before and after it is emitted into the continuum) and the core nucleus is especially important for constructing a theoretical model for (γN) reactions. The nuclear force is mediated by the exchange of mesons⁽³⁰⁻³³⁾, and therefore an exact treatment would involve calculating all possible meson exchange processes between the nucleons. This is a very formidable task and so it is desirable to construct a model in which meson exchange effects are included in a simplified manner.

3.1 Relativistic Hartree Description of Nuclei

A relativistic quantum field theory for the nuclear many-body problem has been developed by B.D. Serot and J.D. Walecka⁽¹¹⁾. Their "quantum hadrodynamic" model (QHD-II) is a relativistic Hartree description of nuclei and is based on the fields shown in Table 1. The couplings between fields are chosen in the usual "minimal" fashion. For example, it is assumed that the neutral scalar meson couples to the scalar density of baryons through $g_s \bar{\psi} \psi \phi$ and the neutral vector meson couples to the conserved baryon current through $g_v \bar{\psi} \gamma^\mu \psi V_\mu$. The quantities γ^μ are the Dirac matrices, g_s and g_v are the relevant field strengths and the adjoint spinor is defined to be $\bar{\psi}(x) = \psi^\dagger(x) \gamma^0$.

In this model the Lagrangian density is

<u>Field</u>	<u>Description</u>	<u>Particles</u>	<u>Mass</u>
ψ	Baryon	p, n, \dots	m
ϕ	Neutral scalar meson	σ	m_s
V_μ	Neutral vector meson	ω	m_v
π	Charged pseudoscalar meson	π	m_π
b_μ	Charged vector meson	ρ	m_ρ
A_μ	Photon	γ	0

Table 1: Fields in the QHD-II Model of Serot and Walecka.

$$\begin{aligned}
\mathcal{L} = & \bar{\Psi} (i\gamma^\mu \partial_\mu - m)\Psi + \frac{1}{2} (\partial^\mu \phi \partial_\mu \phi - m_\phi^2 \phi^2) - \frac{1}{4} G^{\mu\nu} G_{\mu\nu} + \frac{1}{2} m_\nu^2 V^\mu V_\mu \\
& - g_\nu \bar{\Psi} \gamma^\mu \Psi V_\mu + g_s \bar{\Psi} \Psi \phi + \frac{1}{2} (\partial^\mu \pi \cdot \partial_\mu \pi - m_\pi^2 \pi \cdot \pi) - i g_\pi \bar{\Psi} \gamma^5 \tau \cdot \pi \Psi \\
& - \frac{1}{4} \mathbf{B}^{\mu\nu} \cdot \mathbf{B}_{\mu\nu} + \frac{1}{2} m_\rho^2 \mathbf{b}^\mu \cdot \mathbf{b}_\mu - \frac{1}{2} g_\rho \bar{\Psi} \gamma^\mu \tau \cdot \mathbf{b}_\mu \Psi - \frac{1}{4} F^{\mu\nu} F_{\mu\nu} \\
& - e A^\mu [\bar{\Psi} \gamma_\mu \frac{1}{2} (1 + \tau_3) \Psi + (\mathbf{b}^\nu \times \mathbf{B}_{\nu\mu})_3 + (\pi \times (\partial_\mu \pi + g_\rho (\pi \times \mathbf{b}_\mu)))_3] \quad (3.1a)
\end{aligned}$$

where the electromagnetic field strength $F^{\mu\nu}$, the neutral vector meson field strength $G^{\mu\nu}$ and the charged vector meson field strength $\mathbf{B}^{\mu\nu}$ are defined as

$$F^{\mu\nu} \equiv \partial^\mu A^\nu - \partial^\nu A^\mu \quad (3.1b)$$

$$G^{\mu\nu} \equiv \partial^\mu V^\nu - \partial^\nu V^\mu \quad (3.1c)$$

$$\mathbf{B}^{\mu\nu} \equiv \partial^\mu \mathbf{b}^\nu - \partial^\nu \mathbf{b}^\mu - g_\rho (\mathbf{b}^\mu \times \mathbf{b}^\nu) . \quad (3.1d)$$

As well, τ are the Pauli isospin matrices and $\gamma^5 = \gamma^0 \gamma^1 \gamma^2 \gamma^3$. In Eq. (3.1a) the baryon fields are taken to be isospinors, *i.e.*,

$$\Psi = \begin{bmatrix} \Psi_p \\ \Psi_n \end{bmatrix} . \quad (3.1e)$$

At this point the Euler-Lagrange equations⁽³⁴⁾

$$\frac{\partial}{\partial x^\mu} \left(\frac{\partial \mathcal{L}}{\partial (\partial q_i / \partial x^\mu)} \right) - \frac{\partial \mathcal{L}}{\partial q_i} = 0 , \quad (3.2)$$

where q_i represents any one of the fields in the Lagrangian, would give equations for the fields. However, there is no method to solve these nonlinear field equations exactly, and so further approximations must be made to get a solvable problem.

The simplifying assumption that will yield an approximate solution is to replace the meson field operators by their expectation values which are classical fields. Furthermore, only spherically symmetric nuclei with total angular momentum zero are considered. For these cases, current conservation prohibits a three-vector piece $\mathbf{V}(\mathbf{r}) \propto \hat{\mathbf{r}} V(r)$ from appearing as a classical field⁽³⁵⁾. The expectation values of the pseudoscalar field and any

other charged field are zero as well because the nucleus is assumed to have a definite parity and a well-defined charge respectively. The fields that survive are:

$$\phi \rightarrow \langle \phi \rangle \equiv \phi_0 \quad (3.3a)$$

$$V_\mu \rightarrow \langle V_\mu \rangle \equiv \delta_{\mu 0} V_0 \quad (3.3b)$$

$$b_\mu \rightarrow \langle b_\mu \rangle \equiv \delta_{\mu 0} b_0 \quad (3.3c)$$

$$A_\mu \rightarrow \langle A_\mu \rangle \equiv \delta_{\mu 0} A_0. \quad (3.3d)$$

This "mean-field" theory (MFT) is expected to become increasingly valid as the nuclear density increases⁽¹¹⁾.

The Lagrangian density in the MFT becomes

$$\begin{aligned} \mathcal{L}_{\text{MFT}} = & \bar{\Psi} [i\gamma^\mu \partial_\mu - g_v \gamma^0 V_0 - \frac{1}{2} g_\rho \tau_3 \gamma^0 b_0 - e \frac{1}{2} (1 + \tau_3) \gamma^0 A_0 - (m - g_s \phi_0)] \Psi \\ & - \frac{1}{2} [(\nabla \phi_0)^2 + m_s^2 \phi_0^2] + \frac{1}{2} [(\nabla V_0)^2 + m_v^2 V_0^2] + \frac{1}{2} (\nabla A_0)^2 + \frac{1}{2} [(\nabla b_0)^2 + m_p^2 b_0^2]. \quad (3.4) \end{aligned}$$

The field equations resulting from this Lagrangian are

$$(\nabla^2 - m_s^2) \phi_0(\mathbf{x}) = -g_s \rho_s(\mathbf{x}) \quad ; \quad \rho_s(\mathbf{x}) = \langle \Phi_0 | : \bar{\Psi}(\mathbf{x}) \Psi(\mathbf{x}) : | \Phi_0 \rangle \quad (3.5a)$$

$$(\nabla^2 - m_s^2) \phi_0(\mathbf{x}) = -g_s \rho_s(\mathbf{x}) \quad ; \quad \rho_s(\mathbf{x}) = \langle \Phi_0 | : \bar{\Psi}(\mathbf{x}) \Psi(\mathbf{x}) : | \Phi_0 \rangle \quad (3.5a)$$

$$(\nabla^2 - m_p^2) b_0(\mathbf{x}) = -\frac{1}{2} g_\rho \rho_3(\mathbf{x}) \quad ; \quad \rho_3(\mathbf{x}) = \langle \Phi_0 | : \Psi^\dagger(\mathbf{x}) \tau_3 \Psi(\mathbf{x}) : | \Phi_0 \rangle \quad (3.5c)$$

$$\nabla^2 A_0(\mathbf{x}) = -e \rho_p(\mathbf{x}) \quad ; \quad \rho_p(\mathbf{x}) = \langle \Phi_0 | : \Psi^\dagger(\mathbf{x}) \frac{1}{2} (1 + \tau_3) \Psi(\mathbf{x}) : | \Phi_0 \rangle \quad (3.5d)$$

$$(i\gamma^\mu \partial_\mu - g_v \gamma^0 V_0 - \frac{1}{2} g_\rho \tau_3 \gamma^0 b_0 - e \frac{1}{2} (1 + \tau_3) \gamma^0 A_0 - [m - g_s \phi_0]) \Psi(\mathbf{x}) = 0. \quad (3.5e)$$

The densities $\rho(\mathbf{x})$ are expectation values of various products of the baryon field operator between the nuclear ground state $|\Phi_0\rangle$. The field operator can be expanded as a sum of positive and negative energy solutions

$$\Psi(\mathbf{x}) = \sum_\alpha [A_\alpha U_\alpha(\mathbf{x}) + B_\alpha^\dagger V_\alpha(\mathbf{x})]. \quad (3.6)$$

The label α denotes the quantum numbers of the single-particle states. A_α^\dagger and B_α^\dagger may be interpreted as creation operators for baryons and antibaryons. These operators satisfy

the anticommutation relations

$$\{A_\alpha, A_\beta^\dagger\} = \delta_{\alpha\beta} = \{B_\alpha, B_\beta^\dagger\} \quad (3.7)$$

with all other anticommutator combinations being zero. The colons in the expressions for the densities imply "normal-ordering" which means that all destruction operators are placed to the right of creation operators. Normal-ordering removes contributions from the negative energy solutions $V_\alpha(\mathbf{x})$.

The field equations may be written as a set of coupled nonlinear differential equations by writing the positive energy single-particle wave functions $U_\alpha(\mathbf{x})$ in a form that is consistent with a central parity-conserving field (the explicit form is discussed in Subsec. 3.4.2). The resulting relativistic Hartree equations may be solved self-consistently by an iterative procedure. The masses are taken to be the observed meson masses and the coupling constants are determined by fitting properties of nuclear matter and bulk properties of nuclei.

This self-consistent Hartree description of nuclei accurately predicts charge density distributions, neutron densities, and rms radii of the ground states of spherical nuclei such as ^{40}Ca , ^{90}Zr and ^{208}Pb ⁽³⁶⁾. As well, in this model the observed spin-orbit splittings between single-particle levels are reproduced and the existence of the nuclear shell model is predicted.

3.2 Nucleon-Nucleus Scattering

3.2.1 Relativistic Hartree Description of Nucleon-Nucleus Scattering

The relativistic Hartree formalism should be able to describe the scattering of an additional (unbound) nucleon from a nucleus. The continuum nucleon can qualitatively be described as moving in the self-consistent fields calculated for the nucleus. The Dirac equation (3.5e) for a stationary state $\psi(x) = \psi(\mathbf{x}) e^{-iEt}$ becomes

$$\{-i\alpha \cdot \nabla + \beta m + g_v V_0(r) + \frac{1}{2} g_\rho \tau_3 b_0(r) + e \frac{1}{2} (1 + \tau_3) A_0(r) - g_s \beta \phi_0(r)\} \psi(\mathbf{x}) = E \psi(\mathbf{x}) \quad (3.8a)$$

where α and β are related to the Dirac γ matrices by

$$\alpha = \gamma^0 \gamma \quad , \quad \beta = \gamma^0 \quad . \quad (3.8b)$$

Equation (3.8a) can be written in the form

$$[H_{\text{free}} + U_{\text{opt}}(r)]\psi(\mathbf{x}) = E\psi(\mathbf{x}). \quad (3.9a)$$

The free Dirac Hamiltonian is

$$H_{\text{free}} = -i\alpha \cdot \nabla + \beta m \quad (3.9b)$$

and the "optical potential" is given in terms of the fields as

$$U_{\text{opt}}(r) = g_v V_0(r) + \frac{1}{2} g_\rho \tau_3 b_0(r) + e \frac{1}{2} (1 + \tau_3) A_0(r) - g_s \beta \phi_0(r). \quad (3.9c)$$

The fields are known and so the problem could in principle be solved. Of course, the effect that the scattered nucleon has on the nucleus has been ignored. Furthermore, other possible inelastic reaction channels have been ignored. For these reasons, this formalism is not used for doing calculations for nucleon-nucleus scattering. However, the relativistic Hartree description gives an indication of what features a more quantitative model of nucleon-nucleus scattering must contain.

3.2.2 Phenomenological Dirac Optical Potentials

In direct analogy to the Schrödinger calculations for nucleon-nucleus scattering⁽³⁷⁾, a relativistic optical model for nucleon-nucleus scattering can be developed, based on the Dirac equation as the relevant wave equation^(38,39). In this model, the local time-independent Dirac equation is written exactly as in Eqs. (3.9) except that the optical potential is taken in its most general form. The Lorentz character of the Dirac equation specifies that the optical potential can consist of a combination of scalar, pseudoscalar, vector, axial vector and tensor potential types. Thus, the Dirac equation is

$$\{ \alpha \cdot \mathbf{p} + \beta [m + S(\mathbf{x}) + \gamma^\mu V_\mu(\mathbf{x}) + \gamma^5 P(\mathbf{x}) + \gamma^\mu \gamma^5 A_\mu(\mathbf{x}) + \sigma^{\mu\nu} T_{\mu\nu}(\mathbf{x})] \} \psi(\mathbf{x}) = E\psi(\mathbf{x}). \quad (3.10a)$$

where

$$\sigma^{\mu\nu} \equiv \frac{i}{2} (\gamma^\mu \gamma^\nu - \gamma^\nu \gamma^\mu). \quad (3.10b)$$

For the case of a spherically symmetric nucleus with definite parity, only the scalar, vector and tensor potentials survive. Furthermore, if the spatial part of the vector potential is spherically symmetric it can be absorbed into the other terms⁽⁴⁰⁾. The tensor potential is also usually neglected because it is not necessary to describe the elastic scattering⁽⁴¹⁾. The

Dirac equation therefore becomes

$$[\alpha \cdot \mathbf{p} + \beta [m + S(r)] + [V(r) + V_c(r)]] \psi(\mathbf{x}) = E \psi(\mathbf{x}) \quad (3.11)$$

where $V_c(r)$ is the Coulomb potential.

The potentials are usually parameterized as Woods-Saxon functions

$$U(r) = \frac{V}{1 + e^{(r-R_1)/a_1}} + \frac{iW}{1 + e^{(r-R_2)/a_2}} \quad (3.12)$$

which qualitatively have geometries that are similar to the shape of the nuclear density. The strengths V and W , radial parameters R and diffuseness parameters a are varied to give a good description of the scattering observables. The imaginary parts of the potentials take into account in an average way a loss of flux into other reaction channels. The phenomenological potential is found to have strong attractive scalar and repulsive vector pieces. The real potential strengths are of the order of a few hundred MeV.

Calculations done in the relativistic optical model have had rather spectacular success in reproducing the proton elastic scattering data on a wide variety of nuclei over a wide range of incident energies^(38,39,42). The fits to cross section data are usually better than the most sophisticated Schrödinger-equation-based approaches and the spin observable fits are in general superior for Dirac calculations. Furthermore, the distorted waves calculated with the Dirac equation have been used in calculations for inelastic (p, p') reactions^(43,44) and rearrangement reactions such as (p, π) reactions⁽⁴⁵⁾ with good results.

3.2.3 The Relativistic Impulse Approximation

The relativistic impulse approximation⁽⁴⁶⁻⁴⁸⁾ (RIA) gives a microscopic foundation for the phenomenological relativistic optical model. The RIA combines the empirical free-space nucleon-nucleon amplitude with densities obtained from Hartree calculations into the calculation of an optical potential. In order for this approximation to be valid, the energy of the scattering nucleon must be sufficiently high so that the density dependent corrections to the free-space amplitudes can be ignored.

The invariant scattering amplitude that satisfies the constraints of Lorentz covariance, parity conservation and that free nucleons are on their mass shell can be written in terms of five complex functions as⁽⁴⁶⁾

$$F = F_S + F_V \gamma_{(1)}^\mu \gamma_{(2)\mu}^5 + F_P \gamma_{(1)}^5 \gamma_{(2)}^5 + F_A \gamma_{(1)}^5 \gamma_{(1)}^\mu \gamma_{(2)}^5 \gamma_{(2)\mu}^5 + F_T \sigma_{(1)}^{\mu\nu} \sigma_{(2)\mu\nu} \quad (3.13)$$

where the subscripts (1) and (2) refer to the incident and struck nucleon respectively. The complex amplitudes F are functions of the square of the total four-momentum s and the square of the four-momentum transfer t . These amplitudes have their basis in meson exchange processes between nucleons^(49,50), but for the purposes of the RIA are determined empirically from nucleon-nucleon scattering.

The nucleon-nucleus optical potential in the RIA is

$$U_{\text{opt}}(q, T_L) = \frac{-4\pi i k}{m} \langle \Phi_0 | \sum_{i=1}^A e^{-iq \cdot x_{(i)}} F(t, s) | \Phi_0 \rangle \quad (3.14)$$

where k is the wave number of the nucleon in the center-of-mass frame, q is the momentum transfer, T_L is the nucleon lab kinetic energy, A is the number of nucleons in the nucleus and $|\Phi_0\rangle$ is the nuclear ground state. For spin-zero nuclei, only the scalar term and the time-component parts of the vector and tensor terms survive. The optical potential in coordinate space is

$$U_{\text{opt}}(r) = S(r) + \beta V(r) - 2i \alpha_{(1)} \hat{r} T(r) \quad (3.15a)$$

where

$$S(r) = \int \frac{d^3q}{(2\pi)^3} e^{-iq \cdot x} \tilde{\rho}_S(q) \left[\frac{-4\pi i k}{m} F_S(t, s) \right] \quad (3.15b)$$

$$V(r) = \int \frac{d^3q}{(2\pi)^3} e^{-iq \cdot x} \tilde{\rho}_B(q) \left[\frac{-4\pi i k}{m} F_V(t, s) \right] \quad (3.15c)$$

$$T(r) = r \int \frac{d^3q}{(2\pi)^3} e^{-iq \cdot x} \tilde{\rho}_T(q) \left[\frac{-4\pi i k}{m} F_T(t, s) \right] . \quad (3.15d)$$

The densities $\tilde{\rho}_S$ and $\tilde{\rho}_B$ are Fourier transforms of the scalar and baryon densities defined by Eqs. (3.5a) and (3.5b) and $\tilde{\rho}_T$ is the Fourier transform of $\rho_T(r)$ which is defined by

$$[\hat{r} \rho_T(r)]^i = \sum_{\alpha}^{\text{occ}} \bar{U}_{\alpha}(\mathbf{x}) \sigma^{0i} U_{\alpha}(\mathbf{x}) . \quad (3.16)$$

The densities are calculated in the Hartree formalism. The optical potential will naturally

contain both real and imaginary parts since the amplitudes are complex.

The Dirac equation for the incident nucleon in the RIA contains the RIA optical potential:

$$\{\alpha_{(1)} \cdot \mathbf{p} + \beta_{(1)} [m + U_{\text{opt}}(r) + \beta_{(1)} V_c(r)]\} \psi(\mathbf{x}) = E \psi(\mathbf{x}) . \quad (3.17)$$

Both the Coulomb potential $V_c(r)$ and the tensor part of the optical potential are found to have little effect on the scattering⁽⁵¹⁾ and so these are usually omitted. Equation (3.17) can be solved to calculate observables for nucleon-nucleus scattering. Calculations in the RIA for medium energy proton-nucleus scattering have been very successful in describing the cross sections and especially spin observables⁽⁵²⁾.

3.2.4 Microscopic Relativistic Nucleon-Nucleus Scattering

Recent relativistic microscopic calculations^(53,54) go beyond the original RIA. These calculations include effects that are not dealt with properly in the RIA, such as exchange terms in nucleon-nucleus scattering and medium modifications of the NN interaction. Dealing with this important physics beyond the original RIA prescription gives a better description of the scattering, especially at lower energies where these effects are significant. The essential feature of the relativistic microscopic calculations is to model the NN amplitude as arising from the first Born approximation for the exchange of mesons of different Lorentz types (scalar, vector, tensor, pseudoscalar and axial vector). The meson exchange diagrams include the direct interaction and the exchange term as is shown in Fig. 5. The complex coupling constants and form factors for the meson-

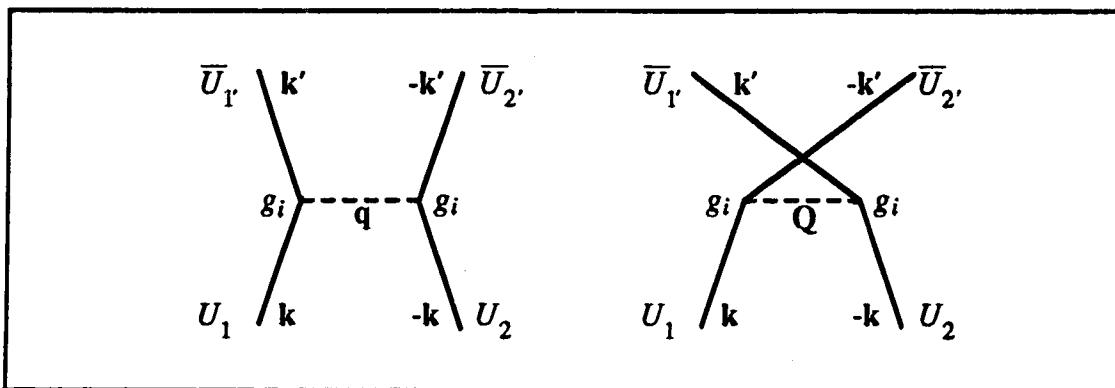


Fig. 5: Meson exchange diagrams for the NN amplitude in the first Born approximation. The U 's are the nucleon spinors and g_i is the strength of the relevant meson-nucleon coupling.

nucleon vertices are fitted to reproduce NN scattering data at separate energies. The direct and exchange amplitudes (calculated using the Feynman rules for the diagrams) are folded with relativistic Hartree densities, using a local density approximation for the exchange part, to get an optical potential. The optical potential is then multiplied by a correction factor that represents the effects of Pauli blocking. The correction factor is obtained from relativistic nuclear matter calculations⁽⁵⁵⁾.

The aforementioned modifications are found to be important at energies below 500 MeV. The optical potential calculated in this framework is good down to at least 200 MeV. Furthermore, the explicit treatment of nucleon exchange allows the unambiguous use of a pseudovector $\not{q}\gamma^5$ coupling for the pion, whereas in the original RIA the pseudovector coupling gives the same result as the pseudoscalar γ^5 coupling. The choice of the pion coupling is important because the pion makes a significant contribution to the scalar and vector potentials through the exchange term.

Another approach that generalizes the original RIA includes the negative energy sectors of the Dirac NN scattering space^(49,56). In the original RIA the five invariants of Eq. (3.13) are sufficient to describe all the matrix elements between positive energy spinors. There are an additional 39 invariants that are non-vanishing when matrix elements between both negative and positive energy spinors are included as possibilities. The amplitudes associated with these invariants are calculated using a relativistic meson exchange model that provides a good description of NN scattering data in the 0 - 1000 MeV energy range^(57,58). This approach includes nucleon exchange contributions and uses pseudovector πN coupling but does not incorporate medium modifications. The resulting local form of the optical potential is

$$U_{\text{opt}}(\mathbf{r}) = S(r) + \beta V(r) - i\alpha \cdot \hat{\mathbf{r}} T(r) - [S_{LS}(r) + \beta V_{LS}(r)] \boldsymbol{\sigma} \cdot \mathbf{L} . \quad (3.18)$$

The new features of this potential are the scalar and vector spin-orbit potentials S_{LS} and V_{LS} . Also, a space vector potential is absorbed into the five terms in Eq. (3.18). Calculations with this extended RIA model give good results for the elastic scattering of 200 MeV protons⁽⁴⁰⁾.

3.3 The Relativistic Nucleon Wave Functions

3.3.1 The Continuum Nucleon Wave Function

The photoejected nucleon dynamics are described by a Dirac equation. In the phenomenological and microscopic models the Dirac equation contains potentials which take into account in an average way the meson exchange processes that may occur when the nucleon is in the vicinity of the nucleus. In solving for the nucleon wave function the optical potential is taken to include scalar and vector potentials only. On theoretical grounds the tensor potential, which is due to the exchange of a ρ meson, is expected to be small; this is supported by phenomenological analyses.

The Dirac equation for the outgoing nucleon of the (γN) reaction is

$$[-i\alpha \cdot \nabla + \beta m + \beta S(r) + V(r) - E] \psi_{s_f}(\mathbf{x}) = 0. \quad (3.19)$$

The Coulomb potential is included in the vector potential in this expression. The distorted wave $\psi_{s_f}(\mathbf{x})$ describes the elastic scattering of a nucleon from the residual nucleus of the (γN) reaction. The matrices α and β are taken in the usual representation⁽¹²⁾ to be

$$\alpha = \begin{bmatrix} 0 & \sigma \\ \sigma & 0 \end{bmatrix}, \quad \beta = \begin{bmatrix} \mathbb{1} & 0 \\ 0 & -\mathbb{1} \end{bmatrix}. \quad (3.20)$$

These 4×4 matrices contain the Pauli matrices

$$\sigma^1 = \begin{bmatrix} 0 & 1 \\ 1 & 0 \end{bmatrix}, \quad \sigma^2 = \begin{bmatrix} 0 & -i \\ i & 0 \end{bmatrix}, \quad \sigma^3 = \begin{bmatrix} 1 & 0 \\ 0 & -1 \end{bmatrix} \quad (3.21)$$

and the 2×2 unit matrix $\mathbb{1}$. The reduction of Eq. (3.19) into an ordinary second-order linear differential equation is accomplished by examining the form of the free solution (*i.e.*, the solution of Eq. (3.19) with no potentials) and in analogy with the distorted wave solutions for the Schrödinger equation⁽⁵⁹⁾.

The positive energy solution to the free Dirac equation for a particle with four-momentum $p^\mu = (E, \mathbf{p})$ is the plane wave⁽¹²⁾

$$\psi_{s_f}^{(\text{free})}(x) = \left(\frac{E+m}{2m} \right)^{1/2} \begin{bmatrix} \mathbb{1} \\ \frac{\sigma \cdot \nabla}{E+m} \end{bmatrix} \chi_{s_f}^{1/2} e^{-ip \cdot x}. \quad (3.22)$$

The two-component spinor $\chi_{1/2}^{s_f}$ is $\begin{bmatrix} 1 \\ 0 \end{bmatrix}$ for positive spin projection on the quantization axis, and $\begin{bmatrix} 0 \\ 1 \end{bmatrix}$ for the opposite projection. The exponential may be expanded in terms of spherical Bessel functions⁽⁶⁰⁾ to give a partial wave expansion of the free solution

$$\psi_{s_f}^{(\text{free})}(x) = \left(\frac{E+m}{2m} \right)^{1/2} e^{-iEt} 4\pi \sum_{LJM} i^L Y_L^{M-s_f}(\hat{\mathbf{k}}_f) (L \ 1/2; M-s_f \ s_f | J M) \times \begin{bmatrix} 1 \\ \frac{\boldsymbol{\sigma} \cdot \nabla}{E+m} \end{bmatrix} j_L(kr) \mathcal{Y}_{L1/2J}^M(\Omega). \quad (3.23)$$

The unit vector $\hat{\mathbf{k}}_f$ is in the direction of the particle and k is the particle's wave number. The \mathcal{Y} 's are generalized spherical harmonics that are eigenfunctions of the angular momentum operators $\boldsymbol{\sigma}^2$, L^2 , J^2 and J_z . Specifically

$$\mathcal{Y}_{L1/2J}^M(\Omega) = \sum_{\mu} (L \ 1/2; M-\mu \ \mu | J M) Y_L^{M-\mu}(\Omega) \chi_{1/2}^{\mu} \quad (3.24)$$

where the Y 's are the familiar spherical harmonics.

The nucleon distorted wave is expanded in partial waves in a form that is similar to the free solution

$$\psi_{s_f}(x) = \left(\frac{E+m}{2m} \right)^{1/2} e^{-iEt} 4\pi \sum_{LJM} i^L Y_L^{M-s_f}(\hat{\mathbf{k}}_f) (L \ 1/2; M-s_f \ s_f | J M) \begin{bmatrix} \phi_1(x) \\ \phi_2(x) \end{bmatrix}. \quad (3.25)$$

The functions $\phi_1(x)$ and $\phi_2(x)$ are products of a radial function and a generalized spherical harmonic

$$\phi_1(x) = f_{LJ}(r) \mathcal{Y}_{L1/2J}^M(\Omega) \quad (3.26a)$$

$$\phi_2(x) = ig_{L'J}(r) \mathcal{Y}_{L'1/2J}^M(\Omega) ; \quad L' \equiv 2J - L . \quad (3.26b)$$

This separation can be done because the potentials have radial dependence only. The form of the lower component is arrived at from Eq. (3.23) through the identities⁽⁶¹⁾

$$\boldsymbol{\sigma} \cdot \nabla = \boldsymbol{\sigma} \cdot \hat{\mathbf{r}} \left(\frac{\partial}{\partial r} - \frac{\boldsymbol{\sigma} \cdot \mathbf{L}}{r} \right) \quad (3.27a)$$

$$\boldsymbol{\sigma} \cdot \mathbf{L} = \mathbf{J}^2 - \mathbf{L}^2 - \mathbf{S}^2 \quad (3.27b)$$

$$\sigma \cdot \hat{r} \mathcal{Y}_{L1/2J}^M(\Omega) = -\mathcal{Y}_{L'1/2J}^M(\Omega) . \quad (3.27c)$$

The Dirac equation (3.19) will give a matrix equation relating the upper and lower components:

$$\left(-i \begin{bmatrix} 0 & \sigma \cdot \nabla \\ \sigma \cdot \nabla & 0 \end{bmatrix} + \begin{bmatrix} m + S(r) & 0 \\ 0 & -m - S(r) \end{bmatrix} + \begin{bmatrix} V(r) - E & 0 \\ 0 & V(r) - E \end{bmatrix} \right) \begin{bmatrix} \phi_1(\mathbf{x}) \\ \phi_2(\mathbf{x}) \end{bmatrix} = 0 \quad (3.28)$$

or equivalently

$$-i \sigma \cdot \nabla \phi_2(\mathbf{x}) + [V(r) + S(r) + m - E] \phi_1(\mathbf{x}) = 0 \quad (3.29a)$$

$$-i \sigma \cdot \nabla \phi_1(\mathbf{x}) + [V(r) - S(r) - m - E] \phi_2(\mathbf{x}) = 0 . \quad (3.29b)$$

Substituting the expressions (3.26) for the upper and lower components into Eqs. (3.29) results in the following set of coupled first-order differential equations:

$$[E + m + S(r) - V(r)] g_{LJ}(r) = \left(\frac{d}{dr} + \frac{1 + \kappa}{r} \right) f_{LJ}(r) \quad (3.30a)$$

$$[E - m - S(r) - V(r)] f_{LJ}(r) = - \left(\frac{d}{dr} + \frac{1 - \kappa}{r} \right) g_{LJ}(r) \quad (3.30b)$$

where

$$\kappa \equiv (L - J)(2J + 1) = \begin{cases} -(L + 1) & \text{for } J = L + 1/2 \\ L & \text{for } J = L - 1/2 \end{cases} . \quad (3.31)$$

The identities (3.27) are used in deriving these results.

The wave function for an elastically scattered nucleon with incident spin projection s therefore has the form

$$\psi_s^{(+)}(\mathbf{x}) = \left(\frac{E + m}{2m} \right)^{1/2} e^{-iEt} 4\pi \sum_{LJM} i^L Y_L^{M-s*}(\hat{\mathbf{k}}_p) (L \ 1/2; M-s \ s \ | \ JM) \times \begin{bmatrix} f_{LJ}(r) \mathcal{Y}_{L1/2J}^M(\Omega) \\ ig_{LJ}(r) \mathcal{Y}_{L'1/2J}^M(\Omega) \end{bmatrix} . \quad (3.32)$$

The (+) superscript signifies that the wave function has outgoing boundary conditions,

i.e., the wave function consists of an incident plane wave and spherical outgoing scattered waves. This boundary condition is required by the physical situation. The radial functions satisfy the set of coupled first-order differential equations (3.30). This system of equations can easily be transformed into a second-order differential equation for the quantity $f(r) \equiv r f_{LJ}(r)$ by substituting the expression (3.30a) for $g_{LJ}(r)$ into Eq. (3.30b). The result is

$$f''(r) - \frac{d'(r)}{d(r)} f'(r) - \left(d(r) s(r) + \frac{\kappa d'(r)}{r d(r)} + \frac{\kappa(\kappa+1)}{r^2} \right) f(r) = 0 \quad (3.33a)$$

where

$$d(r) \equiv [E + m + S(r) - V(r)] \quad (3.33b)$$

$$s(r) \equiv -[E - m - S(r) - V(r)]. \quad (3.33c)$$

The first derivative term can be eliminated by making the transformation $f(r) = y(r)[d(r)]^{1/2}$. The equation then becomes

$$y''(r) + \left(a(r) - \frac{\kappa d'(r)}{r d(r)} - \frac{\kappa(\kappa+1)}{r^2} \right) y(r) = 0 \quad (3.34a)$$

where

$$a(r) \equiv \frac{d''(r)}{2d(r)} - \frac{3}{4} \left(\frac{d'(r)}{d(r)} \right)^2 - d(r) s(r). \quad (3.34b)$$

Equation (3.34a) is of the standard form $y''(x) = f(x)y(x)$ which can be integrated using standard numerical techniques such as the Numerov method (*cf.* Appendix B). Two further pieces of information are required to determine the solution unambiguously. Since $y(r) = [d(r)]^{-1/2} f(r) = [d(r)]^{-1/2} r f_{LJ}(r)$ and the radial function is required to be finite by probability arguments, it is clear that $y(0) = 0$. Once the initial value $y(0)$ is known, only the overall normalization of the solution remains to be determined. The normalization is fixed by requiring that the asymptotic ($r \rightarrow \infty$) radial functions have the same normalization as those for the plane wave solution. The upper component radial function for the plane wave is given in Eq. (3.23) to be a spherical Bessel function which has the asymptotic form

$$j_L(kr) \xrightarrow{r \rightarrow \infty} \frac{\sin(kr - L\pi/2)}{kr}. \quad (3.35)$$

The effect of the nuclear potential will be to introduce a nuclear phase shift δ into this asymptotic form, in analogy with the conventional Schrödinger partial wave analysis for scattering from a nuclear potential⁽⁵⁹⁾. As well, for a scattering proton the long range Coulomb potential will result in a phase shift Σ and a logarithmic term in the sinusoid. The normalization is not affected by these modifications. The desired asymptotic form that satisfies the outgoing boundary conditions is

$$f_{LJ}(kr) \xrightarrow{r \rightarrow \infty} e^{i(\delta_{LJ} + \Sigma_{LJ})} \frac{\sin(kr - \eta \ln(2kr) - L\pi/2 + \Sigma_{LJ} + \delta_{LJ})}{kr} \quad (3.36)$$

where η is the Coulomb parameter

$$\eta = \frac{Zz_N e^2}{4\pi v} = \frac{Zz_N e^2}{4\pi} \left(\frac{E}{p} \right). \quad (3.37)$$

Ze is the nuclear charge, $z_N e$ is the charge of the nucleon and v is the velocity of the nucleon. This result for the upper component is completely analogous to the asymptotic form of the radial functions for the Schrödinger equation⁽⁶²⁾. The phase shifts and Coulomb interaction are discussed in more detail in Appendices C and D.

The normalization convention chosen for the nucleon wave function is arbitrary in the sense that when observables for the elastic scattering are calculated the normalization cancels out. The wave functions (3.22) and (3.32) are often multiplied by a factor of $(2\pi)^{-3/2} (m/E)^{1/2}$. This is the δ -function normalization in which the free wave function satisfies the condition

$$\int \psi_s^\dagger(t, \mathbf{x}') \psi_s(t, \mathbf{x}) d^3x = \delta^3(\mathbf{x}' - \mathbf{x}). \quad (3.38)$$

It is interesting to compare the second-order differential equation (3.34a) for $y(r)$ with the corresponding equation in the Schrödinger formalism. The nonrelativistic equation for the scattering of a spin-1/2 particle from a potential is⁽⁶²⁾

$$y''(r) + \left[k^2 - 2m U_c(r) + m(1 + \kappa) U_{so}(r) - \frac{L(L+1)}{r^2} \right] y(r) = 0 \quad (3.39)$$

where $U_c(r)$ is the central potential and $U_{so}(r)$ is the spin-orbit potential. Comparing this with Eqs. (3.34) gives the identifications

$$k^2 - 2m U_c(r) \longleftrightarrow a(r) + \frac{d'(r)}{r d(r)} \quad (3.40a)$$

$$U_{so}(r) \longleftrightarrow - \frac{d'(r)}{m r d(r)} \quad (3.40b)$$

These equations give Schrödinger-equivalent central and spin-orbit potentials that are arrived at from the Dirac equation. If it is assumed that $E \sim m$ and $m \gg |V(r)|, |S(r)|$ and use is made of Eqs. (3.33b) and (3.34b) then the potentials become

$$U_c(r) \approx S(r) + V(r) \quad (3.41a)$$

$$U_{so}(r) \approx \frac{1}{2m^2 r} \frac{d}{dr} [V(r) - S(r)]. \quad (3.41b)$$

In this approximation the central potential is the sum of large potentials of opposite sign. This agrees qualitatively with the relatively small central potential in Schrödinger calculations. Also, whereas the large surface-peaked spin-orbit potential is put in by hand in the nonrelativistic case, the "Thomas form" of the spin-orbit interaction appears naturally from scalar and vector potentials in the Dirac equation. In general the equivalent potentials given by Eqs. (3.41) have more complicated geometries than Woods-Saxon geometries; if potential geometries of this form are used in Schrödinger calculations the agreement with scattering data is improved for higher incident nucleon energies (using the Dirac-equation-based potentials in Schrödinger calculations yields exactly the same results for elastic scattering observables as the full Dirac calculations⁽⁶³⁾).

3.3.2 The Bound Nucleon Wave Function

The bound state wave function of the nucleon appears in the expression of the amplitude for (γN) reactions. The bound nucleon dynamics are described by a Dirac equation which includes a binding potential. In the Dirac Hartree approximation this potential is given a firmer theoretical basis; the binding potential is due to scalar σ , neutral vector ω and charged vector ρ meson exchange processes between nucleons (*cf.* Eqs. (3.5)). The source of the mean fields is a nuclear density which is relatively large and constant in the nuclear interior. Thus Eqs. (3.5) suggest that the fields will approximately follow the shape of the nuclear density. In analogy with phenomenological

determinations for nucleon-nucleus scattering, the potentials in Eq. (3.5e) may be parameterized as Woods-Saxon functions rather than being solved for self-consistently in the Hartree formalism. The parameterized potentials have magnitudes similar to the Hartree potentials and are constrained to give the empirical binding energy of the nucleon.

The Dirac equation for the bound nucleon with only the scalar and vector potentials is

$$[-i\alpha \cdot \nabla + \beta m + \beta S(r) + V(r) - E] \psi_B(\mathbf{x}) = 0. \quad (3.42)$$

As was the case for the continuum wave function, the tensor potential (due to the ρ meson) gives rise to small effects and is therefore omitted for the sake of simplicity. The Coulomb potential may be included in the vector potential; its effect is also small. The potentials in Eq. (3.42) are real because there are no other channels to account for in the case of a bound nucleon. The four-component spinor with well-defined angular momentum and parity that is a solution of Eq. (3.42) is

$$\psi_B(\mathbf{x}) = e^{-iE_B t} \begin{bmatrix} f_B(r) \mathcal{Y}_{L_B}^{M_B}(\Omega) \\ ig_B(r) \mathcal{Y}_{L'_B}^{M_B}(\Omega) \end{bmatrix}; \quad L'_B \equiv 2J_B - L_B. \quad (3.43)$$

This form is very similar to that of the solution for the distorted wave since the Dirac equations for the bound and distorted wave functions are the same except for the details of the potentials.

The upper and lower radial components are therefore also related by a set of coupled differential equations identical to Eqs. (3.30). Explicitly

$$[E_B + m + S(r) - V(r)] g_B(r) = \left[\frac{d}{dr} + \frac{1 + \kappa_B}{r} \right] f_B(r) \quad (3.44a)$$

$$[E_B - m - S(r) - V(r)] f_B(r) = - \left[\frac{d}{dr} + \frac{1 - \kappa_B}{r} \right] g_B(r) \quad (3.44b)$$

where

$$\kappa_B = (L_B - J_B)(2J_B + 1). \quad (3.45)$$

Using the relationship $E_B = m - E_b$, where E_b is the binding energy of the nucleon, the following quantities may be defined:

$$V_1(r) = E_B - m - S(r) - V(r) = -E_b - S(r) - V(r) \quad (3.46a)$$

$$V_2(r) = E_B + m + S(r) - V(r) = 2m - E_b + S(r) - V(r). \quad (3.46b)$$

Then, substituting the expression (3.44a) for $g_B(r)$ into Eq. (3.44b) results in a second-order differential equation for $f_B(r)$

$$f_B''(r) + B(r) f_B'(r) + A(r) f_B(r) = 0 \quad (3.47a)$$

where

$$A(r) \equiv V_1(r) V_2(r) - \frac{(1 + \kappa_B)}{r^2} \left[\frac{r V_2'(r)}{V_2(r)} + \kappa_B \right] \quad (3.47b)$$

$$B(r) \equiv \frac{2}{r} - \frac{V_2'(r)}{V_2(r)}. \quad (3.47c)$$

The first derivative term may be transformed away by the use of an integrating factor. Specifically, the substitution

$$f_B(r) = y(r) e^{-\frac{1}{2} \int B(\rho) d\rho} = y(r) e^{-\frac{1}{2} [2 \ln r - \ln V_2(r)]} = y(r) \frac{\sqrt{V_2(r)}}{r} \quad (3.48)$$

is made. The differential equation for $y(r)$ becomes

$$y''(r) + a(r) y(r) = 0 \quad (3.49a)$$

where

$$a(r) \equiv A(r) - \frac{1}{2} B'(r) - \frac{1}{4} B^2(r). \quad (3.49b)$$

This equation may be integrated by standard numerical techniques (*cf.* Appendix B).

The behaviour of $y(r)$ at the origin and at large r is determined by physical considerations. The function must be regular at the origin (*i.e.*, $y(0) = 0$) since it is related to the bound upper component by Eq. (3.48). As $r \rightarrow \infty$ the function should vanish since the bound nucleon must be localized in space. The asymptotic form of Eq. (3.49a) is

$$y''(r) = E_b(2m - E_b) y(r). \quad (3.50)$$

In obtaining this result it is assumed that all the potentials are negligible for large r . The

exponentially damped solution

$$y(r) = e^{-\sqrt{E_b(2m - E_b)} r} \quad (3.51)$$

satisfies the physical criteria.

The overall normalization of the bound state is determined by requiring that the probability of finding the bound nucleon in all of space is unity. Mathematically this is expressed as

$$\int \psi_B^\dagger(x) \psi_B(x) d^3x = 1 \quad (3.52)$$

which translates into

$$\int [|f_B(r)|^2 + |g_B(r)|^2] r^2 dr = 1 \quad (3.53)$$

after the angular integrations are carried out.

It is interesting to compare the magnitudes of the upper and lower radial functions in momentum space. Qualitatively the lower component is thought of as the relativistic part of the wave function and is usually much smaller than the upper component. For the case of the bound $1d_{3/2}$ proton of ^{40}Ca the results of a calculation with a phenomenological potential are shown in Fig. 6. The potentials are taken to be Woods-Saxon functions

$$V(r) = \frac{W_v}{1 + e^{(r-R_v)/a_v}} \quad (3.54a)$$

$$S(r) = \frac{W_s}{1 + e^{(r-R_s)/a_s}} \quad (3.54b)$$

The values for the strengths are varied to give the correct binding energy for the state and the geometry is taken to be similar to that of $p + ^{40}\text{Ca}$ scattering optical potentials. It can be seen that in the region of momentum transfer that is characteristic of intermediate energy photonucleon knockout reactions the upper and lower components are of comparable magnitude. Therefore, treating photonucleon knockout reactions with a relativistic approach might lead to fundamental differences with nonrelativistic Schrödinger calculations.

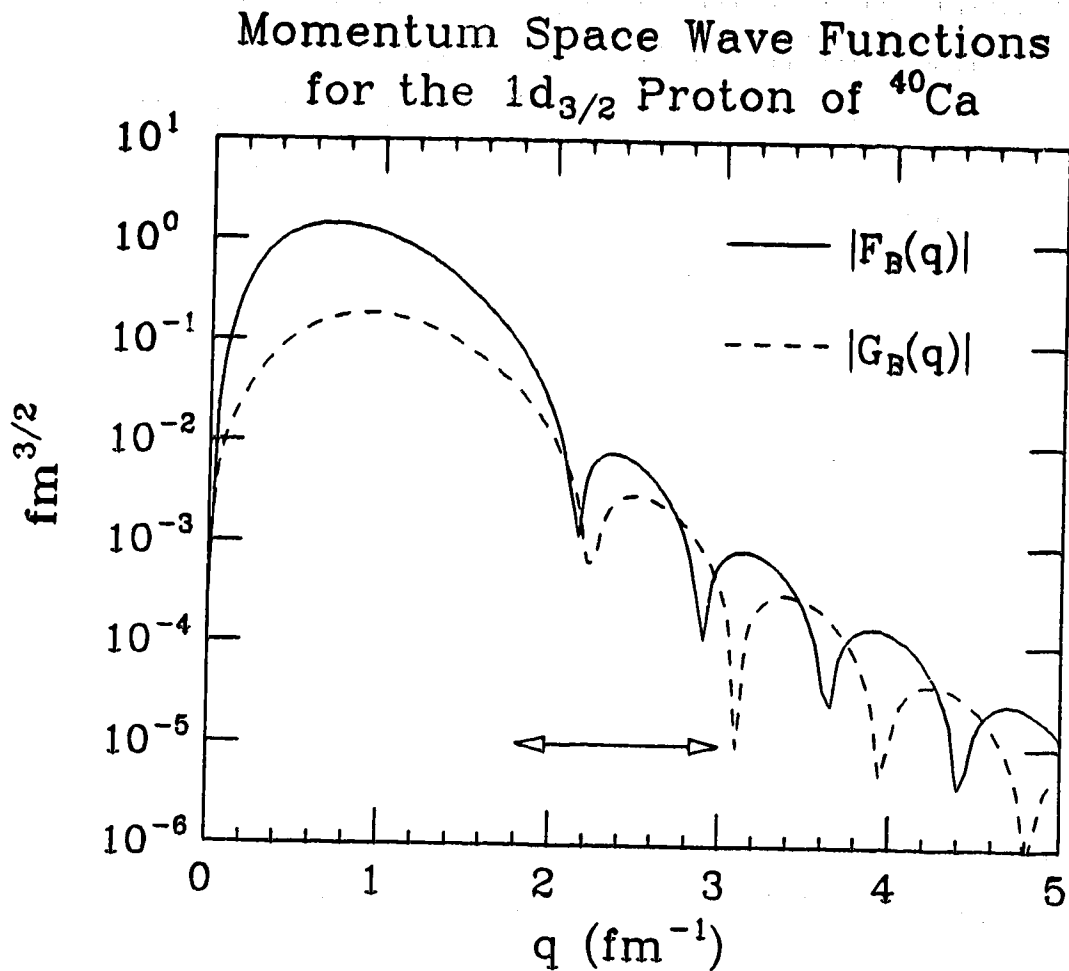


Fig. 6: The upper and lower component momentum-space wave functions of the $1d_{3/2}$ proton of ^{40}Ca . These wave functions are computed from a Dirac equation with Woods-Saxon binding potentials. The geometry parameters for the vector and scalar potentials are $R = 3.73$ fm and $a = 0.6$ fm. The vector strength is 320.0 MeV and the scalar strength is -398.3 MeV. The arrow denotes the region of momentum transfer that is typical of intermediate energy (γ, p) reactions on ^{40}Ca . The functions F_B and G_B are related to the coordinate space radial functions $f_B(r)$ and $g_B(r)$ by

$$F_B(q) \equiv \int r^2 dr f_B(r) j_{L_B}(qr)$$

$$G_B(q) \equiv \int r^2 dr g_B(r) j_{L_B}(qr).$$

4. The One Nucleon Model

The simplest mechanism by which a (γ, N) reaction can proceed is one in which the photon interacts directly with a valence nucleon of the target nucleus. The absorption of the photon results in the nucleon being ejected into a continuum state with the residual nucleus being left in a discrete state. This mechanism constitutes the One Nucleon Model (ONM) for (γ, N) reactions. It is also referred to as the quasifree knockout (QFK) mechanism⁽⁶⁴⁾. Implicit in this model is the assumption that the initial and final nuclear states can be described in terms of the shell model⁽⁶⁵⁾; the nucleon initially moves in a potential that is the average result of its interactions with all the other nucleons and the core is essentially a spectator in the reaction. Schematically the reaction is depicted in the following Feynman diagram:

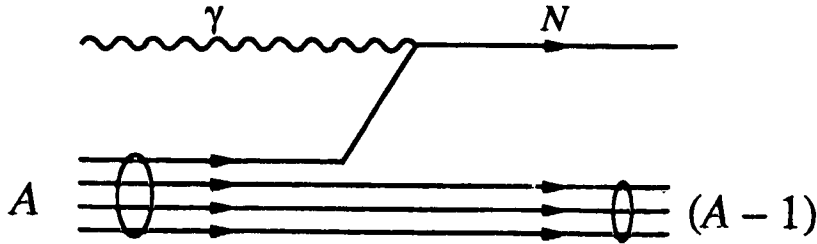


Fig. 7: The Feynman diagram for a (γ, N) reaction in the One Nucleon Model.

The transition matrix element for (γ, N) reactions may be written directly using the Feynman rules for this diagram. As an alternative, a field theoretic approach starting with a Lagrangian will lead to the scattering matrix for the (γ, N) reaction. The Lagrangian is perhaps a more "basic" starting point for the theory and hence this approach will be followed.

4.1 The Lagrangian Formalism for the One Nucleon Model

In the spirit of the ONM, the Lagrangian for (γ, N) reactions includes only one nucleon, the electromagnetic field and the interaction between the nucleon and the electromagnetic field. The nucleonic part of the Lagrangian

$$L_{\text{free}}(t) = \int \bar{\psi}(x)[i\gamma^\mu \partial_\mu - m]\psi(x)d^3x \quad (4.1)$$

is the usual free fermion Lagrangian that through the Euler-Lagrange equations leads to the free Dirac equation for the nucleon field $\psi(x)$. The Lagrangian for the electromagnetic field is⁽⁶⁰⁾

$$L_{\text{em}}(t) = -\frac{1}{4} \int F^{\mu\nu}(x) F_{\mu\nu}(x) d^3x . \quad (4.2)$$

The tensor $F^{\mu\nu}(x)$ is the electromagnetic field tensor defined by

$$F^{\mu\nu}(x) = \partial^\mu A^\nu(x) - \partial^\nu A^\mu(x) \quad (4.3)$$

where $A^\mu(x)$ is the four-vector potential of the photon. The interaction between the nucleon and the electromagnetic field is obtained by making the substitution⁽¹²⁾

$$i\gamma^\mu \partial_\mu \rightarrow \gamma^\mu [i\partial_\mu - e_N A_\mu(x)] \quad (4.4)$$

in the free fermion Lagrangian. The term $e_N \gamma^\mu A_\mu(x)$ describes the interaction of the electromagnetic field with a Dirac particle of charge e_N ; this is the familiar minimal electromagnetic coupling. The total Lagrangian is therefore written as

$$L(t) = \int \bar{\psi}(x) [\gamma^\mu (i\partial_\mu - e_N A_\mu(x)) - m] \psi(x) d^3x - \frac{1}{4} \int F^{\mu\nu}(x) F_{\mu\nu}(x) d^3x . \quad (4.5)$$

The Hamiltonian density $\mathcal{H}(x)$ is related to the Lagrangian density $\mathcal{L}(x)$ (where $L(t) = \int \mathcal{L}(x) d^3x$) by⁽⁶⁶⁾

$$\mathcal{H}(x) = \frac{\partial \mathcal{L}(x)}{\partial \dot{\psi}(x)} \dot{\psi}(x) + \frac{\partial \mathcal{L}(x)}{\partial \dot{A}^k(x)} \dot{A}^k(x) - \mathcal{L}(x) . \quad (4.6)$$

Thus the Hamiltonian $H(t) = \int \mathcal{H}(x) d^3x$ is a sum of free, electromagnetic and interaction terms

$$H(t) = H_{\text{free}}(t) + H_{\text{em}}(t) + H_{\text{int}}(t) \quad (4.7a)$$

where

$$H_{\text{free}}(t) = \int \psi^\dagger(x) [\alpha \cdot \mathbf{p} + \beta m] \psi(x) d^3x \quad (4.7b)$$

$$H_{\text{em}}(t) = \frac{1}{2} \int [E^2(x) + B^2(x)] d^3x \quad (4.7c)$$

$$H_{\text{int}}(t) = \int \bar{\psi}(x) [e_N \gamma^\mu A_\mu(x)] \psi(x) d^3x . \quad (4.7d)$$

In the electromagnetic Hamiltonian, the tensor $F^{\mu\nu}(x)$ has been written explicitly in terms

of the electric and magnetic fields. Also, one of the Maxwell equations has been used to eliminate one term for this part of the Hamiltonian.

In order to account for the anomalous magnetic moment that a nucleon is observed to have, an additional magnetic dipole term

$$\frac{\kappa_N \mu_N}{2} \bar{\psi}(x) \sigma^{\mu\nu} \psi(x) F_{\mu\nu}(x)$$

is included in the interaction Hamiltonian density⁽⁶⁷⁾. The proton has a magnetic moment of $2.79 \mu_N$ and the neutron has a magnetic moment of $-1.91 \mu_N$, where $\mu_N = e/2m_N$ is the nuclear magneton. The predicted Dirac values of the magnetic moment for the proton and neutron are $1 \mu_N$ and $0 \mu_N$ respectively, and so $\kappa_N = 1.79$ for a proton and $\kappa_N = -1.91$ for a neutron. The tensor $\sigma^{\mu\nu}$ is given in terms of the Dirac matrices as

$$\sigma^{\mu\nu} = \frac{i}{2} (\gamma^\mu \gamma^\nu - \gamma^\nu \gamma^\mu) . \quad (4.8)$$

The interaction Hamiltonian with this additional term becomes

$$H_{\text{int}}(t) = \int \bar{\psi}(x) \left[e_N \gamma^\mu A_\mu(x) + \frac{\kappa_N \mu_N}{2} \sigma^{\mu\nu} F_{\mu\nu}(x) \right] \psi(x) d^3x . \quad (4.9)$$

The dynamical equation for the nucleon is derived from the Heisenberg equation of motion

$$\frac{\partial \psi(x)}{\partial t} = i [H(t), \psi(x)] . \quad (4.10)$$

Using the fermion anticommutation relations

$$\{ \psi(t, \mathbf{x}), \psi(t, \mathbf{x}') \} = 0 \quad (4.11a)$$

$$\{ \psi(t, \mathbf{x}), \psi^\dagger(t, \mathbf{x}') \} = \delta^3(\mathbf{x} - \mathbf{x}') \quad (4.11b)$$

and the the expressions (4.7a), (4.7b), (4.7c) and (4.9) for the Hamiltonian in Eq. (4.10) leads to the Dirac equation

$$\left[i \gamma^\mu \partial_\mu - e_N \gamma^\mu A_\mu(x) - \frac{\kappa_N \mu_N}{2} \sigma^{\mu\nu} F_{\mu\nu}(x) - m \right] \psi(x) = 0 . \quad (4.12)$$

A Foldy-Wouthuysen transformation of the Hamiltonian operator in this equation shows explicitly how the additional tensor term accounts for the observed anomalous magnetic

moment⁽¹²⁾.

Two points are worth noting about the preceding formulation for the nucleon anomalous magnetic moment. First, the tensor term is not included in the interaction Lagrangian because it includes time derivatives of the field $A^\mu(x)$. This leads to problems in going to the Hamiltonian by the prescription of Eq. (4.6) in much the same way as a velocity-dependent potential in the interaction Lagrangian does in classical mechanics⁽³⁴⁾. Second, the anomalous magnetic moment can alternatively be attributed to the influence of strong interactions⁽¹²⁾. This would require including pions in the Lagrangian. The end result (for the anomalous moments) turns out to be the same, and so the complicating feature of the pions is avoided by including the tensor term in the Hamiltonian.

4.2 The Scattering Matrix

The quantity that must be determined in order to make predictions of experimental observables for (γN) reactions is the scattering matrix (S -matrix). The square of the S -matrix gives the probability that the photonuclear reaction will take place. In first-order perturbation theory the S -matrix for a reaction is⁽⁶⁸⁾

$$S_{fi} = \langle \Psi_f | (-i) \int_{-\infty}^{\infty} H_{\text{int}}(t) dt | \Psi_i \rangle \quad (4.13)$$

where Ψ_i and Ψ_f are the initial and final states of the system respectively. For the case of (γN) reactions, the initial state contains a photon and a nucleus with A nucleons, and the final state contains a free nucleon and a nucleus with $(A - 1)$ nucleons.

In the One Nucleon Model the initial and final states may be written using creation and annihilation operators. The final state is written as

$$|\Psi_f\rangle = b_{s_f}^\dagger(\mathbf{k}_N) |\Phi_{J_f}^{M_f}\rangle. \quad (4.14)$$

The state $|\Phi_{J_f}^{M_f}\rangle$ is precisely the final nuclear state with angular momentum quantum number J_f and projection M_f . The operator $b_{s_f}^\dagger$ creates a nucleon in the continuum with spin projection s_f and momentum \mathbf{k}_N . The initial state is written as a fractional-parentage expansion of the ground state wave function of the target nucleus in terms of the complete set of wave functions $|\Phi_J^M\rangle$ for the parent states J in the residual nucleus as⁽⁶⁹⁾

$$|\Psi_i\rangle = a^\dagger(\mathbf{k}_\gamma) \sum_{J_B M_B J} (J J_B ; M M_B | J_i M_i) \mathcal{J}_{J_i J}(J_B) b_{J_B M_B}^\dagger |\Phi_J^M\rangle \quad (4.15)$$

where $a^\dagger(\mathbf{k}_\gamma)$ is the creation operator for a photon with momentum \mathbf{k}_γ and $b_{J_B M_B}^\dagger$ is the creation operator for a bound nucleon with angular momentum quantum numbers J_B and M_B bound to the core $|\Phi_J^M\rangle$. The vector sum using Clebsch-Gordan coefficients ensures that the initial nuclear state has a well-defined angular momentum J_i with projection M_i . The \mathcal{J} 's are fractional-parentage coefficients; $\mathcal{J}_{J_i J}^2(J_B)$ gives the probability that the target nucleus is in a configuration that consists of the vector product of a single-particle bound state with total angular momentum J_B and an eigenstate of $(A - 1)$ nucleons that has total angular momentum J .

The present study is restricted to nuclear targets with simple structure, namely those having closed shells ($J_i = 0$) or having one valence nucleon outside closed shells. In the latter instance only transitions to the ground state of the residual nucleus ($J_f = 0$) are considered. For such cases, J_B is required to be $J_B = J_f$ or $J_B = J_i$ respectively. The overlap between nuclear wave functions involved in evaluating the S -matrix will pick out the term in the parentage expansion with $J = J_f$ and $M = M_f$. The shell model assumption implies that the corresponding fractional-parentage coefficient $\mathcal{J}_{J_i J_f}(J_B)$ will be close to unity.

The interaction Hamiltonian (4.9) is written in terms of the four-vector potential of the photon $A^\mu(x)$ and the nucleon field $\psi(x)$. The electromagnetic potential is written in second quantized form as⁽⁶⁶⁾

$$A^\mu(x) = \varepsilon^\mu \int \frac{d^3k}{(2\pi)^{3/2} (2\omega_k)^{1/2}} [a(\mathbf{k}) e^{-ik \cdot x} + a^\dagger(\mathbf{k}) e^{ik \cdot x}] \quad (4.16)$$

where $a^\dagger(\mathbf{k})$ and $a(\mathbf{k})$ are the creation and destruction operators respectively for a photon with momentum \mathbf{k} and energy $\omega_k = |\mathbf{k}|$. These operators obey the commutation relation

$$[a(\mathbf{k}), a^\dagger(\mathbf{k}')] = \delta^3(\mathbf{k} - \mathbf{k}') . \quad (4.17)$$

The electromagnetic field tensor (4.3) is easily derived from the expression for $A^\mu(x)$ as

$$F^{\mu\nu}(x) = i \int \frac{d^3k}{(2\pi)^{3/2} (2\omega_k)^{1/2}} (\varepsilon^\mu k^\nu - \varepsilon^\nu k^\mu) [a(\mathbf{k}) e^{-ik \cdot x} - a^\dagger(\mathbf{k}) e^{ik \cdot x}] . \quad (4.18)$$

The second quantized form of the nucleon field operator $\psi(x)$ is⁽⁶⁶⁾

$$\begin{aligned} \psi(x) = \sum_s \int \frac{d^3k}{(2\pi)^{3/2}} \left(\frac{m}{E}\right)^{1/2} [b_s(\mathbf{k}) u_s(\mathbf{k}, x) + d_s^\dagger(\mathbf{k}) v_s(\mathbf{k}, x)] \\ + \sum_n [b_n u_n(x) + d_n^\dagger v_n(x)] \end{aligned} \quad (4.19)$$

- where (i) $b_s(\mathbf{k})$ is the destruction operator for a nucleon with spin s and momentum \mathbf{k} and $u_s(\mathbf{k}, x)$ is the corresponding space-time continuum wave function,
(ii) $d_s^\dagger(\mathbf{k})$ is the creation operator for an antinucleon with spin s and momentum \mathbf{k} and $v_s(\mathbf{k}, x)$ is the corresponding space-time continuum wave function,
(iii) b_n is the destruction operator for a bound nucleon with quantum numbers denoted by n and $u_n(x)$ is the corresponding space-time continuum wave function,
(iv) d_n^\dagger is the creation operator for a bound antinucleon with quantum numbers denoted by n and $v_n(x)$ is the corresponding space-time continuum wave function.

The creation and annihilation operators obey the usual fermion anticommutation relations

$$\{b_s(\mathbf{k}), b_{s'}^\dagger(\mathbf{k}')\} = \delta_{ss'} \delta^3(\mathbf{k} - \mathbf{k}') \quad (4.20a)$$

$$\{d_s(\mathbf{k}), d_{s'}^\dagger(\mathbf{k}')\} = \delta_{ss'} \delta^3(\mathbf{k} - \mathbf{k}') \quad (4.20b)$$

$$\{b_n, b_m^\dagger\} = \delta_{nm} \quad (4.20c)$$

$$\{d_n, d_m^\dagger\} = \delta_{nm} \quad (4.20d)$$

with all other anticommutator combinations giving zero.

The S -matrix can be evaluated using the expressions (4.14) and (4.15) for the final and initial wave functions, (4.9) for the interaction Hamiltonian and (4.19), (4.16) and (4.18) for $\psi(x)$, $A^\mu(x)$ and $F^{\mu\nu}(x)$. The S -matrix is an expectation value between nuclear states $|\Phi_j^m\rangle$ of a sum of terms involving products of creation/annihilation operators and space-time wave functions. The nuclear states $|\Phi_j^m\rangle$ contain only $(A - 1)$ positive energy bound baryons; there are no antiparticles. It follows that

$$d_n |\Phi_j^m\rangle = 0 \quad (4.21a)$$

$$d_s(\mathbf{k}) |\Phi_j^m\rangle = 0 \quad (4.21b)$$

$$b_s(\mathbf{k}) |\Phi_j^m\rangle = 0 \quad (4.21c)$$

$$a(\mathbf{k}) |\Phi_j^m\rangle = 0. \quad (4.21d)$$

Also, the creation operators b_n^\dagger create bound nucleons only for unoccupied single-particle levels and the destruction operators b_n destroy only occupied levels. Using the commutation and anticommutation relations to evaluate the momentum integrals (via the delta function $\delta^3(\mathbf{k} - \mathbf{k}')$) and spin sums (via the Kronecker delta $\delta_{ss'}$) greatly simplifies the expression for the S -matrix. The S -matrix becomes

$$S_{fi} = -i g_{J_i J_f}(J_B) (J_f J_B; M_f M_B | J_i M_i) \frac{1}{(2\pi)^3} \left(\frac{m}{E}\right)^{1/2} \left(\frac{1}{2\omega_{\mathbf{k}_\gamma}}\right)^{1/2} \\ \times \int d^4x u_{s_f}(\mathbf{k}, x) \varepsilon^\mu \{ e_N \gamma_\mu + i \kappa_N \mu_N \sigma_{\mu\nu} k_\nu \} e^{-ik_\gamma \cdot x} u_{J_B M_B}(x). \quad (4.22)$$

In order to evaluate the S -matrix further, expressions for the bound state wave function $u_{J_B M_B}(x)$ and the continuum wave function $u_{s_f}(\mathbf{k}, x)$ have to be specified. It is not clear how to write these wave functions exactly, since they are a solution to a many-body problem involving A nucleons. Some models in which the wave functions can be approximately evaluated are discussed in Chap. 3. These results for the wave functions are utilized in the following sections.

4.3 The Plane Wave Born Approximation

The lowest order approximation for the continuum nucleon is that it does not interact with the residual nucleus after being photoejected from its bound state. The continuum space-time wave function (which will now be denoted by $\psi_{s_f}(x)$ rather than $u_{s_f}(\mathbf{k}, x)$) therefore satisfies the free Dirac equation⁽¹²⁾

$$(i\gamma^\mu \partial_\mu - m) \psi_{s_f}(x) = 0. \quad (4.23)$$

The positive energy solution is the plane wave four-component spinor

$$\psi_{s_f}(x) = \sqrt{\frac{E+m}{2m}} \begin{bmatrix} \mathbb{1} \\ \frac{\boldsymbol{\sigma} \cdot \mathbf{p}}{E+m} \end{bmatrix} \chi_{1/2}^{s_f} e^{-i\mathbf{k} \cdot \mathbf{x}} \quad (4.24)$$

with energy E , momentum $\mathbf{p} = \mathbf{k}$ and spin s_f . The matrix in this equation is a 2×4 matrix containing the 2×2 unit matrix $\mathbb{1}$ and the Pauli spin matrices $\boldsymbol{\sigma}$. $\chi_{1/2}^{s_f}$ is the two-component spinor with spin projection s_f . The calculation of the S -matrix using this form for the nucleon wave function is the so-called plane wave Born approximation (PWBA).

Because the bound nucleon is localized in space, it cannot be described by a plane wave. The interaction between the bound nucleon and the $(A - 1)$ nucleons cannot be ignored since it is precisely this interaction which binds the nucleon. Furthermore, the core must be present so that energy and momentum can be conserved in the reaction. The core is in fact included in the interaction Lagrangian implicitly by including bound states in $\psi(x)$.

The bound state wave function is discussed in detail in Chap. 3. Another approach to a description of the bound state wave function is to make an analogy with an electron bound by a static Coulomb field. For this case the Dirac equation includes the Coulomb potential⁽¹²⁾

$$\left[i\gamma^\mu \partial_\mu - m + \gamma^0 \frac{Ze^2}{4\pi|\mathbf{x}|} \right] \psi(x) = 0 \quad (4.25)$$

In a qualitative sense, the $(A - 1)$ nucleon core also provides a potential that binds the nucleon. This potential is the average result of the interaction of the valence nucleon with all of the other nucleons, and is justified in more detail in Chap. 3. Including an appropriate central potential in the Dirac equation (again changing notation from $u_{J_B M_B}(x)$ to $\psi_{J_B M_B}(x)$)

$$[i\gamma^\mu \partial_\mu - m + U(r)] \psi_{J_B M_B}(x) = 0 \quad (4.26)$$

will bind the nucleon. The spherically symmetric potential depends only on $r \equiv |\mathbf{x}|$ and so this equation describes the nucleon in the rest frame of the nucleus with the origin at the center of the nucleus.

Since the bound nucleon also has a definite parity (*i.e.*, a definite orbital angular

momentum L_B), its wave function can be written in analogy with the wave function for the bound electron of a Hydrogen atom as⁽¹²⁾

$$\Psi_{J_B M_B}(x) = e^{-iE_B t} \begin{bmatrix} f_B(r) \\ -i g_B(r) \sigma \cdot \hat{r} \end{bmatrix} \mathcal{Y}_{L_B 1/2 J_B}^{M_B}(\Omega). \quad (4.27)$$

The total energy of the nucleon is

$$E_B = m - E_b \quad (4.28)$$

where E_b is the binding energy of the nucleon. $\mathcal{Y}_{L_B 1/2 J_B}^{M_B}(\Omega)$ is the generalized spherical harmonic defined in Eq. (3.24). The radial functions $f_B(r)$ and $g_B(r)$ will satisfy a pair of coupled differential equations which will depend on the form of the potential $U(r)$.

With the wave functions described above, the S -matrix in the PWBA is

$$S_{fi}^{PWBA} = -i \delta(E - E_B - \omega) \int_{J_f J_f}(J_B) (J_f J_B; M_f M_B | J_i M_i) \frac{1}{(2\pi)^3} \left(\frac{m}{E}\right)^{1/2} \left(\frac{1}{2\omega_{k_\gamma}}\right)^{1/2} \left(\frac{E+m}{2m}\right)^{1/2} \\ \times \int d^3x \chi_{1/2}^{s_f \dagger} \left[\mathbb{1} - \frac{\sigma \cdot \mathbf{p}}{E+m} \right] e^{-i\mathbf{q} \cdot \mathbf{x}} \varepsilon^\mu \{ e_N \gamma_\mu + i \kappa_N \mu_N \sigma_{\mu\nu} k_\nu^y \} \begin{bmatrix} f_B(r) \\ -i g_B(r) \sigma \cdot \hat{r} \end{bmatrix} \mathcal{Y}_{L_B 1/2 J_B}^{M_B}(\Omega) \quad (4.29)$$

where $\mathbf{q} = \mathbf{k}_N - \mathbf{k}_\gamma$ is the momentum transfer in the reaction. It is apparent that aside from some spin algebra, the S -matrix is proportional to the Fourier transform of the bound state wave function. Thus, in the PWBA the cross section, which is proportional to the square of the S -matrix, will be given in terms of the momentum-space bound state wave function. The momentum transfer is very high in (γN) reactions and so if the PWBA is a reasonable approximation then (γN) experiments will probe the high momentum components of the nuclear bound state wave function. Indeed, assuming that direct photoemission is the dominant reaction mechanism, experiments will also give an indication of the validity of describing the bound state in terms of a potential in the Dirac equation.

4.4 The S -Matrix in the Distorted Wave Born Approximation

The scattering matrix of Eq. (4.22) for (γN) reactions is written in the relativistic distorted wave Born approximation (DWBA) by using the results of Chap. 3 for the

wave functions of a continuum nucleon distorted by an optical potential and a single nucleon bound by an appropriate Dirac potential. The S-matrix is

$$S_{fi} = -i g_{J_i J_f}(J_B) (J_f J_B; M_f M_B | J_i M_i) \frac{1}{(2\pi)^3} \left(\frac{m}{E}\right)^{1/2} \left(\frac{1}{2\omega_{k_\gamma}}\right)^{1/2} \\ \times \int d^4x \bar{\psi}_{s_f}^{(-)}(\mathbf{k}, x) \varepsilon^\mu \{e_N \gamma_\mu + i k_N \mu_N \sigma_{\mu\nu} k_\nu\} e^{-ik_\gamma \cdot x} \psi_B(x). \quad (4.30)$$

The bound state wave function is given by Eq. (3.43) as

$$\psi_B(x) = e^{-iE_B t} \begin{bmatrix} f_B(r) \mathcal{Y}_{L_B 1/2 J_B}^{M_B}(\Omega) \\ i g_B(r) \mathcal{Y}_{L'_B 1/2 J_B}^{M_B}(\Omega) \end{bmatrix}; \quad L'_B \equiv 2J_B - L_B. \quad (4.31)$$

The Dirac matrices are taken in the usual representation to be

$$\gamma^0 = \begin{bmatrix} \mathbb{1} & 0 \\ 0 & -\mathbb{1} \end{bmatrix}, \quad \boldsymbol{\gamma} = \begin{bmatrix} 0 & \boldsymbol{\sigma} \\ -\boldsymbol{\sigma} & 0 \end{bmatrix} \quad (4.32)$$

where $\boldsymbol{\sigma}$ are the Pauli matrices. The $(-)$ superscript on the nucleon continuum wave function denotes that the wave function asymptotically has a plane wave piece and spherical incoming waves. This is in direct analogy with the nonrelativistic case⁽⁶²⁾. The wave function $\psi_{s_f}^{(-)}(x)$ is the time-reversed wave of $\psi_{s_f}^{(+)}(x)$ (cf. Eq. (3.32)). Thus, its form is⁽⁷⁰⁾

$$\psi_{s_f}^{(-)}(x) = \left(\frac{E+m}{2m}\right)^{1/2} e^{iEt} 4\pi \sum_{LJM} i^{-L} Y_L^{M-s_f}(\hat{\mathbf{k}}_f) (L 1/2; M-s_f s_f | JM) \\ \times \mathcal{Y}_{L 1/2 J}^{M \dagger}(\Omega) \begin{bmatrix} f_{LJ}(r) & i \boldsymbol{\sigma} \cdot \hat{\mathbf{r}} g_{LJ}(r) \end{bmatrix}. \quad (4.33)$$

The integral in Eq. (4.30) is evaluated in the center-of-mass coordinate frame in which the photon momentum is chosen to be parallel to the z-axis and $\hat{\mathbf{k}}_\gamma \times \hat{\mathbf{k}}_N$ defines the y-axis direction. This frame is shown in Fig. 8. The photon polarization vector in this frame is $\varepsilon^\mu = (0, \cos\xi, \sin\xi, 0)$ which satisfies the necessary conditions $\varepsilon^\mu \varepsilon_\mu = -1$ and $\varepsilon_\mu k_\gamma^\mu = 0$. The matrix multiplication and angular momentum algebra then proceed straightforwardly, although the calculations are somewhat lengthy. With the partial wave expansion of the exponential

$$e^{-ik_{\gamma}x} = e^{-i\omega t} \sum_l \sqrt{4\pi(2l+1)} j_l(k_{\gamma}r) Y_l^{0*}(\Omega) \quad (4.34)$$

the angular integrations can be carried out analytically. Furthermore, the time integration gives an energy conserving delta function $\delta(E - \omega - E_B)$.

The final analytic form of the S -matrix is

$$S_{fi} = \frac{e}{2\pi} \mathcal{J}_{J_i J_f}(J_B) (J_f J_B; M_f M_B | J_i M_i) \left(\frac{E+m}{\omega E} \right)^{1/2} \delta(E - \omega - E_B) \\ \times \sum_{iLJ\mu} (-i)^{L+1} (2l+1) Y_L^{M_B+2\mu-s_f}(\theta, \phi=0) (L 1/2; M_B+2\mu-s_f s_f | J M_B+2\mu) \\ \times \left[\begin{array}{l} \frac{\kappa_N \omega}{2m} \left[I_{iLJ}^{L_B} C_{\mu iLJ}^{L_B} - I_{iLJ}^{L_B'} C_{\mu iLJ}^{L_B'} \right] (\sin \xi + i 2\mu \cos \xi) \\ + \left[\left(z_N - \frac{\kappa_N \omega}{2m} \right) I_{iLJ}^{L_B} C_{\mu iLJ}^{L_B} - \left(z_N + \frac{\kappa_N \omega}{2m} \right) I_{iLJ}^{L_B'} C_{\mu iLJ}^{L_B'} \right] (\cos \xi - i 2\mu \sin \xi) \end{array} \right] \quad (4.35a)$$

where z_N is the charge of the nucleon in units of the electronic charge e , the I 's are radial integrals

$$I_{iLJ}^{L_B} = (L_B l; 0 0 | L 0) \int r^2 dr f_B(r) f_{LJ}(r) j_l(k_{\gamma}r) \quad (4.35b)$$

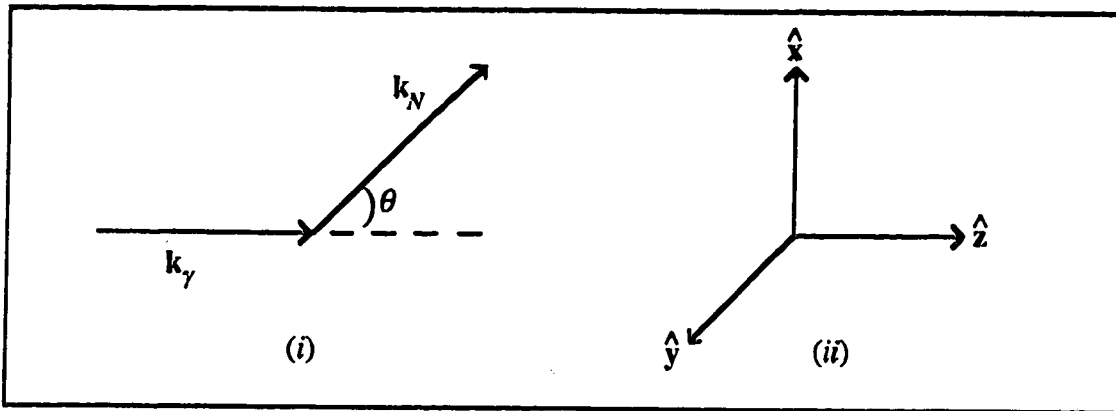


Fig. 8: The coordinate frame in which the S -matrix is evaluated.

(i) A schematic diagram of the reaction (θ is the scattering angle).

(ii) The chosen coordinate frame.

$$I_{lL'J}^{L_B} = (L_B \ l; 0 \ 0 \mid L' \ 0) \int r^2 dr f_B(r) g_{L'J}(r) j_l(kr) \quad (4.35c)$$

$$I_{lL'J}^{L'_B} = (L'_B \ l; 0 \ 0 \mid L \ 0) \int r^2 dr g_B(r) f_{L'J}(r) j_l(kr) \quad (4.35d)$$

$$I_{lL'J}^{L'_B} = (L'_B \ l; 0 \ 0 \mid L' \ 0) \int r^2 dr g_B(r) g_{L'J}(r) j_l(kr) \quad (4.35e)$$

and the C 's are combinations of Clebsch-Gordan coefficients

$$C_{\mu l L' J}^{L_B} = (L_B \ 1/2; M_B + \mu \ -\mu \mid J_B \ M_B) (L \ 1/2; M_B + \mu \ \mu \mid J \ M_B + 2\mu) \\ \times (L \ l; M_B + \mu \ 0 \mid L_B \ M_B + \mu) \quad (4.35f)$$

$$C_{\mu l L' J}^{L_B} = (L_B \ 1/2; M_B + \mu \ -\mu \mid J_B \ M_B) (L' \ 1/2; M_B + \mu \ \mu \mid J \ M_B + 2\mu) \\ \times (L' \ l; M_B + \mu \ 0 \mid L_B \ M_B + \mu) \quad (4.35g)$$

$$C_{\mu l L' J}^{L'_B} = (L'_B \ 1/2; M_B + \mu \ -\mu \mid J_B \ M_B) (L \ 1/2; M_B + \mu \ \mu \mid J \ M_B + 2\mu) \\ \times (L \ l; M_B + \mu \ 0 \mid L'_B \ M_B + \mu) \quad (4.35h)$$

$$C_{\mu l L' J}^{L'_B} = (L'_B \ 1/2; M_B + \mu \ -\mu \mid J_B \ M_B) (L' \ 1/2; M_B + \mu \ \mu \mid J \ M_B + 2\mu) \\ \times (L' \ l; M_B + \mu \ 0 \mid L'_B \ M_B + \mu). \quad (4.35i)$$

The fractional-parentage coefficient either can be obtained empirically from pickup or stripping reactions or is derived from theoretical models for the structure of the nucleus⁽⁷¹⁾. The energy and momentum of the photoejected nucleon are determined by energy and momentum conservation requirements (the relativistic kinematics are described in Appendix A). The sum over angular momentum quantum numbers converges and so the series is cut off in practise at some maximum L . The radial integrals are evaluated numerically.

There are several features of the S -matrix that are interesting to note. The "spin-magnetization" current terms that arise from the anomalous magnetic moment of the nucleon are proportional to $\kappa_N \mu_N \omega$ whereas the "convection" current terms that arise from the minimal electromagnetic coupling are proportional to $z_N e$. For neutrons, only the spin-magnetization current contributes to the S -matrix. For protons, the spin-

magnetization current contributions are a factor of $(\kappa_N \omega/2m)$ smaller than the convection current contributions. At photon energies below about 200 MeV the convection current interaction is expected to dominate the photoproton reaction. Furthermore, in this model the photoproton cross section will be much larger than the corresponding photoneutron cross section. As the photon energy increases, the coupling to the anomalous magnetic moment will become increasingly important.

For proton photoemission the relatively large convection current terms involve radial integrals that contain a product of upper and lower components of Dirac spinors in the integrand. This suggests that a Dirac calculation for this reaction might give different results from nonrelativistic Schrödinger calculations since the lower component is usually thought to be the "relativistic correction" to the wave function. Also, only the anomalous magnetic moment coupling involves an integral with a product of two upper radial components in the integrand. Since the magnitude of the upper radial component of especially the bound state wave function at small momentum transfer is significantly larger than the lower radial component (*cf.* Fig. 6), the spin-magnetization current might be relatively more important at forward angles.

4.5 Observables for (γ, N) Reactions

Observables for (γ, N) reactions are calculated from the S -matrix in the usual way, as is described in Appendix F. In the calculation of observables it is useful to write the S -matrix as

$$S_{fi} = \frac{e}{2\pi} \mathcal{J}_{J_i J_f}(J_B) (J_f J_B; M_f M_B | J_i M_i) \left(\frac{E+m}{\omega E} \right)^{1/2} \delta(E-\omega-E_B) Z_{s_f M_B}^{\xi}(\theta). \quad (4.36a)$$

This defines $Z_{s_f M_B}^{\xi}(\theta)$, which depends on the polarization of the incident photon and the spin projections of the target nucleus and outgoing nucleon, to be

$$Z_{s_f M_B}^{\xi}(\theta) = \sum_{lLJ\mu} (-i)^{L+l} (2l+1) Y_L^{M_B+2\mu-s_f}(\theta, \phi=0) (L \ 1/2; M_B+2\mu-s_f \ s_f | J \ M_B+2\mu) \\ \times \left[\begin{array}{l} \frac{\kappa_N \omega}{2m} \left[I_{lLJ}^{L_B} C_{\mu l L J}^{L_B} - I_{lLJ}^{L'_B} C_{\mu l L' J}^{L'_B} \right] (\sin \xi + i 2\mu \cos \xi) \\ + \left[\left(z_N - \frac{\kappa_N \omega}{2m} \right) I_{lLJ}^{L_B} C_{\mu l L J}^{L_B} - \left(z_N + \frac{\kappa_N \omega}{2m} \right) I_{lLJ}^{L'_B} C_{\mu l L' J}^{L'_B} \right] (\cos \xi - i 2\mu \sin \xi) \end{array} \right]. \quad (4.36b)$$

The cross section is obtained by squaring the S -matrix, dividing by time and incident flux, and summing over the phase space of the outgoing nucleon. For unpolarized photons and target nuclei, and if the polarizations of the photoemitted nucleons and residual nuclei are not measured, the cross section calculation includes averaging over initial polarizations and summing over final polarizations. Recalling that the S -matrix is written for the special case of a spin-zero target or residual nucleus, the Clebsch-Gordan coefficient $(J_f J_B; M_f M_B | J_i M_i)$ changes the sum over M_i and M_f into a sum over M_B . Specifically, for $J_i = 0$

$$(J_f J_B; M_f M_B | J_i M_i) = (J_f J_B; M_f M_B | 0 0) = (-1)^{J-M_f} (2J_f+1)^{-1/2} \delta_{J_f J_B} \delta_{M_f - M_B} \quad (4.37a)$$

and for $J_f = 0$

$$\begin{aligned} (J_f J_B; M_f M_B | J_i M_i) &= (0 J_B; 0 M_B | J_i M_i) = \delta_{J_i J_B} \delta_{M_i M_B} \\ &= (2J_f+1)^{1/2} \delta_{J_i J_B} \delta_{M_i M_B}. \end{aligned} \quad (4.37b)$$

The resultant unpolarized (γN) cross section is

$$\frac{d\sigma}{d\Omega} = \frac{2\pi\alpha p(E+mc^2)}{(2J_i+1)(2J_f+1)\hbar c p_\gamma} g_{J_i J_f}^2(J_B) \sum_{s_f M_B \xi} |Z_{s_f M_B}^\xi|^2. \quad (4.38)$$

The factors of \hbar and c have been included to give the cross section units of area. The quantity α is the fine structure constant which in the system of units used for the electromagnetic potential takes the value

$$\alpha = \frac{e^2}{4\pi} \cong \frac{1}{137}. \quad (4.39)$$

The sum over photon polarizations is for the two independent cases $\xi = 0$ and $\xi = \pi/2$ (i.e., $\varepsilon = (1,0,0)$ and $\varepsilon = (0,1,0)$ respectively).

The polarization of the photoejected nucleons is defined as

$$P(\theta) = \langle \sigma_y \rangle = \frac{(d\sigma/d\Omega)_\uparrow - (d\sigma/d\Omega)_\downarrow}{(d\sigma/d\Omega)_\uparrow + (d\sigma/d\Omega)_\downarrow} \quad (4.40)$$

where $(d\sigma/d\Omega)_\uparrow$ is the differential cross section for nucleons which have spin projection in the $\hat{k}_\gamma \times \hat{k}_N$ (up) direction and $(d\sigma/d\Omega)_\downarrow$ is the differential cross section for nucleons with spin projection in the opposite direction. In the coordinate frame chosen for

evaluating the S-matrix the expression for the nucleon polarization is

$$P(\theta) = \frac{2\theta m \sum_{M_B, \xi} [Z_{1/2M_B}^{\xi}(\theta) Z_{-1/2M_B}^{\xi*}(\theta)]}{\sum_{s_j, M_B, \xi} |Z_{s_j, M_B}^{\xi}|^2} \quad (4.41)$$

The analyzing power for a (γ, N) reaction is defined as

$$A(\theta) = \frac{(d\sigma/d\Omega)_R - (d\sigma/d\Omega)_L}{(d\sigma/d\Omega)_R + (d\sigma/d\Omega)_L} \quad (4.42)$$

where $(d\sigma/d\Omega)_R$ is the differential cross section for right circularly polarized photons ($\epsilon = (1/2)^{1/2}(\hat{x} + i\hat{y})$) and $(d\sigma/d\Omega)_L$ is the differential cross section for left circularly polarized photons ($\epsilon = (1/2)^{1/2}(\hat{x} - i\hat{y})$). Since the formalism above is done for linearly polarized light, the modification for the case of circularly polarized light is that $\sin\xi \rightarrow i\sin\xi$ in the expression for $Z_{s_j, M_B}^{\xi}(\theta)$ and the possible photon polarizations are changed to $\xi = \pi/2$ (right) and $\xi = -\pi/2$ (left).

5. Results of the One Nucleon Model for (γ,p) and (p,γ) Reactions

The results of the One Nucleon Model (ONM) for (γ,p) and (p,γ) reactions will be presented in this chapter. Presently, the experimental data is more extensive for these reactions than was the case when the nonrelativistic models that are exposed in Chapter 2 were put forward. The aim of this chapter will be to compare the ONM results with representative data throughout the intermediate energy range and for a variety of target nuclei. In this way the validity and limitations of the model will be most completely explored. The importance of testing a model with a comprehensive set of data is illustrated by the results of a number of nonrelativistic calculations for the $E_\gamma = 196$ MeV $^{16}\text{O}(\gamma,p)^{15}\text{N}$ differential cross section shown in Fig. 4. Although these models reproduce some limited subset of experimental photonuclear data, it is clear that this reaction presents problems for all the calculations.

5.1 The $^{16}\text{O}(\gamma,p)^{15}\text{N}$ Reaction

Oxygen is the most common target nucleus for (γ,p) experiments. Data exists for angular distributions over most of the intermediate energy range, and the energy dependence of the differential cross section for proton scattering angles of 45° , 90° and 135° is well established from 50 – 300 MeV. Oxygen is also ideal for the ONM calculations because both its structure and the elastic scattering of protons from it have been investigated extensively, particularly in the context of the Dirac framework.

5.1.1 The $E_\gamma = 196$ MeV Differential Cross Section

The differential cross section of the $^{16}\text{O}(\gamma,p)^{15}\text{N}$ reaction for $E_\gamma = 196$ MeV⁽²⁸⁾ is the most complete of the few (γ,p) angular distributions measured above 100 MeV. The observation that nonrelativistic calculations give poor results for this differential cross section suggests that new physics may be coming into play in this reaction. The ONM calculations will probe the possibility of relativistic effects being the solution to the discrepancies between theory and experiment. For these reasons this reaction will be studied in detail. In addition, complementary proton elastic scattering data exists at

$E_p = 200$ MeV (the photoemitted proton kinetic energy in the rest frame of the ^{15}N nucleus is 196 MeV).

The relativistic theoretical calculations for proton-nucleus elastic scattering involve evaluating the proton wave function from a Dirac equation with scalar and vector optical potentials as is described in Sec. 3.2. In a phenomenological analysis the optical potentials are often taken to be Woods-Saxon functions (*cf.* Eq. (3.12)) with a total of sixteen adjustable parameters. More generalized shapes that follow the nuclear density are also used on occasion. The parameters are varied to give an optimum fit to the elastic scattering data by a search algorithm. Since the data often consist of significantly more than sixteen measurements for cross section, analyzing power and sometimes spin rotation function observables, the number of parameters is not excessive. Also, the geometries of the potentials are constrained somewhat by the initial parameter guesses to be reasonably similar to the geometries expected from a microscopic theory.

The 200 MeV $\vec{p} + ^{16}\text{O}$ elastic scattering data includes differential cross section ($d\sigma/d\Omega$) and analyzing power (A) measurements from $0^\circ - 135^\circ$ scattering angles⁽⁷²⁾ as well as some very recent, as yet unpublished, spin rotation function (Q) measurements from $0^\circ - 45^\circ$ scattering angles⁽⁷³⁾. The Q data is of special interest, as it has been shown that Dirac optical model analyses consistently give a better description of this observable. The hope is that the spin rotation function measurements will pin down the proton wave function more precisely. In both nonrelativistic⁽⁷²⁾ and relativistic⁽⁴²⁾ optical model analyses it is found that conventional Woods-Saxon geometries for the potentials do not result in a very good description of the $d\sigma/d\Omega$ and A data above about $\theta_{\text{cm}} = 80^\circ$; more complicated geometries are required to give better agreement with the data.

Figures 9, 11 and 13 show the results of three Dirac calculations for the 200 MeV $\vec{p} + ^{16}\text{O}$ elastic scattering observables and Figs. 10, 12 and 14 show the corresponding Dirac optical potentials and the associated Schrödinger-equivalent potentials (*cf.* Eqs. (3.40)). The Q data is shown without error bars, since these are not available. The calculation shown in Fig. 9 uses scalar and vector optical potentials⁽⁴²⁾ with the generalized Woods-Saxon geometry

$$U(r) = V f_1(r) + i W f_2(r) \quad (5.1a)$$

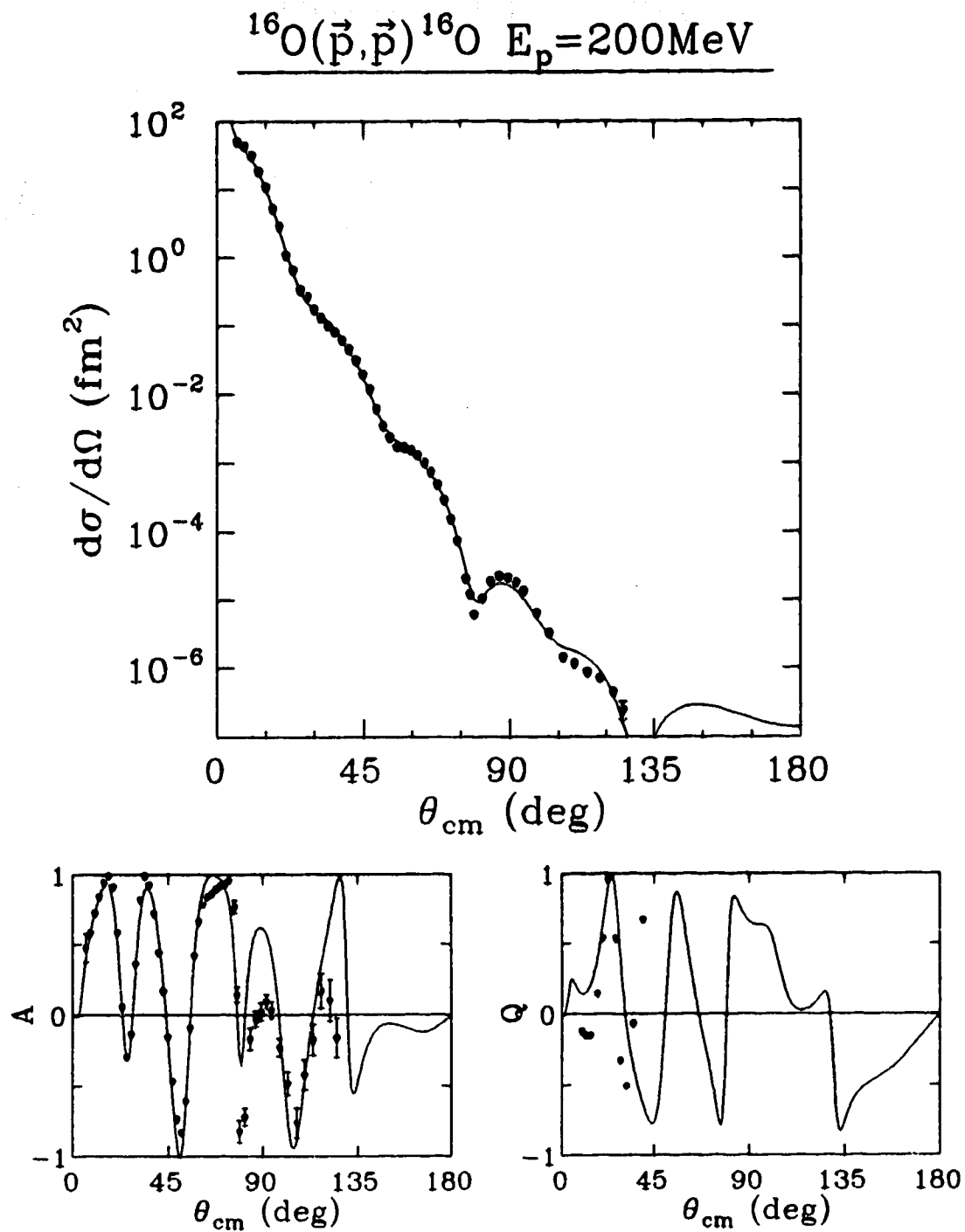


Fig. 9: Relativistic optical model calculation for observables of 200 MeV $\vec{p} + ^{16}\text{O}$ elastic scattering using the parabolic symmetric Woods-Saxon potential characterized by the parameters listed in Table 2. The data are from Ref. 72 and 73.

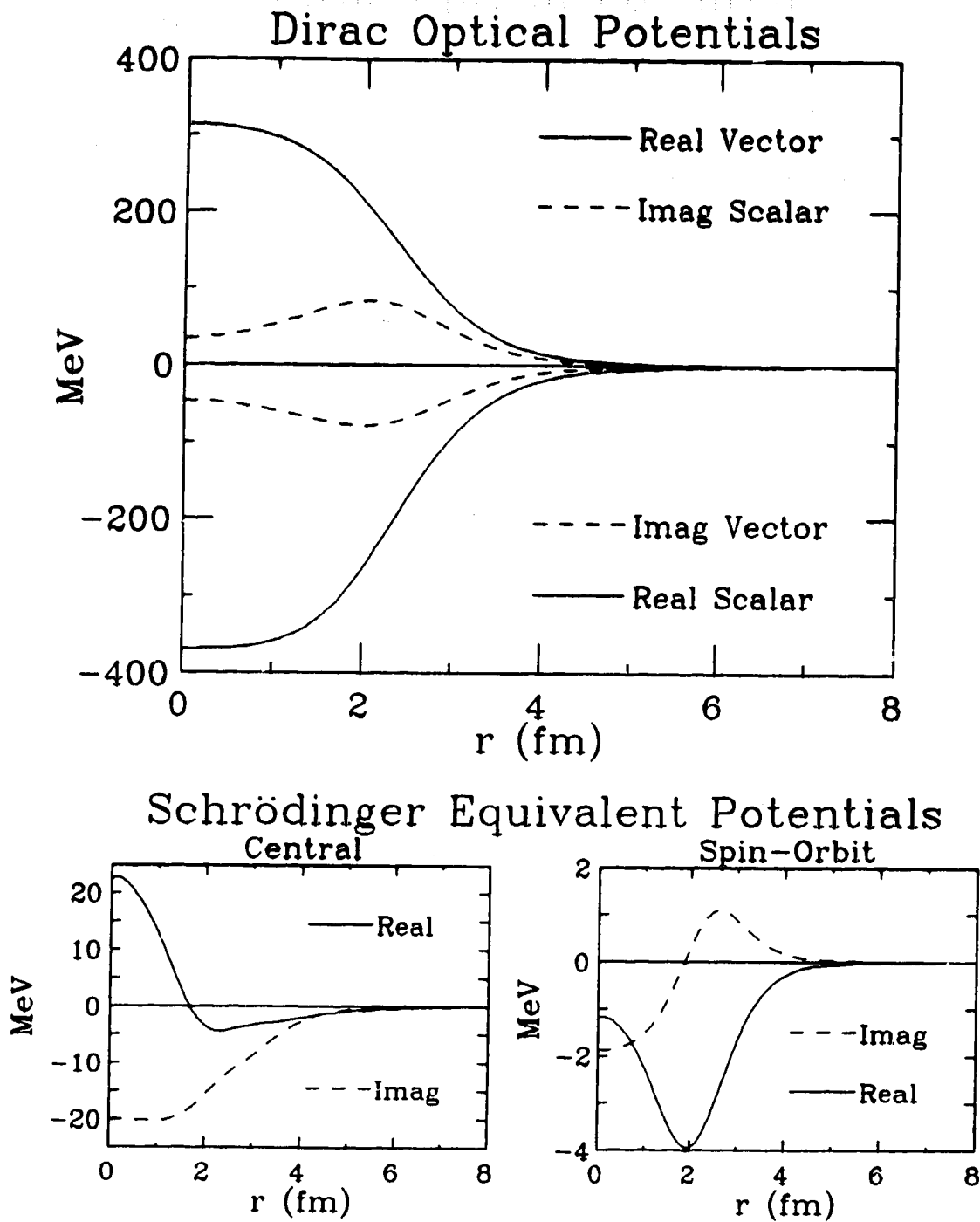


Fig. 10: Phenomenological parabolic symmetric Woods-Saxon optical potential for 200 MeV $\vec{p} + {}^{16}\text{O}$ elastic scattering characterized by the parameters listed in Table 2. The associated Schrödinger-equivalent potentials specified by Eqs. (3.40) are also shown.

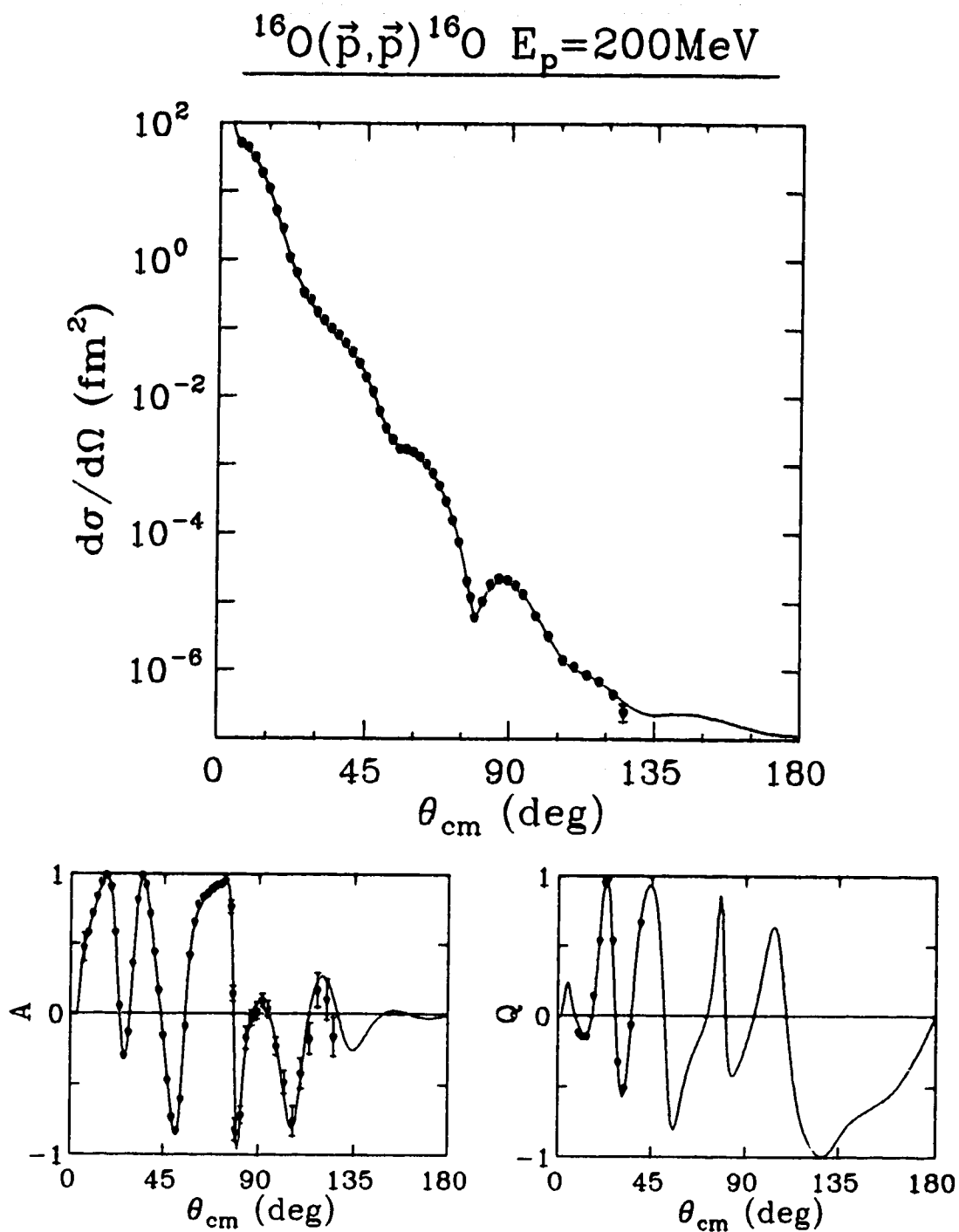


Fig. 11: Relativistic optical model calculation for observables of 200 MeV $\vec{p} + ^{16}\text{O}$ elastic scattering using the Fourier-Bessel parameterization for the potential shown in Fig. 12. The data are from Ref. 72 and 73.

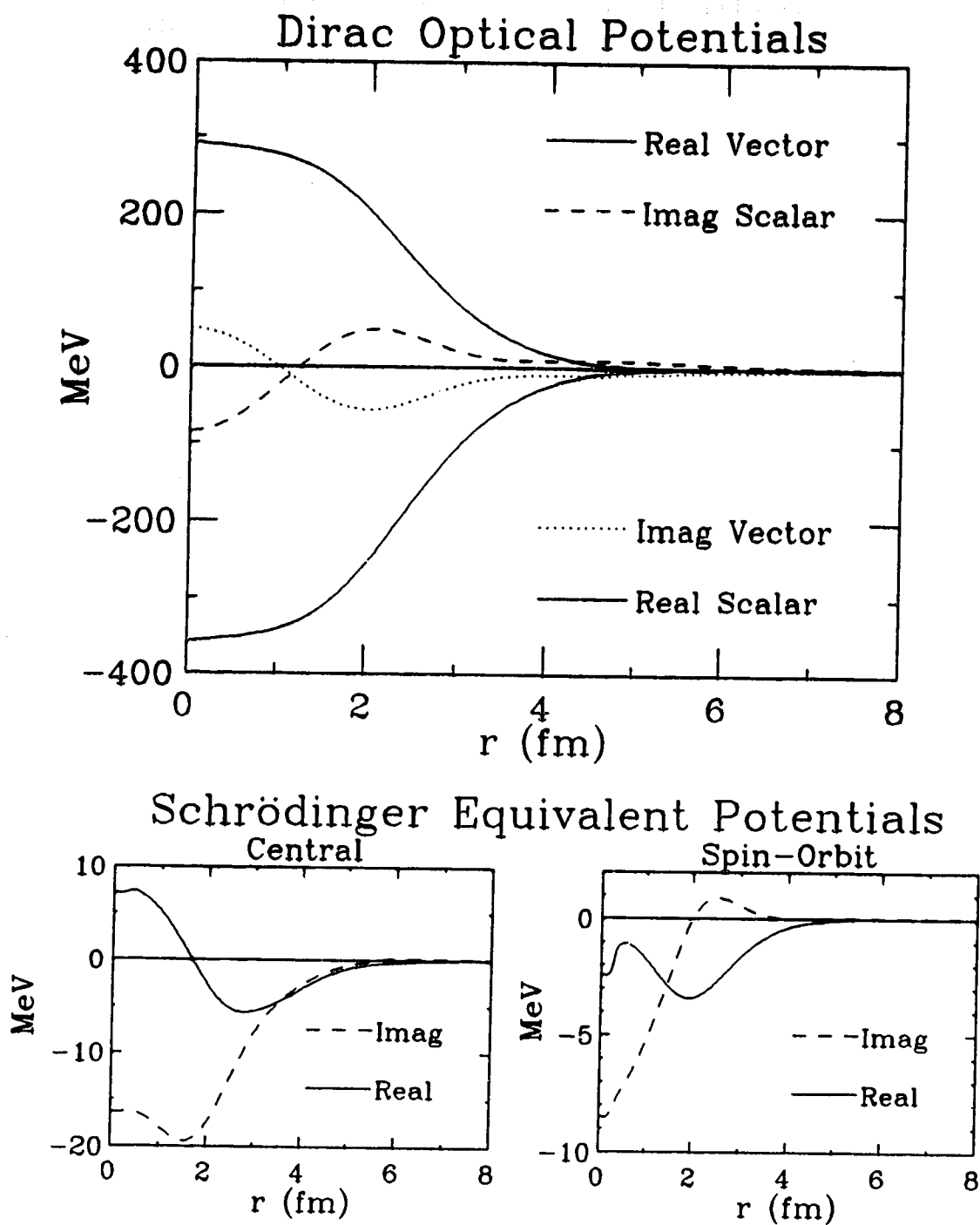


Fig. 12: Fourier-Bessel parameterized optical potential for 200 MeV \vec{p} + ^{16}O elastic scattering. The associated Schrödinger-equivalent potentials specified by Eqs. (3.40) are also shown.

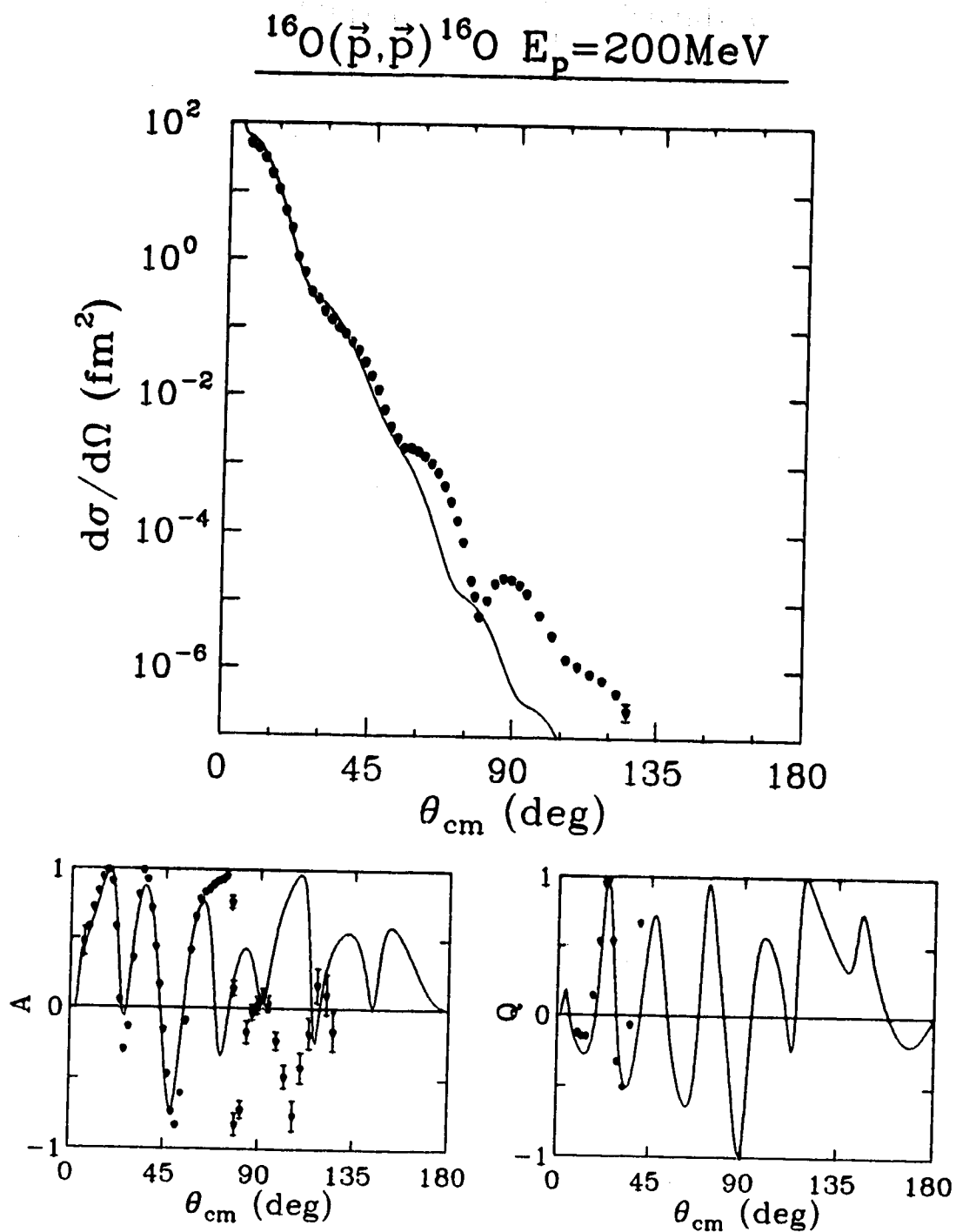


Fig. 13: Relativistic optical model calculation for observables of 200 MeV $\vec{p} + ^{16}\text{O}$ elastic scattering using the microscopic potential shown in Fig. 14. The data are from Ref. 72 and 73.

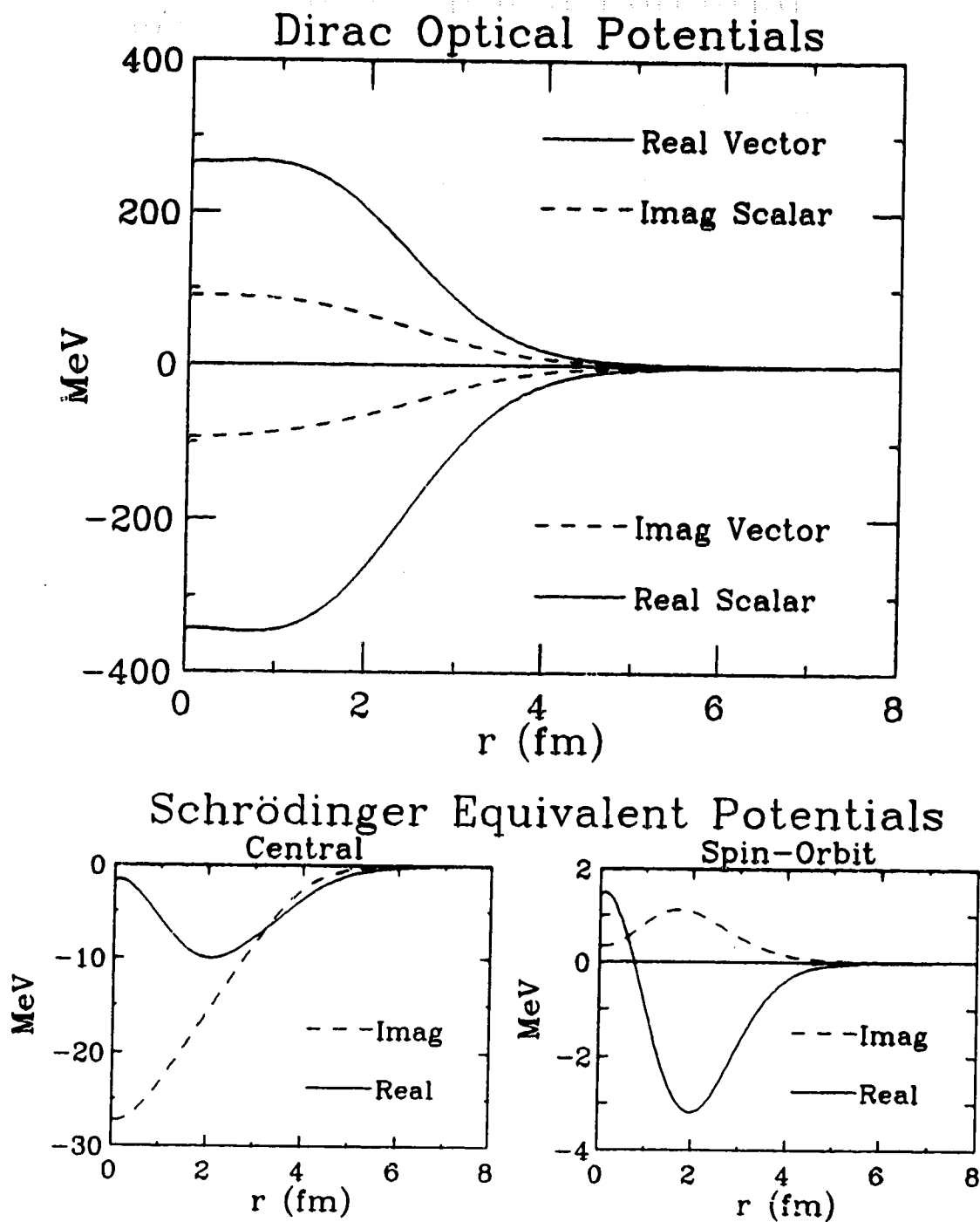


Fig. 14: Microscopic Dirac optical potential for 200 MeV $\bar{p} + {}^{16}\text{O}$ elastic scattering. The associated Schrödinger-equivalent potentials specified by Eqs. (3.40) are also shown.

$$f(r) = \frac{1 + \omega (r/R)^2}{\left[1 + g(r) e^{(r-R)/a} \right] \left[1 + g(r) e^{-(r+R)/a} \right]} \quad (5.1b)$$

$$g(r) = \lambda^2 + (1 - \lambda)^2 (r/R)^2 . \quad (5.1c)$$

The parabolic factor in the numerator of Eq. (5.1b) results in an enhancement of the potential away from the center of the nucleus. This corresponds to the observed central depression in the nuclear density in Dirac Hartree calculations⁽³⁶⁾ and the experimentally observed central depression in the charge density⁽⁷⁴⁾ for ^{16}O . The factor $g(r)$ multiplying the exponentials in Eq. (5.1b) generalizes the standard Woods-Saxon geometry. The factor λ is usually very close to unity and so the shape is not very different from the standard shape. The second factor in the denominator in Eq. (5.1b) also does not affect the shape very much. With this factor the potential is symmetrized in the sense that the derivative of the potential, which is related to the force a nucleon will experience due to the nucleus, will vanish at the origin. This feature of the potential is obviously desirable for a spherically symmetric nucleus and also results in a well-behaved Schrödinger-equivalent spin-orbit potential (*cf.* Eq. (3.41b)). The parameters of this potential are varied by a search algorithm in such a way that the agreement with the elastic data is optimized. The optimized parameters are shown in Table 2. The radial parameters listed are related to the radial parameters of Eq. (5.1b) through the number of nucleons in the nucleus by $R = r_0 A^{1/3}$. Figure 9 shows that this parabolic, symmetric

<u>Description</u>	<u>Vector</u>		<u>Scalar</u>	
	<u>Real</u>	<u>Imaginary</u>	<u>Real</u>	<u>Imaginary</u>
Strength:	322.80	- 47.07	-381.09	35.17
Radius r_0 :	0.9321	0.9945	0.8750	0.9716
Diffuseness a :	0.5439	0.4511	0.5252	0.4317
ω :	0.0111	1.9551	0.2164	3.2894
λ :	1.0116	1.0116	1.0116	1.0116

Table 2: Parabolic symmetric Woods-Saxon optical potential parameters determined for 200 MeV $\vec{p} + ^{16}\text{O}$ elastic scattering.

Woods-Saxon potential gives a very good description of the cross section and analyzing power data up to 80° . Above 80° the description of the data is not as satisfactory. The Q data has not been included in the fitting procedure, which accounts for the poor results for this observable. An even more general optical potential⁽⁷⁵⁾ gives the very impressive results of Fig. 11 for all the observables. The potential is expanded in a Fourier-Bessel series with parameters that are varied to fit all three observables. The main difference between this potential, shown in Fig. 12, and the parabolic symmetric Woods-Saxon potential of Fig. 10 is that the imaginary parts of this potential change sign in the nuclear interior. The predictions for the scattering observables when a Dirac optical potential that is determined from the microscopic calculations^(53,54) described in Subsec. 3.2.4 is used are shown in Fig. 13. The description of the data is good from $0^\circ - 55^\circ$, but is poor at more backward angles. Figure 14 illustrates that the microscopic potential differs from the phenomenological potentials shown in Figs. 10 and 12 mainly in the imaginary pieces. The surface-peaking of the phenomenological imaginary potentials is not manifest in the microscopic potentials. Apparently, the enhancement in the imaginary strengths near the surface of the nucleus is important in accounting for the elastic scattering data.

The distorted wave functions that result from these three potentials are utilized in the ONM calculations for the 196 MeV (γp) reaction on ^{16}O . The photoemitted proton is actually interacting with the residual ^{15}N nucleus but since there is no elastic scattering data from this nucleus the optical potentials for ^{16}O are used. This is considered to be a good approximation because nonrelativistic global optical potential parameterizations (in terms of the nucleon incident energy and the nuclear mass number)⁽⁷⁶⁾ show that a difference of one nucleon is not expected to affect the potential a great deal. Also, the effect of changing the potential strengths proportional to the fraction of nucleons in ^{15}N as compared with ^{16}O does not significantly alter the results of the (γp) calculation. It is assumed that the difference in the ^{16}O and ^{15}N optical potential is sufficiently taken into account by the $A^{1/3}$ dependence of the radial parameters. This supposition ignores the non-zero spin nature of the ^{15}N nucleus which, contrary to the situation for ^{16}O , does not preclude the possibility of processes such as pion exchange contributing to the optical potential.

In the simplest scenario, the bound valence proton wave function is calculated using a Dirac equation with a Woods-Saxon binding potential (*cf.* Subsec. 3.3.2). It is found that there are many "reasonable" choices for the potential shapes that give the same

binding energy, and the results of the (γ, p) calculations are very sensitive to the particular potential chosen. The requirement that the energy eigenvalue of the Hamiltonian containing the Woods-Saxon binding potential corresponds to the empirical binding energy of the nucleon does not constrain the potential sufficiently. With these *caveats* in mind, Fig. 15 shows the results of a ONM calculation with the bound state computed using one such Woods-Saxon binding potential and the proton distorted wave computed using the parabolic symmetrized Woods-Saxon optical potential shown in Fig. 10. The parameters for the binding potential, listed in Table 3, are determined from a search algorithm which gives the best fit to the (γ, p) data. The radial parameters in this case and for all subsequent sets of bound state parameters have a dependence on the number of nucleons in the nucleus (including the bound nucleon of interest) given by $R = r_0(A - 1)^{1/3}$. The fractional-parentage coefficient of the bound state wave function is taken to be 1.0, *i.e.*, it is assumed that the proton is in an ideal $1p_{1/2}$ shell model state. This is expected to be a good approximation for the doubly magic ^{16}O nucleus and will be used for all the subsequent $^{16}\text{O}(\gamma, N)$ calculations. The agreement with the experimental data shown in Fig. 15 is very good for angles less than 90° ; at backward angles the calculation falls increasingly below the data. Although there are difficulties with the computation of the bound state wave function, this calculation suggests that the direct photoejection mechanism has the potential of accounting for most of the experimental points. At higher momentum transfers other processes may be becoming important. The results are certainly closer to experiment than any of the nonrelativistic results shown in Fig. 4. It is noteworthy that the magnitude of the relativistic direct mechanism calculation does not fall below the data nearly so fast with increasing momentum transfer as the nonrelativistic direct mechanism calculation,

<u>Description</u>	<u>Vector</u>	<u>Scalar</u>
Strength:	367.37	-451.13
Radius r_0 :	1.0739	1.0734
Diffuseness a :	0.5728	0.6258

Table 3: Woods-Saxon binding potential parameters for ^{16}O .

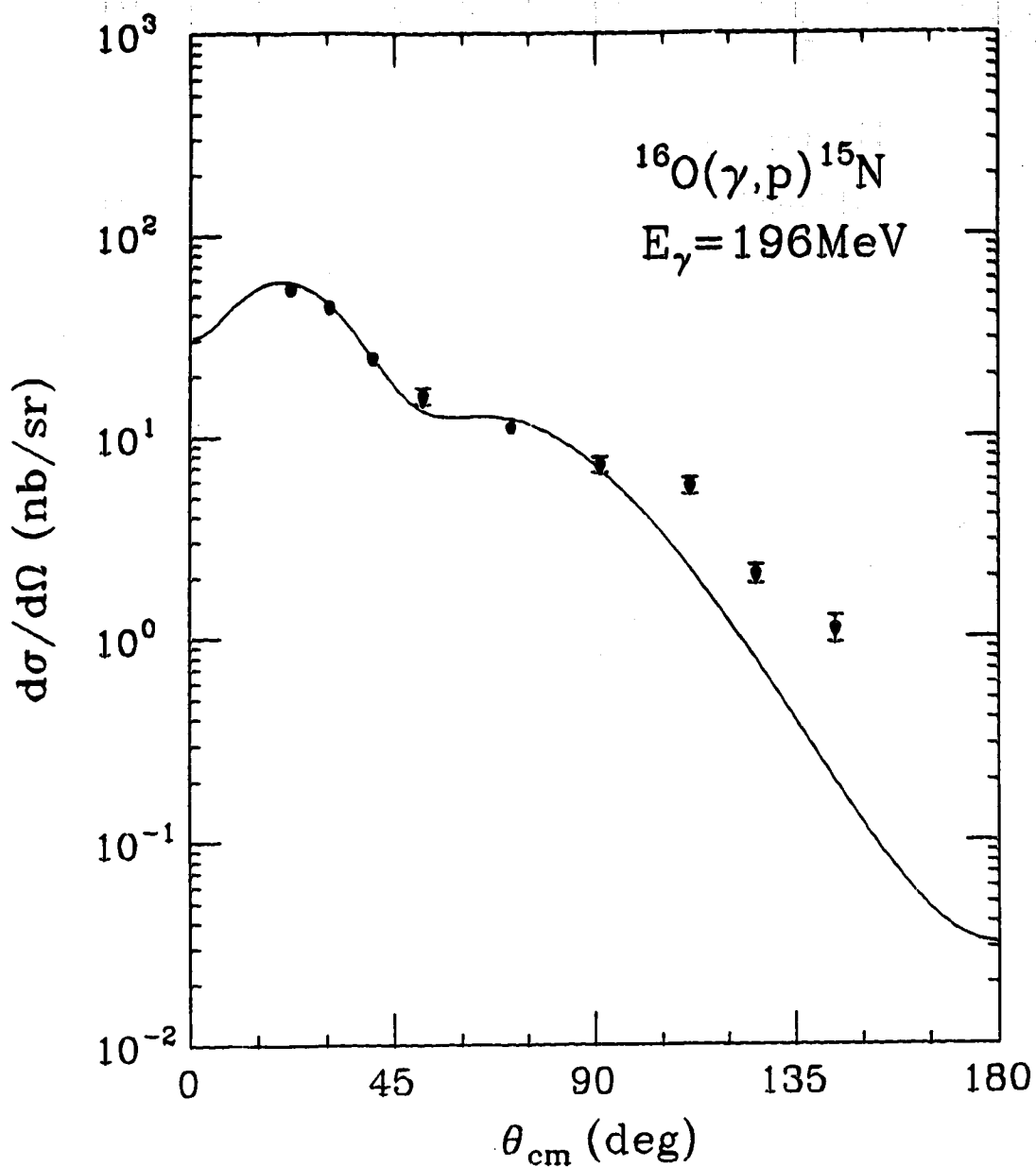


Fig. 15: ONM calculation for the differential cross section of the 196 MeV $^{16}\text{O}(\gamma, p)^{15}\text{N}$ reaction in which the Woods-Saxon binding potential of Table 3 and the parabolic symmetric Woods-Saxon optical potential of Table 2 are used. The data are from Ref. 28.

although qualitatively the shapes of the two calculations are similar.

Using a Hartree bound state wave function circumvents the problems associated with the "phenomenological" bound state wave function described above. The self-consistent Hartree calculations discussed in Sec. 3.1 give a unique bound state wave function for a choice of meson masses and coupling constants that are determined from the bulk properties of nuclei. The outcome of ONM calculations with such a bound state wave function are illustrated in Fig. 16. The three curves shown are differentiated by the proton distorted wave function used in the calculation. The solid and dashed curves are the result of using the phenomenological distorted waves determined with the parabolic symmetrized Woods-Saxon potential shown in Fig. 10 and the Fourier-Bessel potential shown in Fig. 12, respectively. The microscopic Dirac optical potential of Fig. 14 is utilized in the dotted curve calculation. Comparing the solid curve with Fig. 15, it is encouraging that when the same proton distorted wave is used, the calculation using a Hartree potential is not very different from the result obtained with the Woods-Saxon potential that gives good agreement with the data. Moreover, the distorted wave functions that give better results for the elastic scattering also give better agreement with the (γp) data. The three curves give an indication of the sensitivity of the calculations to the distorted wave function employed.

It would certainly be desirable to be able to determine a unique phenomenological binding potential. It is possible that in addition to the binding energy of the valence nucleon, other experimentally determined properties of the nucleus might limit the possibilities for the potential. These might include the energies of excited shell model states, the rms charge radius of the nucleus and the rms radius of the valence nucleon. These possibilities have been investigated with limited success. The empirical binding energy of the $1p_{1/2}$ neutron of ^{16}O is very nearly obtained with the Woods-Saxon potential used in the calculation shown in Fig. 15. Other Woods-Saxon potentials for which the (γp) results are not so good give very disparate neutron binding energies. The bound nucleon wave function may also be constrained by theoretical calculations for other reactions that require this wave function. The major problem in any of these approaches to ascertain a good bound state wave function is that the empirical constraints are sensitive to lower momentum components of the wave function than those germane for the (γp) reaction. In this context, a Hartree calculation provides perhaps the most reasonable choice for the bound nucleon wave function.

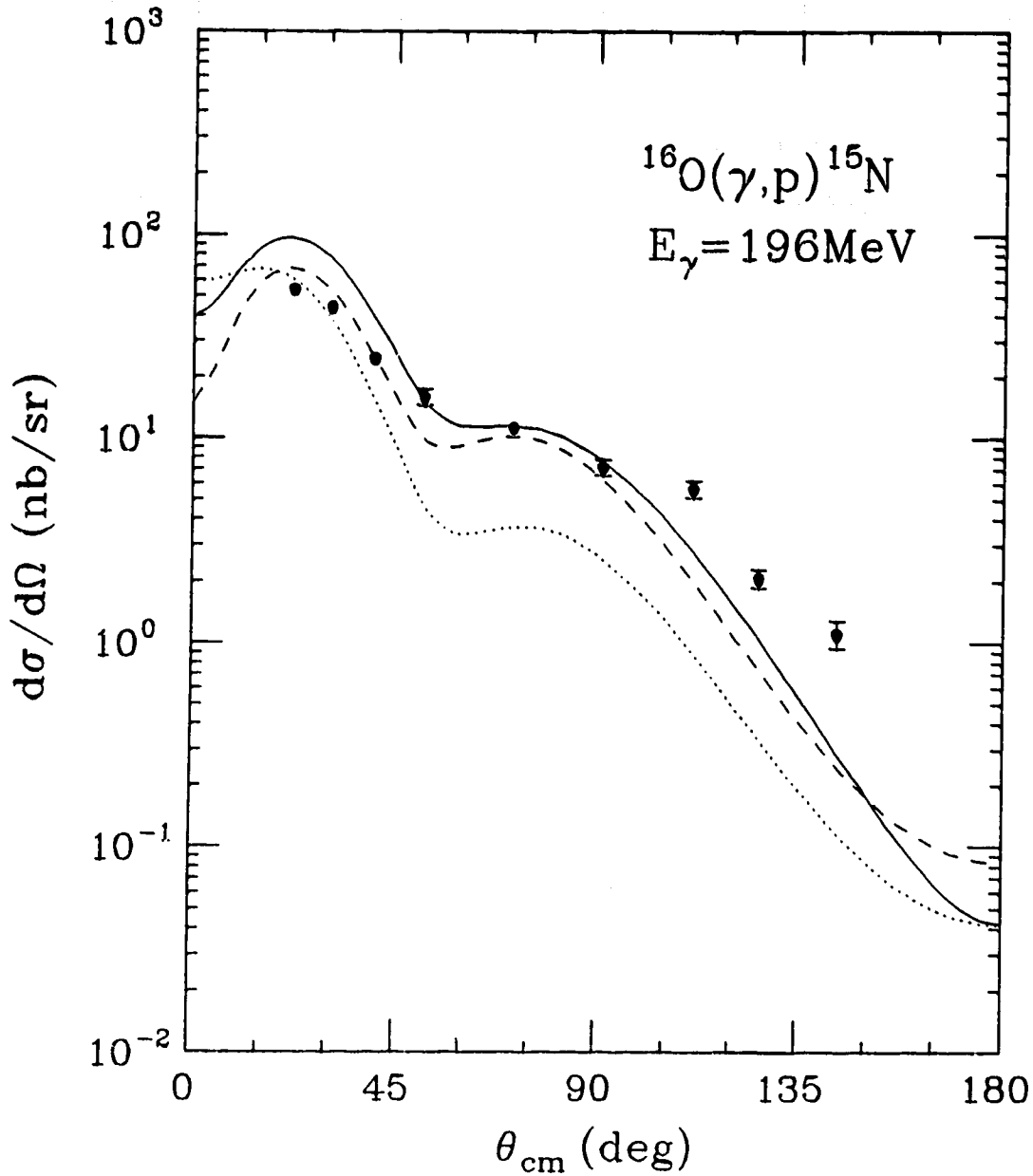


Fig. 16: ONM calculations for the differential cross section of the 196 MeV $^{16}\text{O}(\gamma,p)^{15}\text{N}$ reaction in which a Hartree binding potential and various distorting potentials (solid: parabolic symmetric Woods-Saxon; dashed: Fourier-Bessel; dotted: microscopic) are used. The data are from Ref. 28.

5.1.2 Other Results

Several angular distributions exist for the $^{16}\text{O}(\gamma p)^{15}\text{N}$ reaction at photon energies above 200 MeV⁽⁷⁷⁾. Figures 17 - 19 exhibit the ONM calculations for the incident photon energies 257, 312 and 360 MeV. For these cases a Hartree wave function is used in conjunction with distorted waves calculated with a microscopic optical potential. Phenomenological optical potentials at these high energies do not exist because there is no associated proton elastic scattering data. The NN t -matrices which are utilized in calculating the microscopic optical potentials are available at incident nucleon energies of 200, 300 and 400 MeV and hence two curves are shown for the 257 and 360 MeV cross sections corresponding to optical potentials calculated with the two adjacent NN t -matrices. The 257 MeV angular distribution also includes the results for the two phenomenological potentials determined for 200 MeV elastic scattering described above. The minimum in the differential cross section that becomes more pronounced with increasing energy is reproduced very well by the calculations. The curves that employ the microscopic calculations for the optical potential are all seen to underestimate the data. This was also observed for the 200 MeV calculations shown in Fig. 16. On the other hand, the calculations using phenomenological optical potentials resulted in consistently higher predictions for the differential cross section. Furthermore, it was noted that using microscopic optical potentials results in an inferior description of the 200 MeV proton elastic scattering data compared with using phenomenological potentials. Thus, elastic scattering data that corresponds to the higher proton energies involved in the 257, 312 and 361 MeV (γp) reactions would be welcome so that ONM calculations with phenomenological distorted waves could be investigated.

Two lower energy angular distributions that deserve attention are those at $E_\gamma = 60$ MeV and 100 MeV⁽⁷⁸⁾. The 60 MeV data and ONM results are shown in Fig. 20. The distorted wave comes from a phenomenological analysis of the 49.5 MeV $p + ^{16}\text{O}$ elastic scattering data⁽⁷⁹⁾. The parameters of the Woods-Saxon potential so determined are listed in Table 4. The Hartree wave function used for the bound nucleon is expected to be more reliable at these lower momentum transfers. Noting that the differential cross section is plotted linearly rather than logarithmically, the agreement of the calculation with the data is very good. Similar conclusions follow concerning the calculations for the $E_\gamma = 100$ MeV reaction that are exhibited in Fig. 21. Both of the curves are calculated

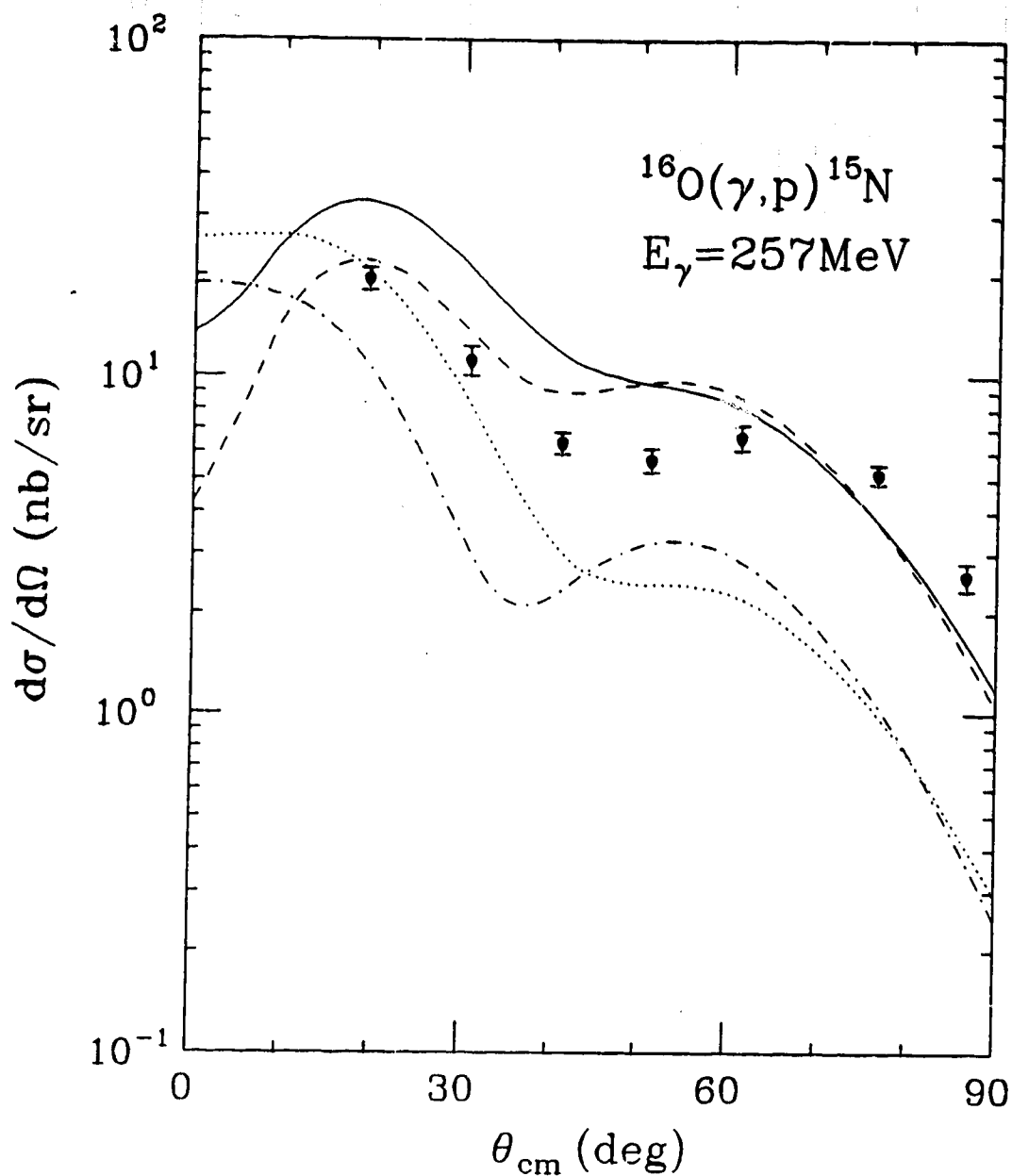


Fig. 17: ONM calculations for the differential cross section of the 257 MeV $^{16}\text{O}(\gamma,p)^{15}\text{N}$ reaction in which a Hartree binding potential and various distorting potentials (solid: parabolic symmetric Woods-Saxon; dashed: Fourier-Bessel; dotted: microscopic using 200 MeV NN t -matrices; dot-dashed: microscopic using 300 MeV NN t -matrices) are used. The data are from Ref. 77.

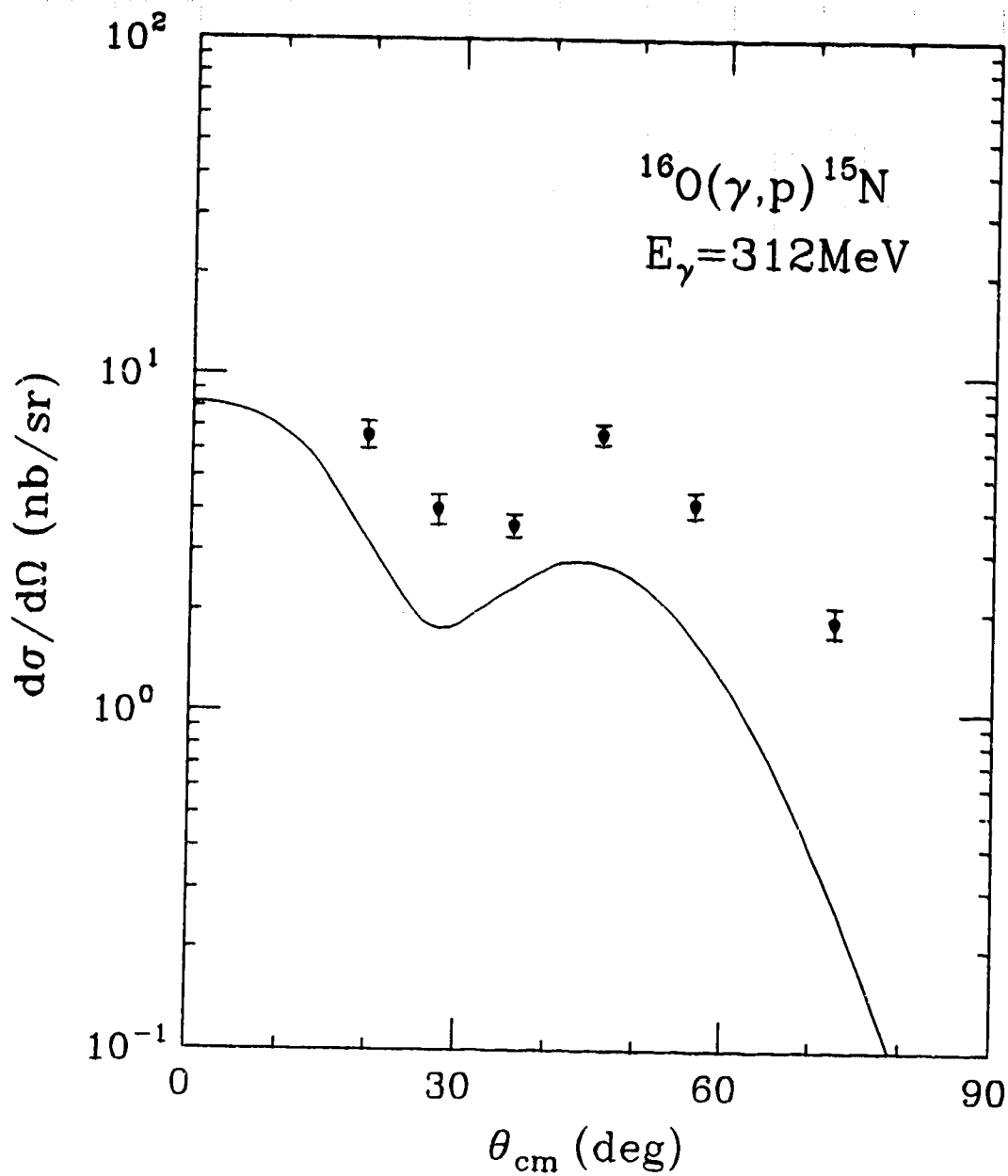


Fig. 18: ONM calculations for the differential cross section of the 312 MeV $^{16}\text{O}(\gamma,p)^{15}\text{N}$ reaction in which a Hartree binding potential and a microscopic distorting potential are used. The data are from Ref. 77.

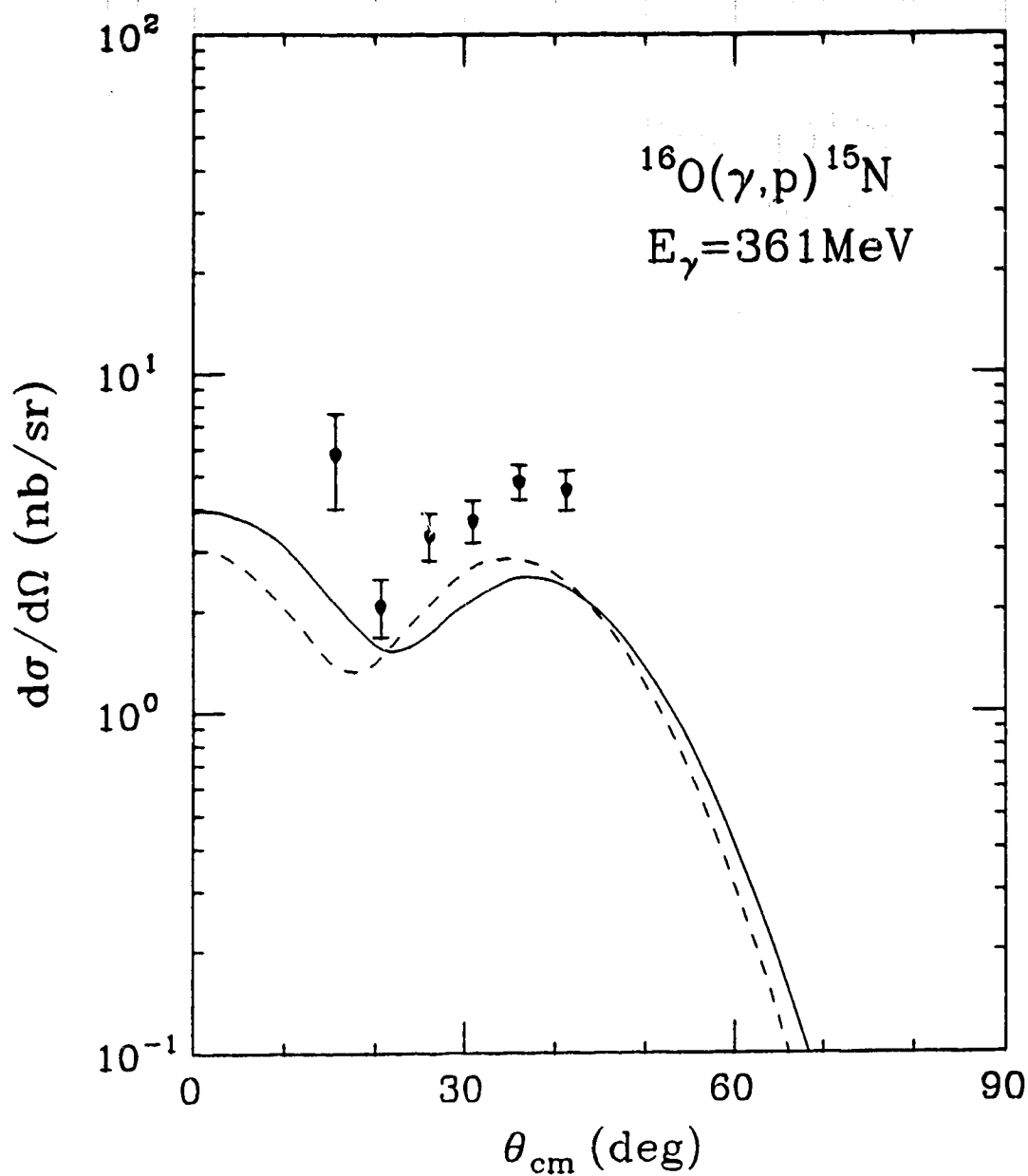


Fig. 19: ONM calculations for the differential cross section of the 361 MeV $^{16}\text{O}(\gamma, p)^{15}\text{N}$ reaction in which a Hartree binding potential and two microscopic distorting potentials (solid: using 300 MeV NN t -matrices; dashed: using 400 MeV NN t -matrices) are used. The data are from Ref. 77.

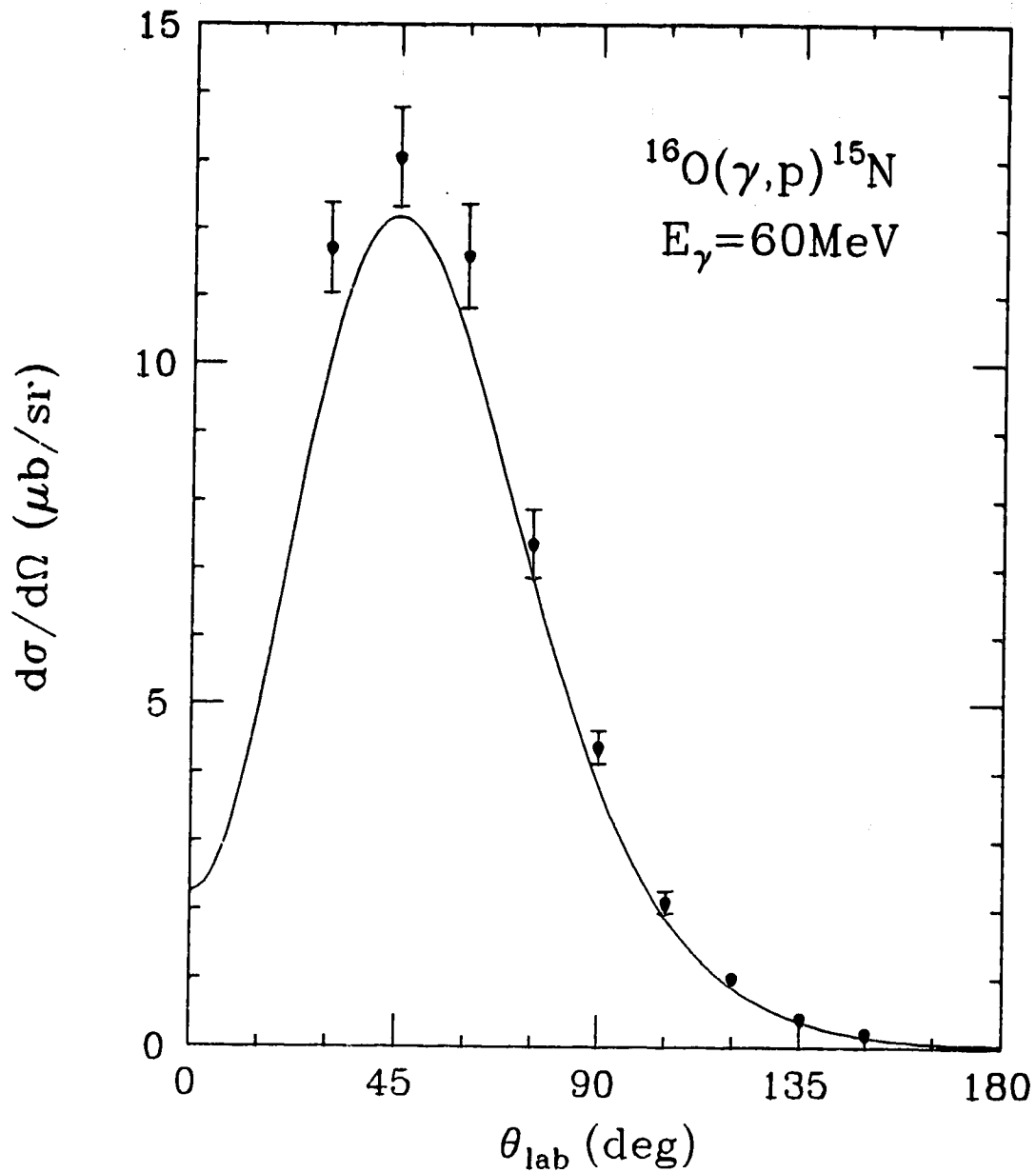


Fig. 20: ONM calculation for the differential cross section of the 60 MeV $^{16}\text{O}(\gamma, p)^{15}\text{N}$ reaction in which a Hartree binding potential and a Woods Saxon distorting potential are used. The data are from Ref. 78.

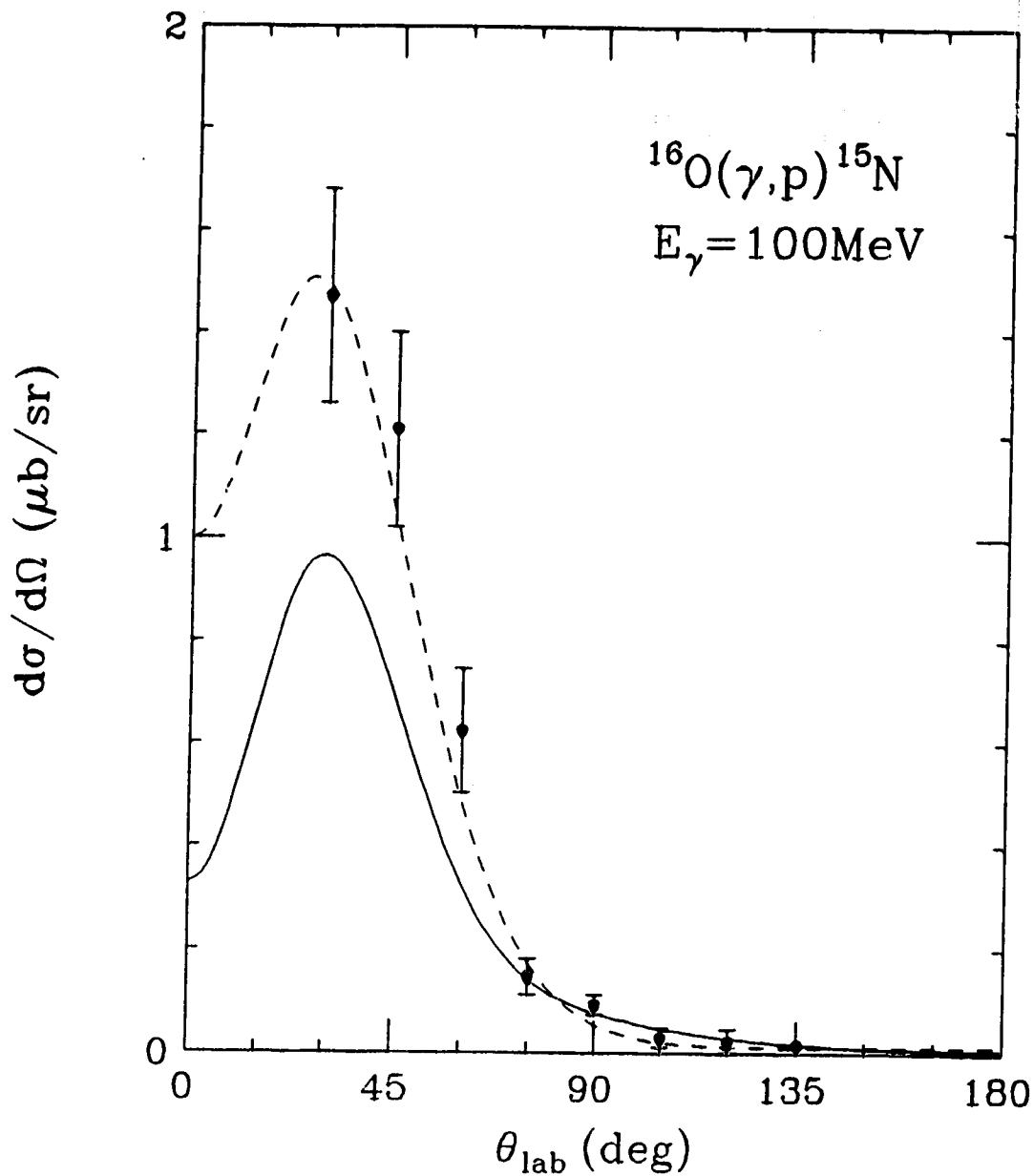


Fig. 21: ONM calculations for the differential cross section of the 100 MeV $^{16}\text{O}(\gamma,p)^{15}\text{N}$ reaction in which a Hartree binding potential and two distorting potentials (solid: Woods-Saxon; dashed: microscopic using 135 MeV NN t -matrices) are used. The data are from Ref. 78.

<u>Description</u>	<u>Vector</u>		<u>Scalar</u>	
	<u>Real</u>	<u>Imaginary</u>	<u>Real</u>	<u>Imaginary</u>
Strength:	312.60	-22.10	-369.73	17.35
Radius r_0 :	0.9278	0.9824	0.8655	0.9630
Diffuseness a :	0.4847	0.4676	0.5183	0.4108
ω :	0.0208	2.1306	0.2053	3.2481

Table 4: Woods-Saxon optical potential parameters determined for 49.5 MeV $p + {}^{16}\text{O}$ elastic scattering.

using a Hartree bound state. The solid curve is calculated using a phenomenological distorted wave function. The parameters of the Woods-Saxon optical potential corresponding to this wave function are listed in Table 5, and these are determined from 100 MeV $p + {}^{16}\text{O}$ elastic scattering⁽⁸⁰⁾. The elastic data is limited to differential cross section measurements from $\theta_{\text{cm}} = 6^\circ - 84^\circ$ and hence the optical potential determined from this data is not expected to be very reliable. Using a microscopic calculation for the distorted wave results in the dashed curve in Fig. 21. The microscopic optical potential is computed using the 135 MeV NN t -matrices. Although the microscopic calculation is not expected to be reliable in this energy region the agreement with the (γp) data is very good. The point of showing these low energy calculations is to illustrate that a direct mechanism can explain the experimental data, in contradistinction to the findings of Gari and Hebach that are outlined in Sec. 2.4.

<u>Description</u>	<u>Vector</u>		<u>Scalar</u>	
	<u>Real</u>	<u>Imaginary</u>	<u>Real</u>	<u>Imaginary</u>
Strength:	295.02	-30.26	-387.09	21.84
Radius r_0 :	0.8189	0.8412	0.7238	0.7753
Diffuseness a :	0.5001	0.6741	0.5279	0.6748
ω :	0.0208	2.1306	0.2053	3.2481

Table 5: Woods-Saxon optical potential parameters determined for 100 MeV $p + {}^{16}\text{O}$ elastic scattering.

The energy dependence of the ONM calculations for the $^{16}\text{O}(\gamma p)^{15}\text{N}$ differential cross section are illustrated in Fig. 22. In these calculations, a Hartree wave function is used together with the energy dependent distorted wave functions from microscopic calculations. The differential cross section is evaluated in 20 MeV steps, and since the NN t -matrices are available only for 135, 160, 200, 300 and 400 MeV, the distorted waves are calculated using the t -matrices that correspond most nearly with the energy in consideration. At lower momentum transfers the calculation agrees quite well with the data. As the energy and/or scattering angle increases, the results of the calculation fall increasingly below the data. This is consistent with two nucleon processes becoming important in higher momentum transfer regimes, as is expected. It must be kept in mind, however, that the higher momentum components of the Hartree wave function are more unreliable. Also, the microscopic distorted wave functions utilized do not describe the elastic data very well and therefore good phenomenological distorted wave functions would be preferable for these calculations. These are not available because the elastic scattering data are not comprehensive enough over the required energy range. It should be noted that in general the relativistic ONM results do not fall below the data as rapidly as the nonrelativistic direct emission calculations⁽¹⁹⁾, especially for larger scattering angles.

5.2 The $^{40}\text{Ca}(\gamma, p)^{39}\text{K}$ Reaction

The "doubly magic" ^{40}Ca nucleus is perhaps an even more suitable target than ^{16}O for investigating the ONM for (γp) reactions. The larger number of nucleons in ^{40}Ca makes it a better candidate for many-body models such as the Dirac Hartree model or the simple Woods-Saxon model for the nuclear potential. Indeed, the scalar meson mass used in the Dirac Hartree model is fixed by the requirement that the rms charge radius of ^{40}Ca is reproduced. The elastic scattering of protons from ^{40}Ca has been extensively investigated. Phenomenological and microscopic Dirac calculations fare relatively better in describing the data than for the case of ^{16}O . Unfortunately, photonucleon knockout experiments with ^{40}Ca are not as extensive as those with ^{16}O ; although the energy dependence of the differential cross section has been measured at specific proton scattering angles in the intermediate energy range, there exist no good angular distributions.

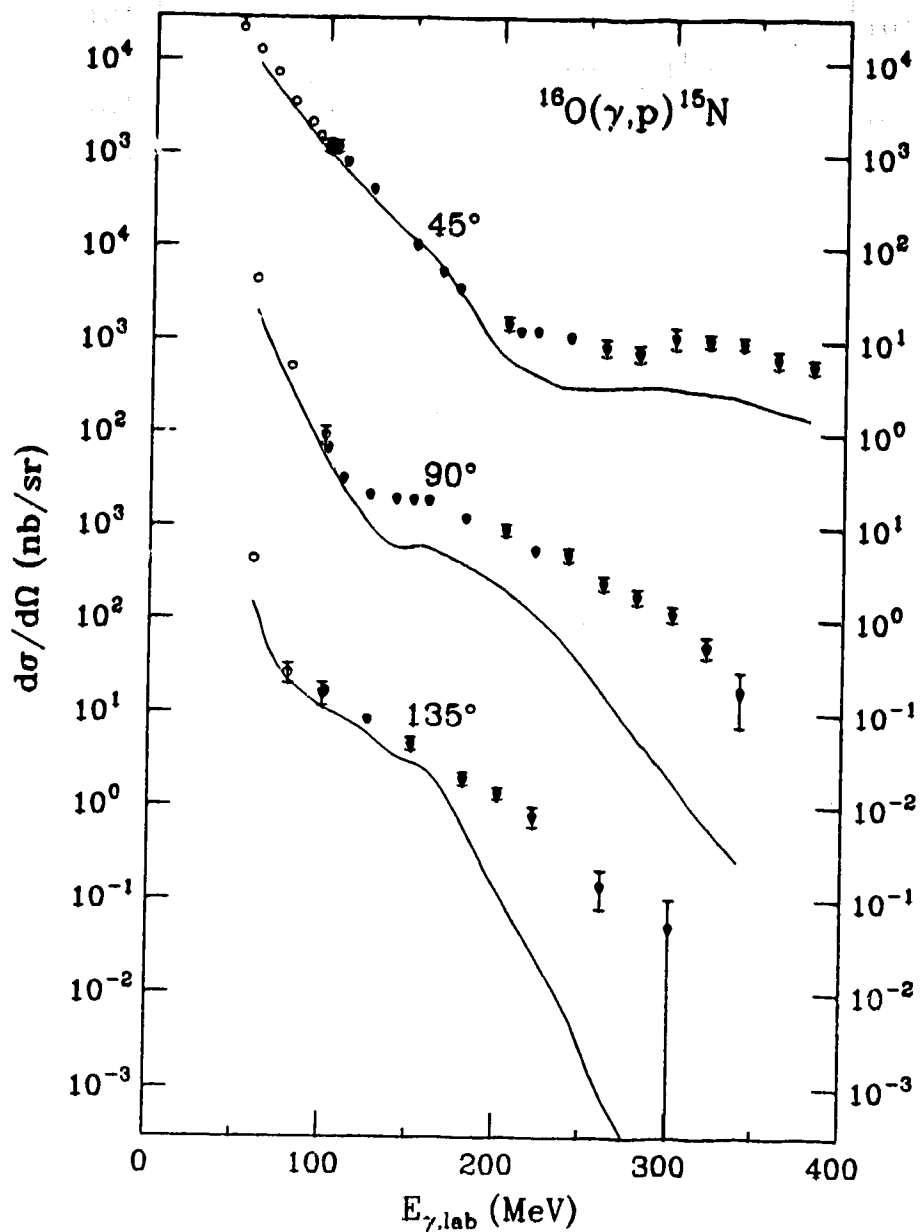


Fig. 22: ONM calculations for the energy dependence of the differential cross section of the $^{16}\text{O}(\gamma,p)^{15}\text{N}$ reaction at $\theta_p = 45^\circ$, 90° and 135° in which a Hartree binding potential and microscopic distorting potentials are used. The data are from Ref. 77 (open circles) and Ref. 4 (closed circles).

Three incomplete differential cross section angular distributions for $E_\gamma = 151.3$, 176.2 and 201.2 MeV are shown in Figs. 23 – 25 along with four ONM calculations for each. All of the calculations employ a Hartree bound state wave function and a fractional-parentage coefficient of unity. The solid curves are calculated using microscopic optical potentials, the dashed and dotted curves are calculated using global optical potentials (fits 1 and 2 from E.D. Cooper *et al.*⁽⁸¹⁾, respectively) and the dot-dashed curves are calculated using Woods-Saxon optical potentials determined from the appropriate elastic scattering data⁽⁴²⁾. The global optical potentials are parameterized by fitting simultaneously the $\vec{p} + {}^{40}\text{Ca}$ elastic scattering data for energies between 21 and 200 MeV. The calculations with phenomenological optical potentials all give similar results whereas the calculation with the microscopic optical potential predicts larger cross sections especially at larger angles. Apparently the calculation with the microscopic optical potential gives the best description of the data, especially for the 135° data points which incidently have considerable error bars. However, it is not clear that any concrete conclusions can be drawn from this observation since the phenomenological optical potentials account for the elastic scattering data better than the microscopic optical potentials do. Also, the good description of the backward angle data is at variance with the ${}^{16}\text{O}(\gamma, p){}^{15}\text{N}$ ONM results which indicate that other reaction mechanisms become important for such high momentum transfers.

The results for the energy dependence of the differential cross section at 45°, 90° and 135° proton scattering angles are shown in Figs. 26 – 28. The curves in Fig. 26 are calculated with a Hartree binding potential and microscopic optical potentials. Although the description of the data is quite good, it is somewhat perplexing that the results are better for larger scattering angles since at higher momentum transfer the single nucleon mechanism is expected to become less important compared with two nucleon mechanisms. This might suggest that the microscopic optical potentials are causing a spurious contribution to the matrix element at high momentum transfers. Figure 27 is consistent with this conclusion in that calculations with phenomenological optical potentials and a Hartree bound state wave function tend to give better results for smaller scattering angles, as is expected. In these calculations the global optical potentials of Ref. 81 are used between 100 and 200 MeV and two parameterizations of global optical potentials that are determined by fitting the $\vec{p} + {}^{40}\text{Ca}$ elastic scattering data between 161

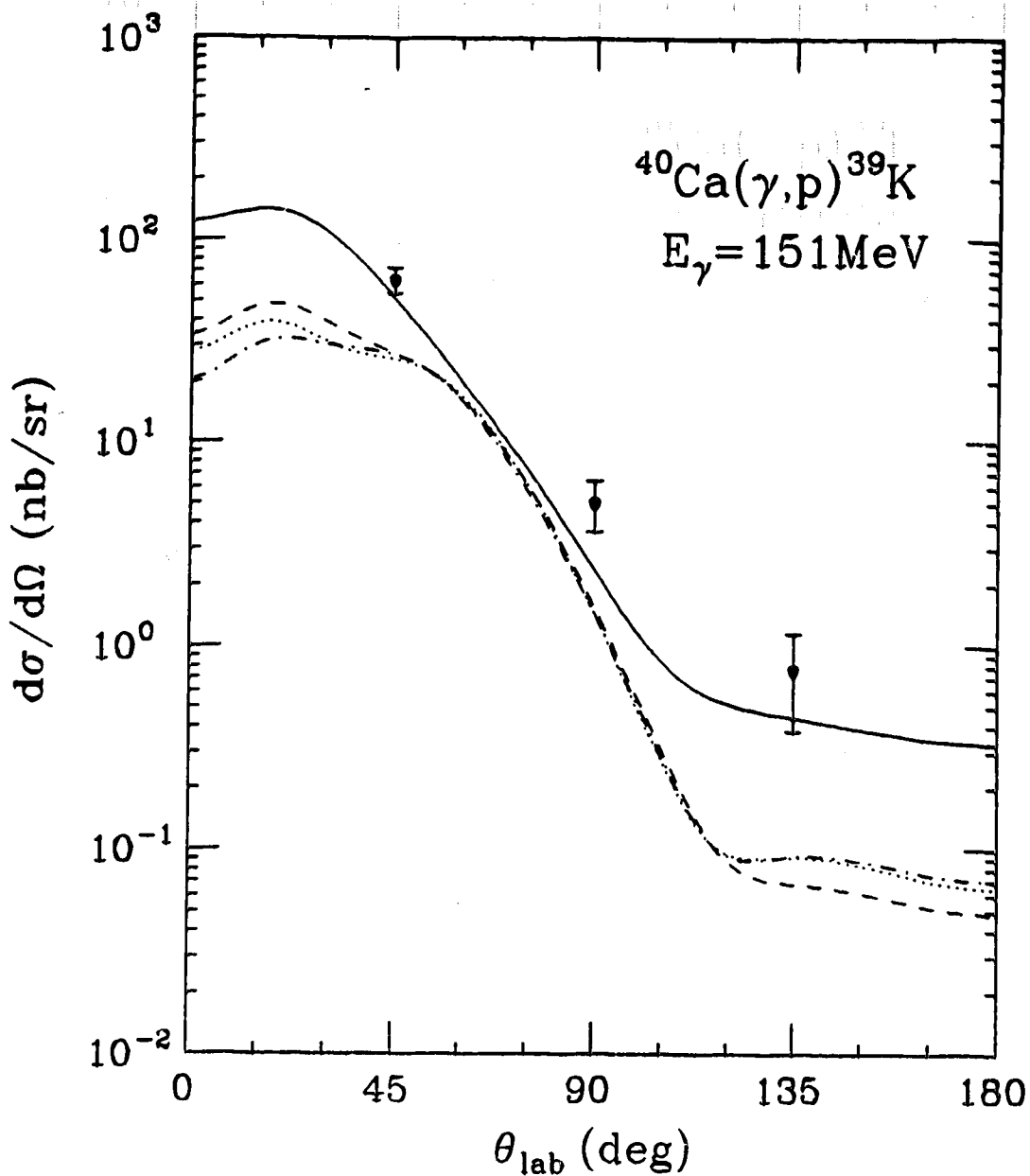


Fig. 23: ONM calculations for the differential cross section of the 151.3 MeV $^{40}\text{Ca}(\gamma, p)^{39}\text{K}$ reaction in which a Hartree binding potential and various distorting potentials (solid: microscopic; dashed; case 1 global potential from Ref. 81; dotted: case 2 global potential from Ref. 81; dot-dashed: Woods-Saxon) are used. The data are from Ref. 64.

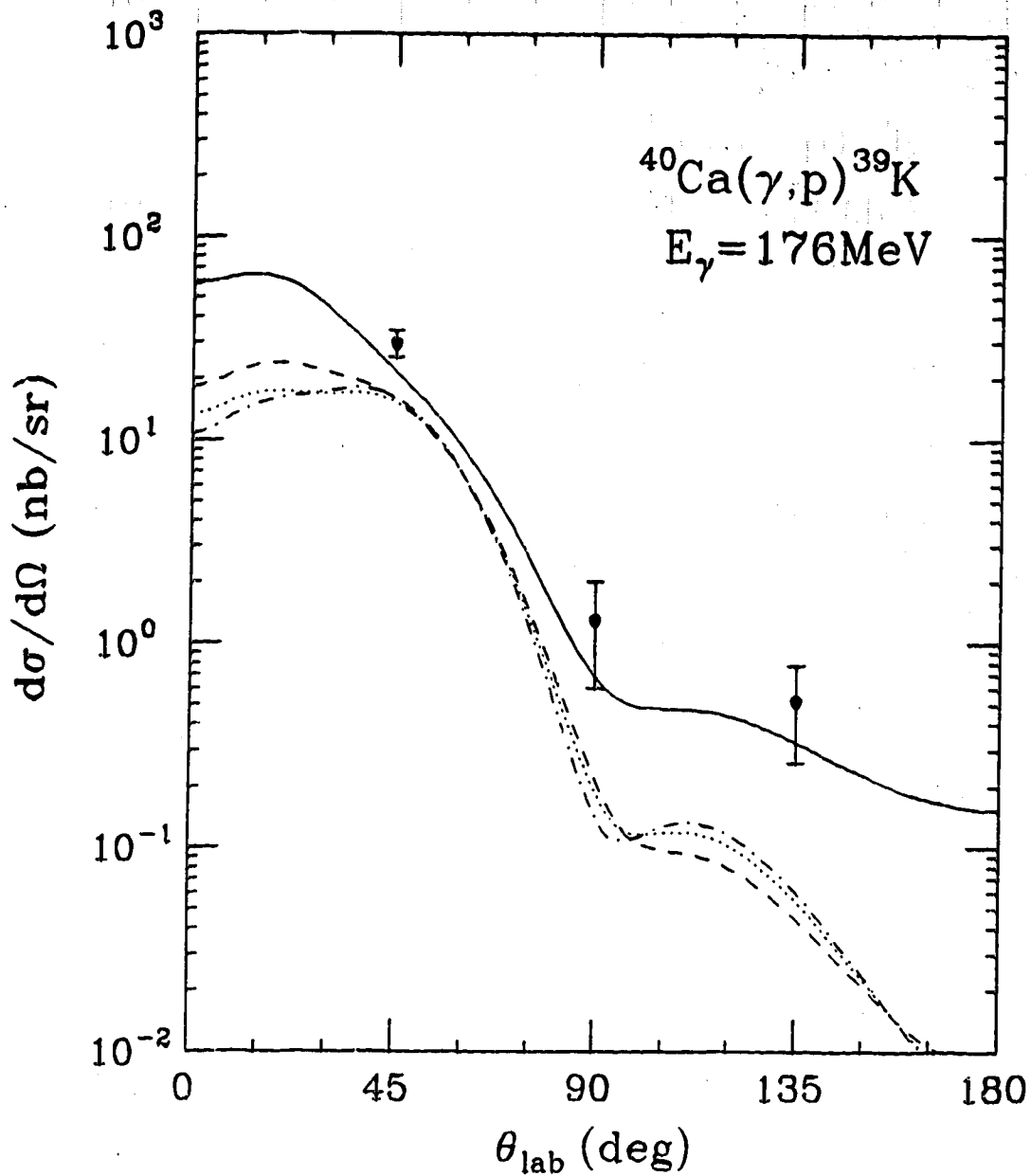


Fig. 24: ONM calculations for the differential cross section of the 176.2 MeV $^{40}\text{Ca}(\gamma, p)^{39}\text{K}$ reaction in which a Hartree binding potential and various distorting potentials (solid: microscopic; dashed; case 1 global potential from Ref. 81; dotted: case 2 global potential from Ref. 81; dot-dashed: Woods-Saxon) are used. The data are from Ref. 64.

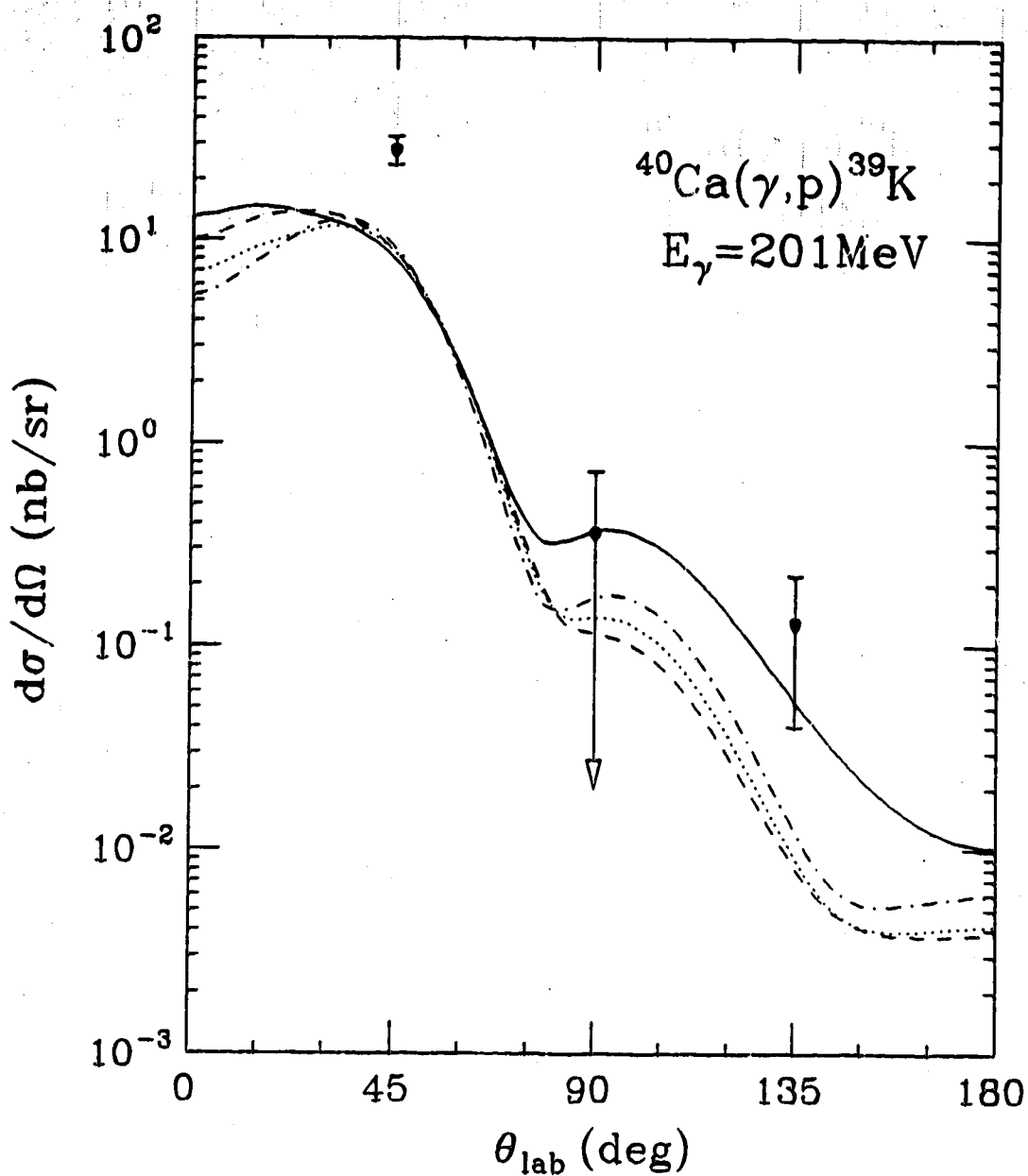


Fig. 25: ONM calculations for the differential cross section of the 201.2 MeV $^{40}\text{Ca}(\gamma, p)^{39}\text{K}$ reaction in which a Hartree binding potential and various distorting potentials (solid: microscopic; dashed; case 1 global potential from Ref. 81; dotted: case 2 global potential from Ref. 81; dot-dashed: Woods-Saxon) are used. The data are from Ref. 64.

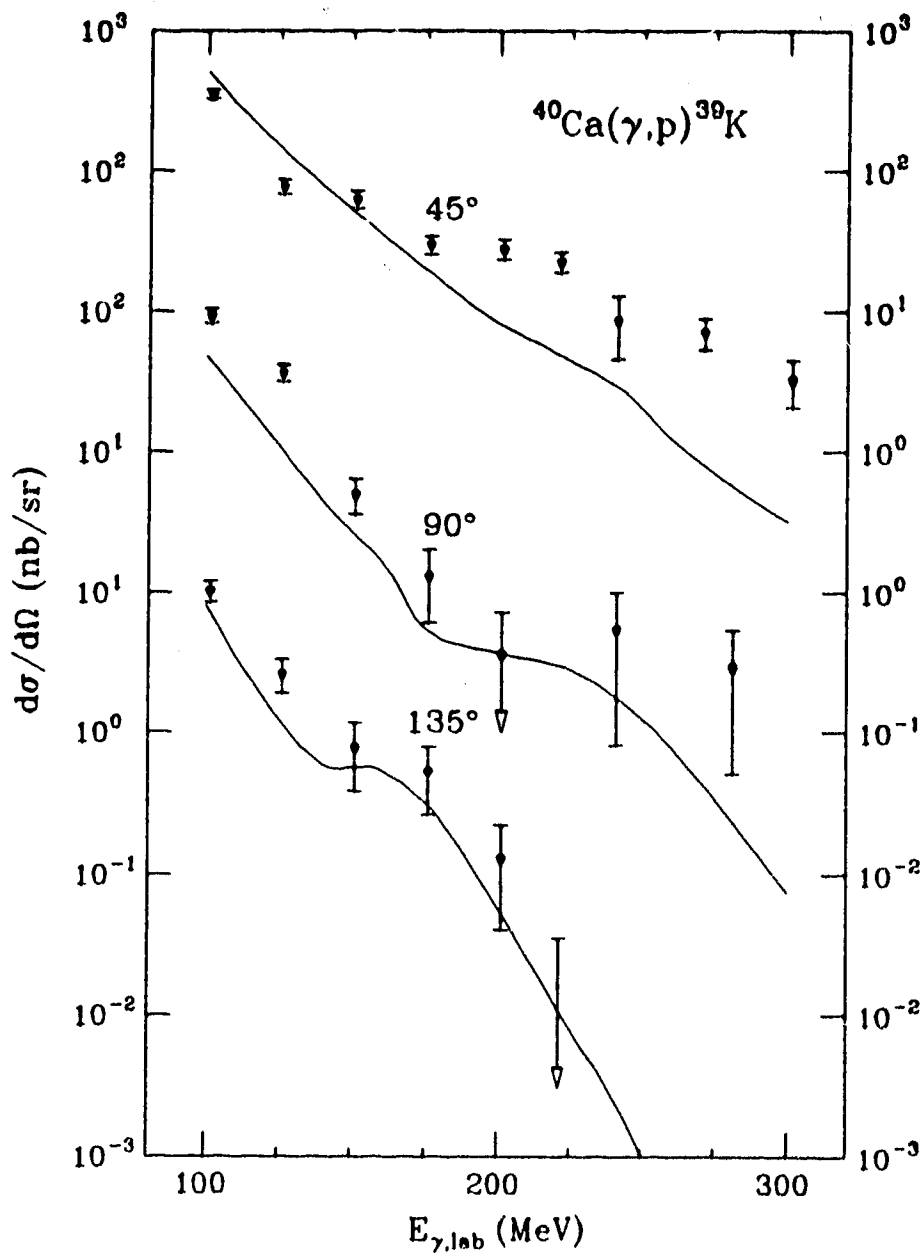


Fig. 26: ONM calculations for the energy dependence of the differential cross section of the $^{16}\text{O}(\gamma,p)^{15}\text{N}$ reaction at $\theta_p = 45^\circ$, 90° and 135° in which a Hartree binding potential and microscopic distorting potentials are used. The data are from Ref. 64.

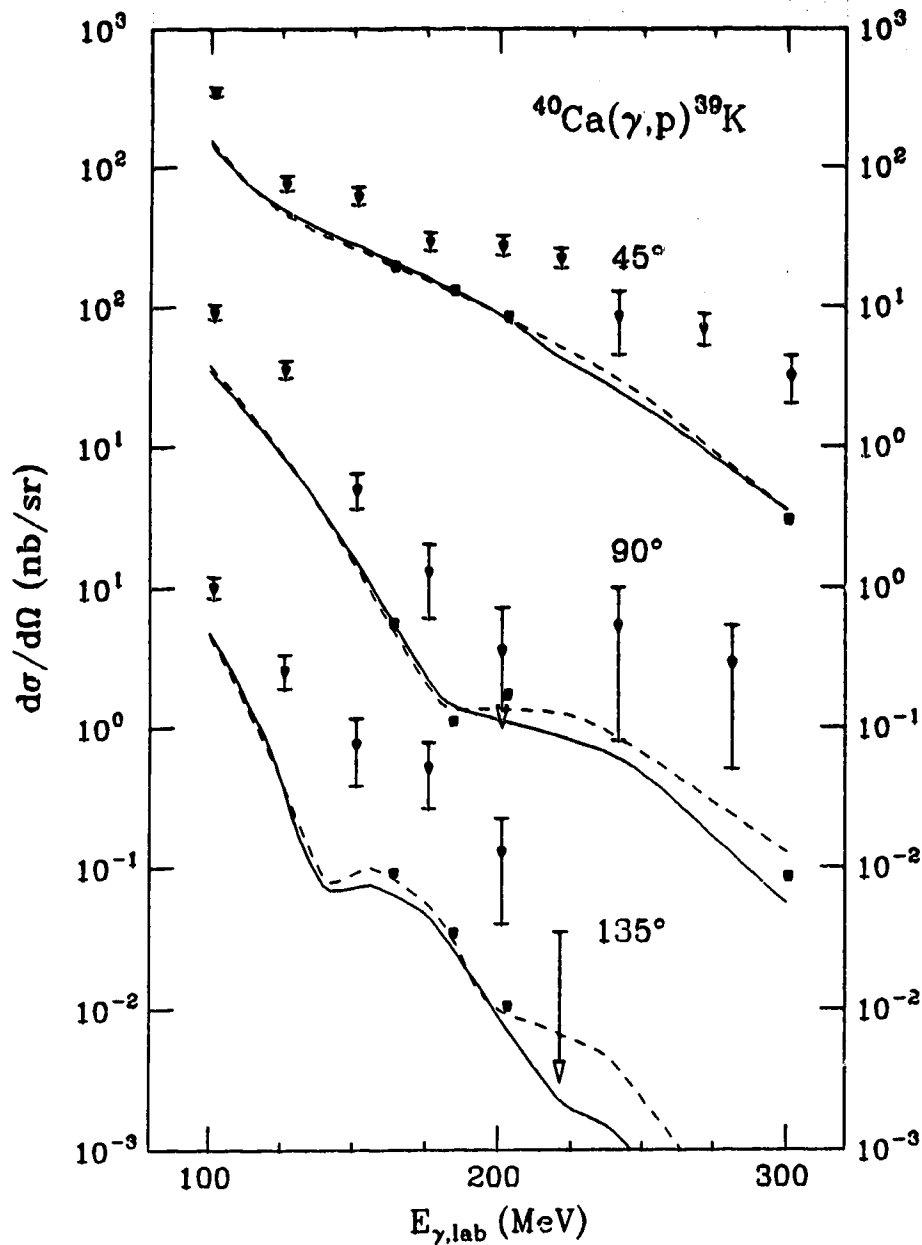


Fig. 27: ONM calculations for the energy dependence of the differential cross section of the $^{16}\text{O}(\gamma,p)^{15}\text{N}$ reaction at $\theta_p = 45^\circ$, 90° and 135° in which a Hartree binding potential and phenomenological distorting potentials (solid curve: case 1 potentials of Refs. 81 and 82; dashed curve: case 2 potentials of Refs. 81 and 82; squares: Woods-Saxon optical potentials of Ref. 42) are used. The data are from Ref. 64.

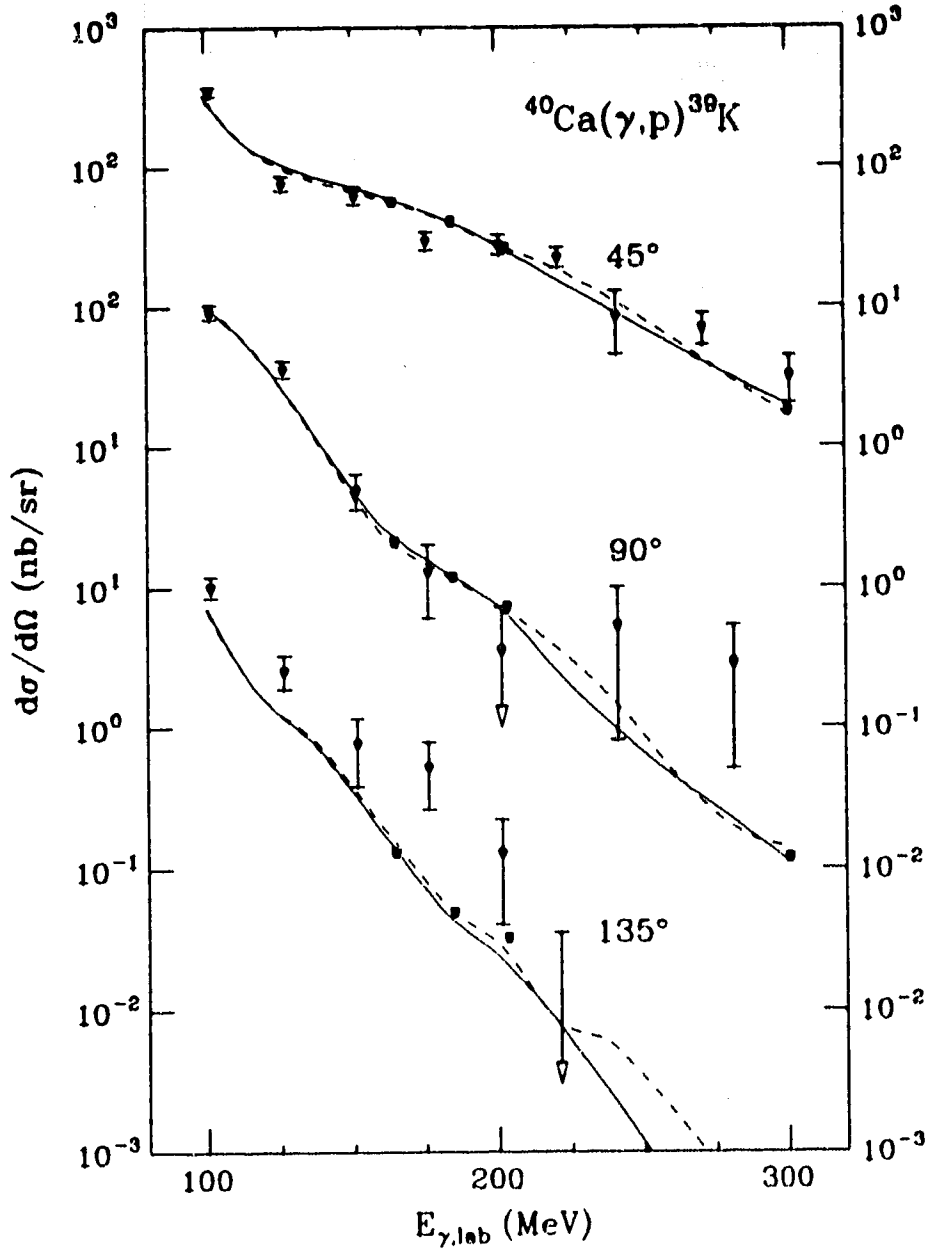


Fig. 28: ONM calculations for the energy dependence of the differential cross section of the $^{16}\text{O}(\gamma,p)^{15}\text{N}$ reaction at $\theta_p = 45^\circ$, 90° and 135° in which the Woods-Saxon binding potential characterized by the parameters of Table 6 and phenomenological distorting potentials (solid curve: case 1 potentials of Refs. 81 and 82; dashed curve: case 2 potentials of Refs. 81 and 82; squares: Woods-Saxon optical potentials of Ref. 42) are used. The data are from Ref. 64.

MeV and 1040 MeV⁽⁸²⁾ are used for higher energies. Using a Woods-Saxon binding potential in the ONM calculations together with phenomenological optical potentials results in the curves shown in Fig. 28 which are very close to the data. The sensitivity of these ONM calculations to the parameters of the Woods-Saxon binding potential is not nearly so great as for the $^{16}\text{O}(\gamma,p)^{15}\text{N}$ reaction and hence the results are thought to be meaningful. The parameters of the Woods-Saxon binding potential, listed in Table 6, are chosen in such a way as to reproduce the empirical rms radius of the $1f_{7/2}$ neutron of ^{41}Ca ⁽⁸³⁾ as well as the binding energy of the $1d_{3/2}$ proton of ^{40}Ca . Very little adjustment has been made in the parameters within these constraints to fit the (γp) data.

Evidently, the uncertainty in the bound state wave function remains a problem in ONM calculations for the $^{40}\text{Ca}(\gamma,p)^{39}\text{K}$ reaction. The inferior description of the data when a Hartree potential is used in the ONM calculation as opposed to a Woods-Saxon binding potential might suggest that the Hartree calculations for ^{40}Ca are not reliable for the high momentum components of the wave function. This was not found to be the case for ^{16}O . As a supplementary note, it is interesting that the Hartree potential for ^{16}O gives the rms radius of the $1d_{5/2}$ neutron orbit of ^{17}O to be 3.54 fm, in agreement with the experimental value of 3.56 ± 0.09 fm⁽⁸⁴⁾. On the other hand, the Hartree potential for ^{40}Ca gives the ^{41}Ca $1f_{7/2}$ neutron orbit radius to be 4.04 fm which is slightly above the experimental value of 3.95 ± 0.06 fm⁽⁸³⁾.

In order to establish if the physical approximations that are inherent in Hartree calculations are responsible for unrealistic high momentum components of the wave function, two refinements of the Hartree model are investigated in the context of the $^{40}\text{Ca}(\gamma,p)^{39}\text{K}$ reaction. In Fig. 29 are shown ONM calculations for the energy dependence of the differential cross section. Both sets of curves are calculated with global

<u>Description</u>	<u>Vector</u>	<u>Scalar</u>
Strength:	450.00	- 541.558
Radius r_0 :	1.1	1.1
Diffuseness a :	0.6	0.6

Table 6: Woods-Saxon binding potential parameters for ^{40}Ca .

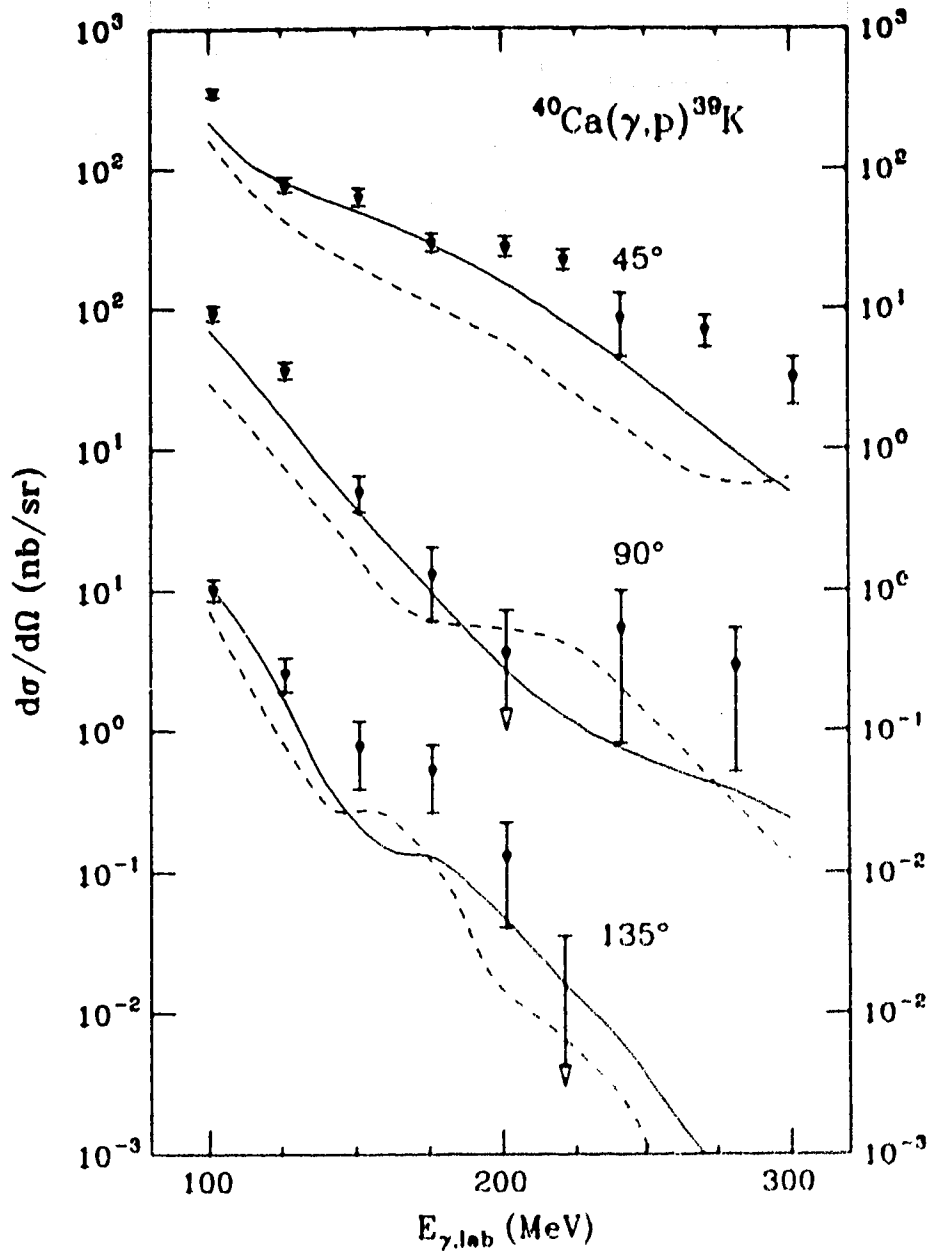


Fig. 29: ONM calculations for the energy dependence of the differential cross section of the $^{16}\text{O}(\gamma,p)^{15}\text{N}$ reaction at $\theta_p = 45^\circ$, 90° and 135° in which bound nucleon wave functions that incorporate modifications to the Hartree approximation (solid: baryon vacuum fluctuations included in the Hartree calculation; dashed: Hartree-Fock bound nucleon wave function) and the case 2 global optical potentials of Refs. 81 and 82 are used. The data are from Ref. 64.

optical potentials. The solid lines are calculated with one-baryon-loop contributions to the quantum vacuum energy included in the relativistic Hartree calculation for the bound state wave function⁽⁸⁵⁾. This modification might be important because the strong scalar potential is a significant fraction of the nucleon mass and hence can result in the production of a nontrivial number of virtual nucleon-antinucleon pairs. The improvement in the quality of the agreement with the experimental points is notable for this case as compared with using the Hartree wave function without baryon vacuum fluctuations (*cf.* Fig. 27). The dashed lines in Fig. 29 are calculated with relativistic Hartree-Fock wave functions^(86,87). The Hartree-Fock calculation involves taking into account the exchange terms of the nucleon-nucleon potential that are illustrated in Fig. 30(b) in addition to the direct meson interaction terms that comprise the Hartree approximation. The σ , ω , ρ and π mesons are included in the calculation. For this case, the ONM calculations also give better agreement with the data compared with the results for a Hartree wave function, especially at higher momentum transfers.

The improvements in ONM calculations for the two aforementioned refinements of Hartree calculations suggests that the correct high momentum components of the the $1d_{3/2}$ proton wave function of ^{40}Ca might depend substantially on processes not included in a Hartree calculation. This is not a firm conclusion, however, in that numerical considerations might also be coming into play. For example, it is not clear if the Hartree-Fock wave functions are dependable at high momentum transfers, since the numerical computations are quite complicated. Whereas the Hartree computations have been extensively examined, the recently formulated Hartree-Fock computations have not yet been thoroughly tested.

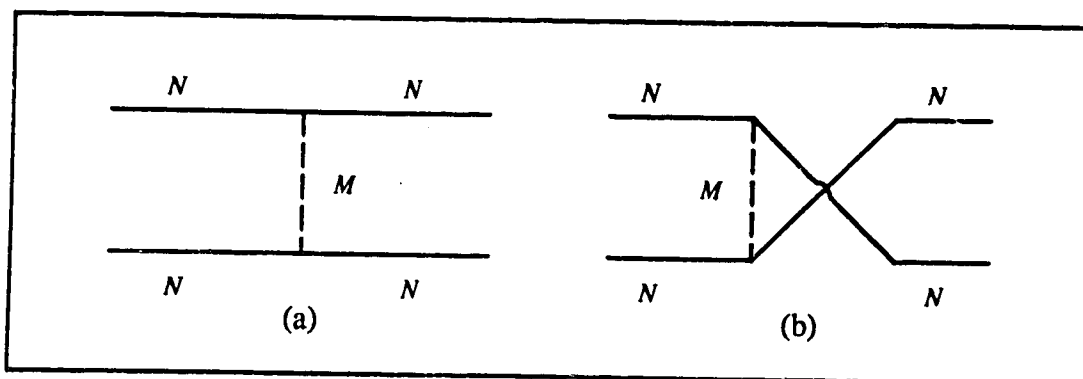


Fig. 30: The meson exchange contributions to the Hartree-Fock potential. (a) The direct meson interaction terms that by themselves constitute the Hartree potential. (b) The exchange terms that are necessary for the proper antisymmetrization of the nucleon wave functions.

5.3 The $^{11}\text{B}(\vec{p},\gamma)^{12}\text{C}$ Reaction

The radiative capture of 50 MeV polarized protons incident on a ^{11}B nucleus has been studied by two experimental groups^(88,89). The analyzing power measurements are especially interesting for a comparison with the ONM predictions. The relatively low incident proton energy precludes the use of microscopic optical potentials but elastic scattering data exists for the $\vec{p} + ^9\text{Be}$ ⁽⁹⁰⁾ and $\vec{p} + ^{12}\text{C}$ ^(91,92) reactions at this proton energy and so phenomenological optical potentials can be determined. The determination of the $1p_{3/2}$ proton wave function of ^{12}C is achieved through a Hartree calculation or with the use of a Woods-Saxon binding potential. Because ^{12}C contains only twelve nucleons, the Hartree approximation might not be as good for this nucleus as for heavier nuclei. On the other hand, the low momentum transfers involved in the (\vec{p},γ) reaction of interest is conducive to the reliability of the wave function. The fractional-parentage coefficient of the valence proton is taken from the theoretical determination of Cohen and Kurath to be -0.8440 ⁽⁷¹⁾.

Figures 31 – 34 show ONM calculations for the differential cross section and analyzing power of the $^{11}\text{B}(\vec{p},\gamma)^{12}\text{C}$ reaction at $E_p = 50$ MeV. A phenomenological Woods-Saxon potential that gives a good description of the 50 MeV $\vec{p} + ^9\text{Be}$ elastic data is used for the calculations shown in Figs. 31 and 32 whereas a phenomenological Woods-Saxon potential that gives a good description of the 50 MeV $\vec{p} + ^{12}\text{C}$ elastic data is used for the calculations shown in Figs. 33 and 34. The parameters of these potentials are listed in Table 7. The solid curves in all the figures are calculated with a Woods-Saxon binding potential that gives good results for both choices of the distorting potentials and the dashed curves are calculated with a Hartree potential. The parameters of the Woods-Saxon binding potential are listed in Table 8.

The calculations that use the ^9Be optical potential give a very good description of the data whereas those that use the ^{12}C optical potential do not fare quite so well. This could give an indication that the use of an optical potential that is determined for a closed shell nucleus is not entirely appropriate for the scattering of a nucleon from a closed-shell-minus-one-nucleon nucleus. The spins of the ^9Be nucleus and the ^{11}B nucleus that the proton is incident on in this reaction are the same since both have an unpaired $p_{3/2}$ nucleon. It is likely that the spin-3/2 nature of ^{11}B has more of an effect on the optical potential than the "bulk effect" of the lack of one nucleon. It is also interesting to note that

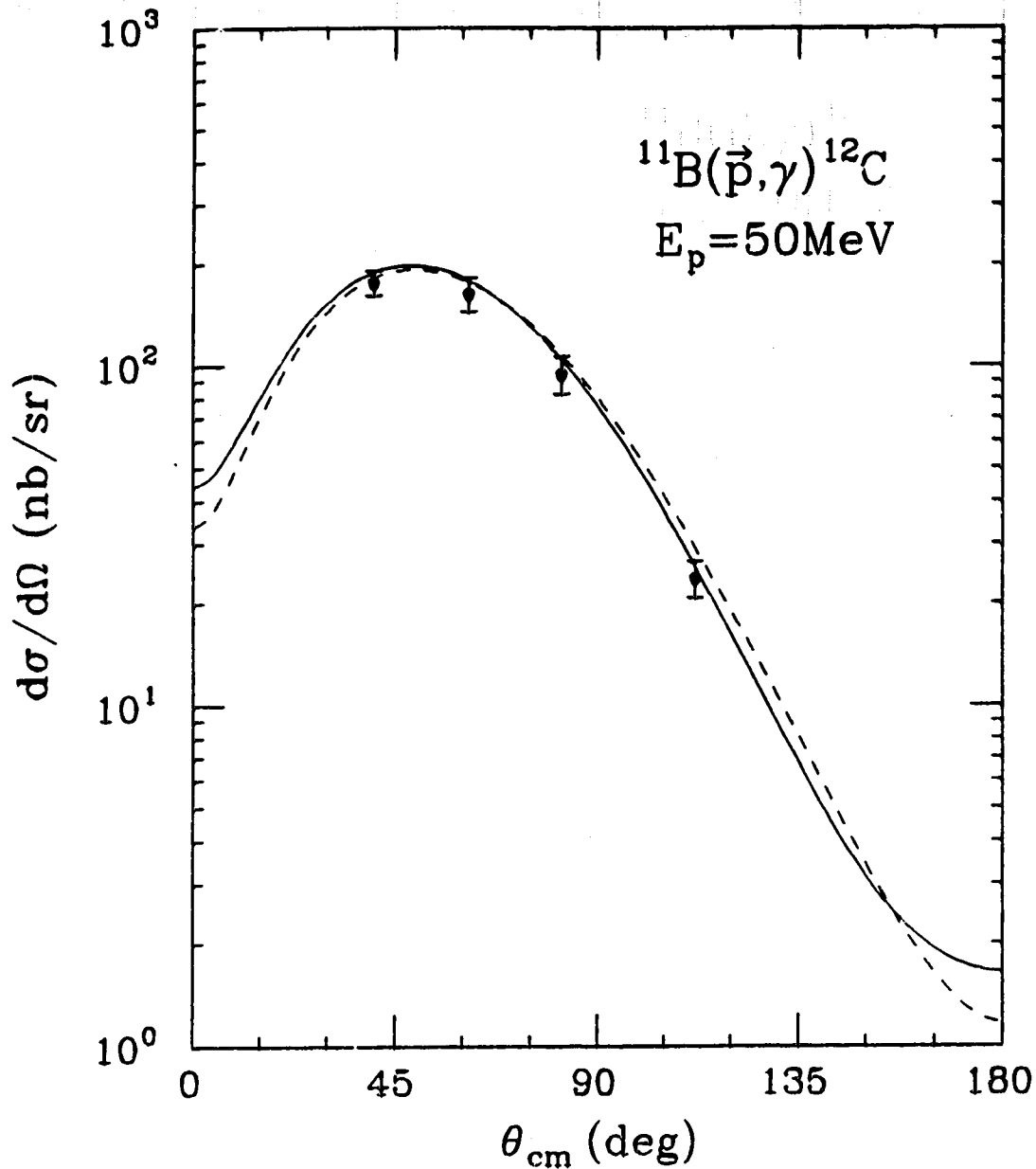


Fig. 31: ONM calculations for the differential cross section of the 50 MeV $^{11}\text{B}(\bar{p}, \gamma)^{12}\text{C}$ reaction in which a Woods-Saxon distorting potential determined for 50 MeV $\bar{p} + {}^9\text{Be}$ elastic scattering and either a Woods-Saxon binding potential (solid curve) or a Hartree binding potential (dashed curve) are used. The data are from Ref. 88.

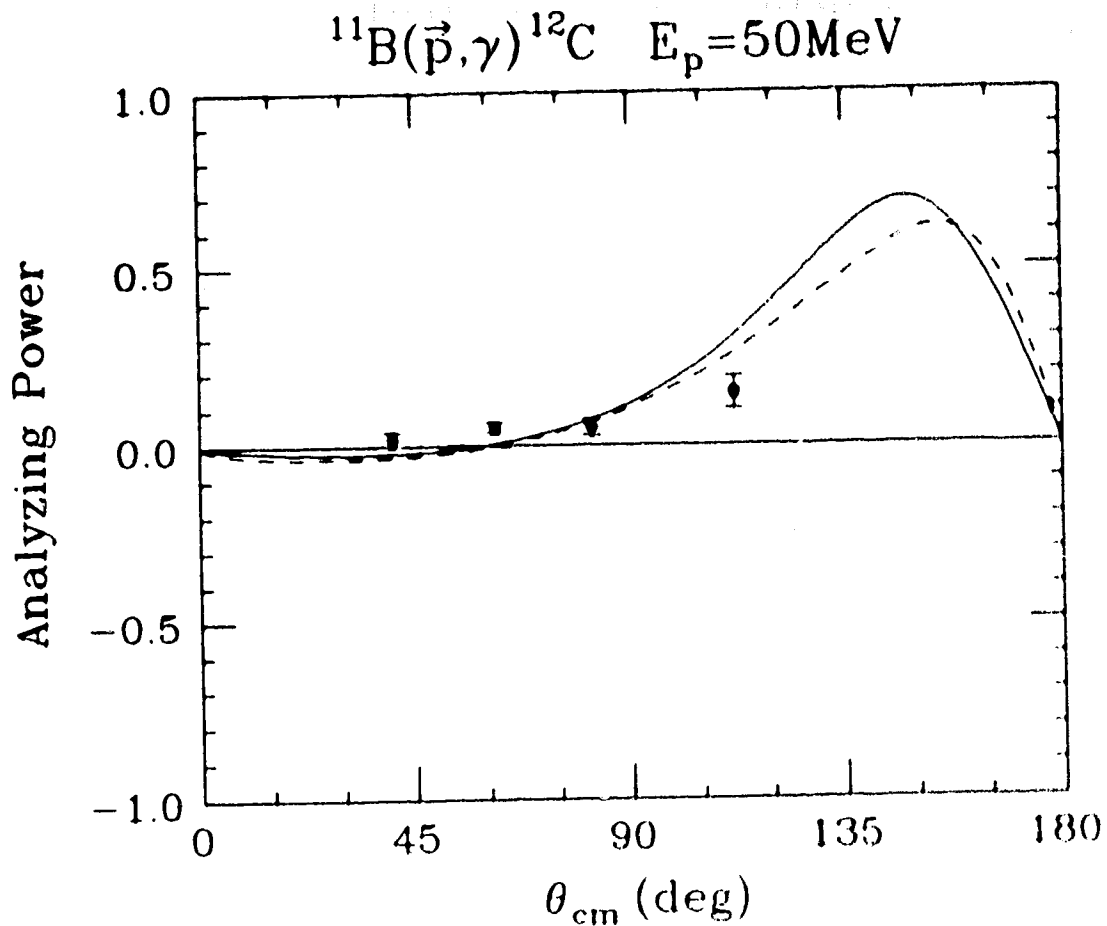


Fig. 32: ONM calculations for the analyzing power of the 50 MeV $^{11}\text{B}(\vec{p}, \gamma)^{12}\text{C}$ reaction in which a Woods-Saxon distorting potential determined for 50 MeV $\vec{p} + {}^9\text{Be}$ elastic scattering and either a Woods-Saxon binding potential (solid curve) or a Hartree binding potential (dashed curve) are used. The data are from Ref. 88.

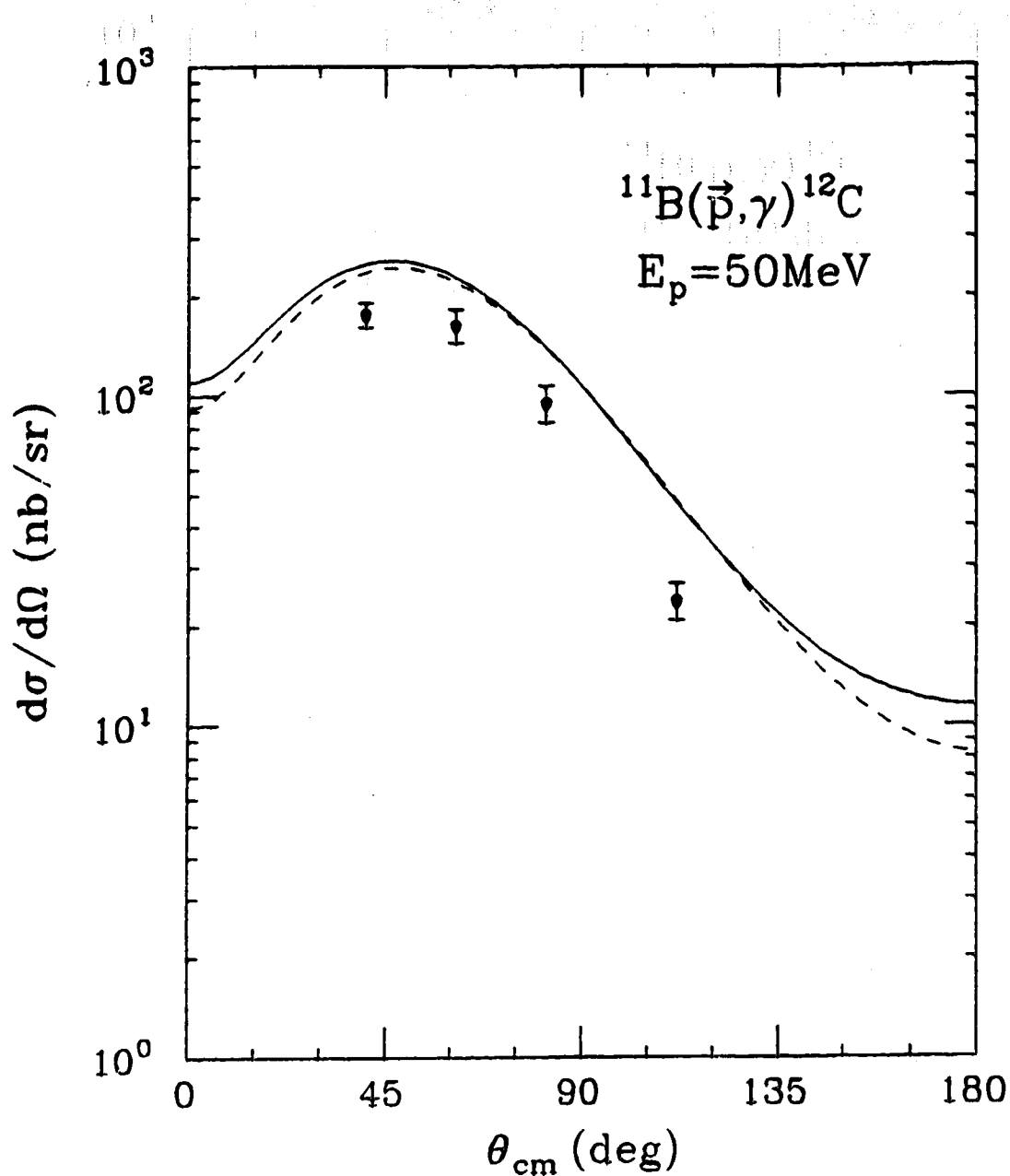


Fig. 33: ONM calculations for the differential cross section of the 50 MeV $^{11}\text{B}(\vec{p}, \gamma)^{12}\text{C}$ reaction in which a Woods-Saxon distorting potential determined for 50 MeV $\vec{p} + ^{12}\text{C}$ elastic scattering and either a Woods-Saxon binding potential (solid curve) or a Hartree binding potential (dashed curve) are used. The data are from Ref. 88.

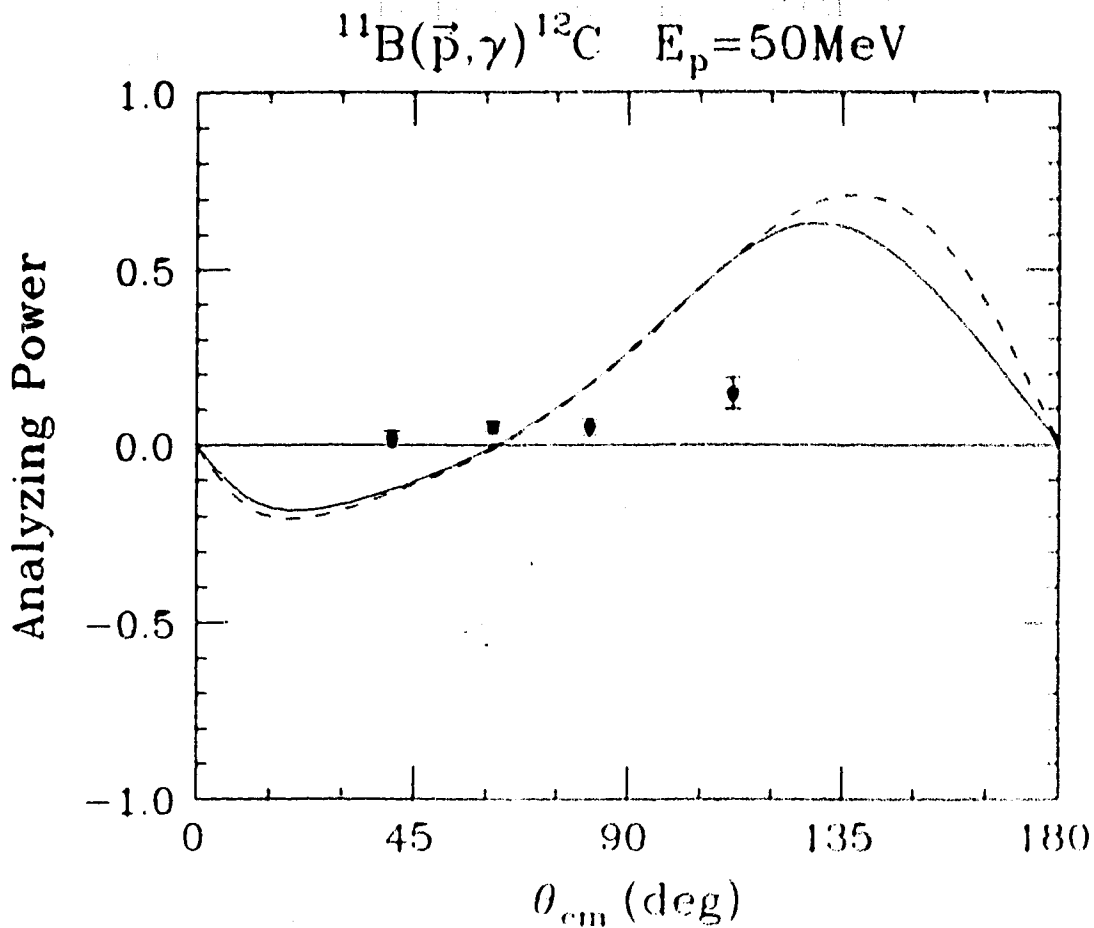


Fig. 34: ONM calculations for the analyzing power of the 50 MeV $^{11}\text{B}(\vec{p}, \gamma)^{12}\text{C}$ reaction in which a Woods-Saxon distorting potential determined for 50 MeV $\vec{p} + ^{12}\text{C}$ elastic scattering and either a Woods-Saxon binding potential (solid curve) or a Hartree binding potential (dashed curve) are used. The data are from Ref. 88.

<u>Description</u>	<u>Vector</u>		<u>Scalar</u>	
	<u>Real</u>	<u>Imaginary</u>	<u>Real</u>	<u>Imaginary</u>
(a) Strength:	243.91	-32.45	-307.56	27.46
Radius r_0 :	1.1154	1.1080	1.1120	0.7793
Diffuseness a :	0.4716	0.7520	0.5174	0.5544
ω :	-0.0387	0.0994	-0.0719	0.9098
(b) Strength:	395.59	-64.31	-466.00	51.48
Radius r_0 :	1.0880	0.8173	1.0831	0.9760
Diffuseness a :	0.4376	0.6509	0.4654	0.3841
ω :	0.0	0.0	0.0	0.0

Table 7: Woods-Saxon optical potential parameters used in the ONM calculations for the $^{11}\text{B}(\vec{p},\gamma)^{12}\text{C}$ reaction at $E_p = 50$ MeV. (a) Parameters determined from 50 MeV polarized proton elastic scattering on ^9Be . (b) Parameters determined from 50 MeV polarized proton elastic scattering on ^{12}C .

the Woods-Saxon and Hartree binding potentials give very similar results. There are other reasonable choices of the Woods-Saxon parameters for which this is not the case. Almost invariably the ONM results are not as good for these potentials however.

5.4 The $^3\text{H}(\vec{p},\gamma)^4\text{He}$ Reaction

Considerable experimental effort has gone into photonuclear reactions involving very light target nuclei. The major interest in these reactions is to test few-body nuclear models. It is not clear that the One Nucleon Model is suitable for these reactions because

<u>Description</u>	<u>Vector</u>	<u>Scalar</u>
Strength:	300.00	-378.63
Radius r_0 :	1.0176	1.0379
Diffuseness a :	0.5410	0.5609

Table 8: Woods-Saxon binding potential parameters for ^{12}C .

it involves approximations that are applicable to many-body nuclei. On the other hand, it is interesting to investigate how deficient the ONM is for light nuclei, thereby getting an indication of the importance of doing more precise few-body calculations.

The reaction that is examined in this vein is ${}^3\text{H}(\vec{p},\gamma){}^4\text{He}$ at 300 MeV incident proton energy. Both the differential cross section and analyzing power have been measured over a reasonable angular range⁽⁹³⁾. Corresponding elastic scattering data is available for both ${}^3\text{He}$ ⁽⁹⁴⁾ and ${}^4\text{He}$ ⁽⁹⁵⁾ targets. The elastic data is in general difficult to fit with phenomenological optical potentials, in part because a Woods-Saxon geometry for the nuclear density is not expected to be a good approximation for these nuclei and also because at large angles exchange effects involving the incident proton and the target nucleons start to become important^(96,97). Optical potential parameters that have been determined for 300 MeV $\vec{p} + {}^3\text{He}$ ⁽⁹⁸⁾ and 350 MeV $\vec{p} + {}^4\text{He}$ ⁽⁴²⁾ elastic scattering are listed in Table 9. The $1s_{1/2}$ bound proton wave function of ${}^4\text{He}$ is determined with a Woods-Saxon binding potential that has been adjusted to give a good account of the (\vec{p},γ) data.

Description	Vector		Scalar	
	Real	Imaginary	Real	Imaginary
(a) Strength:	255.37	-226.52	-302.49	275.56
Radius r_0 :	0.6086	0.8878	0.6145	0.8233
Diffuseness a :	0.2898	0.3912	0.2917	0.3828
ω :	0.47	0.0	0.47	0.0
(b) Strength:	271.87	-193.14	-325.50	208.68
Radius r_0 :	0.5106	0.6599	0.5876	0.8547
Diffuseness a :	0.3292	0.3000	0.3529	0.3303
ω :	0.9283	0.7651	0.7352	0.0710
λ :	1.0757	1.0757	1.0757	1.0757

Table 9: Woods-Saxon optical potential parameters used in the ONM calculations for the ${}^3\text{H}(\vec{p},\gamma){}^4\text{He}$ reaction at $E_p = 300$ MeV. (a) Parameters determined from 300 MeV polarized proton elastic scattering on ${}^3\text{He}$. (b) Parameters determined from 350 MeV polarized proton elastic scattering on ${}^4\text{He}$.

The potential parameters are listed in Table 10. The fractional-parentage coefficient of the valence proton is taken to be unity.

The ONM results for the ${}^3\text{H}(\vec{p},\gamma){}^4\text{He}$ reaction at $E_p = 300$ MeV that use the aforementioned potentials are shown in Figs. 35 and 36. The solid curves are for the ${}^3\text{He}$ optical potential and the dashed curves are for the ${}^4\text{He}$ optical potential. The agreement of both calculations with the cross section data is quite good. It is unfortunate that there is no data at more forward angles, however, since there is an indication of a peak in the angular distribution at about 45° . This characteristic of the differential cross section is seen in the (p,γ) data at $E_p = 156$ MeV⁽⁹⁹⁾ and for the inverse (γ,p) reaction data at $E_\gamma = 334$ MeV⁽¹⁰⁰⁾. If this were the case for this 300 MeV (\vec{p},γ) data, then the calculations would not reproduce this feature. The calculations for the analyzing power are more sensitive to the optical potential; the calculation with the ${}^3\text{He}$ optical potential is out of phase with the A data whereas the calculation with the ${}^4\text{He}$ optical potential gives a very good description of this data.

The meaning of these good ONM results is not totally clear. In addition to the questionable application of the ONM to a light target, the incident proton energy is almost exactly at the Δ isobar formation threshold and so it might be expected that reaction mechanisms involving the Δ would become important. It is possible that the bound state potential, to which these results are very sensitive, may be unrealistic in the sense that the parameters are chosen to mock up some of the effects that are not in the ONM. Of course this is a danger for all the previous calculations, but in this case it is particularly so because of the absence of the independently determined Hartree bound nucleon wave function.

<u>Description</u>	<u>Vector</u>	<u>Scalar</u>
Strength:	350.00	-423.43
Radius r_0 :	1.0911	1.0911
Diffuseness a :	0.2365	0.2365

Table 10: Woods-Saxon binding potential parameters for ${}^4\text{He}$.

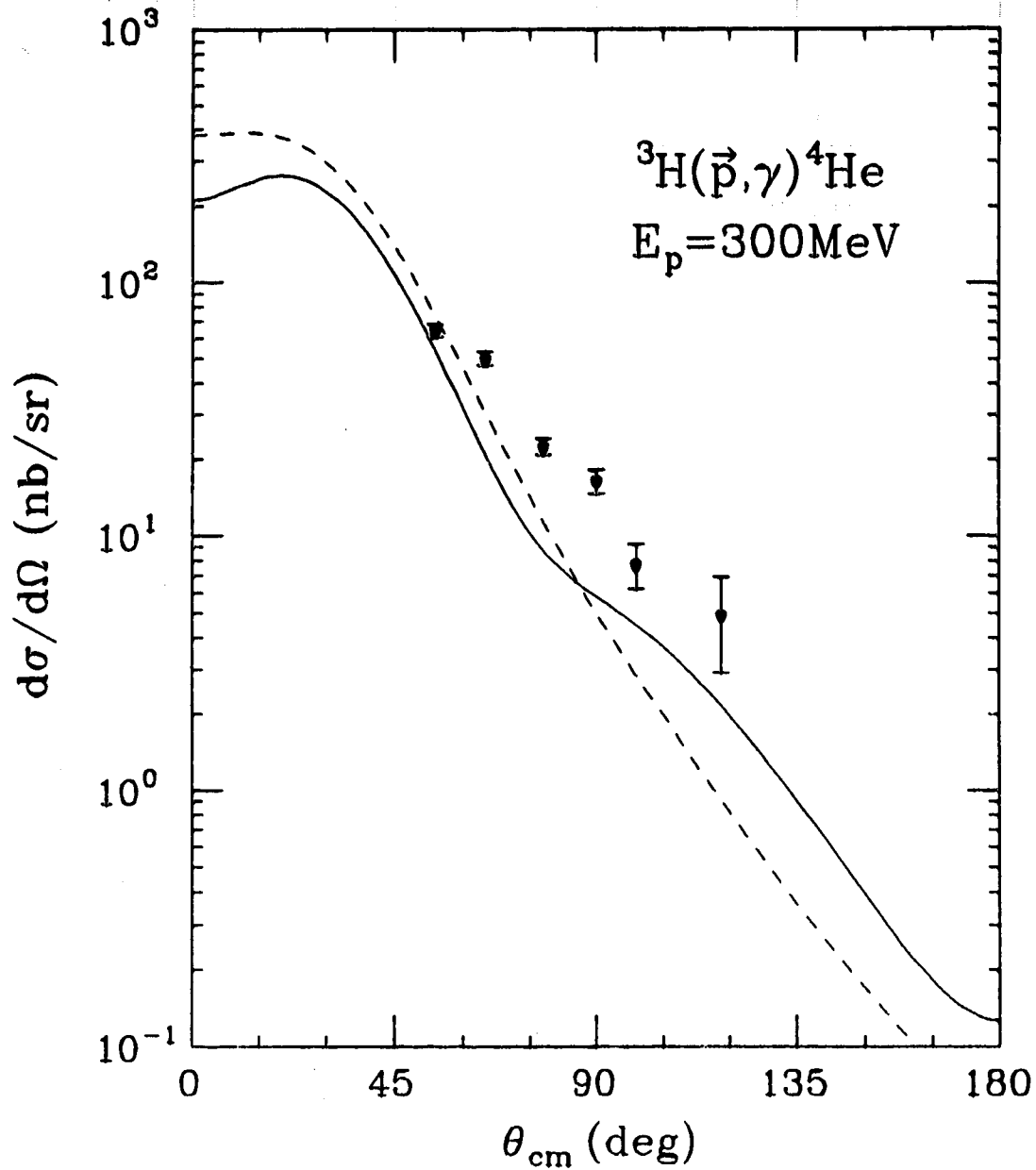


Fig. 35: ONM calculations for the differential cross section of the 300 MeV ${}^3\text{H}(\vec{p}, \gamma){}^4\text{He}$ reaction in which a Woods-Saxon binding potential and Woods-Saxon distorting potentials (solid: ${}^3\text{He}$ optical potential; dashed: ${}^4\text{He}$ optical potential) are used. The data are from Ref. 93.

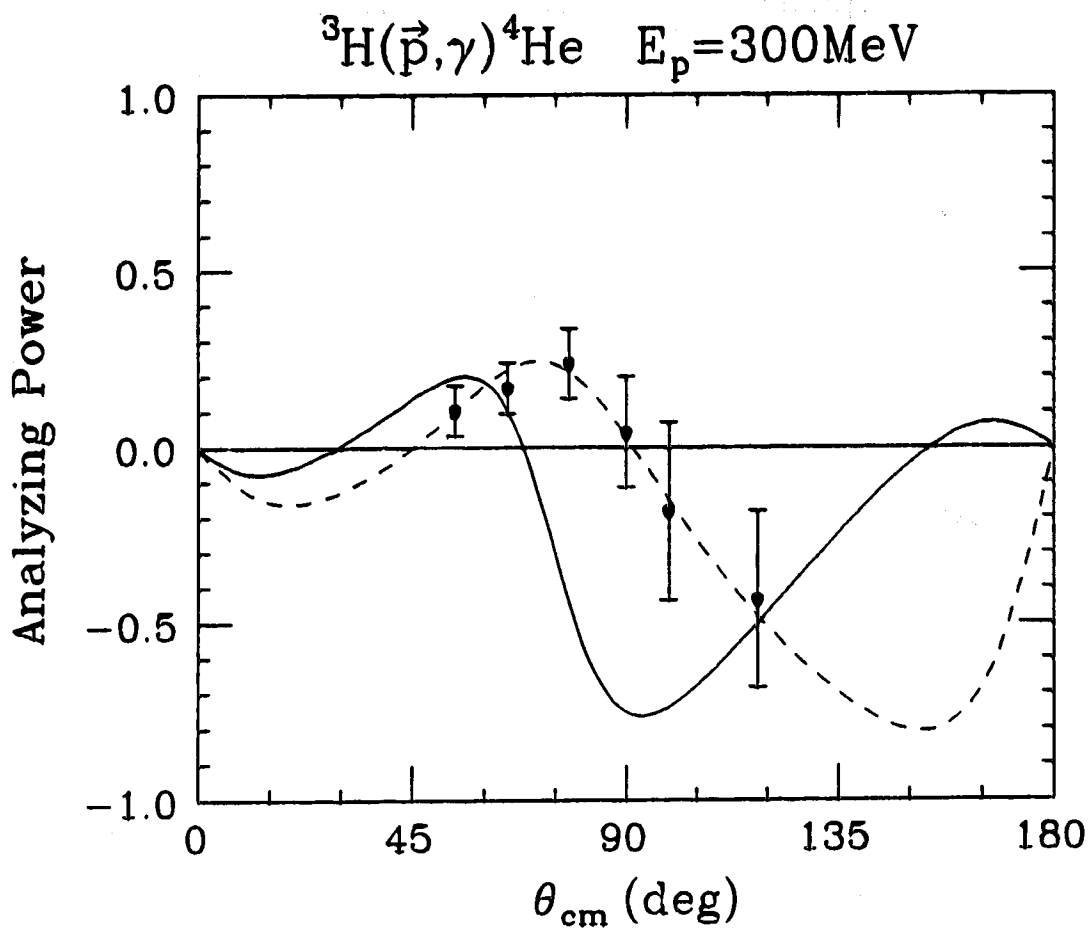


Fig. 36: ONM calculations for the analyzing power of the 300 MeV ${}^3\text{H}(\vec{p}, \gamma){}^4\text{He}$ reaction in which a Woods-Saxon binding potential and Woods-Saxon distorting potentials (solid: ${}^3\text{He}$ optical potential; dashed: ${}^4\text{He}$ optical potential) are used. The data are from Ref. 93.

5.5 Discussion

The results of One Nucleon Model calculations have been compared with data for (γ, p) and (\bar{p}, γ) reactions on representative nuclear targets and at various incident energies in the intermediate energy range. Similar calculations have been done for other ${}^4\text{He}(\gamma, p){}^3\text{H}$, ${}^{12}\text{C}(\gamma, p){}^{11}\text{B}$ and ${}^{16}\text{O}(\gamma, p){}^{15}\text{N}$ reactions that are not presented here because the information that can be gleaned from these calculations is essentially redundant. Individually, the relativistic ONM predictions for the empirical results are better than those given by previous analogous nonrelativistic models. It seems that relativistic dynamics are important for describing these high momentum transfer reactions. The ONM results are more impressive when they are viewed coherently for all the cases presented. Although the results are shown to be sensitive to the distorted wave functions and even more so to the bound state wave functions used, the consistently good description of the experimental observables afforded by the calculations suggests that the ONM is very credible. The momentum transfers for which the ONM is valid are greater than suggested by previous investigations. There are also indications that for higher momentum transfers other reaction mechanisms may be becoming important.

5.5.1 Sensitivity of ONM Results to Wave Functions

The importance of including final state interactions of the photoemitted proton with the residual nucleus is illustrated in Fig. 37. Using a plane wave for the proton in the calculation of the $E_\gamma = 196$ MeV ${}^{16}\text{O}(\gamma, p){}^{15}\text{N}$ cross section results in the curve shown which is quantitatively quite different from the distorted wave result that is represented by the solid curve in Fig. 16. The proper proton distortion is apparently critical in accounting for the data. It is observed that there is some variation in the ONM predictions for (γ, p) observables according to which optical potential is used in determining the continuum proton wave function. Almost invariably, the distorted wave functions for which the elastic scattering data is better described also give the best agreement for the (γ, p) data. Thus, the sensitivity of the ONM calculations to the continuum proton wave function is not a serious obstacle if a good optical potential can be determined from the corresponding elastic scattering data. Since microscopic optical potentials do not in general result in as good description of the elastic scattering data as do phenomenological potentials, the latter are preferred for the (γ, p) calculations.

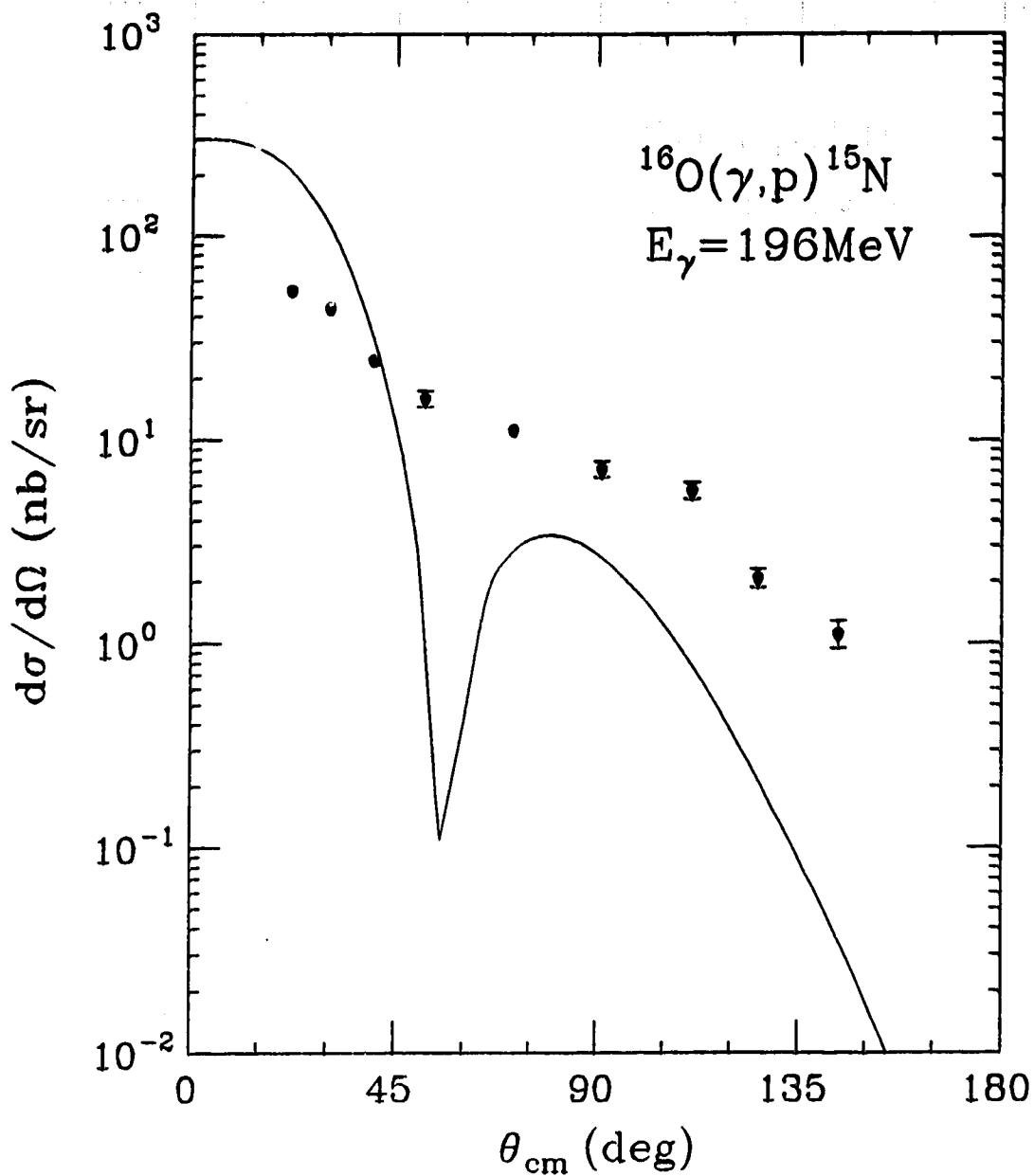


Fig. 37: ONM calculation for the differential cross section of the 196 MeV $^{16}\text{O}(\gamma,p)^{15}\text{N}$ reaction in which a Hartree bound proton wave function and a plane wave continuum proton wave function are used. The data are from Ref. 28.

The sensitivity of the ONM calculations to the bound proton wave function used is a more serious concern. On the one hand this sensitivity is expected and welcome since it might give information about the high momentum components of the bound state wave function. The lack of knowledge of the importance of other reaction mechanisms makes such information uncertain, however. In using bound proton wave functions determined with Woods-Saxon potentials, the parameters have consciously been constrained to be "reasonable" by independent empirical evidence beyond the proton binding energy. These constraints include the potential being consistent with the binding energies of other nucleons in the nucleus, the rms charge radius of the nucleus or the rms radius of an additional neutron, or requiring a geometry for the potential similar to that of the real part of the proton optical potential. In addition, the ONM results with the "good" Woods-Saxon binding potentials are usually very similar to the ONM results with Hartree potentials which intimates that these Woods-Saxon potentials are physically reasonable.

5.5.2 Nuclear Recoil Corrections

The problem of not being able to separate the center-of-mass motion from the relative motion is intrinsic to the Dirac equation. The effect of nuclear recoil has been incorporated into distorted wave calculations according to two somewhat different prescriptions. Ottenstein, Sabutis and Wallace⁽¹⁰¹⁾ start with a propagator that explicitly includes the mass of the target nucleus and derive a wave equation in coordinate space by localizing certain terms. Recoil effects are accounted for by virtue of including the finite nuclear mass in the resulting coupled differential equations for the upper and lower components of the wave function. Cooper and Jennings⁽¹⁰²⁾ develop two-body propagators for use in relativistic systems by eliminating in these propagators as much short range structure as possible. The justification for this is twofold. First, the fact that a nucleon is an extended object suggests that any short range structure in the propagator is spurious. Second, it is pointed out that there may be considerable cancellation of short range structure between various graphs of the interaction between even point objects. The final result of this approach for nucleon-nucleus scattering is that the scalar and vector optical potentials are simply multiplied by kinematic factors to take recoil effects into account.

Recoil effects will be most important for reactions on light nuclei and so both of the prescriptions mentioned were tested for the 196 MeV $^{16}\text{O}(\gamma,p)^{15}\text{N}$ and 300 MeV

It should be mentioned that it is not correct to apply the recoil corrections when phenomenological optical potentials are used to generate the proton distorted wave. The corrections to the wave function that are a result of recoil are already incorporated into these potentials since the nucleus recoils in the elastic scattering. Therefore the recoil corrections should only be incorporated when microscopic optical potentials are used although an indication of the size of these corrections may be obtained by including the recoil corrections artificially when phenomenological potentials are used. Figure 38 illustrates that the ONM calculations do not seem to be very sensitive to recoil corrections. The slight changes in the results are minor compared with the changes that are a consequence of the uncertainty in the distorting and binding potentials.

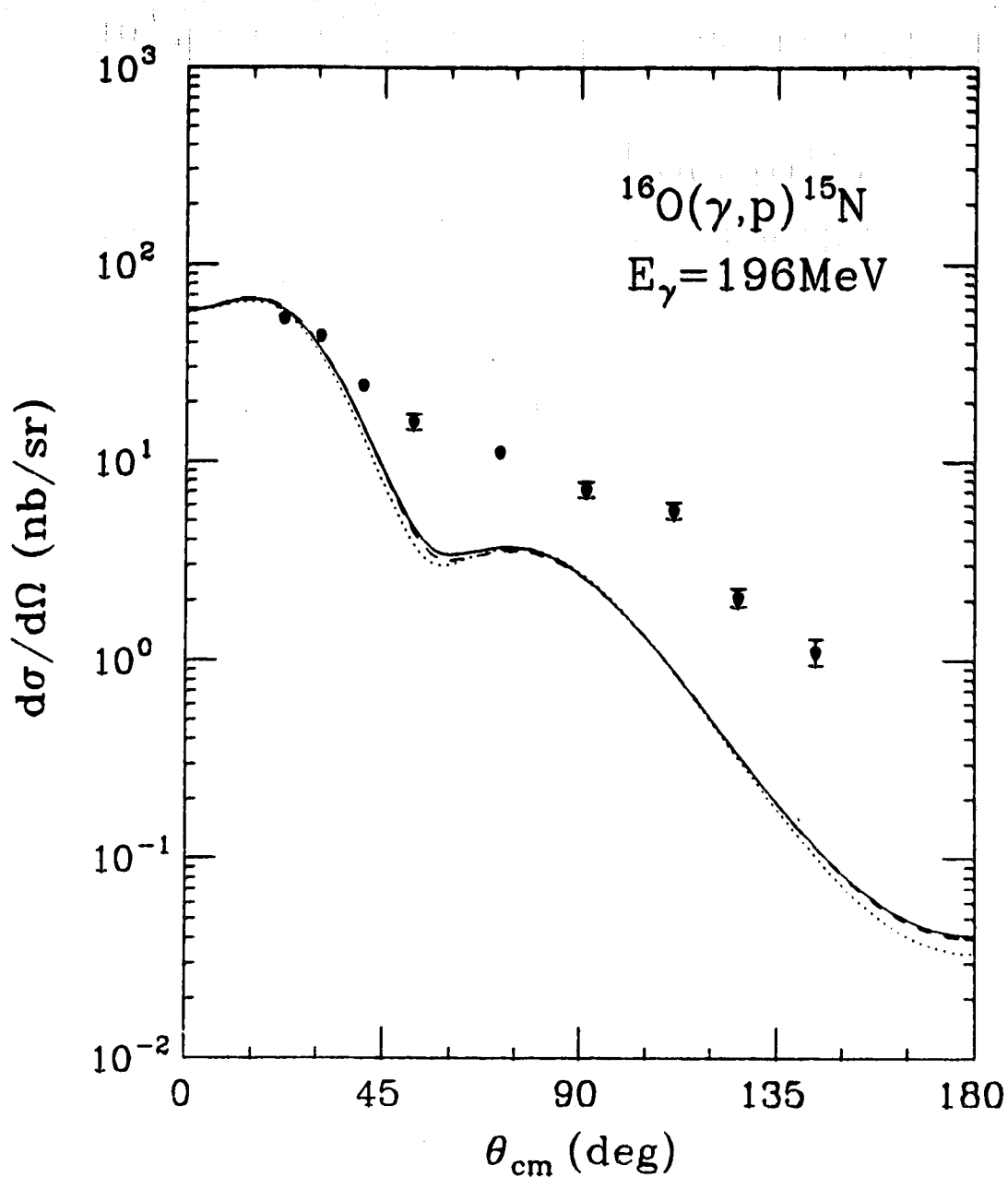


Fig. 38: ONM calculations including recoil corrections (dashed curve: recoil corrections of Ref. 101; dot-dashed curve: recoil corrections of Ref. 102) for the differential cross section of the 196 MeV $^{16}\text{O}(\gamma,p)^{15}\text{N}$ reaction in which a Hartree binding potential and a microscopic distorting potentials are used. The data are from Ref. 28. The solid curve is the result without recoil corrections.

6. Final State Charge Exchange

The success of the One Nucleon Model calculations for (γp) reactions is not carried over to the (γ, n) data. The (γ, n) experiments that have been done for photon energies below 160 MeV indicate that the angular distributions for these reactions are comparable in magnitude and shape to those for (γ, p) reactions on the same target nuclei^(6,103-108). Since the photon couples to the neutron only through the magnetic moment, it is expected that the ONM calculations for photoneutron knockout reactions will yield results that are well below those obtained for photoproton knockout reactions. This is borne out rather dramatically by the ONM calculation for the $^{16}\text{O}(\gamma, n)^{15}\text{O}$ reaction at $E_\gamma = 60$ MeV shown in Fig. 39. The inadequacy of the ONM calculations for (γ, n) reactions has led some to conclude that the direct mechanism is unimportant for (γ, p) reactions as well, relative to reaction mechanisms that are not sensitive to the charge of the emitted nucleon^(25,15) such as those that involve meson exchange currents. The consistently good results of the relativistic ONM calculations for (γ, p) reactions indicate that the direct mechanism is indeed important for these reactions, however, and therefore the observed (γ, n) cross sections deserve further study.

As has been pointed out in Secs. 2.2 and 2.5, there exists the possibility that some reaction mechanisms may contribute much more for a (γ, n) reaction than a (γ, p) reaction. This is the case for the RPA calculations described in Sec. 2.5 in which the correlation contributions are much larger for the (γ, n) amplitude⁽²⁷⁾. The possibility of a (γ, N) reaction proceeding through the direct photoemission of a nucleon followed by a charge exchange reaction is the clearest example of a process that will be more significant for the (γ, n) amplitude, because of the much higher probability that the photon will initially interact with a proton. This chapter will investigate this charge exchange mechanism in a relativistic framework. A similar nonrelativistic calculation for final state charge exchange indicates that this process is important compared with the direct neutron knockout, although the data is still significantly underestimated⁽²²⁾.

6.1 The Charge Exchange Mechanism

From a microscopic standpoint, the charge exchange following a (γ, p) reaction can

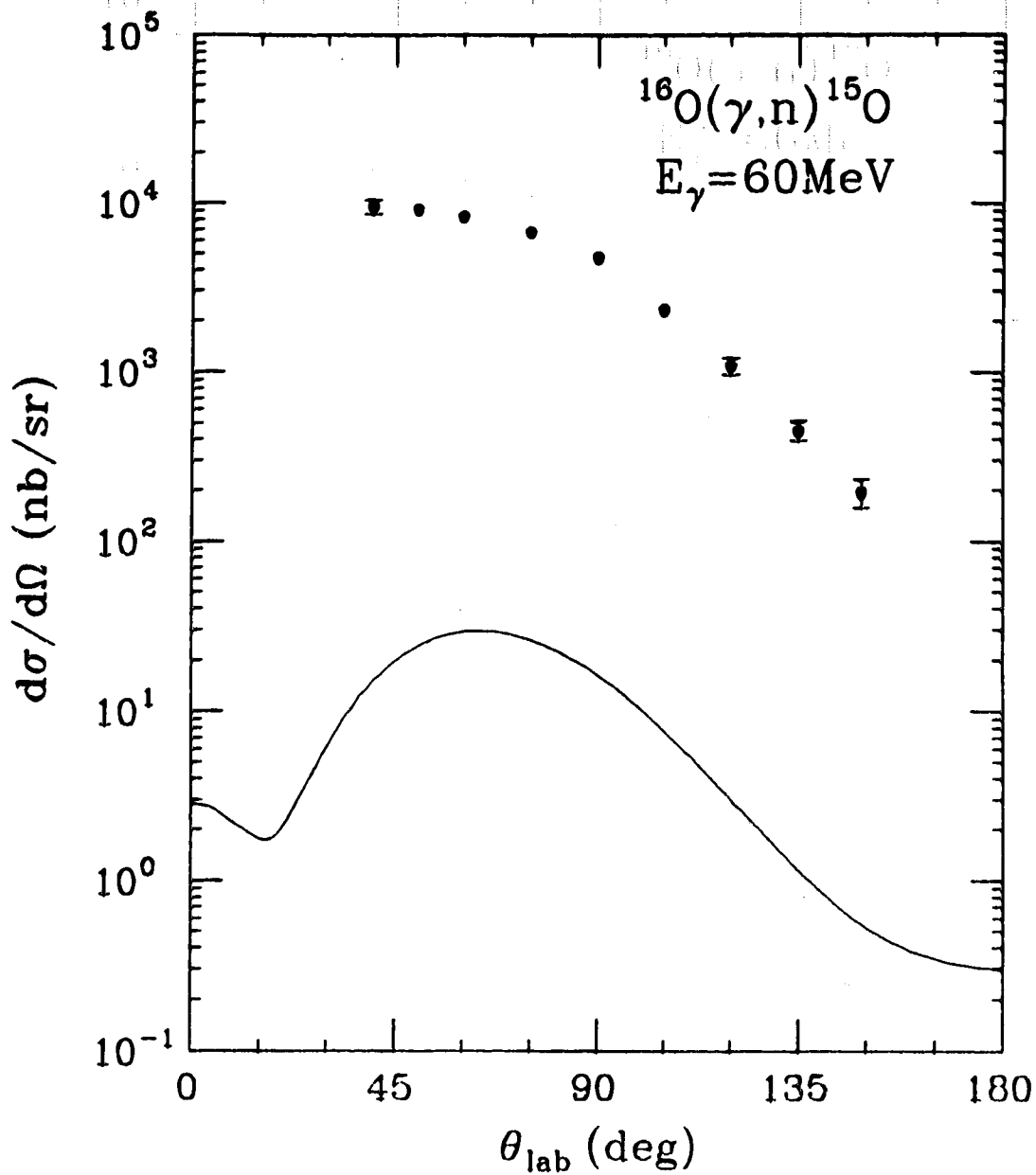


Fig. 39: ONM calculation for the differential cross section of the 60 MeV $^{16}\text{O}(\gamma, n)^{15}\text{O}$ reaction in which a Hartree binding potential and the Woods-Saxon distorting potential characterized by the parameters of Table 4 are used. The data are from Ref. 105.

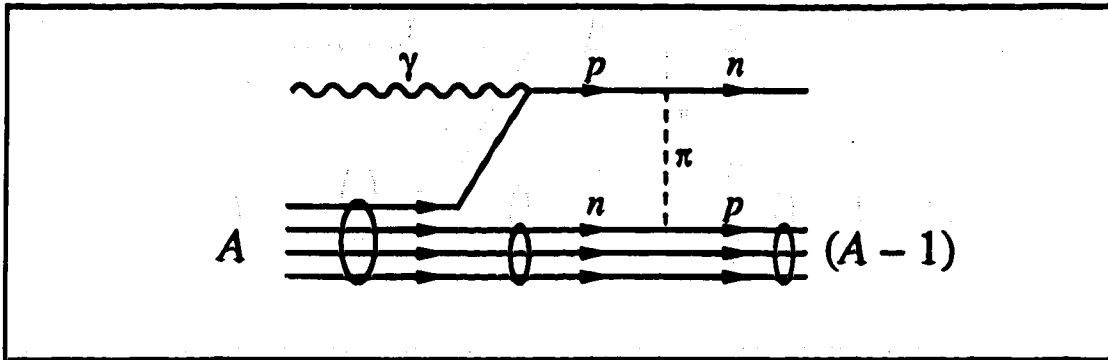


Fig. 40: Feynman diagram for a (γ, p) reaction followed by a (p, n) reaction mediated by charged pion exchange.

be mediated by the exchange of a charged pion as is illustrated in Fig. 40. The amplitude that would be calculated from this diagram would involve a nine-dimensional integral because of the three vertices involved, as well as knowledge of all the nucleon single-particle wave functions of the residual nucleus.

The problems associated with the aforementioned microscopic calculation can be circumvented by going to a potential description in which the optical potential has isovector as well as isoscalar pieces. Such a potential for spin-zero nuclei is written as

$$U(r) = S(r) + \gamma^0 V(r) + [S_{pn}(r) + \gamma^0 V_{pn}(r)]\mathbf{t} \cdot \mathbf{T}/A \quad (6.1)$$

where \mathbf{t} and \mathbf{T} represent the projectile and target isospin operators respectively and A is the number of target nucleons. Since isospin operators are included explicitly in the potential, the nucleon and nucleus wave functions must include isospin pieces as well. The proton and neutron are viewed as different states of an isospin $1/2$ particle with isospin projections $-1/2$ and $+1/2$ respectively. The isospin projection of a nucleus therefore is $T_z = (N - Z)/2$ where N and Z are the number of neutrons and protons in the nucleus. For a nucleus in its ground state the isospin is given by $T = |T_z|$. The $\mathbf{t} \cdot \mathbf{T}$ operator contained in the isovector part of the potential can flip the nucleon isospin projection (*i.e.*, change a proton into a neutron and *vice versa*) and correspondingly change the isospin projection of the nucleus by one unit. The final nucleus will have the same total isospin quantum number as the initial nucleus however. This state is the isobaric analogue state of the initial nuclear state and it will have the same spin and space wave function as the initial nucleus. Transitions to the isobaric analogue state are only possible for cases in which the magnitude of the raised or lowered nuclear isospin

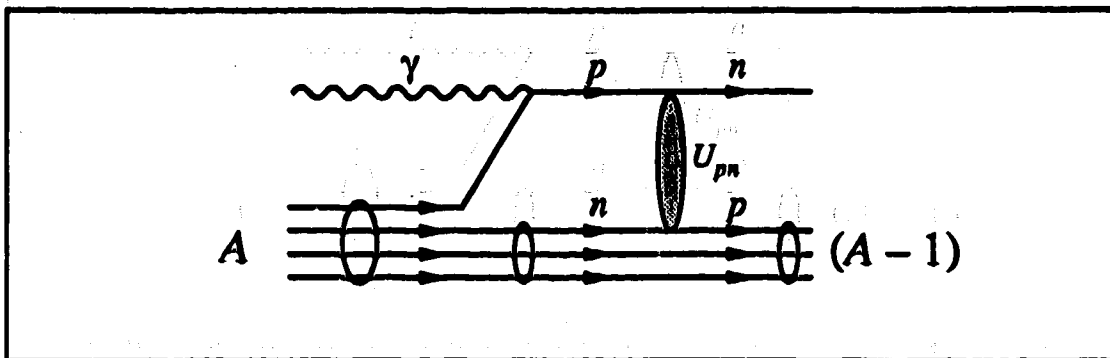


Fig. 41: Diagrammatic representation of a (γ, n) reaction that proceeds through the photoemission of a proton followed by a single charge exchange that is mediated by the isovector optical potential.

projection remains less than the initial total nuclear isospin. The most evident example of this limitation is that charge exchange reactions cannot take place on a target with $N = Z$, as is expected. The magnitude of the Q -value for a charge exchange reaction will be the Coulomb energy difference between the initial and final nuclear states plus the neutron-proton mass difference.

A (γ, n) reaction which proceeds through final state charge exchange in the potential formulation is pictured in Fig. 41. A potential description for the final state charge exchange is consistent with the spirit of the ONM calculations in that the $(A - 1)$ residual nucleons can still be taken to be spectators in the reaction by virtue of the fact that the intermediate nucleus has the same spin and space wave function as the final nucleus. The requirement that the intermediate and final nuclear states be analogues limits the possible nuclear targets to which the formalism can be applied. A clear case for which this condition is satisfied is the $T = 1/2$, $T_z = 1/2$ intermediate state; the final nucleus will then be in its ground state, having $T_z = -1/2$. Such intermediate and final nuclei are said to be mirror nuclei, examples of which are the pairs $({}^3\text{H}, {}^3\text{He})$, $({}^{15}\text{N}, {}^{15}\text{O})$ and $({}^{39}\text{K}, {}^{39}\text{Ca})$. These nuclei are precisely those involved in the (γ, n) reactions on ${}^4\text{He}$, ${}^{16}\text{O}$ and ${}^{40}\text{Ca}$ which could proceed through the final state charge exchange mechanism.

6.2 The Isovector Optical Potential

The optical potential for nucleon-nucleus scattering is expected to have an isovector component for nuclei with $N \neq Z$ because the NN amplitude contains isovector terms

that are a result of processes such as charged pion exchange. Phenomenological analyses have not been attempted for determining the isovector Dirac optical potential because it is not expected that the potential shapes will be simple, as is the case for the isoscalar optical potential. It is, however, straightforward to generalize the microscopic calculations for the isoscalar optical potential, described in Secs. 3.2.3 and 3.2.4, to include isospin and thus determine the isovector optical potential.

In the Relativistic Impulse Approximation (RIA) the isovector optical potentials are given by⁽¹⁰⁹⁾

$$S, V_{pn}(r) = -\frac{4A}{N-Z} C \int d^3q e^{-iq \cdot r} F_{S,V}^1(q) \bar{\rho}_{S,V}^1(q) \quad (6.2a)$$

$$C = -4\pi i k_{cm} / [(2\pi)^3 m] \quad (6.2b)$$

$$F_{S,V}^1 = \frac{1}{2} (F_{S,V}^p - F_{S,V}^n) \quad (6.2c)$$

$$\bar{\rho}_{S,V}^1 = \bar{\rho}_{S,V}^p - \bar{\rho}_{S,V}^n \quad (6.2d)$$

In these equations the superscripts p and n refer to target protons and neutrons. The amplitude given in Eq. (3.13) is separated into proton and neutron amplitudes, as are the scalar and vector densities of Eqs. (3.5a) and (3.5b) to get the isovector quantities in Eqs. (6.2c) and (6.2d). The densities may be obtained from Hartree or Hartree-Fock calculations. The vector proton density may alternatively be determined from electron scattering measurements.

The relativistic microscopic calculations that model the NN t -matrix from meson exchange can similarly be extended to include isospin⁽¹¹⁰⁾. The direct and exchange NN amplitudes are included, as well as Pauli blocking effects. The isovector potentials are determined by folding the isovector amplitudes with the appropriate density combinations.

6.3 The Relativistic Lane Equations and the Transition Matrix for a (γ, n) Reaction with Final State Charge Exchange

The usual method of doing calculations for (p, n) reactions is to write the wave function for the system as a sum of a proton-target nucleus product wave function and a neutron-residual nucleus product wave function. The dynamical equation of motion for

the system will then result in coupled equations for the proton and neutron wave functions. In the nonrelativistic formulation using the Schrödinger equation the coupled equations are the so-called Lane equations⁽¹¹¹⁾.

The relativistic description of a (p,n) reaction follows the same prescription as the nonrelativistic one except that the dynamics are described by the Dirac equation with an appropriate relativistic Hamiltonian. The Hamiltonian that describes both the proton-target nucleus and neutron-final nucleus systems is

$$H = H(\epsilon) + \left(\frac{1}{2} + t_z\right)\Delta E_c + \alpha \cdot \mathbf{p} + \left(\frac{1}{2} - t_z\right)V_c(r) + \beta U(r) + \beta m_p \quad (6.3a)$$

where $H(\epsilon)$ is the nuclear Hamiltonian (ϵ are the internal nuclear coordinates) and ΔE_c is given by

$$\Delta E_c = \beta (m_n - m_p) + E_p - E_n \quad (6.3b)$$

The wave function is

$$\Psi = \Phi_i(\epsilon) \psi_p(\mathbf{x}) |T, T\rangle | \frac{1}{2}, -\frac{1}{2} \rangle + \Phi_f(\epsilon) \psi_n(\mathbf{x}) |T, T-1\rangle | \frac{1}{2}, \frac{1}{2} \rangle \quad (6.4)$$

where Φ_i and Φ_f are the nuclear spin-space wave functions which are identical for the reaction going to the isobaric analogue state. The proton and neutron Dirac four-component spinors are appropriately labelled by the subscripts p and n , and the isospin wave functions are included specifically. Substituting this wave function into the Dirac equation

$$H \Psi = E \Psi \quad (6.5)$$

with the Hamiltonian of Eq. (6.3a) results in the coupled Dirac equations that are the relativistic Lane equations⁽¹⁰⁹⁾

$$\left[\alpha \cdot \mathbf{p} + \beta m_p + \beta S + V + V_c - \frac{N-Z}{4A} (\beta S_{pn} + V_{pn}) - E_p \right] \psi_p + \frac{\sqrt{N-Z}}{2A} (\beta S_{pn} + V_{pn}) \psi_n = 0 \quad (6.6a)$$

$$\left[\alpha \cdot \mathbf{p} + \beta m_n + \beta S + V + \frac{N-Z-2}{4A} (\beta S_{pn} + V_{pn}) - E_n \right] \psi_n + \frac{\sqrt{N-Z}}{2A} (\beta S_{pn} + V_{pn}) \psi_p = 0 \quad (6.6b)$$

In these equations N and Z are the number of neutrons and protons in the nucleus on

which the proton is incident. In order to derive Eqs. (6.6) the isospin wave functions in Eq. (6.4) are coupled and the quantity $H(\epsilon)\Phi(\epsilon)$ is taken arbitrarily to be zero. The relativistic Lane equations may be solved using an iterative technique with the boundary conditions being that Ψ_p has an incoming plane wave piece and outgoing spherical waves and Ψ_n has outgoing spherical waves only. For the inverse (n,p) reaction the coupled equations are the same but the boundary conditions in this case are that Ψ_n has an incoming plane wave piece and outgoing spherical waves and Ψ_p has outgoing spherical waves only.

The transition matrix for a (γ,n) reaction that includes the possibility of the photoemission of a proton with subsequent charge exchange(s) to ultimately give a continuum neutron, as well as the direct photoemission of the neutron, is

$$T_{fi} = \langle \Psi_f | H_{em} | \Psi_i \rangle . \quad (6.7)$$

where the wave functions and the Hamiltonian are explicitly written with the isospin dependence that underlies the relativistic Lane formalism. The final nuclear wave function is given by Eq. (6.4) where the boundary conditions are for the (n,p) reaction and the nuclear spin-space wave functions are labelled further by the total angular momentum J_f and projection M_f . The electromagnetic interaction Hamiltonian is

$$H_{em} = \left(\frac{1}{2} - t_z \right) e \gamma^\mu A_\mu + \frac{1}{2} \left[\left(\frac{1}{2} - t_z \right) \kappa_p \mu_p + \left(\frac{1}{2} + t_z \right) \kappa_n \mu_n \right] \sigma^{\mu\nu} F_{\mu\nu} . \quad (6.8)$$

A ground state target wave function is written in a parentage expansion as⁽⁷¹⁾

$$\begin{aligned} \Psi_i = & \sum_{JTJ_B} \langle J_i T_i \{ | J T J_B \rangle \sum_{M_B} (J J_B ; M M_B | J_i M_i) \Psi_{J_B M_B} \Phi_{JM} \\ & \times \sum_{N_B} (T 1/2 ; N N_B | T_i T_i) | 1/2 N_B \rangle | T N \rangle \end{aligned} \quad (6.9)$$

where the fractional-parentage coefficients $\langle J_i T_i \{ | J T J_B \rangle$ depend explicitly on isospin and generally are different from the spin-orbit fractional-parentage coefficients of Eq. (4.15). For the purposes of the expansion the Coulomb interaction is assumed to be negligible and so protons and neutrons can be treated symmetrically.

Hereafter the only target nuclei that are considered contain the same number of protons as neutrons, *i.e.*, $T_i = 0$, and have total angular momentum $J_i = 0$. The

isospin of the residual nucleus is thus constrained to be $T_f = 1/2$ and the total angular momentum J_B that the knocked out nucleon initially had will be the same as the total nuclear angular momentum J_f . All the relevant (γ, n) experiments have been done for such targets.

With the wave functions and interaction Hamiltonian specified above, the transition matrix of Eq. (6.7) becomes

$$T_{fi} = (-1)^{J_f - M_f} \frac{1}{\sqrt{2J_f + 1}} \frac{\langle 00 (1/2 J_f) \rangle}{\sqrt{2}} \times \left\{ \begin{array}{l} - \int d^4x \bar{\psi}_n^{(-)}(x) \frac{\kappa_n \mu_n}{2} \sigma^{\mu\nu} F_{\mu\nu}(x) \psi_{J_f M_f}(x) \\ + \int d^4x \bar{\psi}_p^{(-)}(x) \left[c \gamma^\mu A_\mu(x) + \frac{\kappa_p \mu_p}{2} \sigma^{\mu\nu} F_{\mu\nu}(x) \right] \psi_{J_f M_f}(x) \end{array} \right\}. \quad (6.10)$$

In deriving this expression the Clebsch-Gordan coefficients have been explicitly evaluated for the restricted class of target nuclei described above. The interpretation of the two terms in the T -matrix for the (γ, n) reaction is intimately connected to the boundary conditions on the neutron and proton wave functions being that $\psi_n^{(-)}$ has an incident plane wave piece and incoming spherical waves and $\psi_p^{(-)}$ has incoming spherical waves only. The first term is the amplitude for the photon knocking out a target neutron that has final state interactions which ultimately result in a free neutron. This implies that the initial neutron either undergoes no charge exchange or an even number of charge exchanges in moving through the region of the nuclear potential. The second term is the amplitude for the photon knocking out a target proton that has final state interactions that also ultimately result in a free neutron. Thus the initial proton must undergo an odd number of charge exchanges which is consistent with the boundary conditions that require the proton to come from an incident neutron. A noteworthy feature of the transition matrix is the relative sign between the two terms that comes about from the isospin Clebsch-Gordan coefficients.

6.4 The Propagator Approach to (γ, n) Reactions with Final State Charge Exchange

As an alternative to solving the coupled Lane equations the continuum proton and neutron may be viewed in a more distinct manner. The mechanism illustrated in Fig. 41 is

interpreted as follows: The incident photon interacts with a valence proton in the target nucleus through the electromagnetic interaction. As a result, the proton is ejected from the nucleus and interacts with the intermediate nucleus through the proton-nucleus optical potential until the charge exchange occurs through the isovector optical potential. Subsequent to the charge exchange, the neutron interacts with the residual nucleus through the neutron-nucleus optical potential without further charge exchange. The transition matrix for this process on a $T_i = 0 = J_i$ target, which is the first-order part of the second term in Eq. (6.10) by virtue of considering only one charge exchange, can be written with a Green function propagator for the proton between the electromagnetic and isovector potential vertices as

$$T_{s_f M_B}^{\xi} = (-1)^{J_f - M_f} \frac{1}{\sqrt{2J_f + 1}} \frac{\langle 00 || J_f 1/2 J_f \rangle}{\sqrt{2}} \\ \times \int d^4x d^4y \bar{\psi}_{s_f}^{(-)}(y) \frac{1}{A} [S_{pn}(y) + \gamma^0 V_{pn}(y)] \langle \mathbf{t} \cdot \mathbf{T} \rangle G_p^{(+)}(y, x) \\ \times \left[e\gamma^{\mu} A_{\mu}^{(\xi)}(x) + \frac{\kappa_p \mu_p}{2} \sigma^{\mu\nu} F_{\mu\nu}^{(\xi)}(x) \right] \psi_{M_B}(x) . \quad (6.11)$$

The superscript (ξ) refers to the polarization of the incident photon. The bound proton wave function ψ_{M_B} with spin projection M_B satisfies the Dirac equation with suitable binding potentials. It is the same wave function that is used for the ONM calculations and is described in detail in Sec. 3.3.2. The continuum neutron wave function $\psi_{s_f}^{(-)}$ with spin projection s_f is the time-reverse of $\psi_{s_f}^{(+)}$ (cf. Eqs. (4.33) and (3.32)) which satisfies the Dirac equation

$$\left[i\gamma^{\mu} \partial_{\mu} - m - S(r) - \gamma^0 V(r) + \frac{1}{4A} [S_{pn}(r) + \gamma^0 V_{pn}(r)] \right] \psi_{s_f}^{(+)}(y) = 0 . \quad (6.12)$$

This is very similar to Eq. (3.19), except that there is a contribution to the optical potential from the isovector potentials since the $\mathbf{t} \cdot \mathbf{T}$ operator has a diagonal piece. This addition to the optical potential is expected to be small by virtue of the $1/(4A)$ factor. The Green function for a proton propagating from x to y that is interacting with the intermediate nucleus optical potential satisfies

$$\left[i\gamma^{\mu} \partial_{\mu} - m - S(r) - \gamma^0 V(r) - \gamma^0 V_c(r) + \frac{1}{4A} [S_{pn}(r) + \gamma^0 V_{pn}(r)] \right] G_p^{(+)}(y, x) = \delta^4(y - x) \quad (6.13)$$

where the derivative operators and the radial coordinate r refer (consistently) to either the

four-vector y or x . The isovector potentials also contribute to the proton-nucleus optical potential. The (+) superscript on the Green function signifies that the proton asymptotically has outgoing spherical waves. The constants that multiply the integral in Eq. (6.11) come from the fractional-parentage expansion of the target nucleus in the same way as for Eq. (6.10) and the diagonal brackets around the isospin operator signify an expectation value between the proton-intermediate nucleus and neutron-final nucleus isospin wave functions.

In order to facilitate the evaluation of the amplitude for the final state charge exchange contribution for (γ, n) reactions, the calculations are done for the inverse (n, γ) reaction. The picture now is that a neutron incident on a nucleus that is a member of a mirror pair first undergoes a charge exchange reaction to give a proton moving relative to the second member of the pair and then a (p, γ) reaction takes place. The matrix algebra turns out to be more straightforward for the inverse reaction, and the asymptotic behaviour of the wave functions is more obvious. The transition matrix for the (n, γ) reaction with single charge exchange is

$$T_{s_f M_B}^{\xi} = (-1)^{J_f - M_f} \frac{1}{\sqrt{2J_f + 1}} \frac{\langle 00 \{1 J_f 1/2 J_f\} \rangle}{\sqrt{2}} \\ \times \frac{1}{2A} \int d^4x d^4y \bar{\psi}_{M_B}(x) \left[e\gamma^{\mu} A_{\mu}^{(\xi)}(x) + \frac{\kappa_p \mu_p}{2} \sigma^{\mu\nu} F_{\mu\nu}^{(\xi)}(x) \right] \\ \times G_p^{(+)}(x, y) [S_{pn}(y) + \gamma^0 V_{pn}(y)] \psi_{s_f}^{(+)}(y) . \quad (6.14)$$

The matrix element of the isospin operator $t \cdot T/A$ has been explicitly evaluated between the proton-intermediate nucleus and neutron-final nucleus isospin wave functions to get the isospin factor $1/(2A)$. This T -matrix is precisely equal to the T -matrix of Eq. (6.11) by virtue of time reversal invariance.

The evaluation of the amplitude (6.14) is achieved through the reduction of the eight-dimensional integral to a four-dimensional integral and a differential equation by using the property (6.13) of the Green function. Defining the quantity

$$I_{s_f}^{(+)}(x) \equiv \frac{1}{2A} \int d^4y G_p^{(+)}(x, y) [S_{pn}(y) + \gamma^0 V_{pn}(y)] \psi_{s_f}^{(+)}(y) \quad (6.15)$$

and operating on the left of Eq. (6.14) with

$$\left[i\gamma^\mu \partial_\mu - m - S(r) - \gamma^0 V(r) - \gamma^0 V_c(r) + \frac{1}{4A} [S_{pn}(r) + \gamma^0 V_{pn}(r)] \right],$$

where the radial coordinate and derivatives are with respect to the four-vector x , yields the following equation:

$$\begin{aligned} \left[i\gamma^\mu \partial_\mu - m - S(r) - \gamma^0 V(r) - \gamma^0 V_c(r) + \frac{1}{4A} [S_{pn}(r) + \gamma^0 V_{pn}(r)] \right] I_{s_f}^{(+)}(x) \\ = \frac{1}{2A} [S_{pn}(r) + \gamma^0 V_{pn}(r)] \psi_{s_f}^{(+)}(x). \end{aligned} \quad (6.16)$$

This is a Dirac-type equation for $I_{s_f}^{(+)}(x)$ with a source term that is a product of the known isovector potentials and the incident neutron wave function. The solution can be put into Eq. (6.14) to yield the straightforward four-dimensional integral

$$\begin{aligned} T_{s_f M_B}^\xi = (-1)^{J_f - M_f} \frac{1}{\sqrt{2J_f + 1}} \frac{\langle 00 | J_f 1/2 J_f \rangle}{\sqrt{2}} \\ \times \int d^4x \bar{\psi}_{M_B}(x) \left[e\gamma^\mu A_\mu^{(\xi)}(x) + \frac{\kappa_p \mu_p}{2} \sigma^{\mu\nu} F_{\mu\nu}^{(\xi)}(x) \right] I_{s_f}^{(+)}(x). \end{aligned} \quad (6.17)$$

The Dirac equation (6.16) and this T -matrix clearly identify $I_{s_f}^{(+)}(x)$ as a proton distorted wave function. Indeed, a comparison of the Dirac equation (6.16) and the Lane equation (6.6b) establishes that $I_{s_f}^{(+)}(x)$ is the first-order part of the full Lane proton wave function. The previous identification of the transition matrix (6.11) as the first-order estimate for the second term in the Lane transition matrix (6.10) is thus confirmed. This approximation is deemed to be reasonable since it is expected that the charge exchange amplitude is small.

The method of solving for $I_{s_f}^{(+)}(x)$ is very similar to that used for the distorted wave described in Sec. 3.3.1. The modifications from the direct mechanism case are that a source term is present in the equation and that the boundary conditions are different. These are a consequence of the proton in the intermediate state originating from a charge exchange reaction, rather than existing in the initial state.

The form of the differential equation (6.16) suggests that $I_{s_f}^{(+)}(x)$ can be expanded as

$$I_{s_f}(x) = \sqrt{\frac{E+m}{2m}} e^{-iEt} 4\pi \sum_{LJM} i^L Y_L^{M-s_f}(\hat{k}_n) (L \ 1/2; M-s_f \ s_f | J M) \times \begin{bmatrix} F_{LJ}(r) \mathcal{Y}_{L \ 1/2 J}^M(\Omega) \\ iG_{LJ}(r) \mathcal{Y}_{L' \ 1/2 J}^M(\Omega) \end{bmatrix} \quad (6.18)$$

in analogy with Eq. (3.32). Using this expansion and recalling that the solution for the neutron wave function is

$$\psi_{s_f}^{(+)}(x) = \sqrt{\frac{E+m}{2m}} e^{-iEt} 4\pi \sum_{LJM} i^L Y_L^{M-s_f}(\hat{k}_n) (L \ 1/2; M-s_f \ s_f | J M) \times \begin{bmatrix} f_{LJ}(r) \mathcal{Y}_{L \ 1/2 J}^M(\Omega) \\ ig_{LJ}(r) \mathcal{Y}_{L' \ 1/2 J}^M(\Omega) \end{bmatrix}, \quad (6.19)$$

the equation (6.16) gives the following coupled first-order differential equations for the radial functions $F_{LJ}(r)$ and $G_{LJ}(r)$:

$$\begin{aligned} & \left[E + m + S(r) - V(r) - V_c(r) - \frac{1}{4A} [S_{pn}(r) - V_{pn}(r)] \right] G_{LJ}(r) \\ & = \left[\frac{d}{dr} + \frac{1+\kappa}{r} \right] F_{LJ}(r) - \frac{1}{2A} [S_{pn}(r) - V_{pn}(r)] g_{LJ}(r) \end{aligned} \quad (6.20a)$$

$$\begin{aligned} & \left[E - m - S(r) - V(r) - V_c(r) + \frac{1}{4A} [S_{pn}(r) + V_{pn}(r)] \right] F_{LJ}(r) \\ & = - \left[\frac{d}{dr} + \frac{1-\kappa}{r} \right] G_{LJ}(r) + \frac{1}{2A} [S_{pn}(r) + V_{pn}(r)] f_{LJ}(r). \end{aligned} \quad (6.20b)$$

These equations can be transformed into a second-order differential equation by the same method as for Eqs. (3.30). The procedure and results are summarized by the following equations:

$$y''(r) + \left[a(r) - \frac{\kappa d'(r)}{r d(r)} - \frac{\kappa(\kappa+1)}{r^2} \right] y(r) = h(r) \quad (6.21a)$$

$$y(r) = F(r) [d(r)]^{-1/2} \quad (6.21b)$$

$$F(r) = r F_{LJ}(r) \quad (6.21c)$$

$$a(r) \equiv \frac{d''(r)}{2d(r)} - \frac{3}{4} \left(\frac{d'(r)}{d(r)} \right)^2 - d(r) s(r) \quad (6.21d)$$

$$d(r) \equiv \left[E + m + S(r) - V(r) - V_c(r) - \frac{1}{4A} [S_{pn}(r) - V_{pn}(r)] \right] \quad (6.21e)$$

$$s(r) \equiv - \left[E - m - S(r) - V(r) - V_c(r) + \frac{1}{4A} [S_{pn}(r) + V_{pn}(r)] \right] \quad (6.21f)$$

$$h(r) \equiv [d(r)]^{-1/2} \left[d(r)v(r)f(r) - u'(r)g(r) - u(r)g'(r) + \frac{u(r)g(r)d'(r)}{d(r)} + \frac{\kappa u(r)g(r)}{r} \right] \quad (6.21g)$$

$$u(r) \equiv \frac{1}{2A} [V_{pn}(r) - S_{pn}(r)] \quad (6.21h)$$

$$v(r) \equiv -\frac{1}{2A} [V_{pn}(r) + S_{pn}(r)] \quad (6.21i)$$

$$f(r) \equiv r f_{LJ}(r) \quad (6.21j)$$

$$g(r) \equiv r g_{LJ}(r) \quad (6.21k)$$

$$\kappa = (L - J)(2J + 1) . \quad (6.21l)$$

The second-order differential equation (6.21a) may be solved numerically using the method described in Appendix B. The two integration constants are determined by an initial value and the normalization of the solution. The relationship of $y(r)$ to the upper radial part of the wave function, $y(r) = [d(r)]^{-1/2} r F_{LJ}(r)$, requires that $y(0) = 0$. The asymptotic ($r \rightarrow \infty$) boundary conditions for $F_{LJ}(r)$ are fixed by the outgoing boundary conditions of the Green function; $F_{LJ}(r)$ must asymptotically be an outgoing spherical wave⁽⁵⁹⁾

$$F_{LJ}(r) \xrightarrow{r \rightarrow \infty} \left(\frac{v_p}{v_n} \right)^{1/2} e^{i\Sigma_{LJ}} \sin \delta_{LJ} \frac{e^{i(kr - \eta \ln 2kr - L\pi/2 + \Sigma_{LJ} + \delta_{LJ})}}{kr} . \quad (6.22)$$

The normalization convention for this function is consistent with the normalization chosen for the neutron wave function. The ratio of the velocities of the proton and neutron assures that the neutron flux is consistent with the propagating proton flux. This factor will essentially be unity since the masses of the proton and neutron are similar. The

nuclear phase shift δ_{LJ} is evaluated by matching the numerical solution for $F_{LJ}(r)$ with the analytic asymptotic solution. The details of the numerics are described in Appendix C.

Once the solution for $I_{s_f}^{(+)}(x)$ has been established, it is straightforward to evaluate the amplitude (6.14). It is now convenient, however, to write an S -matrix for the (γ, n) reaction that proceeds through final state charge exchange to establish a connection with the S -matrix for the direct reaction mechanism which is given by Eq. (4.30). In direct analogy with Eq. (4.30), the "charge exchange" S -matrix is

$$S_{fi} = -i \mathcal{J}_{0J_f}(J_f) (J_f J_f; M_f -M_f | 0 0) \frac{1}{(2\pi)^3} \left(\frac{m}{E}\right)^{1/2} \left(\frac{1}{2\omega_{k_\gamma}}\right)^{1/2} \\ \times \int d^4x \bar{I}_{s_f}^{(-)}(x) \epsilon^\mu \{e_p \gamma_\mu + i \kappa_p \mu_p \sigma_{\mu\nu} k_\nu^V\} e^{-ik_\gamma \cdot x} \Psi_B(x) . \quad (6.23)$$

The function $I_{s_f}^{(-)}(x)$ is related to $I_{s_f}^{(+)}(x)$ in the same manner as the distorted wave with incoming boundary conditions is related to the distorted wave with outgoing boundary conditions (*cf.* Eq. (4.33)), *i.e.*

$$I_{s_f}^{(-)\dagger}(x) = \sqrt{\frac{E+m}{2m}} e^{iEt} 4\pi \sum_{LJM} i^{-L} Y_L^{M-s_f}(\hat{k}_n) (L 1/2; M-s_f s_f | J M) \\ \times \mathcal{Y}_{L 1/2 J}^M(\Omega) [F_{LJ}(r) - i \sigma \cdot \hat{r} G_{LJ}(r)] . \quad (6.24)$$

The relationship between the isospin dependent fractional-parentage coefficients and the spin-orbit fractional-parentage coefficients is established by comparing the constants in Eq. (6.14) with those in Eq. (4.30) to be

$$\langle 0 0 | 1 J_f 1/2 J_f \rangle = \sqrt{2} \mathcal{J}_{0J_f}(J_f) . \quad (6.25)$$

The structure of Eq. (6.23) is precisely the same as that of the S -matrix for the direct mechanism. Therefore the matrix multiplication and the angular momentum algebra are the same for the two S -matrices and hence the results of Eqs. (4.35) may be carried over for the charge exchange S -matrix. The only difference will be that the distorted nucleon radial functions are replaced by the radial functions of $I_{s_f}^{(+)}(x)$.

In determining the total amplitude for the direct neutron photoemission and the proton photoemission followed by charge exchange, care must be taken to establish the relative signs of the two S -matrices. Isospin is included explicitly in the charge exchange calculation and so it must be included as well for the direct neutron emission calculation.

The spin-orbit Clebsch-Gordan coefficients for proton and neutron knockout will have opposite signs as has been noted in deriving the Lane transition matrix (6.10). Thus, the spin-orbit fractional-parentage coefficient for a neutron must be of opposite sign to that for the corresponding proton to be consistent with the phase between the direct and charge exchange terms that comes about in the Lane description. The observables are calculated from the resulting total S -matrix as outlined in Sec. 4.5.

6.5 Results of Final State Charge Exchange Calculations

Few photoneutron knockout experiments have been done compared with experiments for photoproton knockout due to the difficulty of detecting the neutron. Most (γ, n) experiments have been done on light targets for energies below 100 MeV; only recently have measurements been made at higher energies. Nevertheless, the available data is sufficient to give an indication of the importance of final state charge exchange.

The result of the (γ, n) calculation with final state charge exchange is shown for the $E_\gamma = 60$ MeV $^{16}\text{O}(\gamma, n)^{15}\text{O}$ reaction in Fig. 42. A Hartree potential is used to determine the bound state wave function. The isoscalar optical potential for the propagating proton is taken to be the parabolic symmetric Woods-Saxon potential of Table 4 that is determined for 50 MeV $p + ^{16}\text{O}$ elastic scattering, again noting that this is an approximation to the $p + ^{15}\text{N}$ optical potential that is actually required. Since this potential is determined for scattering from a nucleus with the same number of protons as neutrons, it must be the isoscalar optical potential. The proton optical potential is used in determining the neutron distorted wave function as well since there is no relevant neutron elastic scattering data to determine a neutron optical potential. This is expected to be a good approximation on the grounds of the charge independence of the strong interaction⁽¹¹²⁾. The isovector optical potential is evaluated microscopically using the prescription of Iqbal *et al.*⁽¹¹⁰⁾, in which the isovector NN amplitudes are folded into appropriate densities for ^{15}N . The ^{15}N densities are determined by subtracting the single-particle $1p_{1/2}$ proton density from the corresponding ^{16}O densities. The single-particle and nuclear densities are both taken from a Hartree calculation for ^{16}O .

It is apparent that the charge exchange amplitude is relatively large compared with the direct mechanism amplitude, especially at backward angles. The inclusion of final state charge exchange is not, however, sufficient to reproduce the data. At backward angles

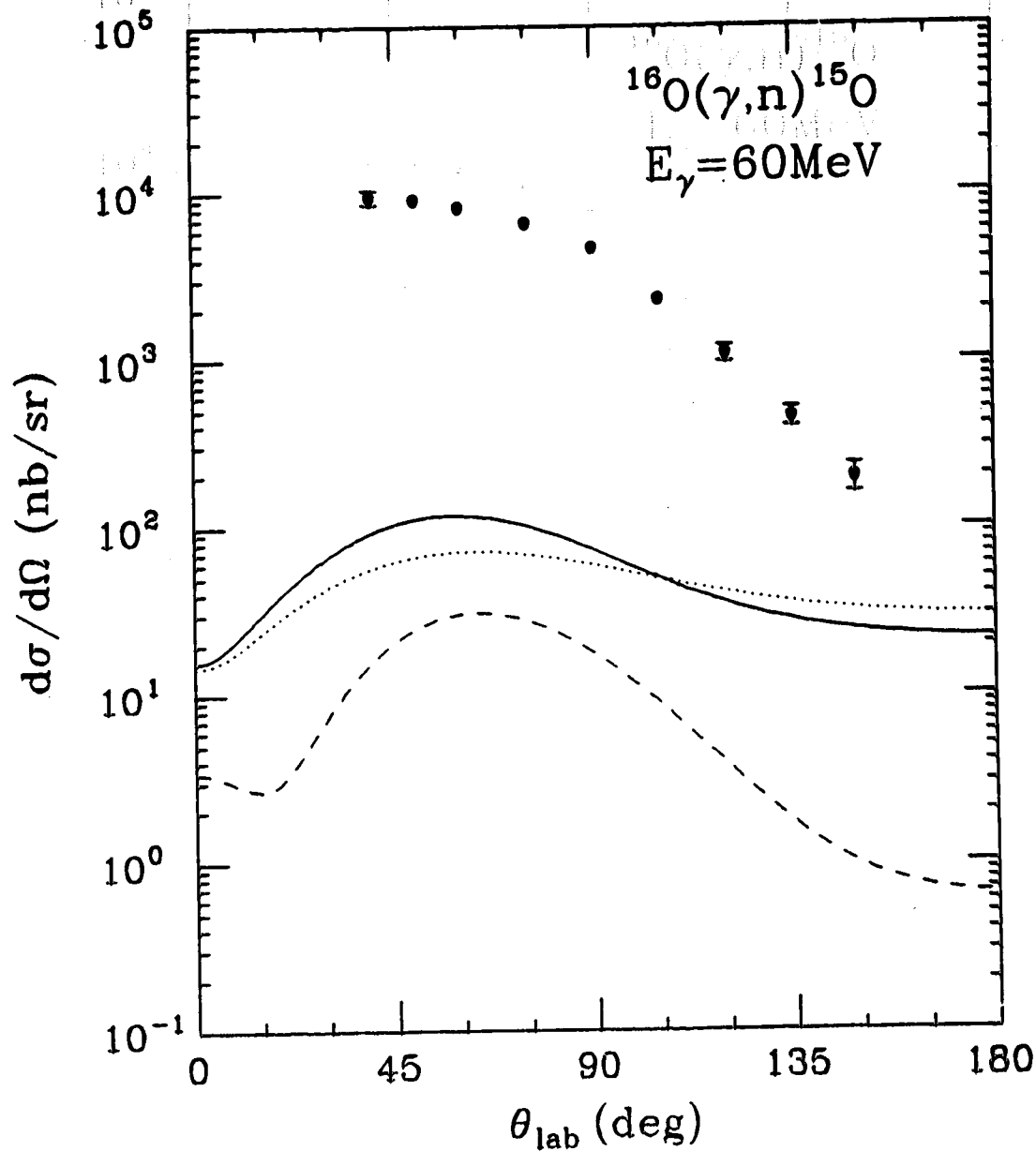


Fig. 42: Final state charge exchange calculations for the differential cross section of the 60 MeV $^{16}\text{O}(\gamma, n)^{15}\text{O}$ reaction in which a Hartree binding potential, phenomenological isoscalar optical potential and microscopic isovector optical potential are used. The dashed curve shows the ONM calculation, the dotted curve shows the charge exchange calculation and the solid curve is the coherent sum. The data are from Ref. 105.

there is an indication that charge exchange could be important. The comparatively large contribution at backward angles is expected since the additional (p,n) reaction will "spread" the outgoing nucleon momentum.

Cross section data for the $^{16}\text{O}(\gamma,n)^{15}\text{O}$ reaction at the higher photon energies $E_\gamma = 150, 200$ and 250 MeV have very recently been measured⁽⁹⁾. Although the error bars are quite large, the data indicates that the (γ,n) cross section is very much the same as the (γ,p) cross section at $E_\gamma = 150$ MeV and actually gets larger than the (γ,p) cross section with increasing energy. The data and calculations for $E_\gamma = 150$ and 200 MeV are shown in Figs. 43 and 44. For both instances a Hartree potential is used in the determination of the bound nucleon wave function and the isovector optical potential is evaluated microscopically. For the 150 MeV calculation the isoscalar optical potential is evaluated microscopically, since there is no corresponding elastic scattering data from which to extract a phenomenological optical potential. For the 200 MeV calculation the isoscalar optical potential is the phenomenological Fourier-Bessel potential for 200 MeV $\vec{p} + ^{16}\text{O}$ elastic scattering that is shown in Fig. 12. The contribution due to the interaction of the photon with the neutron magnetic moment increases with increasing photon energy and this is reflected in the relatively larger direct amplitude compared with the 60 MeV case. At these energies the charge exchange contribution becomes small compared with the direct contribution.

It might be expected that final state charge exchange would be more important for lighter targets since the isovector potentials come into the equations for the proton and neutron radial functions with a $1/A$ dependence. The calculation results for the $^{12}\text{C}(\gamma,n)^{11}\text{C}$ reaction at $E_\gamma = 63$ MeV are shown in Fig. 45. The binding potential used is taken from a Hartree calculation, the magnitude of the fractional-parentage coefficients for the valence nucleons is taken to be unity and the isovector optical potential is evaluated microscopically. The diagonal optical potential used is the Woods-Saxon potential determined for 50 MeV $\vec{p} + ^9\text{Be}$ elastic scattering data that is specified in Table 7. This potential is assumed to be the sum of the isoscalar and the diagonal part of the isovector potential because ^9Be has both the same neutron excess and spin as ^{11}B . The calculations are well below the data as is the case for the $^{16}\text{O}(\gamma,n)^{15}\text{O}$ reaction. The effect of a lighter target nucleus does not affect the results of the charge exchange calculations very much. It is somewhat surprising that the charge exchange contribution is relatively smaller than the direct contribution for the reaction on ^{12}C as compared with

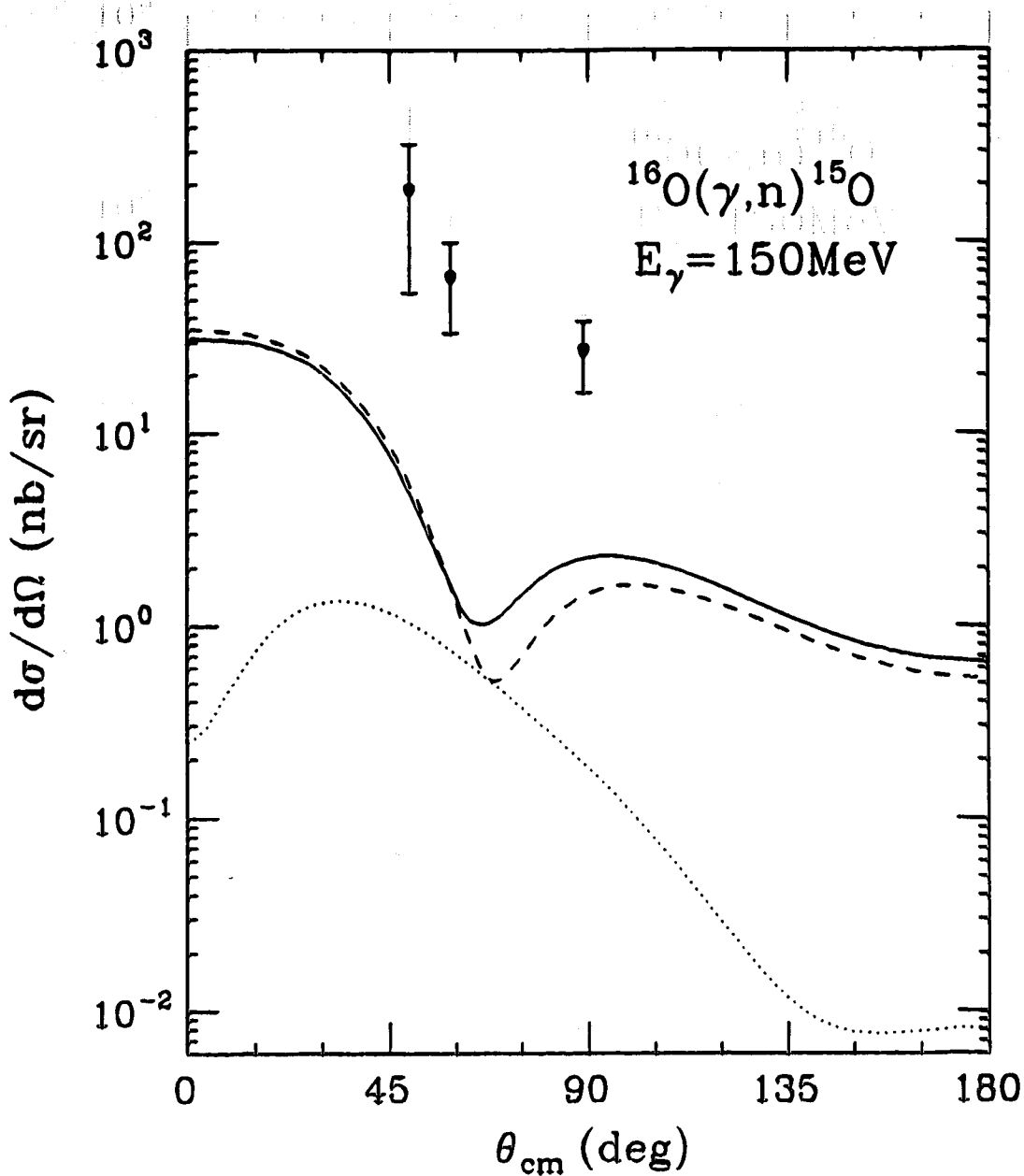


Fig. 43: Final state charge exchange calculations for the differential cross section of the 150 MeV $^{16}\text{O}(\gamma, n)^{15}\text{O}$ reaction in which a Hartree binding potential and microscopic isoscalar and isovector optical potentials are used. The dashed curve shows the ONM calculation, the dotted curve shows the charge exchange calculation and the solid curve is the coherent sum. The data are from Ref. 9.

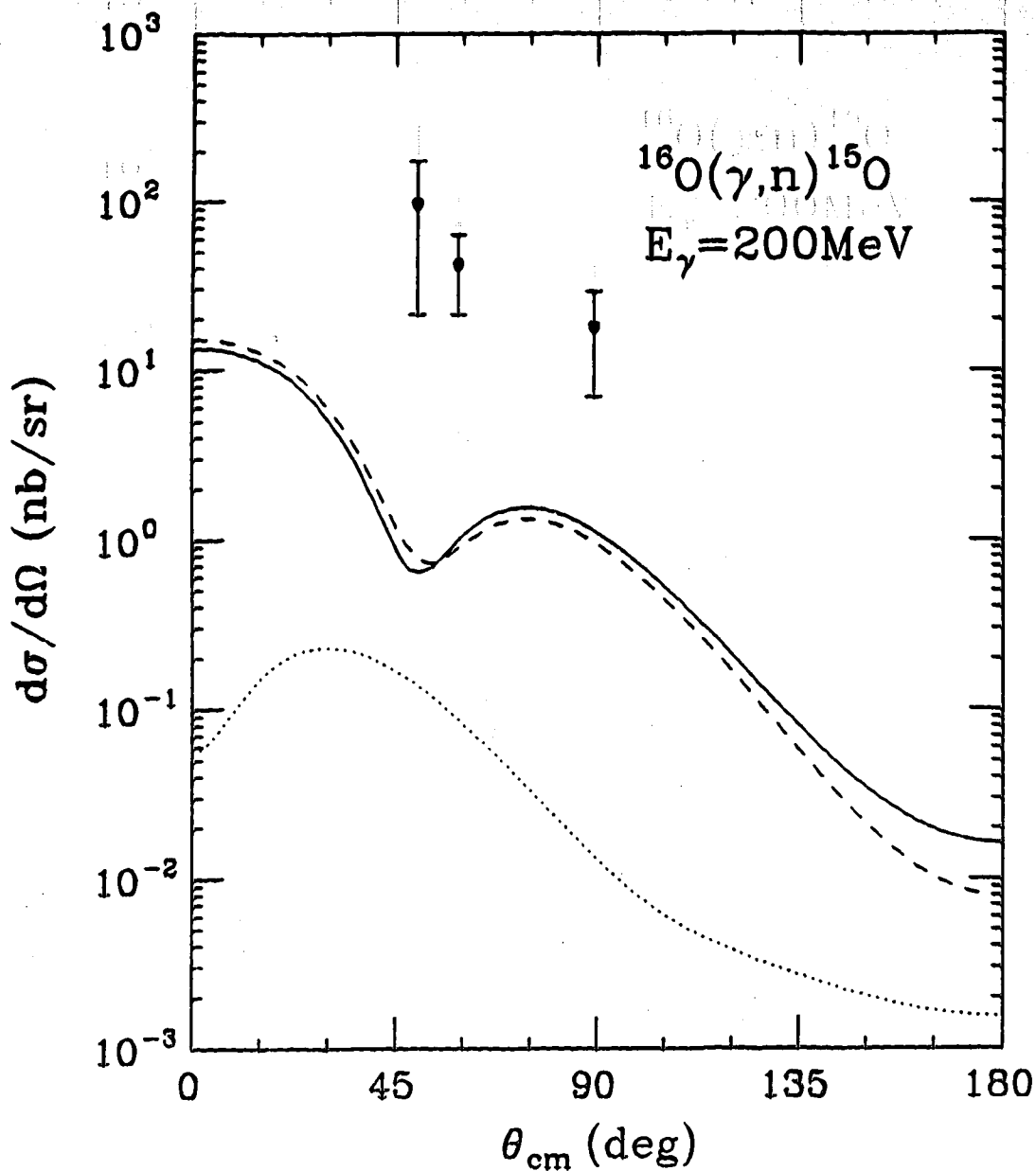


Fig. 44: Final state charge exchange calculations for the differential cross section of the 200 MeV $^{16}\text{O}(\gamma, n)^{15}\text{O}$ reaction in which a Hartree binding potential, phenomenological isoscalar optical potential and microscopic isovector optical potential are used. The dashed curve shows the CNM calculation, the dotted curve shows the charge exchange calculation and the solid curve is the coherent sum. The data are from Ref. 9.

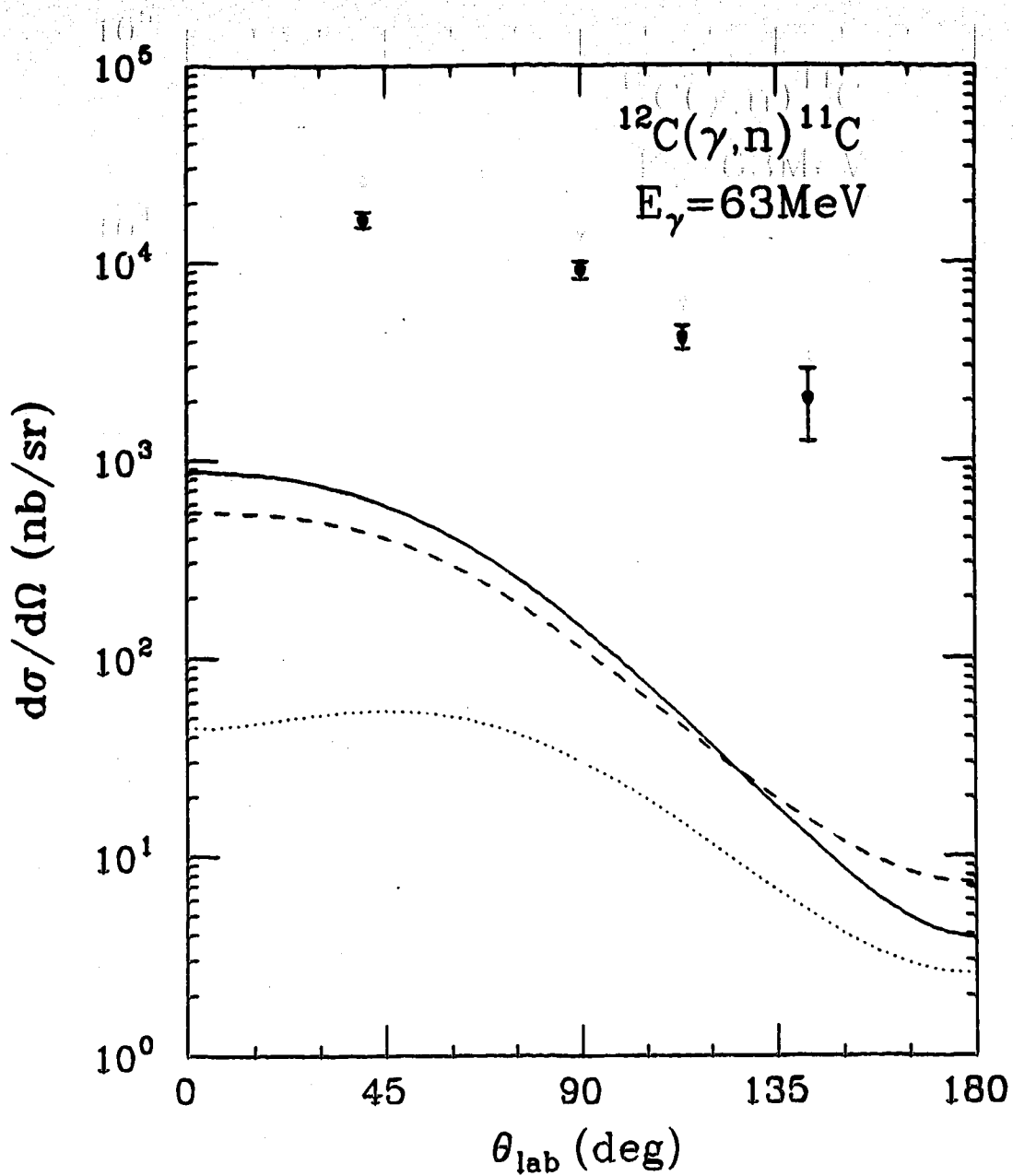


Fig. 45: Final state charge exchange calculations for the differential cross section of the 63 MeV $^{12}\text{C}(\gamma, n)^{11}\text{C}$ reaction in which a Hartree binding potential, phenomenological diagonal optical potential and microscopic isovector optical potential are used. The dashed curve shows the ONM calculation, the dotted curve shows the charge exchange calculation and the solid curve is the coherent sum. The data are from Ref. 106.

^{16}O . This could be due to the nucleon being knocked out of a $1p_{3/2}$ shell in the former case as opposed to it being knocked out of the $1p_{1/2}$ shell in the latter case.

6.6 Discussion

The calculations for final state charge exchange indicate that the addition of this mechanism to the direct mechanism is inadequate to describe the (γ, n) observables. Although the charge exchange channel is significant compared with the direct mechanism, especially for ^{16}O at lower photon energies, it is apparent that other reaction mechanisms must be important for (γ, n) reactions. It remains an open question as to what these mechanisms are. The short-range nucleon-nucleon correlations that are higher-order corrections to the shell model and optical potential descriptions may play a significant role at the energies under consideration. It is expected that a proton will have larger correlations with a neutron rather than another proton because of exclusion arguments. Correlations therefore can lead to an emitted neutron subsequent to the interaction of the photon with a proton and it is expected that this amplitude will be larger than the corresponding one for an emitted proton in much the same way as for charge exchange. Meson exchange current mechanisms are another possibility for explaining the large (γ, n) cross sections. Intuitively, pion exchange and delta isobar photoproduction mechanisms might be thought to contribute the same for (γ, n) and (γ, p) reactions. A detailed calculation of these mechanisms is necessary, however, to determine if this premise is true. The interference between the various meson exchange amplitudes could indeed result in very different contributions for the (γ, n) and (γ, p) reactions.

In order to illustrate the insignificance of the final state charge exchange contribution to a (γ, p) reaction, the results of a calculation for the 60 MeV $^{16}\text{O}(\gamma, p)^{15}\text{N}$ cross section are shown in Fig. 46. The amplitudes are determined using the parabolic Woods-Saxon optical potential described in Table 4 as the isoscalar potential, a microscopic isovector optical potential and a Hartree binding potential. The direct mechanism clearly dominates the amplitude, in contrast to the situation for the parallel 60 MeV $^{16}\text{O}(\gamma, n)^{15}\text{O}$ cross section shown in Fig. 42. This is expected because of the greater likelihood of the photon interacting with a target proton.

The relative importance of final state charge exchange is less at higher energies. This is due to the charge exchange probability decreasing with increasing energy⁽¹¹³⁾ and the spin magnetization current interaction becoming more important. The observation that the

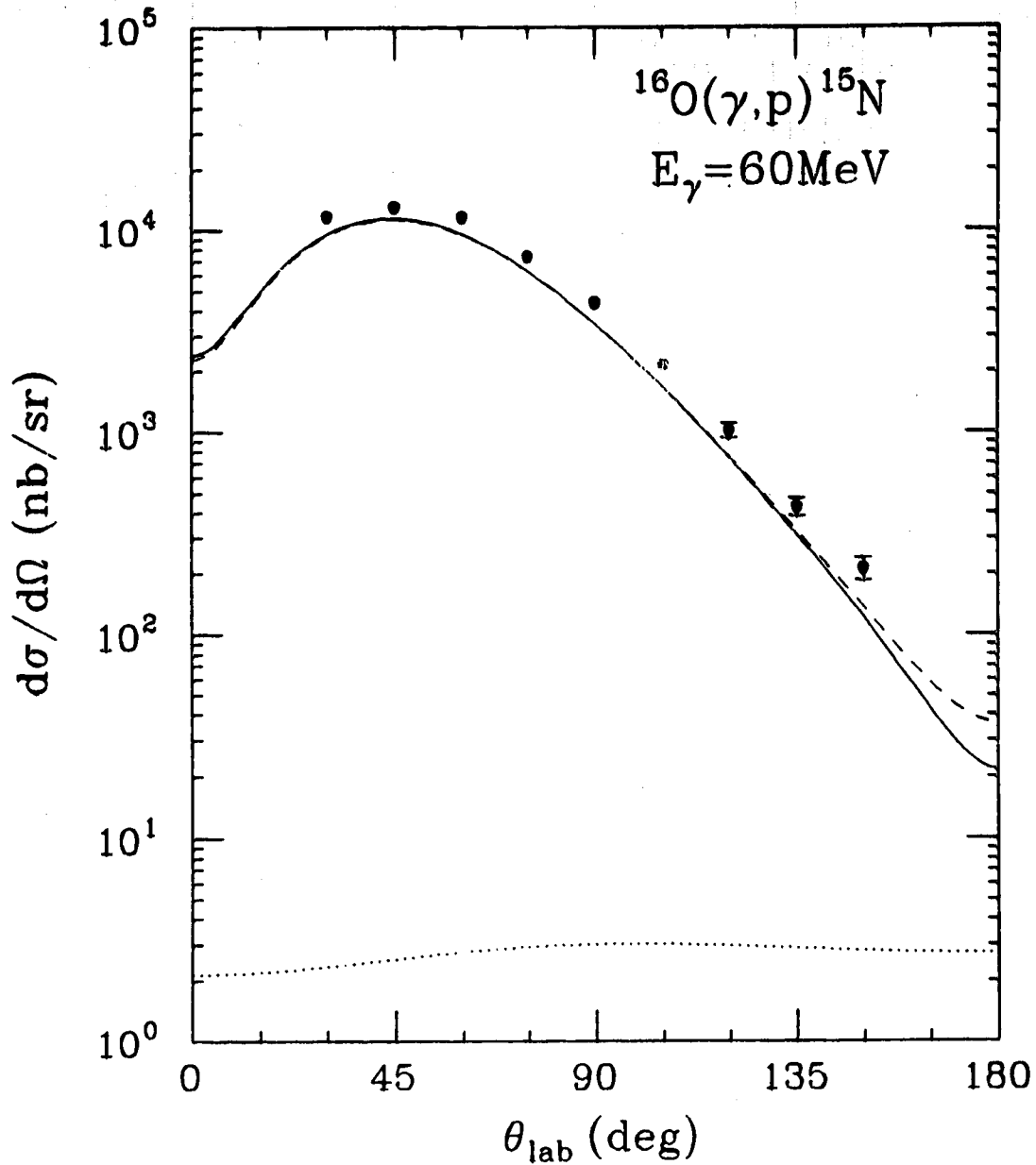


Fig. 46: Final state charge exchange calculations for the differential cross section of the 60 MeV $^{16}\text{O}(\gamma, p)^{15}\text{N}$ reaction in which a Hartree binding potential, phenomenological isoscalar optical potential and microscopic isovector optical potential are used. The dashed curve shows the ONM calculation, the dotted curve shows the charge exchange calculation and the solid curve is the coherent sum. The data are from Ref. 78.

$^{16}\text{O}(\gamma, n)^{15}\text{O}$ cross sections get larger than the corresponding (γ, p) cross sections as the photon energy increases might be a result of the increased contribution of the spin magnetization current interaction adding to whatever other mechanisms are predominantly responsible for (γ, n) reactions.

7. Discussion and Conclusions

The purpose of this thesis has been to investigate photonucleon knockout reactions in a relativistic framework. This research is a logical outgrowth of the recently developed subject of relativistic nuclear physics and is motivated by the large momentum transfer involved and the failure of nonrelativistic calculations to comprehensively describe the available experimental data. Many of the conclusions that can be drawn from the relativistic calculations have been mentioned in the previous two chapters and will not be reiterated here. A general overview of the calculations will be presented and an indication will be given of some of the problems that were not addressed as well as possible direction for further investigation of (γN) reactions.

The One Nucleon Model (ONM) for the direct reaction mechanism involves modelling the interaction of the bound and continuum nucleon with the rest of the nucleons by using relativistic vector and scalar potentials. The model is by-and-large parameter free in the sense that the nucleon wave functions are determined from microscopic theory and/or independent empirical evidence. Only for the bound state wave function determined with Woods-Saxon binding potentials is there any direct parameter input, and care has been taken not to arbitrarily vary these parameters for the sole purpose of fitting the (γp) data. It should be mentioned that somewhat similar relativistic calculations for the direct reaction mechanism have been done independently by McDermott *et al.*⁽¹¹⁴⁾. A comparison of results has been a valuable check of the numerical computations.

The bound nucleon wave function is evaluated through the use of potentials in the Dirac equation that simulate meson exchange processes in the nucleus. It is found that using Woods-Saxon shapes for the binding potentials that are constrained only by the empirical binding energy of the nucleon is inadequate; there are many reasonable choices of potential parameters that give significantly different results for the (γN) observables. Further empirical constraints might give more unique potentials, and this should be investigated further. The ambiguity that exists for wave functions determined from Woods-Saxon potentials suggests that a potential that is determined from a Hartree calculation⁽³⁶⁾ is preferred. Reservations exist also for the high momentum components of the resulting wave function but since the relativistic Hartree approximation is based on

the fundamental meson exchanges that mediate the nucleon-nucleon force it might be reasonable that the description is accurate even beyond the momentum transfer region for which the parameters of the calculation are fixed. Refinements of the Hartree approximation such as taking into account the polarization of the vacuum⁽⁸⁵⁾ or including the Fock term⁽⁸⁶⁾ might be important for the high momentum behaviour of the wave function. It would be desirable to have the computations for these effects consolidated so that they could be applied to the (γN) calculations with confidence. In any case, the hope of securing spectroscopic information from photonucleon knockout has proved to be elusive. The reaction is indeed very sensitive to the high momentum components of the bound nucleon wave function as is expected, but ambiguity exists in the determination of this wave function that renders the results somewhat inconclusive. A better idea of the high momentum behaviour of the wave function might be realizable when the other mechanisms that are important for the reaction are examined.

The interaction of the emitted nucleon with the residual nucleus is approximated by complex scalar and vector potentials and this distortion of the wave function is found to be very important for the description of the data. In this sense the ONM label for the reaction is to some extent misleading since the other nucleons are involved through the optical potential. The ONM designation actually means that a second nucleon is not explicitly included microscopically. The optical potentials are either taken from phenomenological proton elastic scattering analyses⁽⁴²⁾ or are determined from microscopic calculations that fold the nucleon-nucleon potential into Hartree nuclear densities⁽⁵⁴⁾. A better description of the proton elastic scattering data ensues from phenomenological potentials and hence these are deemed to give a more realistic continuum nucleon wave function. Unfortunately, there is not always elastic scattering data corresponding to the (γN) experiments that have been done. Relativistic global optical potentials would be very desirable for such situations, especially for the ^{16}O nucleus which is the most common (γN) target.

Although there are a range of results corresponding to various choices of binding and distorting potentials, the One Nucleon Model is deemed to be in good accord with most of the experiments for (γp) reactions; the (γp) data at lower momentum transfers consistently falls within the area defined by the calculations. It is encouraging that the agreement with the (γp) data is almost invariably most favorable for the "best" potentials; the optical potentials that best describe the proton elastic scattering data also

give the best (γp) results and there is a similar indication for the binding potentials that give good agreement with a range of nuclear characteristics. The success of the calculations with realistic potentials for a variety of nuclei and for a range of incident energies really gives credibility to the One Nucleon Model and suggests that investigating (γp) reactions with this model can, in conjunction with other high momentum transfer reactions such as (p, π) and $(e, e'p)$, lead to a better description of the nucleon wave functions involved.

The results of the relativistic ONM calculations are especially interesting when contrasted to the corresponding nonrelativistic calculations^(19,21,28). The ONM results are qualitatively similar to the results of the rigorous nonrelativistic calculations for the direct mechanism, but are significantly closer to the data at higher momentum transfers. Furthermore, the ONM results cast doubt on some of the nonrelativistic investigations^(15,25) that conclude that the direct reaction mechanism is relatively unimportant for (γp) reactions. Although the specific relativistic features that might account for the favorable ONM results have not been investigated in detail, for example by doing a nonrelativistic reduction of the relativistic amplitude, it is felt that in general the relativistic wave functions are responsible. The relevance of doing a relativistic calculation is attested to by the observation that the predominant terms in the amplitude involve the lower component of one of the relativistic nucleon spinors.

In the process of formulating a workable model for (γN) reactions by making simplifying approximations some of the original features of the theory are necessarily abandoned. Most obviously, the use of potentials in the Dirac equation rather than the full meson field operators surrenders the relativistic covariance of the theory. Furthermore, the use of different potentials for the bound and continuum nucleon forgoes wave function orthogonality. It has been mentioned that this is a consequence of restricting the calculation to one reaction channel and is necessary to obtain realistic nucleon wave functions. Orthogonalizing the wave functions using a Gram-Schmidt procedure such as has been done for the nonrelativistic wave functions⁽²⁶⁾ is not expected to have a large effect. Related to the problem of wave function orthogonality is the lack of gauge invariance of the interaction. The requirement of gauge invariance is that under the transformation

$$A^\mu \rightarrow A^\mu + \partial^\mu \chi \quad (7.1)$$

there is no change in physical quantities⁽¹¹⁵⁾, which means that the scattering matrix should remain invariant. Under the gauge transformation (7.1) the S -matrix for the minimal electromagnetic coupling becomes

$$S = -e \int \bar{\psi} \gamma^\mu \phi A_\mu d^4x \rightarrow -e \int \bar{\psi} \gamma^\mu \phi A_\mu d^4x - e \int \bar{\psi} \gamma^\mu \phi \partial_\mu \chi d^4x . \quad (7.2)$$

The last term should be zero for gauge invariance to hold. Integrating this term by parts and noting that the surface term vanishes leaves the integral

$$e \int \partial_\mu [\bar{\psi} \gamma^\mu \phi] \chi d^4x .$$

The derivative of the quantity in the square brackets can be reexpressed using the Dirac equations

$$[i\gamma^\mu \partial_\mu - m - S - \gamma^0 V] \psi \equiv [i\gamma^\mu \partial_\mu - \Sigma] \psi = 0 \quad (7.3a)$$

$$[i\gamma^\mu \partial_\mu - m - S' - \gamma^0 V'] \phi \equiv [i\gamma^\mu \partial_\mu - \Sigma'] \phi = 0 \quad (7.3b)$$

for the continuum and bound nucleon (the primes indicate that the quantities are different from the unprimed quantities) as

$$\partial_\mu [\bar{\psi} \gamma^\mu \phi] = i \bar{\psi} [\Sigma^* - \Sigma'] \phi . \quad (7.4)$$

This quantity is nonzero by virtue of the unlike potentials and so gauge invariance does not hold. The interaction of the photon with the nucleon anomalous magnetic moment is trivially gauge invariant, on the other hand. The way to address the problem of the gauge invariance is not clear. Perhaps nothing can be done without sacrificing the realistic wave functions that come about by using distinct potentials for the bound and continuum nucleon.

A problem that is related to the magnetic moment interaction is that Dirac calculations for the nuclear magnetic moments which involve using the same electromagnetic interaction Hamiltonian used in the ONM do not reproduce the experimental values^(116,117). This has been solved to some extent by considering "backflow" corrections⁽¹¹⁸⁾, which take into account the response of the spectator core to the single-particle motion. These have not been included in the ONM calculations and it would

perhaps be worthwhile to do so, although it is not clear how to do this for the large momentum transfers involved in the reactions. The contribution of the magnetic moment interaction is small compared with the charge interaction for (γ,p) reactions which suggests that the backflow correction likely will be small.

A more general problem of relativistic calculations that is related to the structure of the Dirac equation itself and not the ONM is that the center-of-mass motion cannot be separated from the relative motion. This deficiency is not considered to be very serious because the targets considered are relatively heavy. Calculations that estimate the effect of a finite mass target^(101,102) show very little sensitivity to the nuclear recoil, although there seems to be some disagreement over how to incorporate recoil corrections consistently.

The inadequacies that are evident in a comparison of the ONM predictions with experimentally measured observables are the consistent underprediction of the (γ,p) data at high momentum transfers and the complete failure to account for the (γ,n) data. The underestimation of the high q data seems to indicate, as expected, that at some point reaction mechanisms that involve two nucleons sharing the momentum mismatch between the photon and the emitted nucleon will predominate. The ONM calculations suggest in which momentum transfer region this will occur, although a really good indication will come only through actually doing calculations for other reaction mechanisms. The similar magnitude of the (γ,n) and (γ,p) cross sections represents a more confounding observation for the ONM; it is not clear why a direct reaction mechanism is principally responsible for (γ,p) reactions, whereas other mechanisms give rise to (γ,n) events. Most of the likely nondirect mechanisms involve meson exchanges that are similar for protons and neutrons since the strong interaction is symmetric in the two types of nucleons. There are, however, plausible contributions that will be more significant for the (γ,n) amplitude such as the inclusion of nucleon-nucleon correlations and charge exchange of the emitted nucleon subsequent to the direct interaction.

In an attempt to address the large (γ,n) cross sections, the contribution of charge exchange following proton photoemission has been investigated. The charge exchange is mediated by an isovector potential that is determined from microscopic calculations⁽¹¹⁰⁾. The addition of the charge exchange has not been found to substantially improve the agreement of the calculation with the data, although it can contribute on the same level as the direct mechanism. A shortcoming of the charge exchange calculation is the uncertainty

that exists for the isovector potential since (γ, n) data corresponding to the relevant nuclear targets and energies does not exist, the reliability of the microscopic calculations must be indirectly inferred from the adequacy of similar microscopic calculations for the isoscalar potential and from the description of quite different charge exchange data. The evidence suggests that the microscopic isovector potentials are reasonable and the inaccuracies certainly would not affect the calculation to the extent that is required to give agreement with the (γ, n) data. Final state charge exchange is not the reason for the observed (γ, n) cross sections.

The aforementioned deviations of the ONM with the (γ, N) data are felt to be indications of additional physics coming into play. Although there are problems, the encouraging results of the ONM suggest that the direct mechanism is described well by the model. In this sense the (γ, N) reaction remains a potentially interesting source of information about some aspects of nuclear dynamics; the (γ, n) reaction especially seems to be very sensitive to processes such as nucleon-nucleon correlations and meson exchange currents that are difficult to extract information about from other nuclear reactions. The exploration of the direct reaction mechanism in a relativistic framework that is the subject of this thesis is an essential forerunner to investigating correlations and meson exchange currents. Such investigations have not yet been done thoroughly in a relativistic model and hence it would be very interesting to proceed in this direction. One calculation that includes pion exchange has been attempted⁽¹¹⁴⁾ but the details have not been published.

Relativistic calculations of meson exchange current mechanisms for photonucleon knockout reactions have some compelling rationale. Primarily, meson exchanges between nucleons are fundamentally described by a relativistic field theory, and not by the Schrödinger equation. The meson-nucleon vertices are given by well-established principles in a relativistic description whereas uncertainties may exist for the corresponding nonrelativistic vertices. This is especially apparent for the πNN vertex that is the most important for the meson exchange current mechanisms and is not well-established nonrelativistically⁽¹⁻³⁾. The $\gamma N\Delta$ and $\pi N\Delta$ couplings are also straightforward in principle in a relativistic model. A relativistic description of reaction mechanisms involving the delta isobar would be very interesting because of the spin-3/2 nature of the delta. The covariant dynamical equation that a noninteracting spin-3/2 field satisfies is⁽¹¹⁹⁾

$$(i\gamma^\mu \partial_\mu - m) \psi_\nu = 0 \quad (7.5a)$$

with the supplementary conditions

with the supplementary conditions

$$\gamma^\nu \psi_\nu = 0 \quad (7.5b)$$

$$\partial^\nu \psi_\nu = 0 \quad (7.5c)$$

The vector index on ψ indicates that there are four separate four-component spinors that make up the field. The supplementary conditions reduce the number of independent components from sixteen to eight. Now the delta isobar actually propagates in the nuclear medium. The interaction of the delta isobar with the nucleus is an outstanding problem that could be addressed in the calculation of delta mechanisms for (γN) reactions. The purpose of showing these field equations is to stress the difference between a relativistic delta wave function and a Schrödinger delta wave function. The spin is intrinsic in the relativistic description whereas it is put in by hand in a nonrelativistic treatment. In fact this is also the case for nucleons; that the Dirac equation is the dynamical equation for spin-1/2 particles commends its use in nuclear physics.

The calculations for reaction mechanisms that involve two nucleons will be more complicated than the ONM calculations. However, many of the details, such as the nucleon wave functions for example, will be directly taken over from the ONM. Furthermore, the rather elegant method of evaluating the transition matrix for the final state charge exchange process could be applied to meson exchange and correlation calculations since all of these are essentially two-step processes that involve some intermediate propagating particle. The additional reaction mechanisms are definitely worth investigating. Further theoretical and experimental work for photonucleon knockout reactions undoubtedly has the potential of elucidating more interesting physics of the nucleus.

References

1. H.W. Fearing, in: *Progress in Particle and Nuclear Physics*, (D. Wilkinson, ed.), Vol. 7, p. 113, Pergamon Press, Toronto (1981).
2. D.F. Measday and G.A. Miller, *Ann. Rev. Nucl. Part. Sci.* **29**, 121 (1979).
3. E.D. Cooper and H.S. Sherif, *Phys. Rev. C* **30**, 232 (1984).
4. M.J. Leitch, J.L. Matthews, W.W. Sapp, C.P. Sargent, S.A. Wood, D.J.S. Findlay, R.O. Owens and B.L. Roberts, *Phys. Rev. C* **31**, 1633 (1985).
5. R.A. Schumacher, J.L. Matthews, W.W. Sapp, R.S. Turley, G.S. Adams and R.O. Owens, *Phys. Rev. C* **33**, 50 (1986).
6. P.D. Harty, M.N. Thompson, G.J. O'Keefe, R.P. Rassool, K. Mori, Y. Fujii, T. Suda, I. Nomura, O. Konno, T. Terasawa and Y. Torizuka, *Phys. Rev. C* **37**, 13 (1988).
7. A.C. Shotter, S. Springham, D. Branford, J. Yorkston, J.C. McGeorge, B. Schoch and P. Jennewein, *Phys. Rev. C* **37**, 1354 (1988).
8. E. De Sanctis, M. Anghinolfi, G.P. Capitani, P. Corvisiero, P. Di Giacomo, C. Guaraldo, V. Lucherini, E. Polli, A.R. Reolon, G. Ricco, M. Sanzone and A. Zucchiatti, *Phys. Rev. C* **34**, 413 (1986).
9. E.J. Beise, G. Dodson, M. Garçon, S. Høibråten, C. Maher, L.D. Pham, R.P. Redwine, W. Sapp, K.E. Wilson, S.A. Wood and M. Deady, *Phys. Rev. Lett.* **62**, 2593 (1989).
10. E.D. Cooper, Ph.D. Thesis, University of Alberta (1981), unpublished.
11. B.D. Serot and J.D. Walecka, *Advances in Nuclear Physics* (J.W. Negele and E. Vogt, eds.), Vol. 16, Plenum Press, New York (1986).
12. J.D. Bjorken and S.D. Drell, *Relativistic Quantum Mechanics*, McGraw-Hill, New York (1964).
13. M.M. Giannini, in: *Proceedings of the Fifth Course of the International School of Intermediate Energy Nuclear Physics* (R. Bergere, S. Costa and C. Schaerf, ed.), p. 97, Verona, Italy (1985).
14. J.T. Londergan, in: *Pion Production and Absorption in Nuclei - 1981* (R.D. Bent, ed.), AIP Conference Proceedings No. 79, p. 339, American Institute of Physics, New York (1981).

15. B. Schoch, *Phys. Rev. Lett.* **41**, 80 (1978).
16. F. Partovi, *Ann. Phys.* **27**, 79 (1964).
17. R. Kose, W. Paul, K. Stockhorst and K.H. Kissler, *Z. Phys.* **202**, 364 (1967).
18. Katsuyuki Ebisawa, Ph. D. Thesis, University of Washington (1978), unpublished.
19. S. Boffi, C.Giusti and F.D. Pacati, *Nucl. Phys.* **A359**, 91 (1981).
20. J.T. Londergan and L.D. Ludeking, *Phys. Rev. C* **25**, 1722 (1982).
21. J.T. Londergan and G.D. Nixon, *Phys. Rev. C* **19**, 998 (1979).
22. S. Boffi, F. Capuzzi, C.Giusti and F.D. Pacati, *Nucl. Phys.* **A436**, 438 (1981).
23. J. Ryckebusch, M. Waroquier, K. Heyde and D. Ryckbosch, *Phys. Lett.* **194B**, 453 (1987).
24. C.Y. Cheung and B.D. Keister, *Phys. Rev. C* **33**, 776 (1986).
25. M. Gari and H. Hebach, *Phys. Rep.* **72**, 1 (1981).
26. S. Boffi, F. Cannata, F. Capuzzi, C.Giusti and F.D. Pacati, *Nucl. Phys.* **A379**, 509 (1982).
27. J. Ryckebusch, M. Waroquier, K. Heyde, J. Moreau and D. Ryckbosch, *Nucl. Phys.* **A476**, 237 (1988).
28. R.S. Turley, E.R. Kinnee, J.L. Matthews, W.W. Sapp, E.J. Scheidker, R.A. Schumacher, S.A. Wood, G.S. Adams and R.O. Owens, *Phys. Lett.* **157B**, 19 (1985).
29. R.S. Turley, Ph. D. Thesis, Massachusetts Institute of Technology (1984), unpublished.
30. A.E.S. Green and T. Sawada, *Nucl. Phys.* **B2**, 276 (1967) and *Rev. Mod. Phys.* **39**, 594 (1967).
31. K. Erkelenz, *Phys. Rep.* **C13**, 191 (1974).
32. K. Holinde, *Phys. Rep.* **C68**, 121 (1981).
33. R. Vinh Mau, in: *Mesons in Nuclei* (M. Rho and D.H. Wilkinson, eds.), Vol. 1, p. 151, North-Holland, Amsterdam (1979).
34. H. Goldstein, *Classical Mechanics*, Addison-Wesley, Reading, Mass. (1950).
35. J.D. Walecka, *Ann. Phys.* **83**, 491 (1974).
36. C.J. Horowitz and B.D. Serot, *Nucl. Phys.* **A368**, 503 (1986).

37. A.K. Kerman, H. McManus and R.M. Thaler, *Ann. Phys.* **8**, 551 (1959).
38. B.C. Clark, S. Hama and R.L. Mercer, in: *The Interaction Between Medium Energy Nucleons in Nuclei-1982* (H.O. Meyer, ed.), AIP Conference Proceedings No. 97, p. 260, American Institute of Physics, New York (1983).
39. L.G. Arnold, B.C. Clark, R.L. Mercer and P. Schwandt, *Phys. Rev. C* **23**, 1949 (1981).
40. S.J. Wallace, in: *Annual Review of Nuclear and Particle Science* (J.D. Jackson, H.E. Gove and R.F. Schwitters, ed.), Vol. 37, Annual Reviews Inc., Palo Alto, Calif. (1987).
41. B.C. Clark, S.G. Klübermann, E.D. Cooper and R.L. Mercer, *Phys. Rev. C* **31**, 694 (1985).
42. A.M. Kobos, E.D. Cooper, J.I. Johansson and H.S. Sherif, *Nucl. Phys.* **A445**, 605 (1985).
43. H.S. Sherif, R.I. Sawafta and E.D. Cooper, *Nucl. Phys.* **A449**, 709 (1986).
44. J.I. Johansson, E.D. Cooper and H.S. Sherif, *Nucl. Phys.* **A476**, 663 (1988).
45. E.D. Cooper and H.S. Sherif, *Phys. Rev. Lett.* **47**, 818 (1981) and *Phys. Rev. C* **25**, 3024 (1982).
46. J.A. McNeil, L. Ray and S.J. Wallace, *Phys. Rev. C* **27**, 2123 (1983).
47. J.A. McNeil, J.R. Shepard and S.J. Wallace, *Phys. Rev. Lett.* **50**, 1439 (1983).
48. J.R. Shepard, J.A. McNeil, and S.J. Wallace, *Phys. Rev. Lett.* **50**, 1443 (1983).
49. J.A. Tjon and S.J. Wallace, *Phys. Rev. Lett.* **54**, 1357 (1985).
50. L.S. Celenza, A. Harindranath and C.M. Shakin, *Phys. Rev. C* **31**, 63 (1985).
51. B.C. Clark, S. Hama, J.A. McNeil, R.L. Mercer, L. Ray, G.W. Hoffman, B.D. Serot, J.R. Shepard and S.J. Wallace, *Phys. Rev. Lett.* **51**, 1808 (1983).
52. B.C. Clark, S. Hama, R.L. Mercer, L. Ray and B.D. Serot, *Phys. Rev. Lett.* **50**, 1644 (1983).
53. C.J. Horowitz and D. Murdock, *Phys. Lett.* **168B**, 31 (1986).
54. D.P. Murdock and C.J. Horowitz, *Phys. Rev. C* **35**, 1442 (1987).

54. C.J. Horowitz and B.D. Serot, *Nucl. Phys. A* **461**, 611 (1987).
55. C.J. Horowitz and B.D. Serot, *Nucl. Phys. A* **464**, 613 (1987).
56. J.A. Tjon and S.J. Wallace, *Phys. Rev. C* **32**, 267 (1985).
57. E.E. van Faasen and J.A. Tjon, *Phys. Rev. C* **28**, 2354 (1983).
58. E.E. van Faasen and J.A. Tjon, *Phys. Rev. C* **30**, 285 (1984).
59. G.R. Satchler, *Direct Nuclear Reactions*, Oxford, New York (1983).
60. J.D. Jackson, *Classical Electrodynamics*, 2nd edition, Wiley, New York (1975).
61. M.E. Rose, *Elementary Theory of Angular Momentum*, Wiley, New York (1957).
62. N.K. Glendenning, *Direct Nuclear Reactions*, Academic, New York (1983).
63. R. Sawafta, M.Sc. Thesis, University of Alberta (1984), unpublished.
64. M.J. Leitch, F.C. Lin, J.L. Matthews, W.W. Sapp, C.P. Sargent, D.J.S. Findlay, R.O. Owens and B.C. Roberts, *Phys. Rev. C* **33**, 1511 (1986).
65. A. Bohr and B.R. Mottleson, *Nuclear Structure*, Benjamin, New York (1969).
66. J.D. Bjorken and S.D. Drell, *Relativistic Quantum Fields*, McGraw-Hill, New York (1965).
67. S. Schweber, H. Bethe and F. de Hoffmann, *Mesons and Fields*, Row-Peterson, Evanston, Illinois (1955).
68. B.A. Lippmann and J. Schwinger, *Phys. Rev.* **79**, 469 (1949).
69. D.F. Jackson, in: *Advances in Nuclear Physics* (M. Baranger and E. Vogt, ed.), Plenum Press, New York (1971).
70. J. Johansson, M.Sc. Thesis, University of Alberta (1987), unpublished.
71. S. Cohen and D. Kurath, *Nucl. Phys. A* **101**, 1 (1967).
72. C.W. Glover, P. Schwandt, H.O. Meyer, W.W. Jacobs, J.R. Hall, M.D. Kaitchuck and R.P. Devito, *Phys. Rev. C* **31**, 1 (1985).
73. E.D. Cooper, private communication.
74. I. Sick and J.S. McCarthy, *Nucl. Phys. A* **150**, 631 (1970).
75. E.D. Cooper, private communication.
76. R.L. Varner, T.B. Clegg, T.L. McAbee and W.S. Thompson, *Phys. Lett.* **185B**, 6 (1987).
77. G.S. Adams, E.R. Kinney, J. L. Matthews, W.W. Sapp, T. Soos, R.O. Owens, R.S. Turley and G. Pignault, to be published in *Phys. Rev. C*.

78. D.J.S. Findlay and R.O. Owens, *Nucl. Phys.* **A279**, 385 (1977).
79. F.A. Fannon, E.J. Burge and D.A. Smith, *Nucl. Phys.* **A97**, 263 (1967).
80. A.J. Houdayer, T.Y. Li and S.K. Mark, *Can. J. Phys.* **48**, 765 (1970).
81. E.D. Cooper, B.C. Clark, S. Hama and R.L. Mercer, *Phys. Lett.* **206B**, 588 (1988) [*Erratum: Phys. Lett.* **220B**, 658 (1989)].
82. E.D. Cooper, B.C. Clark, R. Kozack, S. Shim, S. Hama, J.I. Johansson, H.S. Sherif, R.L. Mercer and B.D. Serot, *Phys. Rev. C* **36**, 2170 (1987).
83. S. Platchkov, A. Amroun, P. Bricault, J.M. Cavedon, P.K.A. de Witt Huberts, P. Dreux, B. Frois, C.D. Goodman, D. Goutte, J. Martino, V. Meot, G.A. Peterson, X.H. Phan, S. Raman and I. Sick, *Phys. Rev. Lett.* **61**, 1465 (1988).
84. R.S. Hicks, *Phys. Rev. C* **25**, 695 (1982).
85. C.J. Horowitz and B.D. Serot, *Phys. Lett.* **140B**, 181 (1984).
86. P.G. Blunden and M.J. Iqbal, *Phys. Lett.* **196B**, 295 (1987).
87. P.G. Blunden and M.J. Iqbal, to be published.
88. M. Nomachi, T. Shibata, K. Okada, T. Motobayashi, F. Ohtani, H. Ejira and T. Kishimoto, *Phys. Rev. C* **31**, 242 (1985).
89. H.J. Hausman, S.L. Blatt, T.R. Donoghue, J. Kalen, W. Kim, D.G. Marchlinski, T.W. Rackers, P. Schmalbrock, M.A. Kovash and A.D. Bacher, *Phys. Rev. C* **37**, 503 (1988).
90. G.S. Mani, D. Jacques and A.D.B. Dix, *Nucl. Phys.* **A165**, 145 (1971).
91. R.M. Craig, J.C. Dore, G.W. Greenlees, J. Lowe and D.L. Watson, *Nucl. Phys.* **A83**, 493 (1966).
92. J.A. Fannon, E.J. Burge and D.A. Smith, *Nucl. Phys.* **A93**, 263 (1967).
93. J. Thekkumthala, J.M. Cameron, C.A. Davis, P. Kitching, J. Pasos, J. Soukup, J. Uegaki, H.S. Wilson, R. Abegg, D.A. Hutcheon, C.A. Miller, A.W. Stetz and A.H. Hussein, *Nucl. Phys.* **A455**, 687 (1986).
94. D.K. Hasell, A. Bracco, H.P. Gubler, W.P. Lee, W.T.H. van Oers, R. Abegg, D.A. Hutcheon, C.A. Miller, J.M. Cameron, L.G. Greeniaus, G.A. Moss, M.P. Epstein and D.J. Margaziotis, *Phys. Rev. C* **34**, 236 (1986).
95. G.A. Moss, L.G. Greeniaus, J.M. Cameron, D.A. Hutcheon, R.L. Liljestrang, C.A. Miller, G. Roy, B.K.S. Koene, W.T.H. van Oers, A.W. Stetz, A. Willis and N. Willis, *Phys. Rev. C* **21**, 1932 (1980).

96. H.S. Sherif, M.S. Abdelmonem and R.S. Sloboda, *Phys. Rev. C* **27**, 2759 (1983).
97. H.S. Sherif and M.S. Abdelmonem, *Phys. Rev. C* **36**, 1900 (1987).
98. H.S. Sherif and M.S. Abdelmonem, private communication.
99. J.P. Didelez, H. Langevin-Joliot, N. Bijedic and Z. Maric, *Nouvo Cimento* **67A**, 388 (1970).
100. J. Arends, J. Eyink, A. Hegerath, H. Hartmann, B. Mecking, G. Nöldeke and H. Rost, *Nucl. Phys.* **A322**, 253 (1979).
101. N.A. Ottenstein, J. Sabutis and S.J. Wallace, *Phys. Rev. C* **35**, 369 (1987).
102. E.D. Cooper and B.K. Jennings, to be published.
103. H.Göringer and B. Schoch, *Phys. Lett.* **97B**, 41 (1980).
104. B. Schoch and H.Göringer, *Phys. Lett.* **109B**, 11 (1982).
105. H.Göringer, B. Schoch and G. Lührs, *Nucl. Phys.* **A384**, 414 (1982).
106. H. Schier and B. Schoch, *Nucl. Phys.* **A229**, 93 (1974).
107. M.R. Sené, I. Anthony, D. Branford, A.G. Flowers, A.C. Shotter, C.H. Zimmerman, J.C. McGeorge, R.O. Owens and P.J. Thorley, *Phys. Rev. Lett.* **50**, 1831 (1983).
108. M.R. Sené, I. Anthony, D. Branford, A.G. Flowers, A.C. Shotter, C.H. Zimmerman, J.C. McGeorge, R.O. Owens and P.J. Thorley, *Nucl. Phys.* **A442**, 215 (1985).
109. B.C. Clark, S. Hama, E. Sugarbaker, M.A. Franey, R.L. Mercer, L. Ray, G.W. Hoffmann and B.D. Serot, *Phys. Rev. C* **30**, 314 (1984).
110. M.J. Iqbal, J.I. Johansson, S. Hama and H.S. Sherif, *Nucl. Phys.* **A487**, 626 (1988).
111. A.M. Lane, *Nucl. Phys.* **35**, 676 (1962).
112. S. DeBenedetti, *Nuclear Interactions*, Wiley, New York (1964).
113. C.D. Goodman, in: *The (p,n) Reaction and the Nucleon-Nucleon Force*, (C.D. Goodman, S.M. Austin, S.D. Bloom, J. Rapaport and G.R. Satchler, ed.), p. 149, Wiley, New York (1979).
114. J. F. McDermott, E. Rost, J.R. Shepard and C.Y. Cheung, *Phys. Rev. Lett.* **61**, 814 (1988).
115. I.J.R. Aitchinson and A.J.G. Hay, *Gauge Theories in Particle Physics*, Adam Hilger, Bristol (1982).

116. L.D. Miller, *Ann. Phys.* **91**, 40 (1975).
117. A. Bouyssy, S. Marcos and J.-F. Mathiot, *Nucl. Phys.* **A415**, 497 (1984).
118. J.A. MacNeil, R.D. Amado, C.J. Horowitz, M. Oka, J.R. Shepard and D.A. Sparrow, *Phys. Rev. C* **34**, 746 (1984).
119. Y. Takahashi, *An Introduction to Field Quantization*, Pergamon, Oxford (1969).
120. Particle Data Group, *Particle Properties Data Booklet*, North Holland, Amsterdam (1986).
121. B.V. Numerov, *Mont. Not. R. Astron. Soc.* **84**, 592 (1924).
122. J.M. Blatt, *J. Comp. Phys.* **1**, 382 (1967).
123. J. Raynal, *Optical Model and Coupled Channel Calculations in Nuclear Physics*, Trieste, 1971 and IAEA, Vienna, 1972.
124. A.E. Thorlacius and E.D. Cooper, *J. Comp. Phys.* **72**, 70 (1987).
125. M. Abramowitz and I.A. Stegun (editors), *Handbook of Mathematical Functions*, National Bureau of Standards Applied Mathematics Series 55, U.S. Department of Commerce (1964).
126. J. Comfort, in computer code COMFY.
127. E.D. Cooper, private communication.
128. E. Segrè, *Nuclei and Particles*, W.A. Benjamin, Reading, Massachusetts (1977).

Appendix A

Kinematics for Photonucleon Knockout Reactions

In this appendix the relativistic kinematics of the photon and nucleon involved in a photonuclear reaction is described. In a (γN) experiment the incident lab kinetic energy of the photon is given. Using the known masses of the target nucleus, photoemitted nucleon and residual nucleus all other kinematic quantities are determined.

The S -matrix, and hence the cross section, are evaluated in the center-of-mass coordinate frame and so the kinematic transformation to this frame from the laboratory coordinate frame is required. The relationship between the laboratory and center-of-mass energies of the photon is derived by equating the invariant mass-squared $[\sum_i E_i]^2 - [\sum_i \mathbf{p}_i]^2$ in the two frames. In the laboratory frame the total energy is

$$E_{\text{lab}} = E_{\gamma, \text{lab}} + m_T \quad (\text{A.1})$$

where m_T is the target nucleus rest mass and the vector sum of momenta is just $\mathbf{p}_{\gamma, \text{lab}}$. In the center-of-mass frame the total energy is

$$E_{\text{cm}} = E_{\gamma, \text{cm}} + \sqrt{E_{\gamma, \text{cm}}^2 + m_T^2} \quad (\text{A.2})$$

and the vector sum of momenta is zero. Thus

$$(E_{\gamma, \text{lab}} + m_T)^2 - \mathbf{p}_{\gamma, \text{lab}}^2 = [E_{\gamma, \text{cm}} + \sqrt{E_{\gamma, \text{cm}}^2 + m_T^2}]^2 \quad (\text{A.3})$$

Solving this equation for the photon center-of-mass energy gives

$$E_{\gamma, \text{cm}} = E_{\gamma, \text{lab}} \sqrt{\frac{m_T}{m_T + 2E_{\gamma, \text{lab}}}} \quad (\text{A.4})$$

The magnitude of the photoemitted nucleon momentum is related to the conserved total center-of-mass energy given in Eq. (A.2). Energy conservation requires that the total final center-of-mass energy, which is $E_{N, \text{cm}} + E_{F, \text{cm}}$ (where $E_{N, \text{cm}}$ is the total energy of the nucleon and $E_{F, \text{cm}}$ is the total energy of the residual nucleus), is precisely equal to the initial center-of-mass energy E_{cm} . Together with momentum conservation, which requires that $\mathbf{p}_{N, \text{cm}} = -\mathbf{p}_{F, \text{cm}}$ the following expression for the momentum of the nucleon is arrived at:

$$p_{N,cm} = \frac{1}{2} \sqrt{E_{cm}^2 - 2(m^2 + m_F^2) + [(m_F^2 - m^2)/E_{cm}]^2} \quad (\text{A.5})$$

where m is the nucleon rest mass and m_F is the rest mass of the residual nucleus.

The kinetic energy of the nucleon in the lab frame depends on the scattering angle and can be calculated straightforwardly from energy and momentum conservation arguments. This quantity is superfluous to the (γN) calculations, however, since all calculations are done in the center-of-mass frame. On the other hand, the kinetic energy of the nucleon in the rest frame of the recoil nucleus is required so that the appropriate energy dependent optical potential for the nucleon is used. This can be derived by equating the invariant mass-squared in the center-of-mass frame with the invariant mass-squared in the frame in which the residual nucleus remains at rest. The kinetic energy of the nucleon in this frame is

$$T_{N,lab} = \frac{E_{cm}^2 - (m_F + m)^2}{2m_F} \quad (\text{A.6})$$

For (N, γ) reactions, the kinematic relations are derived in a completely analogous manner. The results are:

$$p_{N,cm}^2 = m_T^2 \left[\frac{T_{N,lab}(T_{N,lab} + 2m)}{m^2 + m_T^2 + 2m_T(T_{N,lab} + m)} \right] \quad (\text{A.7})$$

$$E_{N,cm}^2 = p_{N,cm}^2 + m^2 \quad (\text{A.8})$$

$$E_{T,cm}^2 = p_{N,cm}^2 + m_T^2 \quad (\text{A.9})$$

$$E_{cm} = E_{N,cm} + E_{T,cm} \quad (\text{A.10})$$

$$E_{\gamma,cm} = (E_{cm}^2 - m_F^2)/2E_{cm} \quad (\text{A.11})$$

$$E_{F,cm}^2 = E_{\gamma,cm}^2 + m_F^2 \quad (\text{A.12})$$

$$E_{\gamma, \text{lab}} = \frac{(E_{N, \text{lab}} + m_T)^2 - p_{N, \text{lab}}^2 - m_F^2}{2(E_{N, \text{lab}} + m_T - p_{N, \text{lab}} \cos \theta_{\text{lab}})} \quad (\text{A.13})$$

For this case the target nucleus is the nucleus on which the nucleon is incident.

In most cases the cross sections for photonucleon knockout reactions are given in the center-of-mass frame. However, on occasion laboratory cross sections may be given and so the relationship between the laboratory and the center-of-mass cross sections is desirable. Because the total scattering cross section

$$\sigma_{\text{scatt}} = \int \frac{d\sigma}{d\Omega} d\Omega \quad (\text{A.14})$$

is a scalar, the integrand

$$\frac{d\sigma}{d\Omega} d\Omega = \frac{d\sigma}{d\Omega} d(\cos \theta) d\phi \quad (\text{A.15})$$

must be the same in every frame. In particular

$$\left. \frac{d\sigma}{d\Omega} \right)_{\text{cm}} = \left. \frac{d\sigma}{d\Omega} \right)_{\text{lab}} \frac{d(\cos \theta_{\text{lab}})}{d(\cos \theta_{\text{cm}})} \quad (\text{A.16})$$

gives the relationship between the center-of-mass and laboratory cross sections. The laboratory scattering angle is related to the center-of-mass scattering angle by⁽¹²⁰⁾

$$\tan \theta_{\text{lab}} = \frac{p_{\text{cm}} \sin \theta_{\text{cm}}}{\gamma^* (p_{\text{cm}} \cos \theta_{\text{cm}} + \beta^* E_{\text{cm}})} \quad (\text{A.17})$$

where β^* is the center-of-mass velocity in the lab frame and $\gamma^* = (1 - \beta^{*2})^{-1/2}$. The quantities p_{cm} and E_{cm} are the momentum and energy of the photoemitted nucleon. Using Eq. (A.17), it is straightforward to evaluate $[d(\cos \theta_{\text{lab}})/d(\cos \theta_{\text{cm}})]$ and hence find that

$$\left. \frac{d\sigma}{d\Omega} \right)_{\text{lab}} = \frac{\gamma^{*2} [\beta^{*2} p_{\text{cm}}^2 \cos^2 \theta_{\text{cm}} + 2\beta^* E_{\text{cm}} p_{\text{cm}} \cos \theta_{\text{cm}} + p_{\text{cm}}^2 + \beta^{*2} m^2]^{3/2}}{p_{\text{cm}}^2 (\beta^* E_{\text{cm}} \cos \theta_{\text{cm}} + p_{\text{cm}})} \left. \frac{d\sigma}{d\Omega} \right)_{\text{cm}} \quad (\text{A.18})$$

Appendix B

Numerov Integration of Second-Order Differential Equations

B.1 Homogeneous Equations

The second-order differential equation that has to be integrated in order to solve for the radial functions of a four-component solution of the Dirac equation is of the form

$$y''(r) = f(r) y(r) . \quad (\text{B.1})$$

The solution of this differential equation may be found numerically using the Numerov method⁽¹²¹⁾.

The Numerov method involves using a Taylor expansion for $y(r + h)$ and $y(r - h)$:

$$y(r + h) = \sum_{n=0}^{\infty} h^n \frac{y^{(n)}(r)}{n!} \quad (\text{B.2})$$

$$y(r - h) = \sum_{n=0}^{\infty} (-h)^n \frac{y^{(n)}(r)}{n!} . \quad (\text{B.3})$$

Adding these two equations gives

$$\frac{1}{2} [y(r + h) + y(r - h)] = y(r) + \frac{1}{2!} h^2 y''(r) + \frac{1}{4!} h^4 y^{(4)}(r) + \frac{1}{6!} h^6 y^{(6)}(r) + \dots . \quad (\text{B.4})$$

This equation is differentiated twice, multiplied by $(h^2/12)$ and then subtracted from Eq. (B.4) to get

$$\frac{1}{2} \left[y(r + h) - \frac{h^2}{12} y''(r + h) + y(r - h) - \frac{h^2}{12} y''(r - h) \right] = y(r) + \frac{5h^2}{12} y''(r) + O[h^6] . \quad (\text{B.5})$$

Using the differential equation (B.1) for y'' and dropping the terms of order h^6 gives

$$y(r + h) [1 - T(r + h)] + y(r - h) [1 - T(r - h)] = y(r) [2 + 10T(r)] \quad (\text{B.6a})$$

$$T(r) \equiv \frac{h^2}{12} f(r) . \quad (\text{B.6b})$$

Finally, Eq. (B.6a) can be rewritten in terms of the quantity

$$w(r) \equiv y(r) [1 - T(r)] \quad (\text{B.7})$$

as

$$w(r+h) + w(r-h) = \left[\frac{2 + 10T(r)}{1 - T(r)} \right] w(r) . \quad (\text{B.8})$$

It can be seen that the Numerov method is self-starting if the values of $w(0)$ and $w(h)$ are known. In practise, $w(0)$ is usually zero and the value of $w(h)$ is taken to be an arbitrary small number. The solution then will have a normalization that depends on the choice of $w(h)$. The solution may be renormalized to the desired normalization of the known asymptotic ($r \rightarrow \infty$) solution. The derivative may be found by subtracting Eq. (B.3) from Eq. (B.2) and following a procedure similar to that used for the function to eliminate the term proportional to h^3 . If terms of order h^5 are neglected, the derivative formula is

$$2h y'(r) = y(r+h) [1 - 2T(r+h)] - y(r-h) [1 - 2T(r-h)] . \quad (\text{B.9})$$

B.2 Inhomogeneous Equations

If the differential equation contains a source term

$$y''(r) = f(r) y(r) + g(r) \quad (\text{B.10})$$

then the same procedure as is followed for the homogeneous case results in the equations

$$w(r+h) + w(r-h) = \left[\frac{2 + 10T(r)}{1 - T(r)} \right] w(r) + z(r+h) + 10z(r) + z(r-h) \quad (\text{B.11a})$$

$$z(r) \equiv \frac{h^2}{12} g(r) \quad (\text{B.11b})$$

$$2h y'(r) = y(r+h) [1 - 2T(r+h)] - y(r-h) [1 - 2T(r-h)] - 2[z(r+h) - z(r-h)] . \quad (\text{B.12})$$

This integration procedure will give a particular solution for the inhomogeneous equation. Any linear combination of the solution to the homogeneous equation may be added to the particular solution to give a general solution for the inhomogeneous differential equation.

It is clear that the Numerov method will become increasingly accurate as the step size of the integration h is decreased. The size of h in turn determines the amount of computing time the algorithm requires. The Numerov method can be modified to be more

efficient⁽¹²²⁻¹²⁴⁾ but for the purpose of the (γ) calculation the aforementioned method is sufficient.

Appendix C

Numerics and the Calculation of Phase Shifts for the Nucleon Distorted Wave Function

C.1 The Continuum Nucleon Distorted Wave Function

The evaluation of the radial functions of the nucleon distorted wave reduces to numerically integrating Eq. (3.34a):

$$y''(r) + \left[a(r) - \frac{\kappa d'(r)}{r d(r)} - \frac{\kappa(\kappa + 1)}{r^2} \right] y(r) = 0 . \quad (\text{C.1})$$

This equation is integrated using the Numerov method (*cf.* Appendix B).

Small r Behaviour

For the purpose of the numerical integration it is necessary to know the quantity

$$f(r)y(r) \equiv - \left[a(r) - \frac{\kappa d'(r)}{r d(r)} - \frac{\kappa(\kappa + 1)}{r^2} \right] y(r) \quad (\text{C.2})$$

at two adjacent points of the integration mesh. Although $y(r)$ is regular at the origin, it is not clear what the behaviour of $f(r)y(r)$ is near the origin since $f(r)$ contains terms proportional to $1/r$ and $1/r^2$. Observing that $\kappa(\kappa + 1) = L(L + 1)$ leads to the conclusion that there are two distinct cases, namely $L = 0$ and $L > 0$. For $L = 0$ the asymptotic equation for small r is

$$y''(r) + \frac{1}{r} \frac{d'(r)}{d(r)} y(r) = 0 . \quad (\text{C.3})$$

Now $d(r)$ involves a linear combination of potentials (*cf.* Eq. (3.33b)) and so its radial derivative, which is related to the force experienced by the nucleon, should vanish at the origin. Therefore, for $L = 0$, $f(r)y(r) \xrightarrow{r \rightarrow 0} 0$ and the numerical integration may be started by taking the quantity $w(r)$, defined in Appendix B to be

$$w(r) = y(r) \left[1 - \frac{\hbar^2}{12} f(r) \right] , \quad (\text{C.4})$$

as zero at the origin and by arbitrarily setting $w(h)$ to be a small number which determines the normalization of the numerical solution.

For $L > 0$ the asymptotic equation for small r is

$$y''(r) - \frac{L(L+1)}{r^2} y(r) = 0 \quad (\text{C.5})$$

which shows that the regular solution near the origin goes as

$$y(r) \xrightarrow{r \rightarrow 0} cr^{l+1} \quad (\text{C.6})$$

where c is an arbitrary non-zero constant. For all the cases in which $L > 1$ it is clear that $f(r)y(r) \xrightarrow{r \rightarrow 0} 0$ and so the integration is started by taking $w(0) = 0$ and $w(h) = \xi$ (ξ is a small number). The case $L = 1$ presents a problem because if the result (C.6) is used then it is seen that $f(r)y(r) \xrightarrow{r \rightarrow 0} 2c$.

For the case $L = 1$ the solution near the origin is $y(r) = cr^2$. Therefore, if h is small enough then the first two values of $w(r)$ will be

$$w(0) = y(0) \left[1 - \frac{h^2}{12} f(0) \right] = -\frac{1}{6} h^2 c \quad (\text{C.7})$$

$$w(h) = y(h) \left[1 - \frac{h^2}{12} f(h) \right] = \frac{5}{6} h^2 c \quad (\text{C.8})$$

If $w(h) = \xi$ is chosen arbitrarily as before, then $w(0) = -\xi/5$. With the first two values of $w(r)$ specified, the numerical integration proceeds straightforwardly.

Large r Behaviour

The normalization of the solution is fixed by requiring that the radial function determined numerically have the same normalization as the analytic large r asymptotic solution. For the sake of simplicity the long range Coulomb interaction will be ignored in the present discussion. The modifications that come about when the Coulomb potential is included will be discussed later.

For large enough r the nuclear potentials will vanish and Eq. (C.1) becomes

$$y''(r) + \left[k^2 - \frac{L(L+1)}{r^2} \right] y(r) = 0 \quad (\text{C.9})$$

where k is the nucleon's asymptotic momentum. Equations (3.34b) and (3.33b) have been used to arrive at this result. For no potentials, Eq. (3.34b) can be simplified to

$$a(r) = E^2 - m^2 = k^2 \quad (\text{C.10})$$

The radial functions in the distorted wave expansion (3.32) are related to $y(r)$ by

$$y(r) = [d(r)]^{-1/2} r f_{LJ}(r) \quad (\text{C.11})$$

where $d(r)$ is defined in Eq. (3.33b). Therefore, for the case of vanishing potentials, Eq. (C.9) can be transformed into the equation

$$f_{LJ}''(r) + \frac{2}{r} f_{LJ}'(r) + \left[k^2 - \frac{L(L+1)}{r^2} \right] f_{LJ}(r) = 0 \quad (\text{C.12})$$

This familiar equation has the regular solution

$$f_{LJ}(r) = j_L(kr) \quad (\text{C.13})$$

where the $j_L(kr)$ are the spherical Bessel functions⁽⁶⁰⁾. The normalization of this solution corresponds exactly to the normalization chosen for the plane wave solution (3.23). The plane wave in this case is normalized with the delta function normalization

$$\frac{1}{(2\pi)^3} \frac{m}{E} \int \psi_{s,p}(\mathbf{x}) \psi_{s',p'}(\mathbf{x}) d^3x = \delta^3(\mathbf{p} - \mathbf{p}') \delta_{s,s'} \quad (\text{C.14})$$

The $(1/2\pi)^3(m/E)$ factor comes from the factors in Eq. (4.19).

The asymptotic form of the spherical Bessel function is

$$j_L(kr) \xrightarrow{r \rightarrow \infty} \frac{\sin(kr - L\pi/2)}{kr} \quad (\text{C.15})$$

This is the solution for the radial functions if no potentials are present. In analogy with the nonrelativistic case⁽⁶²⁾, the effect of the nuclear potentials will be to introduce a nuclear phase shift into the sinusoid. In more detail, the scattered wave will have a plane wave piece and outgoing spherical waves. This means that if $w_{LJ}(r)$ is defined as

$$w_{LJ}(r) \equiv kr f_{LJ}(r) \quad (\text{C.16})$$

and the regular solution (*i.e.*, the solution that goes asymptotically as $\sin(kr - L\pi/2)$) is written as $F_L(r)$ and the irregular solution (*i.e.*, the solution that goes asymptotically as $\cos(kr - L\pi/2)$) is written as $G_L(r)$ then

$$w_{LJ}(r) = F_L(r) + C_{LJ}[G_L(r) + i F_L(r)] \quad (\text{C.17})$$

$$w_{LJ}(r) \xrightarrow{r \rightarrow \infty} \sin(kr - L\pi/2) + C_{LJ} e^{i(kr - L\pi/2)} \quad (\text{C.18})$$

The quantity C_{LJ} is the coefficient of the scattered wave and is thus determined by the nuclear potentials. If C_{LJ} is defined to be

$$C_{LJ} \equiv -\frac{i}{2}(e^{2i\delta_{LJ}} - 1) \quad (\text{C.19})$$

then Eq. (C.18) becomes

$$w_{LJ}(r) \xrightarrow{r \rightarrow \infty} e^{i\delta_{LJ}} \sin(kr - L\pi/2 + \delta_{LJ}) \quad (\text{C.20})$$

which identifies δ_{LJ} as the nuclear phase shift.

The Coulomb potential introduces a logarithmic term and an additional phase shift into the asymptotic transcendental functions. The radial solutions of the Dirac equation with a Coulomb potential asymptotically are

$$F_{LJ}(r) \xrightarrow{r \rightarrow \infty} \sin(kr - \eta \ln 2kr - L\pi/2 + \Sigma_{LJ}) \quad (\text{C.21})$$

$$G_{LJ}(r) \xrightarrow{r \rightarrow \infty} \cos(kr - \eta \ln 2kr - L\pi/2 + \Sigma_{LJ}) \quad (\text{C.22})$$

where $\eta = Ze^2(E/p)$ is the Coulomb parameter and Σ_{LJ} is the Dirac Coulomb phase shift (the Dirac Coulomb wave functions are discussed in detail in Appendix D). Thus, when the Coulomb potential is included, the asymptotic form of $w_{LJ}(r)$ becomes

$$w_{LJ}(r) \xrightarrow{r \rightarrow \infty} e^{i(\Sigma_{LJ} + \delta_{LJ})} \sin(kr - \eta \ln 2kr - L\pi/2 + \Sigma_{LJ} + \delta_{LJ}) \quad (\text{C.23})$$

The nuclear phase shifts are calculated by matching the logarithmic derivatives of the numerical and analytic solutions at a radius where the nuclear potentials have vanished. The analytic solution is the obvious generalization of Eqs. (C.17) and (C.19)

$$w_{LJ}(r) = e^{i\Sigma_{LJ}} \{F_{LJ}(r) + C_{LJ}[G_{LJ}(r) + iF_{LJ}(r)]\} \quad (\text{C.24})$$

$$C_{LJ} \equiv -\frac{i}{2}(e^{2i\delta_{LJ}} - 1) \quad (\text{C.25})$$

Using these equations and remembering that the numerical solution has associated with it an arbitrary normalization, the matching equations are

$$N_{LJ} \mathcal{F}_{LJ}(r) = e^{i(\Sigma_{LJ} + \delta_{LJ})} [\cos\delta_{LJ} F_{LJ}(r) + \sin\delta_{LJ} G_{LJ}(r)] \quad (\text{C.26})$$

$$N_{LJ} \mathcal{F}'_{LJ}(r) = e^{i(\Sigma_{LJ} + \delta_{LJ})} [\cos\delta_{LJ} F'_{LJ}(r) + \sin\delta_{LJ} G'_{LJ}(r)] \quad (\text{C.27})$$

In these equations N_{LJ} renormalizes the numerical solution $\mathcal{F}_{LJ}(r)$ and the the right-

hand-side of Eq. (C.26) is precisely the quantity $w_{LJ}(r)$ of Eq. (C.24), when use has been made of Eq. (C.25). Equations (C.26) and (C.27) can be solved for the nuclear phase shift as

$$\delta_{LJ} = \tan^{-1} \left[\frac{\mathcal{F}'_{LJ}(r) F_{LJ}(r) - \mathcal{F}_{LJ}(r) F'_{LJ}(r)}{\mathcal{F}_{LJ}(r) G'_{LJ}(r) - \mathcal{F}'_{LJ}(r) G_{LJ}(r)} \right]. \quad (\text{C.28})$$

Once the nuclear phase shift is known, Eq. (C.26) can be used to evaluate the normalization constant N_{LJ} by which the numerical solution must be multiplied to get the desired normalization.

C.2 The Propagating Proton Wave Function

The evaluation of the radial functions of the propagating proton wave function reduces to numerically integrating Eq. (6.21a):

$$y''(r) + \left[a(r) - \frac{\kappa d''(r)}{r d(r)} - \frac{\kappa(\kappa + 1)}{r^2} \right] y(r) = h(r) \quad (\text{C.29})$$

This equation is integrated using the Numerov method for inhomogeneous equations (*cf.* Appendix B).

Small r Behaviour

For $r \rightarrow 0$ the source term on the right-hand-side of Eq. (C.29) vanishes. Thus, the small r behaviour of $y(r)$ is identical to that for the solution of the homogeneous equation (C.1): For $L \neq 1$ the integration is started by taking $w(0) = 0$ and $w(h) = \xi$. For $L = 1$ the first two values of $w(r)$ are $w(0) = -\xi/5$ and $w(h) = \xi$. The integration can then proceed with only the normalization of the numerical solution, which depends on the choice of the small number ξ , being undetermined.

Large r Behaviour

Equation (C.29) for large r takes the same form as the homogeneous equation because the source term $h(r)$ vanishes as the nuclear potentials vanish. Hence the asymptotic solutions are a linear combination of the Dirac Coulomb wave functions. The linear combination for the quantity $w_{LJ}(r) = krF_{LJ}(r)$ that satisfies the conditions of

an outgoing spherical wave and no incoming plane wave is

$$w_{LJ}(r) = e^{i\Sigma_{LJ}} C_{LJ} [G_{LJ}^{(c)}(r) + iF_{LJ}^{(c)}(r)] \quad (\text{C.30})$$

$$w_{LJ}(r) \xrightarrow{r \rightarrow \infty} e^{i\Sigma_{LJ}} C_{LJ} e^{i(kr - \eta \ln 2kr - L\pi/2 + \Sigma_{LJ})} . \quad (\text{C.31})$$

The Dirac Coulomb wave functions are now denoted with the superscript (c) to differentiate them from the propagating proton radial functions. The ratio of the proton to neutron velocities that is included in Eq. (6.22) is taken to be unity in these equations. The coefficient C_{LJ} is defined in terms of the nuclear phase shift in Eq. (C.25).

In order to determine the coefficient C_{LJ} , a linear combination of the numerical solutions of the homogeneous and inhomogeneous differential equations is matched to the expression (C.31) at a radius at which the nuclear potentials have effectively vanished. Denoting the homogeneous and inhomogeneous numerical solutions as $\mathcal{F}_{LJ}^{(P)}$ and $\mathcal{F}_{LJ}^{(H)}$ respectively, the matching equations are

$$\mathcal{F}_{LJ}^{(P)}(r) + N_{LJ} \mathcal{F}_{LJ}^{(H)}(r) = e^{i\Sigma_{LJ}} C_{LJ} [G_{LJ}^{(c)}(r) + iF_{LJ}^{(c)}(r)] \quad (\text{C.32a})$$

$$\mathcal{F}_{LJ}^{(P)'}(r) + N_{LJ} \mathcal{F}_{LJ}^{(H)'}(r) = e^{i\Sigma_{LJ}} C_{LJ} [G_{LJ}^{(c)'}(r) + iF_{LJ}^{(c)'}(r)] . \quad (\text{C.32b})$$

Solving these equations for the constants N_{LJ} and C_{LJ} gives

$$N_{LJ} = \frac{\mathcal{F}_{LJ}^{(P)'}(r) [G_{LJ}^{(c)}(r) + iF_{LJ}^{(c)}(r)] - \mathcal{F}_{LJ}^{(P)}(r) [G_{LJ}^{(c)'}(r) + iF_{LJ}^{(c)'}(r)]}{\mathcal{F}_{LJ}^{(H)}(r) [G_{LJ}^{(c)'}(r) + iF_{LJ}^{(c)'}(r)] - \mathcal{F}_{LJ}^{(H)'}(r) [G_{LJ}^{(c)}(r) + iF_{LJ}^{(c)}(r)]} \quad (\text{C.33})$$

$$C_{LJ} = e^{-i\Sigma_{LJ}} \frac{\mathcal{F}_{LJ}^{(H)}(r) \mathcal{F}_{LJ}^{(P)'}(r) - \mathcal{F}_{LJ}^{(H)'}(r) \mathcal{F}_{LJ}^{(P)}(r)}{\mathcal{F}_{LJ}^{(H)}(r) [G_{LJ}^{(c)'}(r) + iF_{LJ}^{(c)'}(r)] - \mathcal{F}_{LJ}^{(H)'}(r) [G_{LJ}^{(c)}(r) + iF_{LJ}^{(c)}(r)]} . \quad (\text{C.34})$$

Appendix D

The Dirac Coulomb Wave Functions

D.1 The Analytic Form of the Dirac Coulomb Wave Functions

For a Coulomb potential only, the coupled equations (3.30) for the upper and lower radial components of the Dirac wave function are

$$[E - m - V_c(r)] f_{LJ}(r) = - \left[\frac{d}{dr} + \frac{1 - \kappa}{r} \right] g_{LJ}(r) \quad (D.1a)$$

$$[E + m - V_c(r)] g_{LJ}(r) = \left[\frac{d}{dr} + \frac{1 + \kappa}{r} \right] f_{LJ}(r) \quad (D.1b)$$

where $V_c(r) = Ze^2/4\pi r$ is the Coulomb potential of a proton incident on a charge Z nucleus.

If $f(r) \equiv r f_{LJ}(r)$ and $g(r) \equiv r g_{LJ}(r)$, then Eqs. (D.1) become

$$\left[\frac{Ze^2}{4\pi r} - (E + m) \right] g(r) + f'(r) + \frac{\kappa}{r} f(r) = 0 \quad (D.2a)$$

$$\left[\frac{Ze^2}{4\pi r} - (E - m) \right] f(r) - g'(r) + \frac{\kappa}{r} g(r) = 0 \quad (D.2b)$$

With the definitions

$$x \equiv kr \quad (D.3a)$$

$$Z\alpha \equiv \frac{Ze^2}{4\pi} \quad (D.3b)$$

$$\epsilon_{(\pm)} \equiv E \pm m \quad (D.3c)$$

$$\eta_{(\pm)} \equiv \frac{Z\alpha}{k} \epsilon_{(\pm)} \quad (D.3d)$$

$$u(x) \equiv \frac{f(r)}{\sqrt{\epsilon_{(+)}}} \quad (D.3e)$$

$$v(x) \equiv \frac{g(r)}{\sqrt{\epsilon_{(-)}}} \quad (\text{D.3f})$$

Eqs. (D.2) become

$$\left[\frac{\eta_{(-)}}{x} - 1 \right] v(x) + u'(x) + \frac{\kappa}{x} u(x) = 0 \quad (\text{D.4a})$$

$$\left[\frac{\eta_{(+)}}{x} - 1 \right] u(x) - v'(x) + \frac{\kappa}{x} v(x) = 0 \quad (\text{D.4b})$$

Further defining the complex functions

$$F(x) \equiv u(x) + iv(x) \quad (\text{D.5a})$$

$$F^*(x) \equiv u(x) - iv(x) \quad (\text{D.5b})$$

results in the coupled equations

$$-\left[\frac{2i\kappa + \eta_{(+)} - \eta_{(-)}}{x} \right] F^*(x) = \left[\frac{\eta_{(+)} + \eta_{(-)}}{x} - 2 \right] F(x) + 2iF'(x) \quad (\text{D.6a})$$

$$\left[\frac{-2i\kappa + \eta_{(+)} - \eta_{(-)}}{x} \right] F(x) = \left[2 - \frac{\eta_{(+)} + \eta_{(-)}}{x} \right] F^*(x) + 2iF^{*'}(x) \quad (\text{D.6b})$$

A second-order differential equation for $F(x)$ is obtained by substituting $F^*(x)$ from Eq. (D.6a) into Eq. (D.6b). The resulting equation for $F(x)$ is

$$F''(x) + \frac{1}{x} F'(x) + \left[1 + \frac{i-2\eta}{x} + \frac{Z^2 \alpha^2 - \kappa^2}{x^2} \right] F(x) = 0 \quad (\text{D.7})$$

where $\eta = (\eta_{(+)} + \eta_{(-)})/2$ is the Coulomb parameter.

The equation for $F(x)$ is a general confluent equation defined in Eq. (13.1.35) of *Handbook of Mathematical Functions*⁽¹²⁵⁾, edited by M. Abramovitz and I. Stegun. In the following, frequent use will be made of results quoted in this book which will be denoted by AMS. Solutions for $F(x)$ are (AMS 13.1.36)

$$F(x) = x^t e^{-ix} M(t - i\eta, 2t + 1, 2ix) \quad (\text{D.8})$$

where $t = \pm \sqrt{\kappa^2 - \alpha^2}$ and M is the Kummer function (AMS 13.1.2). Taking the positive

value of the square root for t gives a regular function at the origin whereas the negative value of the square root will give an irregular solution.

The regular solution of Eq. (D.7) is

$$F_R(x) = x^s e^{-ix} M(s - i\eta, 2s + 1, 2ix) \quad (D.9)$$

where $s = \sqrt{\kappa^2 - \alpha^2}$. The regular parts of the functions f and g that appear in Eqs. (D.2) may be written in terms of the real and imaginary parts of $F_R(x)$ as

$$f_R(r) = \sqrt{\mathcal{E}_{(+)}} \Re e \lambda_R (kr)^s e^{-ikr} M(s - i\eta, 1 + 2s, 2ikr) \quad (D.10a)$$

$$g_R(r) = \sqrt{\mathcal{E}_{(-)}} \Im m \lambda_R (kr)^s e^{-ikr} M(s - i\eta, 1 + 2s, 2ikr) \quad (D.10b)$$

The constant λ_R is complex and therefore may be written

$$\lambda_R = N_R e^{i\phi_R} \quad (D.11)$$

Using the Kummer transformation AMS 13.1.27, Eqs. (D.10) become

$$f_R(r) = \frac{1}{2} \sqrt{\mathcal{E}_{(+)}} N_R (kr)^s \{ e^{i(\phi_R - kr)} M(s - i\eta, 1 + 2s, 2ikr) + e^{-i(\phi_R + kr)} M(s + 1 - i\eta, 1 + 2s, 2ikr) \} \quad (D.12a)$$

$$g_R(r) = -\frac{i}{2} \sqrt{\mathcal{E}_{(-)}} N_R (kr)^s \{ e^{i(\phi_R - kr)} M(s - i\eta, 1 + 2s, 2ikr) - e^{-i(\phi_R + kr)} M(s + 1 - i\eta, 1 + 2s, 2ikr) \} \quad (D.12b)$$

In order to get a constraint on the phase ϕ_R these expressions for $f_R(r)$ and $g_R(r)$ are substituted into the original differential equation (D.2a). Using recurrence relations and differential properties of the Kummer function ultimately leads to the result

$$e^{-2i\phi_R} = \frac{-(\kappa + i Z \alpha m/p)}{s + i\eta} \quad (D.13)$$

Although it is not obvious, ϕ_R is real. This can be verified by showing that $|e^{-2i\phi_R}|^2 = 1$.

The constant N_R depends on the asymptotic normalization convention chosen for $f_R(r)$. The asymptotic form of the Kummer function is (AMS 13.5.1)

$$M(s - i\eta, 2s + 1, 2ikr) \xrightarrow{r \rightarrow \infty} \frac{\Gamma(2s+1)}{|\Gamma(1+s+i\eta)|} 2^{-s} (kr)^{-s} e^{\pi\eta/2} \times e^{-i \arg \Gamma(1+s+i\eta) + i\pi s/2 + i\eta \ln 2kr} \quad (D.14)$$

which leads to

$$f_R(r) \xrightarrow{r \rightarrow \infty} \frac{N_R \sqrt{\varepsilon_{(+)}} \Gamma(2s+1) e^{\pi\eta/2}}{2^s |\Gamma(1+s+i\eta)|} \cos(\phi_R - kr - \arg \Gamma(1+s+i\eta) + \eta \ln 2kr + \pi s/2) \quad (D.15)$$

where $\Gamma(z)$ is the well-known gamma function⁽¹²⁵⁾. The asymptotic form of the regular part of $f(r)$ may be written

$$f_R(r) \xrightarrow{r \rightarrow \infty} \frac{1}{k} \sin(kr - \eta \ln 2kr - L\pi/2 + \Sigma_{LJ}) \quad (D.16)$$

where Σ_{LJ} is the Dirac Coulomb phase shift. This is consistent with the plane wave normalization of Eq. (C.14) and also is analogous to the nonrelativistic result for Coulomb functions. Comparing Eqs. (D.15) and (D.16) leads to the identifications

$$N_R = \frac{1}{k} \frac{2^s e^{-\pi\eta/2} |\Gamma(1+s+i\eta)|}{\sqrt{\varepsilon_{(+)}} \Gamma(2s+1)} \quad (D.17)$$

and

$$\Sigma_{LJ} = \arg \Gamma(1+s+i\eta) + \frac{\pi}{2}(L-s+1) - \phi_R \quad (D.18)$$

An irregular solution for $f(r)$ can be obtained by taking $t = -\sqrt{\kappa^2 - \alpha^2}$ in Eq. (D.8). The results for this irregular solution, denoted by $f_{-s}(r)$, can be obtained directly from Eqs. (D.10), (D.13) and (D.17) by replacing s by $-s$:

$$f_{-s}(r) = \sqrt{\varepsilon_{(+)}} \Re e \lambda_I (kr)^{-s} e^{-ikr} M(-s-i\eta, 1-2s, 2ikr) \quad (D.19a)$$

$$g_{-s}(r) = \sqrt{\varepsilon_{(-)}} \Im m \lambda_I (kr)^{-s} e^{-ikr} M(-s-i\eta, 1-2s, 2ikr) \quad (D.19b)$$

$$\lambda_I = N_I e^{i\phi_I} \quad (D.19c)$$

$$e^{-2i\phi_I} = \frac{-(\kappa + iZ\alpha m/p)}{-s+i\eta} \quad (D.19d)$$

$$N_I = \frac{1}{k} \frac{2^{-s} e^{-\pi\eta/2} |\Gamma(1-s+i\eta)|}{\sqrt{\varepsilon_{(+)}} \Gamma(1-2s)} \quad (D.19e)$$

However, in the calculation of the phase shifts described in Appendix C the irregular solution is taken to lead the regular solution in phase by 90° . Noting that any linear

combination of irregular and regular solutions is irregular, the irregular solution that leads $f_s(r) \equiv f_R(r)$ in phase by 90° can be shown to be⁽¹⁰⁾

$$f_I(r) = \cot\theta f_s(r) - \operatorname{cosec}\theta f_{-s}(r) \quad (\text{D.20a})$$

$$\theta = -\pi s - \tan^{-1}(\cot\pi s \tanh\pi\eta) + (-1)^K \pi/2 \quad (\text{D.20b})$$

Specifically, the asymptotic form of $f_I(r)$ will be

$$f_I(r) \xrightarrow{r \rightarrow \infty} \frac{1}{k} \cos(kr - \eta \ln 2kr - L\pi/2 + \Sigma_{LJ}) \quad (\text{D.21})$$

Once the upper component $f_{LJ}(r)$ is known, the lower component $g_{LJ}(r)$ may be evaluated using Eq. (D.2a). The asymptotic forms of the regular and irregular parts of the the lower component can therefore be obtained by using Eqs. (D.16) and (D.21) in Eq. (D.2a) to get

$$g_R(r) \xrightarrow{r \rightarrow \infty} \frac{1}{k} \left[\frac{p}{E+m} \right] \cos(kr - \eta \ln 2kr - L\pi/2 + \Sigma_{LJ}) \quad (\text{D.22a})$$

$$g_I(r) \xrightarrow{r \rightarrow \infty} -\frac{1}{k} \left[\frac{p}{E+m} \right] \sin(kr - \eta \ln 2kr - L\pi/2 + \Sigma_{LJ}) \quad (\text{D.22a})$$

D.2 Numerical Evaluation of the Dirac Coulomb Functions

The regular and irregular Dirac Coulomb functions of Eqs. (D.10a) and (D.20a) can be evaluated numerically using a power series expansion for the Kummer function⁽¹⁰⁾. This method involves very accurate and time-consuming computations. As an alternative it is possible to express the Kummer functions M in terms of Coulomb functions. Since well-established computer subroutines have been written for the Coulomb functions, this method is used to compute Dirac Coulomb functions⁽¹²⁶⁾.

The upper regular solution (D.10a) contains $M(s - i\eta, 1 + 2s, 2ikr)$. The recurrence relations AMS 13.4.3 and AMS 13.4.4 can be used to get

$$M(s - i\eta, 1 + 2s, 2ikr) = \frac{s - i\eta}{-2s(2s + 1)} 2ikr M(s + 1 - i\eta, 2s + 2, 2ikr) + M(s - i\eta, 2s, 2ikr) \quad (\text{D.23})$$

The Kummer function is related to the regular Coulomb function $F_L(\eta, x)$ by

$$M(L+1-i\eta, 2L+2, 2ix) = e^{ix} F_L(\eta, x) x^{-L-1} / C_L(\eta) \quad (\text{D.24a})$$

$$C_L(\eta) = \frac{2^L e^{-\pi\eta/2} |\Gamma(L+1+i\eta)|}{\Gamma(2L+2)} \quad (\text{D.24b})$$

(AMS 13.6.8 and AMS 14.1.7 respectively). Using Eqs. (D.23), (D.24), and (D.17) in Eq. (D.12a) gives

$$f_R(r) = \frac{1}{k} \left[\frac{(s \sin\phi_R - \eta \cos\phi_R)}{s} F_s(\eta, kr) + \frac{\sqrt{s^2 + \eta^2}}{s} \cos\phi_R F_{s-1}(\eta, kr) \right]. \quad (\text{D.25})$$

This analytic form can easily be computed if an algorithm is available for computing Coulomb functions for non-integer order s and $s-1$.

It is not straightforward to get a similar expression for the irregular upper component (D.20a). However, in analogy with the regular solution (D.25), the following expression may be inferred to be the irregular solution:

$$f_I(r) = \frac{1}{k} \left[\frac{(s \sin\phi_R - \eta \cos\phi_R)}{s} G_s(\eta, kr) + \frac{\sqrt{s^2 + \eta^2}}{s} \cos\phi_R G_{s-1}(\eta, kr) \right]. \quad (\text{D.26})$$

This expression is obtained by replacing the regular Coulomb function in Eq. (D.25) by the irregular Coulomb function $G_L(\eta, kr)$. An indication that this is the correct form can be seen from the asymptotic behaviour of Eq. (D.26). Asymptotically,

$$G_L(\eta, kr) \xrightarrow{r \rightarrow \infty} \cos(kr - \eta \ln 2kr - L\pi/2 + \sigma_L) \quad (\text{D.27a})$$

$$\sigma_L = \arg \Gamma(1 + s + i\eta) \quad (\text{D.27b})$$

(AMS 14.5.6). Using Eqs. (D.27) as well as the identity

$$\sigma_{s-1} = \sigma_s - \tan^{-1} \eta/s \quad (\text{D.28})$$

(AMS 14.5.7) in Eq. (D.26) results in the asymptotic form

$$f_I(r) \xrightarrow{r \rightarrow \infty} \frac{1}{k} \cos(kr - \eta \ln 2kr - L\pi/2 + \Sigma_{LJ}) \quad (\text{D.29})$$

which is precisely what is required (*cf.* Eq. (D.21)). Results of Eq. (D.26) have further been tested against the power series method results and the agreement is excellent⁽¹²⁷⁾.

Similar considerations for the regular and irregular parts of the lower component lead

to

$$g_R(r) = \frac{1}{k} \left(\frac{p}{E+m} \right) \left[\frac{-(s \cos \phi_R + \eta \sin \phi_R)}{s} F_s(\eta, kr) + \frac{\sqrt{s^2 + \eta^2}}{s} \sin \phi_R F_{s-1}(\eta, kr) \right] \quad (\text{D.30a})$$

$$g_I(r) = \frac{1}{k} \left(\frac{p}{E+m} \right) \left[\frac{-(s \cos \phi_R + \eta \sin \phi_R)}{s} G_s(\eta, kr) + \frac{\sqrt{s^2 + \eta^2}}{s} \sin \phi_R G_{s-1}(\eta, kr) \right]. \quad (\text{D.30b})$$

Appendix E

Numerics for the Bound Nucleon Wave Function

The evaluation of the radial functions of the bound nucleon wave function reduces to numerically integrating Eq. (3.49a)

$$y''(r) + a(r)y(r) = 0 \quad (\text{E.1})$$

where $a(r)$ is defined by Eqs. (3.49b), (3.47b), (3.47c) and (3.46). This equation is integrated using the Numerov method (*cf.* Appendix B). In this case the quantity $w(r)$ defined in Appendix B is

$$w(r) = y(r) \left[1 - \frac{\hbar^2}{12} a(r) \right]. \quad (\text{E.2})$$

In order to start the integration this quantity must be known at two consecutive points.

The value of $w(r)$ at the origin and $r = h$ is found by arguments very similar to those for the distorted wave case described in Appendix C. For the case $L_B = 0$, $a(r)$ near the origin is

$$a(r) \xrightarrow[r \rightarrow 0]{L_B = 0} V_1(r)V_2(r) \quad (\text{E.3})$$

and so $w(0) = 0$ since $y(r)$ is regular at the origin. Choosing $w(h) = \xi$ to be a small number (associated to the overall normalization of the solution) allows the integration to proceed. For the case $L_B > 0$, Eq. (E.1) near the origin becomes

$$y''(r) - \frac{L_B(L_B + 1)}{r^2} y(r) = 0 \quad (\text{E.4})$$

which is precisely the same as Eq. (C.5). This suggests that for $L_B > 0$

$$y(r) \xrightarrow[r \rightarrow 0]{L_B > 0} cr^{L_B + 1}. \quad (\text{E.5})$$

Thus, for $L_B = 1$ the integration is started by taking $w(0) = -\xi/5$ and $w(h) = \xi$ whereas for $L_B > 1$ the initial values of $w(r)$ are $w(0) = 0$ and $w(h) = \xi$.

A further numerical problem exists in solving Eq. (E.1), which can be seen by looking at the asymptotic form of $y(r)$. For $r \rightarrow \infty$ Eq. (E.1) becomes

$$y''(r) = E_b(2m - E_b) y(r) \quad (\text{E.6})$$

the physical solution to which is

$$y(r) \xrightarrow{r \rightarrow \infty} e^{-\xi r} \quad (\text{E.7a})$$

$$\xi = \sqrt{E_b(2m - E_b)} \quad (\text{E.7b})$$

A typical radial solution for the bound state is shown in Fig. E.1. This solution has an exponentially damped tail which is required because the nucleon is localized in space (this behaviour is what causes the radial integrals in the S -matrix for photonucleon knockout reactions to converge). Now if the differential equation is integrated outwards from $r = 0$ the undesired exponentially increasing solution would eventually dominate due to the imprecision in the numerical integration.

The solution to this problem lies in integrating the equation from $r = 0$ to a radius near the peak of the function $y(r)$ (call this radius the matching radius) and integrating backwards from some large radius where the function is small to the matching radius. In order to carry out the inward integration the value of $y(r)$ must be known at two consecutive points for large r . Since $a(r)$ is finite for large r , knowing $y(r)$ will

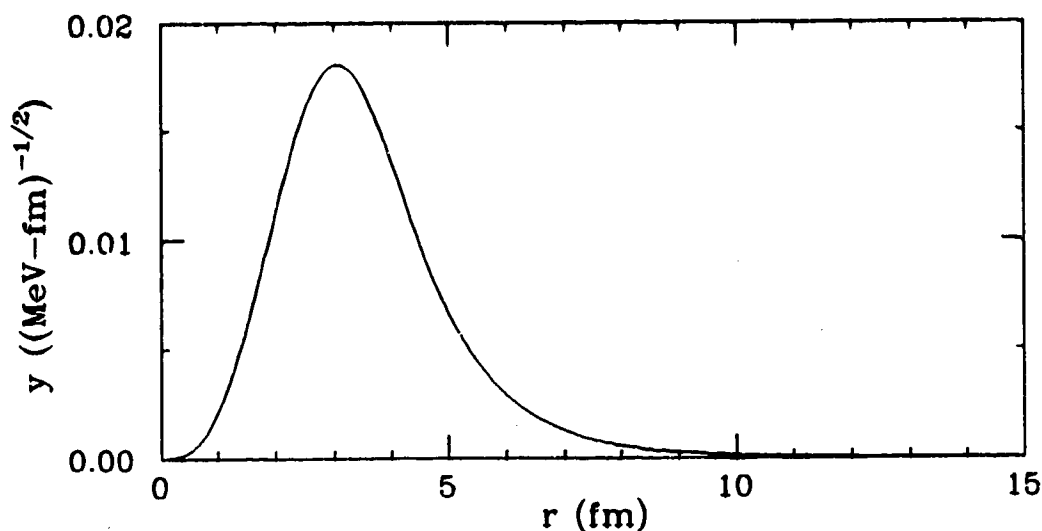


Fig. 47: The radial function $y(r)$ for the $1d_{3/2}$ proton of ^{40}Ca . The Woods-Saxon binding potentials for this case have vector and scalar strengths of 320.0 MeV and -398.3 MeV respectively and the geometry parameters are $R = 3.73$ fm and $a = 0.6$ fm.

determine $w(r)$. By large r it is meant that the potentials are negligible. For this case Eq. (E.1) is

$$y''(r) = \left[E_b(2m - E_b) + \frac{L_B(L_B + 1)}{r^2} \right] y(r) . \quad (\text{E.8})$$

The asymptotic behaviour of $y(r)$ suggests that the solution for large r can be written

$$y(r) = h(r) e^{-\xi r} \quad (\text{E.9})$$

with ξ defined in Eq. (E.7b). The equation for h then is

$$h''(x) - 2h'(x) - \frac{L_B(L_B + 1)}{x^2} h(x) = 0 \quad (\text{E.10})$$

where $x \equiv \xi r$. Expanding $h(x)$ in a power series as

$$h(x) = \sum_{n=0}^{\infty} \frac{a_n}{x^n} \quad (\text{E.11})$$

and substituting this into Eq. (E.10) yields a recursion relation for the coefficients a_n

$$a_n = \frac{1}{2n} [L_B(L_B + 1) - n(n - 1)] a_{n-1} . \quad (\text{E.12})$$

Clearly the series will terminate at the coefficient a_N where $N = L_B + 1$. The normalization is arbitrarily fixed by letting $a_0 = 1$. For a given L_B , two consecutive values of y at $r = R$ and $r = R - h$ can be found by using Eqs. (E.11) and (E.12). The inward integration can then proceed.

At the matching radius the value of the functions and their derivatives arrived at from the outward and inward integrations will not necessarily match. The logarithmic derivatives are matched by adjusting the potential strengths or the binding energy and then the functions are renormalized on both sides to meet smoothly. The overall normalization is then adjusted so that the volume integral of the modulus of the bound state wave function is unity, *i.e.*,

$$\int r^2 dr [f_B^2(r) + g_B^2(r)] = 1 . \quad (\text{E.13})$$

Appendix F

Calculation of Observables for Photonucleon Knockout Reactions

For the purpose of calculating observables for (γ, N) reactions, the S -matrix is written as in Eq. (4.36a)

$$S_{fi} = \frac{e}{2\pi} \frac{J_i J_f (J_B)}{\sqrt{2J_f + 1}} \left(\frac{E + m}{\omega E} \right)^{1/2} \delta(E - \omega - E_B) Z_{J_f M_B}^{\xi}(\theta) \quad (\text{F.1})$$

for the special cases of $J_i = 0$ or $J_f = 0$, with $Z_{J_f M_B}^{\xi}(\theta)$ defined by Eq. (4.36b). Implicit also in this expression is that the sum over initial and final nuclear polarizations will reduce to a sum over the spin projection M_B of the bound nucleon.

F.1 Cross Section

The cross section for (γ, N) reactions is obtained from the S -matrix as follows:

(1) Square S_{fi} to obtain a transition probability:

$$|S_{fi}|^2 = \frac{e^2}{4\pi^2} \frac{J_i^2 J_f^2 (J_B)^2}{(2J_f + 1)^2} \frac{E + m}{\omega E} [\delta(E - \omega - E_B)]^2 |Z_{J_f M_B}^{\xi}(\theta)|^2 \quad (\text{F.2})$$

(2) Divide by the time to form a rate:

Following Bjorken and Drell⁽¹²⁾, the energy delta function would be smeared out if transitions were considered in a time interval $(-T/2, T/2)$, i.e.,

$$2\pi \delta(E_f - E_i) \rightarrow \int_{-T/2}^{T/2} dt e^{i(E_f - E_i)t} = \frac{2\sin[(T/2)(E_f - E_i)]}{E_f - E_i} \quad (\text{F.3})$$

This suggests that for large but finite T

$$[2\pi \delta(E_f - E_i)]^2 \rightarrow \frac{4\sin^2[(T/2)(E_f - E_i)]}{(E_f - E_i)^2} \quad (\text{F.4})$$

The area under the curve defined by the expression (F.4), considered as a function of E_f , is $2\pi T$ and so the identification

$$[2\pi \delta(E_f - E_i)]^2 = [2\pi \delta(0)] 2\pi \delta(E_f - E_i) = 2\pi T \delta(E_f - E_i) \quad (\text{F.5})$$

is made. The time T may therefore be written

$$T = 2\pi \delta(0) \quad (\text{F.6})$$

The rate will then be

$$\frac{|S_{fi}|^2}{T} = \frac{\alpha}{2\pi^2} \frac{J_{J_i J_f}^2(J_B)}{(2J_f + 1)} \frac{E + m}{\omega E} \delta(E - \omega - E_B) |Z_{J_f M_B}^{\xi}(\theta)|^2 \quad (\text{F.7})$$

where $\alpha = e^2/4\pi \cong 1/137$ is the fine structure constant.

(3) Divide by the incident flux to give the probability of finding a proton in a unit phase space element around momentum p due to the interaction of one photon with one target nucleus:

Since the speed of light $c = 1$ is a constant in any reference frame, the incident flux will be

$$J_{\text{inc}} = \frac{c}{(2\pi)^3} = \frac{1}{(2\pi)^3} \quad (\text{F.8})$$

The $(2\pi)^3$ factor comes from the normalization convention chosen for the photon, *i.e.* (cf. Eq. (4.16)),

$$A^\mu(x) \sim \frac{\epsilon^\mu}{(2\omega)^{1/2} (2\pi)^{3/2}} [e^{-ik \cdot x} + e^{ik \cdot x}] \quad (\text{F.9})$$

Normally the flux is $J = (\text{velocity}/\text{volume})$, but for this case the δ -function normalization was used for the photon. If the photon were normalized to unit probability in a box of volume V , the four-vector potential would be

$$A^\mu(x) \sim \frac{\epsilon^\mu}{(2\omega)^{1/2} V^{1/2}} [e^{-ik \cdot x} + e^{ik \cdot x}] \quad (\text{F.10})$$

The energy in the wave A^μ would then be precisely ω , *i.e.*,

$$U = \frac{1}{2} \int_V d^3x (E^2 + B^2) = \int_V d^3x B^2 = \int_V d^3x (\nabla \times \mathbf{A})^2 = \omega \quad (\text{F.11})$$

The flux for this case would be

$$J_{\text{inc}} = \frac{c}{V} = \frac{1}{V} \quad (\text{F.12})$$

It can be seen that in going from the box to the δ -function normalization involves the replacement of V by $(2\pi)^3$. Thus, for the case under consideration

$$\frac{|S_{fi}|^2}{J_{\text{inc}} T} = \frac{\alpha}{2\pi^2} (2\pi)^3 \frac{J_{J_i J_f}^2(J_B)}{(2J_f + 1)} \frac{E + m}{\omega E} \delta(E - \omega - E_B) |Z_{s_f M_B}^\xi(\theta)|^2 \quad (\text{F.13})$$

(4) Sum over the phase space:

For the δ -function normalization the phase space sum involves an integral over all possible proton momenta. Since $E^2 = p^2 + m^2$ the identity $p dp = E dE$ holds and thus

$$\begin{aligned} \int \frac{|S_{fi}|^2}{J_{\text{inc}} T} d^3p &= \frac{\alpha}{2\pi^2} (2\pi)^3 \frac{J_{J_i J_f}^2(J_B)}{(2J_f + 1)} \int \frac{E + m}{\omega E} \delta(E - \omega - E_B) |Z_{s_f M_B}^\xi(\theta)|^2 p E dE d\Omega \\ &= 4\pi\alpha \frac{J_{J_i J_f}^2(J_B)}{(2J_f + 1)} \frac{p(E + m)}{\omega} |Z_{s_f M_B}^\xi(\theta)|^2 d\Omega \end{aligned} \quad (\text{F.14})$$

where the nucleon energy is understood to be determined by energy conservation considerations (*cf.* Appendix A).

(5) For unpolarized photons and targets, and if the polarization of the nucleon is not measured, then average over the initial and sum over the final polarizations:

$$\frac{d\sigma}{d\Omega} = \frac{1}{2} \frac{1}{2J_i + 1} 4\pi\alpha \frac{J_{J_i J_f}^2(J_B)}{(2J_f + 1)} \frac{p(E + m)}{\omega} \sum_{s_f M_B \xi} |Z_{s_f M_B}^\xi(\theta)|^2 \quad (\text{F.15})$$

The final result for the unpolarized (γ, N) cross section is

$$\frac{d\sigma}{d\Omega} = \frac{2\pi\alpha p(E + mc^2)}{(2J_i + 1)(2J_f + 1)\hbar c p_\gamma} J_{J_i J_f}^2(J_B) \sum_{s_f M_B \xi} |Z_{s_f M_B}^\xi(\theta)|^2 \quad (\text{F.16})$$

In this expression the units of \hbar and c have been included to give the cross section in the proper units of square fermis. The sum over the photon polarizations includes the two independent choices $\xi = 0$ and $\xi = \pi/2$.

The cross section for the reverse (N, γ) reaction is calculated in a similar manner.

The differences are as follows:

(1) The incident nucleon flux in the center-of-mass frame is

$$J_{\text{inc}} = \frac{|\mathbf{v}|}{(2\pi)^3} = \frac{1}{(2\pi)^3} \frac{p}{E} \quad (\text{F.17})$$

where \mathbf{v} is the velocity of the nucleon. This result is arrived at by evaluating the relativistic flux operator α between plane wave states:

$$\mathbf{J} = \psi_s^\dagger \alpha \psi_s \quad (\text{F.18a})$$

where

$$\psi_s = \frac{1}{(2\pi)^{3/2}} \left(\frac{m}{E}\right)^{1/2} \left(\frac{E+m}{2m}\right)^{1/2} \begin{bmatrix} 1 \\ \frac{\boldsymbol{\sigma} \cdot \mathbf{p}}{E+m} \end{bmatrix} e^{-i\mathbf{p} \cdot \mathbf{x}} \chi_{1/2}^s. \quad (\text{F.18b})$$

(2) The phase space integration is over the photon momentum $\int d^3 p_\gamma$.

(3) The spin average results in the factor

$$\frac{1}{2} \frac{1}{2J_i + 1}$$

where J_i is the spin of the target nucleus.

The final result for the unpolarized (N, γ) cross section is

$$\frac{d\sigma}{d\Omega} = \frac{2\pi\alpha p_\gamma (E + mc^2)}{(2J_i + 1)^2 \hbar c p} g_{J_i J_f}^2(J_B) \sum_{s_f M_B \xi} |Z_{s_f M_B}^\xi(\theta)|^2. \quad (\text{F.19})$$

This equation may also be arrived at from the principle of detailed balance⁽⁵⁹⁾.

F.2 Polarization

The polarization of the photoemitted nucleon is calculated from the S -matrix using the density matrix formalism⁽¹²⁸⁾. This method is the most straightforward for the case under consideration because the quantization axis is chosen to be parallel to the photon momentum direction, which is in the scattering plane. The density matrix for the outgoing nucleon can be written

$$\rho = \frac{1}{2} \frac{1}{(2J_i + 1)} MM^\dagger \quad (\text{F.20})$$

where M is the scattering amplitude. The M -matrix is related to S -matrix by the requirement that

$$\frac{d\sigma}{d\Omega} = \text{tr} \rho . \quad (\text{F.21})$$

This equation may be compared with Eq. (F.16) to get

$$M_{s_f M_B}^{\xi} = \left(\frac{4\pi\alpha p (E + mc^2)}{(2J_f + 1) \hbar c p_{\gamma}} \right)^{1/2} \mathcal{D}_{J_f J_f}^{(J_B)} Z_{s_f M_B}^{\xi} \quad (\text{F.22})$$

The trace in Eq. (F.21) is equivalent to a sum over the polarizations s_f , M_B and ξ , *i.e.*, Z can be thought of as a $2 \times (2J_B + 1) \times 2$ matrix labelled by the spin projections s_f , M_B and ξ respectively.

The polarization defined by Eq. (4.40) is the expectation value of the Pauli spin matrix σ_y . In the density matrix formalism this is given by

$$P(\theta) = \frac{\text{tr} \rho \sigma_y}{\text{tr} \rho} = \frac{\text{tr}(Z Z^{\dagger} \sigma_y)}{\text{tr}(Z Z^{\dagger})} . \quad (\text{F.23})$$

Writing

$$Z = \begin{bmatrix} Z_{-1/2 - M_B}^{\xi} & Z_{-1/2 - M_B + 1}^{\xi} & \cdots & Z_{-1/2 M_B}^{\xi} \\ Z_{1/2 - M_B}^{\xi} & Z_{1/2 - M_B + 1}^{\xi} & \cdots & Z_{1/2 M_B}^{\xi} \end{bmatrix} \quad (\text{F.24})$$

and evaluating the traces leads to the result

$$P(\theta) = \frac{2g_m \sum_{M_B \xi} [Z_{1/2 M_B}^{\xi}(\theta) Z_{-1/2 M_B}^{\xi *}(\theta)]}{\sum_{s_f M_B \xi} |Z_{s_f M_B}^{\xi}|^2} . \quad (\text{F.25})$$

Since time reversal invariance is a good symmetry, the analyzing power $A(\theta)$ for (N, γ) reactions will be given by this expression as well.